

Universidad de Málaga
Escuela Técnica Superior de Ingeniería de Telecomunicación
(Programa de doctorado en Ingeniería de Telecomunicación)



TESIS DOCTORAL

Suspended Waveguide Platforms for Mid-Infrared Group IV Photonics

Autor:

ALEJANDRO SÁNCHEZ POSTIGO

Directores:


J. GONZALO WANGÜEMERT PÉREZ
ALEJANDRO ORTEGA MOÑUX

2019



UNIVERSIDAD
DE MÁLAGA

AUTOR: Alejandro Sánchez Postigo

 <http://orcid.org/0000-0003-4782-0105>

EDITA: Publicaciones y Divulgación Científica. Universidad de Málaga



Esta obra está bajo una licencia de Creative Commons Reconocimiento-NoComercial-SinObraDerivada 4.0 Internacional:

<http://creativecommons.org/licenses/by-nc-nd/4.0/legalcode>

Cualquier parte de esta obra se puede reproducir sin autorización pero con el reconocimiento y atribución de los autores.

No se puede hacer uso comercial de la obra y no se puede alterar, transformar o hacer obras derivadas.

Esta Tesis Doctoral está depositada en el Repositorio Institucional de la Universidad de Málaga (RIUMA): riuma.uma.es





D. Juan Gonzalo Wangüemert Pérez y **D. Alejandro Ortega Moñux**, profesores doctores del Departamento de Ingeniería de Comunicaciones de la Universidad de Málaga,

CERTIFICAN:

Que D. Alejandro Sánchez Postigo, Ingeniero de Telecomunicación, ha realizado en el Departamento de Ingeniería de Comunicaciones de la Universidad de Málaga, bajo su dirección, el trabajo de investigación correspondiente a su TESIS DOCTORAL, titulada:

Suspended Waveguide Platforms for Mid-Infrared Group IV Photonics

En dicho trabajo se ha expuesto el desarrollo de nuevas plataformas fotónicas integradas para la banda del infrarrojo medio. En concreto, se han propuesto las plataformas de guiado de silicio suspendido y de germanio suspendido con rejillas laterales en régimen sublongitud de onda. Se han diseñado, fabricado y demostrado experimentalmente guías de onda a diferentes longitudes de onda, entre las que destaca la de $7.67 \mu\text{m}$. Asimismo, el problema del acoplo chip-fibra, cuya resolución es imprescindible para el desarrollo de cualquier plataforma integrada competitiva, se ha abordado mediante el diseño de acopladores chip-fibra de alta eficiencia y banda ancha, a saber: una microantena de germanio suspendido y un acoplador de rejilla de orden cero. Los resultados presentados han dado lugar a publicaciones en revistas y a aportaciones a congresos internacionales.

Por todo ello, consideran que esta Tesis es apta para su presentación al tribunal que ha de juzgarla. Y para que conste a efectos de lo establecido en el Real Decreto 99/2011, de 28 de enero, por el que se regulan las enseñanzas oficiales de doctorado, AUTORIZAN la presentación de esta Tesis en la Universidad de Málaga.

Málaga, a ____ de _____ de 2019

Fdo.: Dr. D. J. Gonzalo Wangüemert Pérez

Fdo.: Dr. D. Alejandro Ortega Moñux

E.T.S.I. Telecomunicación, Campus de Teatinos, 29071 MÁLAGA, Tlf.: 952131440





UNIVERSIDAD
DE MÁLAGA

Suspended Waveguide Platforms for Mid-Infrared Group IV Photonics

Alejandro Sánchez Postigo



UNIVERSIDAD
DE MÁLAGA

*A mis padres,
a abuela Pepa,
a abuelo Paco*

AGRADECIMIENTOS

Durante los cuatro años que han transcurrido desde el inicio del trabajo de investigación que ha culminado en esta tesis, he conocido a personas que, de una forma u otra, consciente o inconscientemente, interesada o desinteresadamente, han contribuido a que ahora mismo yo esté escribiendo estas líneas. Quiero expresar mi gratitud a aquéllas que han tenido un impacto positivo más directo en este trabajo.

Desde antes de empezar esta tesis doctoral, Gonzalo Wangüemert Pérez y Alejandro Ortega Moñux, mis directores, me han transmitido sus conocimientos y me han ayudado para seguir adelante pese a las dificultades técnicas, muchas, que surgían. Estas actitudes, que harían merecedores de ser nombrados en esta página a cualesquiera otros directores de tesis, son, en el caso de Gonzalo y Alejandro, las menos importantes. Lo que más les agradezco es su dedicación completa y su disponibilidad casi constante para solucionar cualquier problema, no sólo académico, sino sobre todo personal; agradezco que siempre creyeran en mí y en mi trabajo, incluso cuando yo mismo no lo hacía; agradezco su habilidad para captar lo que me afligía y animarme aun cuando yo no lo pedía; agradezco que, siendo ambos tan distintos entre sí, se complementasen para ofrecerme, dependiendo del momento y la situación, la ayuda que yo necesitaba; agradezco, en fin, que durante este tiempo se hayan comportado no como directores o jefes, sino como maestros y amigos.

Hubo *papers* en los que descubrí, justo antes de su envío a la revista correspondiente, pequeños errores que desembocaron en instantes de crisis y pánico. A Íñigo Molina agradezco que, en esos momentos de angustia, siempre fuera capaz de dar una idea sencilla que me permitiese salvar el obstáculo. Le agradezco su esfuerzo para que esos artículos —y otros de mis trabajos— acabasen publicados.

A Robert Halir agradezco la ayuda técnica y académica (¡y burocrática!) que me ha proporcionado siempre que se la he pedido. Le agradezco, sobre todo, su pragmatismo, rigor y eficacia, que me han servido de inspiración durante los últimos años.

En 2017 realicé mi primera estancia de investigación, en el National Research Council de Canadá. Allí dirigió mi trabajo el doctor Pavel Cheben, quien me causó una honda impresión. Lo que realmente me asombró no fue su excelencia científica —que Pavel es una eminencia en el campo de la fotónica integrada es bien sabido por todos—, sino su personalidad. No recuerdo haber conocido nunca una persona tan generosa y hospitalaria y que valore el concepto de amistad con tanta energía, lealtad y justicia. A Pavel agradezco el cariño y la devoción con que me acogió en Ottawa y con los que me ha tratado en nuestras conversaciones telefónicas y telemáticas desde que volví a Málaga. Le agradezco el tiempo que ha invertido y el esfuerzo que ha realizado para que yo tuviese resultados científicos de calidad en esta tesis y en mi currículo. Le agradezco, además,

haberme enseñado el afán por alcanzar la perfección, la pulcritud y el estilo depurado al escribir artículos científicos.

A los doctores Jens Schmid y Dan-Xia Xu, que me asistieron cuando Pavel estaba ausente, agradezco el trato amable que me dieron durante mi visita al National Research Council. Dan-Xia, con su amor por la naturaleza, consiguió que mi tiempo en Canadá fuese más agradable.

Entre 2018 y 2019 realicé dos estancias en la Universidad de Southampton, que han sido decisivas para la culminación satisfactoria del trabajo central de esta tesis. Al profesor Goran Mashanovich agradezco que me recibiese en su grupo de investigación como si fuese yo uno más de sus doctorandos, agradezco que me proporcionase los medios materiales necesarios —imprescindibles— para el desarrollo de mi tesis y, sobre todo, agradezco su extraordinaria amabilidad.

A los doctores Milos Nedeljkovic y Jordi Soler Penadés agradezco el soporte técnico que me brindaron diariamente durante mis estancias con ellos en Southampton, así como su empeño por conseguir que funcionasen los dispositivos suspendidos de silicio y de germanio desarrollados en esta tesis. Les agradezco también a ellos su amabilidad. A Jordi, además, agradezco que siga fabricando y midiendo dispositivos para obtener todavía más resultados, y le agradezco la lectura y corrección de la sección de esta tesis referente a la fabricación de estructuras suspendidas.

Por último, me gustaría recordar en esta página a mis compañeros del Laboratorio 1.3.2, con los que he compartido tantas horas de trabajo y ocio durante los últimos años.

A. S. P.

Málaga, septiembre de 2019

Quisiera dedicar el espacio que me queda para escribir unas palabras de agradecimiento a mis padres. Ahora, tras varios intentos, tras varias líneas borradas y reescritas, me doy cuenta de que es una tarea fallida. He fracasado y lo seguiré haciendo. Todo agradecimiento hacia ellos recogido en estas páginas sería finito y, por tanto, limitado e injusto. Nunca podré expresarlo. Lo lamento. La lengua castellana, tan inexacta, tan maleable, tan ambigua —tan perfecta, por tanto—, no está capacitada para completar el enunciado de agradecimiento con el complemento directo que se merecen y que yo quiero. Habré de dejarlo incompleto, abierto, ilimitado, infinito. A mis padres agradezco



The research work leading to this doctoral thesis has been funded by a Formación del Profesorado Universitario scholarship (reference FPU14/06121) from the Spanish Ministerio de Ciencia, Innovación y Universidades, as well as by projects TEC2013-46917-C2-1-R and TEC2016-80718-R.

ACRONYMS

AINOI	Aluminum nitride on insulator
BOX	Buried oxide
CMOS	Complementary metal-oxide-semiconductor
DFB	Distributed feedback (laser)
FCA	Free-carrier absorption
FDM	Finite-difference method
FDTD	Finite-difference time-domain (method)
FEM	Finite-element method
FEXEN	Fourier expansion simulation environment
FIB	Focused ion beam
FSO	Free-space optical (communications)
FTIR	Fourier transform infrared (spectroscopy/spectrometer)
FWHM	Full width at half maximum
GOI	Germanium on insulator
GON	Germanium on nitride
GOS	Germanium on silicon
GOSOI	Germanium on silicon on insulator
HF	Hydrofluoric (acid)
ICL	Interband cascade laser
ICP	Inductively coupled plasma
IRT	Infrared thermography
LPD	Light point defect
MCT	Mercury cadmium telluride (HgCdTe)

x

MFD	Mode field diameter
MFS	Minimum feature size
MIR	Mid-infrared
MMI	Multimode interference (coupler)
MZI	Mach-Zehnder interferometer
NIR	Near-infrared
NRC	National Research Council Canada
ORC	Optoelectronics Research Centre
QCL	Quantum cascade laser
SEM	Scanning electron microscope/microscopy
SGOS	Silicon-germanium (SiGe) alloy on silicon
SGOSG	Silicon-germanium (SiGe) alloy on silicon-germanium (SiGe) alloy
SiCOI	Silicon carbide on insulator
SiNOI	Silicon nitride on insulator
SiPSi	Silicon on porous silicon
SNC	Southampton Nanofabrication Centre
SOCF	Silicon on calcium fluoride
SOG	Spin-on glass
SOI	Silicon on insulator
SOLN	Silicon on lithium niobate
SON	Silicon on nitride
SOS	Silicon on sapphire
SWG	Subwavelength grating
TDD	Threading dislocation density
TE	Transverse electric
TM	Transverse magnetic
UMA	Universidad de Málaga
ZGC	Zero-order grating coupler

CONTENTS

1	Introduction	1
1.1	General Framework	1
1.1.1	The Mid-Infrared Band	1
1.1.2	Infrared Spectroscopy	3
1.1.3	Mid-Infrared Group IV Photonics	7
1.2	Overview of This Thesis	9
1.2.1	Suspended Platforms for the Mid-Infrared Band	10
1.2.2	Fiber-Chip Surface Couplers	11
1.3	Organization of This Thesis	12
2	Review of Photonic Integrated Platforms for the Mid-Infrared Band	15
2.1	Introduction	15
2.2	Conventional Platforms	17
2.2.1	Silicon-Core Platforms	17
2.2.2	Germanium-Core Platforms	21
2.2.3	Alternative Platforms	24
2.3	Suspended Platforms	25
2.3.1	Suspended Membranes	25
2.3.2	SWG-Cladding Suspended Platforms	26
2.3.3	Other Suspended Platforms	27
2.4	Summary of Platforms	27
3	Suspended Platforms for the Mid-Infrared Band	31
3.1	Introduction	31
3.2	Waveguide Design	34
3.2.1	Waveguiding Requirements	34
3.2.2	Design Methodology and Modeling	35
3.2.3	Design of a Suspended Silicon Waveguide	39
3.2.4	Design of Suspended Germanium Waveguides	42
3.3	Fabrication	44
3.3.1	Mask Definition	45
3.3.2	Lithography Procedure	47
3.3.3	Fabricated Structures	49
3.4	Characterization of Suspended Waveguides	50
3.4.1	Measurement Setup	50
3.4.2	Measurement Procedure	53
3.4.3	Results (Suspended Silicon)	54



3.4.4	Results (Suspended Germanium)	54
3.5	Suspended Silicon Beamsplitters	56
3.5.1	Multimode Interference Couplers	56
3.5.2	Mode-Evolution-Based 3-dB Splitter	59
3.6	Conclusions	61
4	Fiber-Chip Surface Couplers	63
4.1	Fundamentals of Surface Grating Couplers	64
4.1.1	Introduction	64
4.1.2	Working Principle of Periodic Waveguides	65
4.1.3	Performance Metrics of Surface Grating Couplers	70
4.2	Suspended Grating Couplers	74
4.2.1	General Design Approach	74
4.2.2	Design of a Suspended Silicon Grating Coupler	75
4.2.3	Design of a Suspended Germanium Grating Coupler	76
4.3	Suspended Germanium Micro-antenna	77
4.3.1	Motivation	77
4.3.2	Design	78
4.3.3	Discussion	81
4.3.4	Fabrication and Characterization	85
4.4	Zero-Order Grating Coupler	87
4.4.1	Motivation	87
4.4.2	Geometry	88
4.4.3	Working Principle	88
4.4.4	Design of a Longitudinal Zero-Order Grating Coupler	89
4.4.5	Design of a Transverse Zero-Order Grating Coupler	93
4.4.6	Fabrication and Characterization	94
4.4.7	Migration to the Mid-Infrared Band	95
4.5	Conclusions	96
5	Conclusions and Prospects	99
5.1	Conclusions	99
5.1.1	Suspended Platforms	99
5.1.2	Fiber-Chip Surface Couplers	100
5.2	Prospects	102
5.2.1	Suspended Silicon Platform	102
5.2.2	Suspended Germanium Platforms	102
5.2.3	Suspended Platforms with Tilted SWG Lateral Cladding	103
5.2.4	Sensing Experiments with Suspended Waveguides	103
5.2.5	Micro-antennas	104
5.2.6	Zero-Order Grating Couplers	105
A	Curriculum Vitae	107
B	Resumen en español	111
B.1	Introducción	111
B.1.1	La banda del infrarrojo medio y la fotónica del Grupo IV	111
B.1.2	Objetivos y aportaciones	113

CONTENTS

xiii

B.2	Plataformas suspendidas	114
B.2.1	Introducción	114
B.2.2	Diseño	115
B.2.3	Fabricación	119
B.2.4	Caracterización experimental	121
B.3	Acopladores chip-fibra por superficie	123
B.3.1	Introducción	123
B.3.2	Microantena de germanio suspendido	124
B.3.3	Acoplador de rejilla de orden cero	125

Bibliography

129



CHAPTER ONE

INTRODUCTION

In the last fifteen years, the mid-infrared band has attracted increasing attention of researchers in Group IV photonics because of the promising opportunities that this wavelength range offers for optical communications and, especially, for sensing. This thesis is concerned with the development of photonic integrated platforms for the mid-infrared spectral region, with an emphasis on waveguides and fiber-chip surface couplers.

The purpose of this chapter is to introduce the reader to the mid-infrared band and its applications, showing that Group IV photonics can be used as a tool to exploit this wavelength range (Section 1.1). Then, the goals and main contributions of this thesis are outlined (Section 1.2). Finally, the organization of this work is presented (Section 1.3).

1.1 General Framework

1.1.1 The Mid-Infrared Band

The mid-infrared (MIR) band is a region of the electromagnetic spectrum. In this work, MIR wavelengths are considered to span from 2 μm to 20 μm [1], yet different boundaries can be found in the literature [2].

Many applications are possible in the MIR regime [3,4]. Most of them can be grouped into three main categories, as shown in Fig. 1.1a:

- (i) *Infrared spectroscopy*. The study of the interaction of electromagnetic fields with the matter is called *spectroscopy* [5]. Infrared radiation stimulates the vibrational and rotational motions of molecules. Light is absorbed by a given molecule at specific infrared wavelengths, which define the own unique absorption spectrum of the molecule. Thus, the presence and concentration of the substances in a sample can be unambiguously determined by measuring the amount of energy absorbed by their molecules. In the MIR band, functional groups (e.g., hydroxyl and carboxyl) can be identified in the *functional group* region (2.5 μm to $\sim 6.7 \mu\text{m}$), while most absorption peaks take place in the *fingerprint* region ($\sim 6.7 \mu\text{m}$ to $\sim 16.7 \mu\text{m}$) [6]. In Fig. 1.1b, the absorption spectra of three different samples are shown. Infrared spectroscopy can be used for environmental monitoring [7,8], biochemical sensing [9], medical diagnosis [10–12], food analysis [13,14], or astronomy [15–17], among other applications.

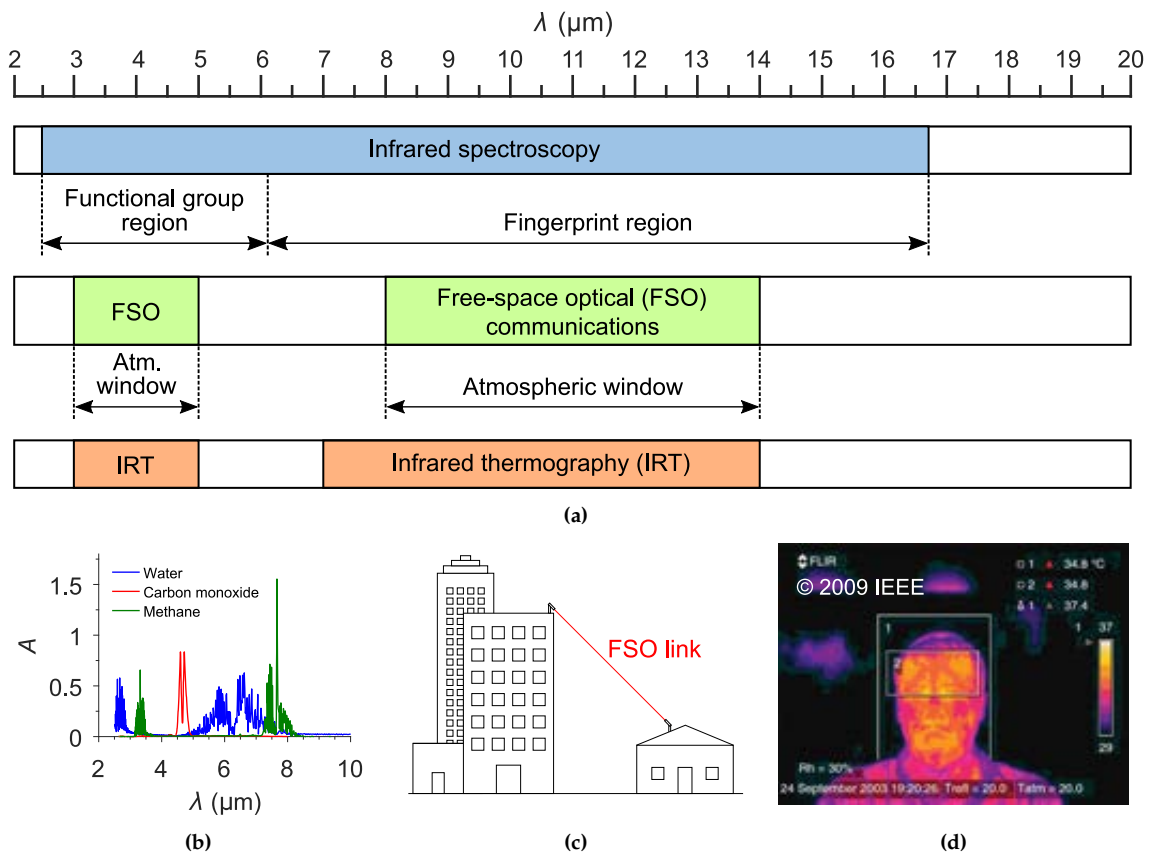


Figure 1.1: The mid-infrared wavelength range and its most common applications. (a) Wavelength ranges associated to each application. Infrared spectroscopy is performed in two different regions of the MIR band: the *functional group* region and the *fingerprint* region. The former enables the identification of functional groups (e.g., $-\text{OH}$ and $-\text{COOH}$), whereas the latter contains the specific signature of each substance. In (b), the absorption spectra of different samples of water vapor, methane, and carbon monoxide are shown [18–20]. Free-space optical communication links, schematically represented in (c), operate in the two atmospheric windows: 3–5 μm and 8–14 μm [21–24]. Thermographs are typically taken in the ranges of 3–5 μm and 7–14 μm [23]. In (d), an example of thermal image is shown. Source: [25].

Because of its relevance, infrared spectroscopy will be examined in more detail in section 1.1.2.

- (ii) *Free-space optical communications.* Compared to radiofrequency (RF), free-space optical (FSO) communications offer high data rates without the costs and inconveniences of spectrum licensing [26]. A FSO link is schematically illustrated in Fig. 1.1.c. In the near-infrared (NIR) band ($\lambda \sim 1.55 \mu\text{m}$), water vapor, carbon dioxide, ozone, and dust increase the Earth’s atmospheric absorption and scattering, thus hindering FSO links at long distances [27]. The MIR band emerges as a great opportunity for FSO communications, since two atmospheric windows are at 3–5 μm and 8–14 μm [21–24]. In addition, background noise caused by Sun, Earth, Moon, or city lights is minimum at $\sim 3.5 \mu\text{m}$ [22]. Communication systems designed to work in this band provide reliable communication links under adverse weather conditions, such as fog or rain [26, 28, 29].

- (iii) *Infrared thermography.* All objects whose temperature is higher than 0 K emit infrared radiation. Infrared cameras can be utilized to detect this body radiation and visualize it, avoiding any contact with the target object. Commercial cameras operate in the MIR ranges of 3–5 μm and 7–14 μm [23]. A real example of a thermal image is shown in Fig. 1.1d [25]. Infrared thermography (IRT) is used for homeland security [30] and biomedical applications [31, 32], to name a few.

1.1.2 Infrared Spectroscopy

Infrared spectroscopy can be used to obtain the infrared spectrum of a sample, which is a graphical representation of the light intensity absorbed by or transmitted through the sample as a function of some property of light, typically the wavenumber or the wavelength (see Fig. 1.1b). The absorption and transmission spectra are useful tools for detecting substances in a sample and determining their concentrations.

Fundamentals of Infrared Absorption

Infrared absorption is originated by the motions of the molecules. In the MIR band, vibrational absorption is predominant. The overall vibrational motion of a molecule can be decomposed as a sum of independent vibrations or *normal modes* [33]. Each mode has a natural wavelength λ and is associated to a quantized energy level. The frequencies of the vibrations of most chemical bonds correspond to wavelengths in the MIR range. At room temperature, normal modes are typically in their ground states (lowest energy level, E_0), as shown in Fig. 1.2. A transition to the first excited state (E_1) can occur if the energy $\Delta E = E_1 - E_0$ is supplied to the molecule [6, 33]. When infrared radiation interacts with a molecule, a photon with a wavelength λ can be absorbed,¹ as its energy is

$$\Delta E = E_1 - E_0 = \frac{hc}{\lambda}, \quad (1.1)$$

where h is the Planck's constant and c is the light speed. This absorption of energy at characteristic wavelengths is responsible for the infrared absorption spectra.

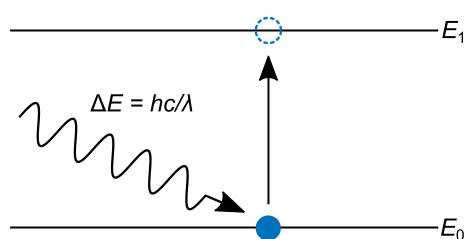


Figure 1.2: Quantized energy levels associated to a molecular vibration. A quantum of energy is absorbed, fitting the gap required for a transition from the ground state to the excited state.

For the molecule of water vapor (H_2O), some types of vibration are illustrated in Fig. 1.3. The energy gap between the ground vibrational state and the first excited state for each vibrational mode is shown in terms of wavelength according to Eq. (1.1). The infrared spectrum of water vapor exhibits absorption bands centered at those specific wavelengths [33].

¹The infrared absorption associated to a normal mode occurs if the vibration produces a change in the dipole moment of the molecule. This condition explains why infrared spectroscopy of homonuclear diatomic molecules such as O_2 and N_2 , whose dipole moment is always zero, is not possible [6].

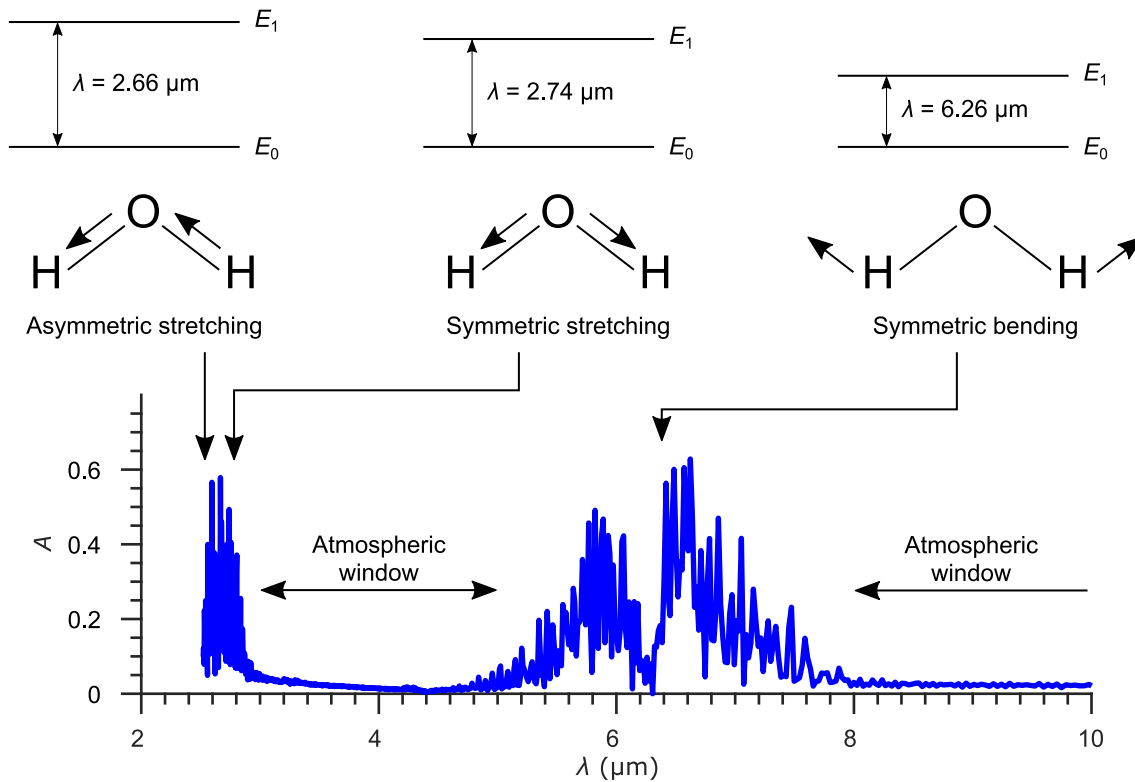


Figure 1.3: Vibrational normal modes of the molecule of water vapor, schematic representation of the levels of energy, and absorption spectrum. The spectrum is expressed in terms of absorbance, which accounts for the amount of light that is absorbed by a sample at a given wavelength. The closely-spaced narrow lines in the spectrum are caused by the excitation of rotational motions during vibrational transitions, and are a consequence of the gas phase of the substance [6]. The high-transmission regions between 3 μm and 5 μm and above 8 μm corresponds to the MIR atmospheric windows [34]. Figure adapted from [33] using absorption data from [18].

The Beer-Lambert Law

According to the Beer-Lambert law [35,36],² when a monochromatic light beam of wavelength λ impinges on a homogeneous absorbing sample, as depicted in Fig. 1.4, the transmitted intensity is

$$I(\lambda) = I_0(\lambda)e^{-\kappa(\lambda)CL}, \quad (1.2)$$

where $I_0(\lambda)$ is the intensity of the light before interacting with the sample, κ is the molar napierian absorption coefficient of the substance (in $\text{m}^2 \text{mol}^{-1}$), C is the concentration (in mol m^{-3}) and L is the path length (in m). The Beer-Lambert law can also be expressed as

$$I(\lambda) = I_0(\lambda)10^{-\epsilon(\lambda)CL}, \quad (1.3)$$

where $\epsilon = \kappa / \ln(10)$ denotes the molar (decadic) absorption coefficient (in $\text{m}^2 \text{mol}^{-1}$).

The infrared spectrum can be plotted in terms of the absorbance A (absorption spectrum) or the transmittance T (transmission spectrum), which can be calculated via the Beer-Lambert law as follows:

$$A(\lambda) = -\log [T(\lambda)] = -\log \left[\frac{I(\lambda)}{I_0(\lambda)} \right] = \epsilon(\lambda)CL. \quad (1.4)$$

²Strictly, the Beer-Lambert law is only valid when certain requirements are satisfied, as indicated in [36].

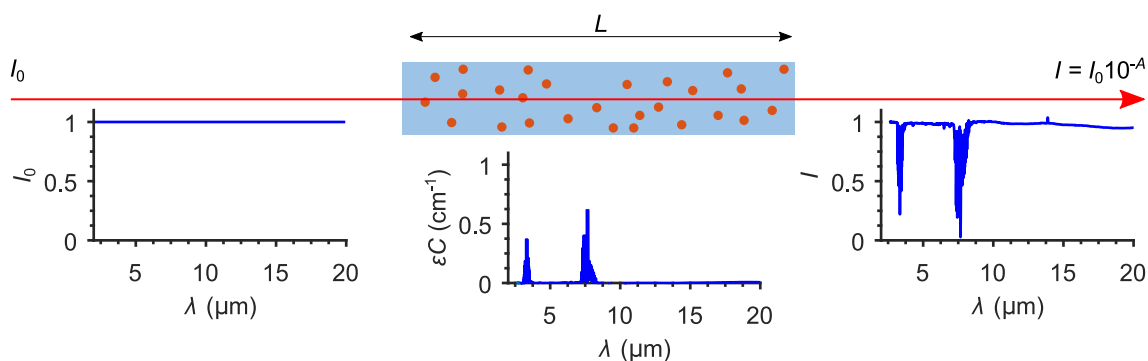


Figure 1.4: Example of use of the Beer–Lambert law. The intensity of the light that passes through a sample depends on the path length L , the molar absorptivity ϵ of the absorbing substance at the operating wavelength, and the concentration C . The Beer–Lambert law can be used to obtain the absorption or transmission spectra of the sample.

Using the absorption spectrum, the substances in a sample can be detected unequivocally and their concentrations can be calculated. As an example, Fig. 1.5 shows the absorption spectra of two organic compounds: 1-propanol and 2-propanol [37, 38]. The peaks around $\lambda = 3\ \mu\text{m}$ appear in the spectra of both 1-propanol and 2-propanol, revealing their functional group C–OH (alcohols). In the region from $7\ \mu\text{m}$ to $15\ \mu\text{m}$, the molecular structure of each substance produces a completely different spectrum. These absorption peaks act as a signature or fingerprint for the substances: (i) the positions of the peaks allow for the identification of the compounds, whereas (ii) the heights are proportional to the concentration by means of the Beer–Lambert law [Eq. (1.4)].

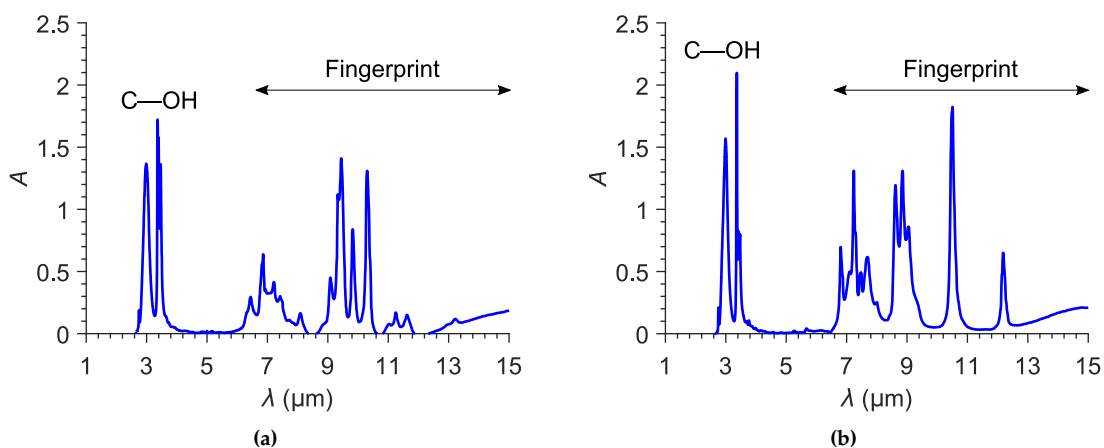


Figure 1.5: Absorption spectra of (a) 1-propanol and (b) 2-propanol. The alcohol functional group (C–OH) is highlighted, as well as the fingerprint region, which is different for each molecule.

Spectrum Measurement

In general, the optical systems used to obtain the infrared spectrum of a sample comprise an infrared source, a structure for enabling the interaction between the infrared beam and the molecules of the sample, and a detector for measuring the absorption of light. Additionally, devices for processing and routing the light may be required, depending

on the architecture of the spectroscopy system. As an example, three different schemes used for infrared spectroscopy are succinctly described as follows.

In Fig. 1.6a, a conventional Fourier transform infrared (FTIR) spectrometer is schematized [5]. FTIR is a traditional spectroscopy technique that is widely utilized when the complete MIR spectrum of a substance is needed. A broadband beam is radiated by an infrared black-body thermal emitter. An interferogram is generated using a Michelson interferometer. After interacting with the sample under test, the signal is detected and converted into the transmission spectrum of the sample by a computational Fourier-transform post-processing.

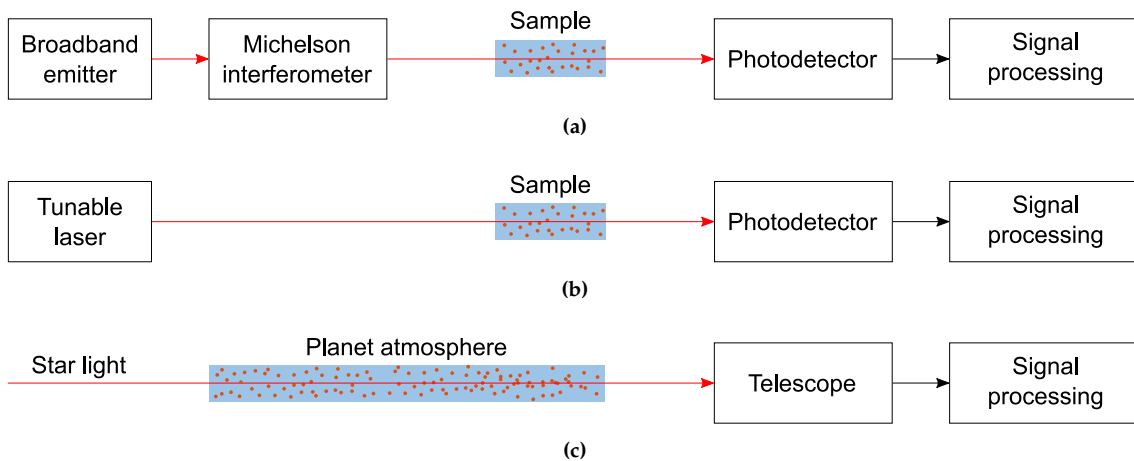


Figure 1.6: Different schemes for infrared spectroscopy in the MIR band. (a) FTIR. (b) TDLAS. (c) Astronomical spectroscopy.

The advent of quantum cascade lasers (QCLs) and interband cascade lasers (ICLs) [39, 40] has motivated the progress in tunable diode laser absorption spectroscopy (TDLAS) [41]. QCLs and ICLs are single-frequency, narrow-linewidth, tunable sources that can emit MIR radiation at room temperature [41]. In Fig. 1.6b, a simple TDLAS setup is schematized. In the most basic configuration, the wavelength of a light beam is scanned around a specific absorption peak of the molecules of a sample, which allows for the quick identification of the substance without measuring the complete MIR spectrum. Because they do not need moving parts to process the infrared light and to generate the spectrum, TDLAS setups can be more compact and simpler than FTIR spectrometers.

A third scenario is specific to astronomical spectroscopy (see Fig. 1.6c). The absorption at MIR wavelengths can be used, for example, to study exoplanets and search for biosignatures in their atmospheres. This objective is one of the envisioned aims of the Origins Space Telescope (OST) mission concept [17]. The infrared light from a host star is attenuated at specific wavelengths when the target planet passes between the star and a telescope, which receives the light. By measuring the absorption spectrum, the composition of the planet can be analyzed.

Figure 1.7 shows three commercial spectroscopy systems. Benchtop FTIR spectrometers are capable of determining the complete infrared spectrum of a sample in less than five minutes. As they are designed for laboratory environments, these spectrometers are typically bulky. For instance, the Thermo Scientific's Nicolet iS 50 FTIR spectrometer shown in Fig. 1.7a has a base of $63 \times 70 \text{ cm}^2$, a height of 51 cm, and a weight of 64 kg [42]. Because of these dimensions, the collection of the sample and the FTIR spectroscopy are

performed at different points in time. This delay may render the analysis useless if the sample degrades over time or if on-the-go sensing of hazardous gases is required. Furthermore, some samples cannot be removed from their locations and carried to a laboratory. Portable spectrometers and gas analyzers allow for in-field usage, but the need for user's action and their relatively high weights (~ 2 kg for the Agilent's 4300 Handheld FTIR in Fig. 1.7b [43], and ~ 13 kg for the AMETEK's 5100P TDLAS in Fig. 1.7c [44]) prevent their utilization for continuous environmental monitoring and sensing.



Figure 1.7: Examples of commercial spectroscopy systems. (a) Benchtop FTIR model, Thermo Scientific's Nicolet iS 50 FTIR [42]. (b) Handheld FTIR model, Agilent's 4300 Handheld FTIR [43]. (c) Portable TDLAS gas analyzer, AMETEK's 5100P TDLAS [44]. The three images have different scales.

Today, more compact solutions are desired. Miniaturized spectroscopy systems can open up a whole new world of possibilities for in situ environmental monitoring or health care devices that would constantly provide information to the patients. In this context, integrated photonics, and Group IV photonics in particular, offers excellent prospects for a new generation of infrared absorption sensors that can move from the laboratory to the smartphone and next wearable devices.

1.1.3 Mid-Infrared Group IV Photonics

Group IV photonics, also known as silicon photonics, is a fundamental technology for datacom and telecom applications in the NIR band, around $\lambda = 1.55 \mu\text{m}$ [45–49]. Group IV photonics enables the integration of optical devices into standard wafers made of Group IV materials, such as silicon and silicon nitride. Structures are typically etched into a silicon layer on top of silicon dioxide, forming the silicon-on-insulator (SOI) platform (see Fig. 1.8). As shown in the figure, the propagating mode field is strongly confined within the waveguide core, because of the high index contrast between silicon and silicon dioxide ($\Delta n \sim 2$). Moreover, photonic and electronic integrated circuits can be implemented using the same complementary metal-oxide-semiconductor (CMOS) techniques employed in well-established foundries. These characteristics make Group IV photonics an ideal technology to cope with the challenging bandwidth requirements of current societies, providing high-performance, low-power, low-cost, and compact optical devices that can be mass produced [50–53].

At NIR wavelengths, a myriad of active and passive devices have been presented, and new ones are continuously being demonstrated, including laser sources, photodetectors, interconnecting waveguides, directional couplers, splitters, multimode interference couplers (MMIs), Mach-Zehnder interferometers (MZIs), grating couplers, Bragg filters,

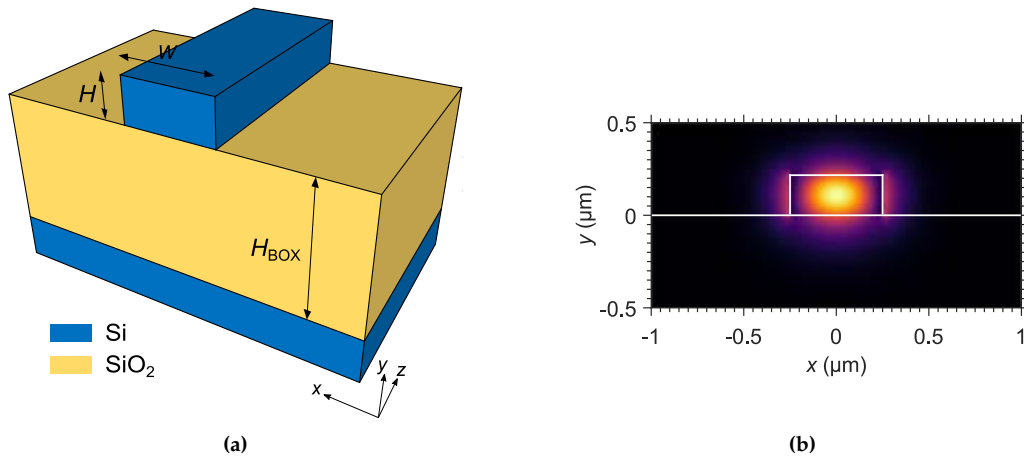


Figure 1.8: Conventional silicon-on-insulator strip waveguide. (a) Geometry. (b) Transverse field distribution of the fundamental mode supported by a waveguide with a core width (W) of 500 nm, a core thickness (H) of 220 nm, and an infinite insulator layer ($H_{\text{BOX}} \rightarrow \infty$) at $\lambda = 1.55 \mu\text{m}$.

multiplexers, and modulators [49,54]. Companies like Luxtera and Intel are already commercializing transceivers for optical interconnects based on Group IV photonics [55,56]. Sensing experiments have also been conducted in this band [57–59].

The optical devices that have been extensively developed at NIR wavelengths can be redesigned to take advantage of the potential applications of the MIR range. Thus, Group IV photonics can enable the realization of label-free, cost-effective, and compact lab-on-chip systems for exploiting the infrared absorption of most molecules. Integrated waveguides and devices can be employed for routing and processing of light in spectroscopy systems. For instance, in [60], the authors propose an integrated FTIR spectrometer in which, by following the principle of spatial heterodyning, the Michelson interferometer is substituted with an array of Mach-Zehnder interferometers, as reproduced in Fig. 1.9a. Alternatively, in addition to guiding the light, the planar waveguides can also serve as the sensing devices. In such a case, which is illustrated in Fig. 1.9b, the evanescent tails of the fundamental mode that is supported by the waveguides interact with the molecules of the sample in the upper cladding [61–64].

Group IV photonic devices can not only be useful for sensing applications, but also for FSO communications. For example, in [24], a broadband 1×2 multimode interference coupler with polarization insensitivity is designed to cover multiple FSO channels in the second atmospheric window between wavelengths of $7.5 \mu\text{m}$ and $13 \mu\text{m}$.

Furthermore, the MIR band offers technological possibilities for Group IV photonic devices. As integrated structures are large compared to their NIR counterparts because of the increased wavelength, MIR devices should be more tolerant to fabrication imperfections. Additionally, germanium, which has high loss in the NIR band, can be used as a guiding material, offering higher modal confinement and nonlinearity [65].

However, despite the benefits of moving to the MIR band, the migration is complicated. Unfortunately, the conventional SOI platform is not the best suited for the MIR band. As shown in Fig. 1.10, the intrinsic loss of silicon dioxide and silicon becomes prohibitive over $\lambda \sim 4 \mu\text{m}$ and $\lambda \sim 8 \mu\text{m}$, respectively, thus frustrating SOI utilization at long MIR wavelengths [66]. To overcome this problem, materials other than silicon and silicon dioxide can be combined [67,68], leading to waveguide platforms such as

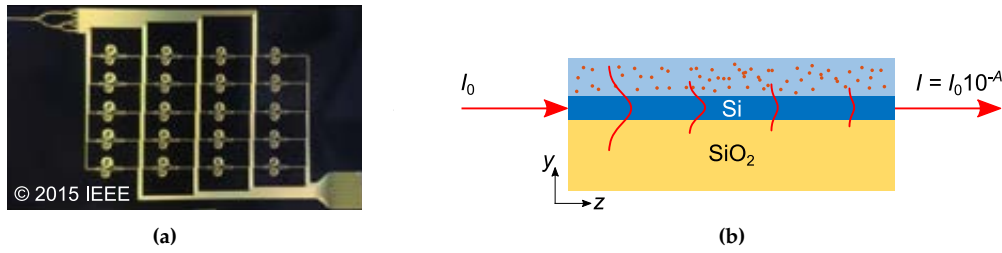


Figure 1.9: Usages of Group IV photonics for infrared spectroscopy. (a) Integrated FTIR spectrometer based on spatial heterodyne spectroscopy. Source: [60]. (b) Illustration of a sensing waveguide. The evanescent tails of the fundamental mode supported by the waveguide interact with the molecules of the sample in the upper cladding.

silicon on sapphire [69], silicon on (silicon) nitride [70], germanium on silicon [71], or silicon-germanium-based platforms [72, 73]. Alternatively, the silicon dioxide layer can be removed to create suspended silicon and suspended germanium platforms [74–77]. Although many solutions have been proposed, the search for the best MIR platform continues.

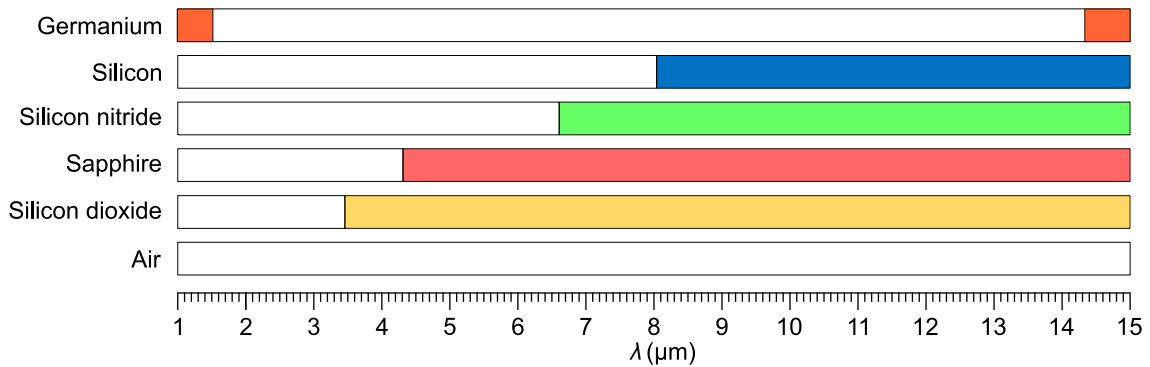


Figure 1.10: Transparency (white) and opaqueness (colored) windows of several materials used in Group IV photonics. Transparency is considered for intrinsic material losses smaller than 2 dB cm^{-1} . Depending on the waveguide geometry, the wavelength range over which the fundamental mode has a loss smaller than 2 dB cm^{-1} can be wider. Figure adapted from [66].

The pursuit of appropriate MIR platforms is an important challenge. Some novel guiding structures need new simulation approaches and design procedures. In many cases, alternative manufacturing techniques and non-standard measurement setups are required. Besides, the absence of mature laser sources and detectors, as well as robust optical fibers, hinders the characterization of new devices. Therefore, while some complex systems are being proposed for the most promising platforms (e.g., [24, 60, 78]), the main focus still remains on the development of the basic structures (such as waveguides and couplers), which should cover the largest possible range of MIR wavelengths.

1.2 Overview of This Thesis

The main goal of this thesis is to make progress toward the development of Group IV photonics for the MIR band. This basic objective has motivated a number of significant contributions. Specifically, suspended silicon and suspended germanium platforms have

been developed to potentially cover the MIR band up to $\lambda \sim 15 \mu\text{m}$ with low loss. Furthermore, novel solutions have been proposed to cope with the problem of fiber-chip coupling of light, yielding new surface couplers with outstanding efficiency and bandwidth that outperform conventional grating couplers.

The waveguides and devices that are proposed in this thesis can be part of more complex systems for potential applications such as sensing and optical communications. The design of those systems is beyond the scope of this work.

In this section, the fundamental contributions of this thesis are detailed. A graphical overview can be found in Fig. 1.11 (main contributions) and Fig. 1.12 (minor contributions), which include illustrations, simulated electric field propagations, and scanning electron microscope (SEM) images of the fabricated structures.

1.2.1 Suspended Platforms for the Mid-Infrared Band

The main limitation of the SOI technology, which is typically used in the NIR band, is the high loss of silicon dioxide beyond $\lambda \sim 4 \mu\text{m}$. The silicon dioxide is removed in the suspended silicon and suspended germanium platforms, thereby enabling low-loss waveguiding up to the transparency limits of silicon ($\lambda \sim 8 \mu\text{m}$) and germanium ($\lambda \sim 15 \mu\text{m}$), respectively.

Suspended silicon waveguides have been realized at $\lambda = 7.67 \mu\text{m}$. A propagation loss as low as 3.1 dB cm^{-1} has been demonstrated. This result constitutes, to the best of this author's knowledge, the lowest propagation loss achieved in a silicon-based integrated platform at such a long wavelength, and is still comparable to the propagation loss of state-of-the-art waveguides that use other materials such as germanium. Suspended silicon waveguides and bends were reported in [79,80]. Other building blocks — multimode interference couplers (MMIs) and a mode-evolution-based power splitter — have been designed [80], and some preliminary experimental results have already been obtained.

Suspended germanium waveguides have also been validated experimentally. Silicon loss is already noticeable ($\sim 2 \text{ dB cm}^{-1}$) at $\lambda = 7.67 \mu\text{m}$, and prohibitive at longer wavelengths. By replacing silicon by germanium, this high loss can be potentially reduced. At the time of writing, propagation losses of $\sim 5 \text{ dB cm}^{-1}$ have been achieved for suspended germanium waveguides at wavelengths of $3.8 \mu\text{m}$ and $7.67 \mu\text{m}$. The high loss compared to that of their silicon counterparts is mainly attributed to a known contamination of the utilized wafers. New fabrication runs are planned for the next months with the aim of improving the performance. Additionally, designs at $9.6 \mu\text{m}$ are currently being fabricated and will be measured within the next months. These first results constitute a major step toward the practical implementation of suspended building blocks and systems at long MIR wavelengths at which silicon-based devices cannot operate.

The design of the suspended structures was primarily carried out at the Universidad de Málaga (UMA), whereas the fabrication and experimental characterization were performed in the Optoelectronics Research Centre (ORC) at the University of Southampton, within the framework of two research stays under the supervision of Prof. Goran Mashanovich. The entire design process and a large part of the experimental measurements were done by the author of this thesis; on the other hand, the fabrication was accomplished by the researchers of the ORC. The design of both suspended platforms required an iterative refinement according to the information about geometrical constraints that was being continuously provided by the various fabrication runs. Consequently, the

prototyping cycle of the presented structures at different wavelengths took more than two years.

1.2.2 Fiber-Chip Surface Couplers

Fiber-chip couplers are essential devices in integrated photonics, as they enable the coupling of light between the optical fibers and the chips. In this thesis, two relevant contributions have been made: a suspended germanium micro-antenna and a zero-order grating coupler. Both couplers are introduced in the following paragraphs. Besides, conventional surface grating couplers were designed with the aim of coupling light during the characterization of the suspended silicon and germanium waveguides.

The suspended germanium micro-antenna, which is a novel, grating-inspired fiber-chip surface coupler for the MIR suspended germanium platform, has been proposed at a wavelength of $7.67\ \mu\text{m}$. The field radiated by this structure matches the small mode field diameter of MIR optical fibers, which benefits an increase in the bandwidth and the tolerance to fiber tilt angles. Specifically, a bandwidth of $\sim 430\ \text{nm}$ is predicted, which is almost twice the typical fractional bandwidth of conventional grating couplers for the NIR band. The proposed micro-antenna is markedly tolerant to fiber tilt misalignments of $\pm 10^\circ$. Moreover, this micro-antenna is, as far as this author knows, the first efficient fiber-chip surface coupler that operates with two supported radiation orders between the fourth and fifth Bragg regimes. The micro-antenna was fabricated in the ORC and its wide angular bandwidth was experimentally confirmed. This all-dielectric micro-antenna design paves the way for efficient fiber-chip coupling in long-wavelength MIR integrated platforms. The suspended germanium micro-antenna concept was published in [81].

The zero-order grating coupler (ZGC) has been designed to optimize both the coupling efficiency and the bandwidth. Fiber-chip surface couplers with broadband operation are needed in general, not only for MIR applications but also in the NIR band. Despite the maturity level of NIR grating couplers, the trade-off between coupling efficiency and bandwidth is apparent in the literature: most grating couplers designed for high efficiency tend to suffer from narrow bandwidths; on the contrary, broadband couplers typically lack high coupling efficiencies. The operational bandwidth of grating couplers is limited by the wavelength dependence of the radiation angle. ZGCs minimize such a dependence, thereby increasing the bandwidth while enhancing the coupling efficiency. The ZGC was initially designed for the NIR band, since realization should be easier at $\lambda = 1.55\ \mu\text{m}$ because of the high availability of lasers, detectors, and optical fibers. At this wavelength, an unprecedented performance is predicted by simulation: a subdecibel coupling efficiency of $\sim 90\%$ and a broad 1-dB bandwidth of $\sim 130\ \text{nm}$. Finally, the design was migrated to the MIR band at $\lambda = 3.8\ \mu\text{m}$, yielding a theoretical bandwidth of $\sim 560\ \text{nm}$. At that wavelength, the material loss of silicon dioxide is relatively low, so that BOX removal is not necessary for this design. The ZGC concept was published in [82]. The design of the ZGC was initiated at UMA and finished later in the National Research Council Canada (NRC), within the framework of a short stay under the supervision of Dr. Pavel Cheben. Because the ZGC is a novel device, its characterization is not standard. At the time of writing, researchers in the NRC are trying to experimentally demonstrate this broadband coupler.

1.3 Organization of This Thesis

This thesis is organized as follows:

Chapter 1 is the current introduction.

Chapter 2 provides a review of the state of the art in MIR integrated photonics. The most significant Group IV platforms — in the author's view — are covered, and their prime properties are highlighted, as well as their disadvantages. At the end of the chapter, summarizing tables are included.

Chapter 3 is devoted to the design, fabrication, and characterization of suspended waveguides. The entire design procedure is detailed for the suspended silicon platform at a wavelength of $7.67\ \mu\text{m}$, and is applied, yet not thoroughly described again in the chapter, to the design of suspended germanium waveguides. The latter are designed at $3.8\ \mu\text{m}$ as a proof of concept, and then migrated to $7.67\ \mu\text{m}$ and $9.6\ \mu\text{m}$. The fabrication process is briefly explained and experimental results at $3.8\ \mu\text{m}$ and $7.67\ \mu\text{m}$ are shown. The design of some suspended silicon building blocks (MMIs and a mode-evolution-based 3-dB splitter) is also shown.

Chapter 4 starts with the fundamentals of surface grating couplers. A succinct description of the conventional grating couplers that were designed for chip characterization of suspended waveguides is given. Then, the design of the suspended germanium micro-antenna at a wavelength of $7.67\ \mu\text{m}$ is presented and discussed. Finally, the zero-order grating coupler concept is described, and theoretical results are provided, firstly in the NIR regime and lastly in the MIR band.

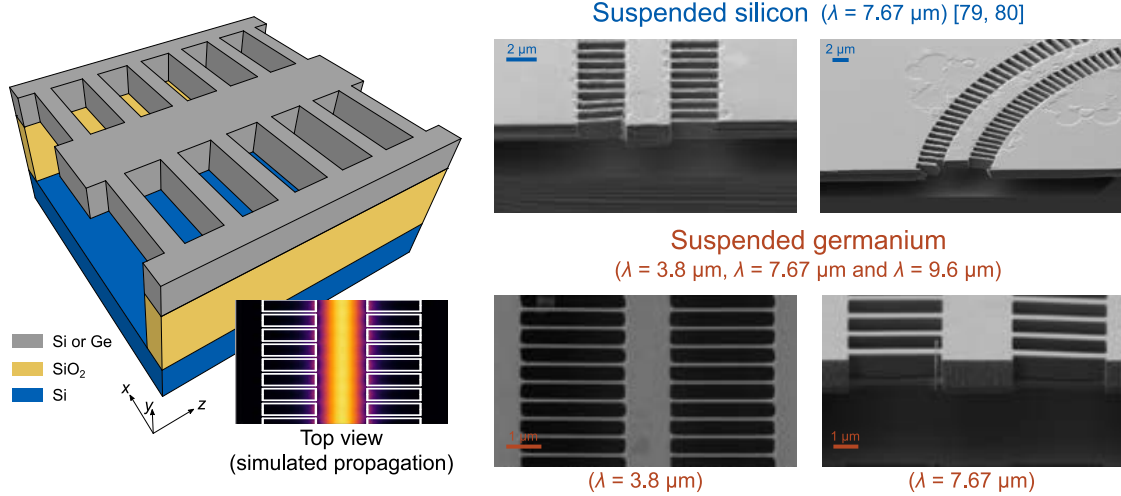
Chapter 5 draws the conclusions and proposes future research lines.

In addition, two appendices are included:

Appendix A shows a brief curriculum vitae of the author of this thesis, including a list of the journal papers authored or co-authored to date.

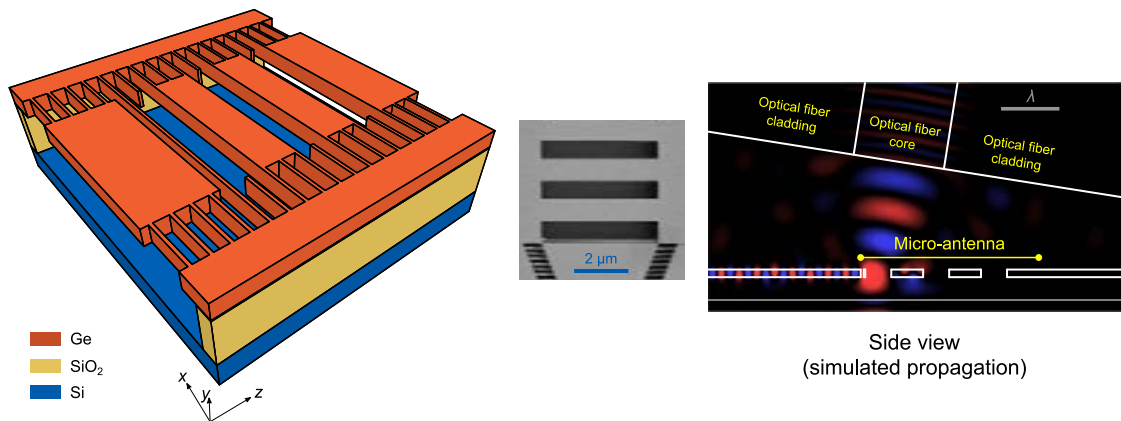
Appendix B summarizes the thesis in Spanish.

Chapter Three | Suspended Platforms for the Mid-Infrared Band



Chapter Four | Fiber-Chip Surface Couplers

Suspended germanium micro-antenna ($\lambda = 7.67 \mu\text{m}$) [81]



Zero-order grating coupler (design)

($\lambda = 1.55 \mu\text{m}$ and $\lambda = 3.8 \mu\text{m}$) [82]

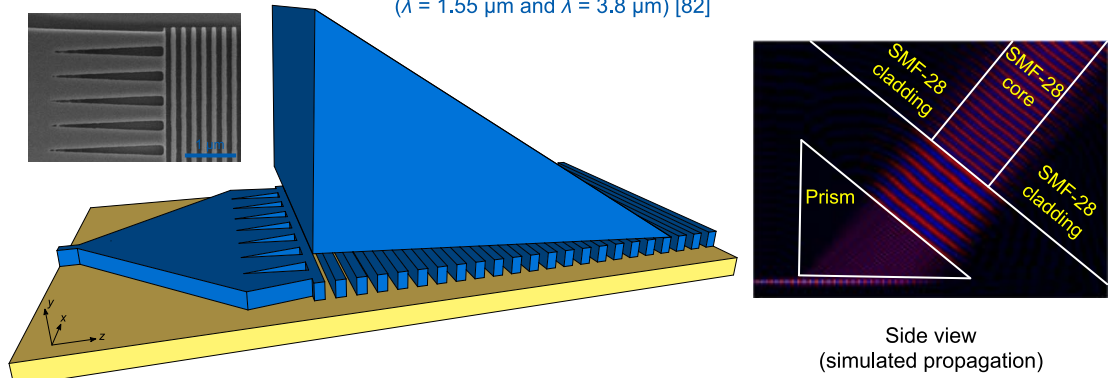
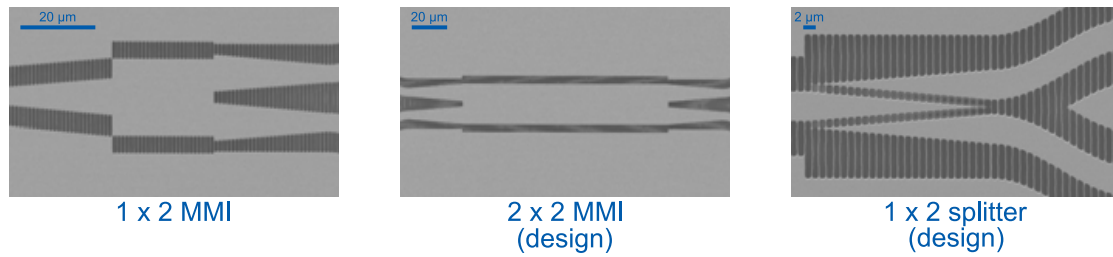


Figure 1.11: Overview of this thesis. Main contributions, including 3D illustrations (not to scale), simulations of electric field propagations and SEM images.

Chapter Three | Suspended Platforms for the Mid-Infrared Band

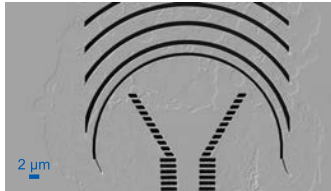
Suspended silicon devices ($\lambda = 7.67 \mu\text{m}$) [80]



Chapter Four | Fiber-Chip Surface Couplers

Conventional grating couplers

Suspended silicon ($\lambda = 7.67 \mu\text{m}$) [79, 80]



Suspended germanium ($\lambda = 3.8 \mu\text{m}$)

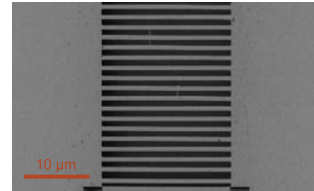


Figure 1.12: Overview of this thesis. Minor contributions, including SEM images of the fabricated structures.

CHAPTER TWO

REVIEW OF PHOTONIC INTEGRATED PLATFORMS FOR THE MID-INFRARED BAND

Group IV photonics is an excellent tool to exploit the multiple applications that are possible in the MIR band, which include sensing and atmospheric communications. While MIR sources and detectors are already available, and optical fibers are becoming low-loss at long wavelengths, there is still no standard platform for MIR integrated waveguides and devices.

With the aim of contextualization, in this chapter the most relevant (at author's discretion) waveguide platforms that have been demonstrated so far for the MIR band are reviewed. First, a general classification for MIR platforms is provided (Section 2.1). Then, conventional and suspended platforms are analyzed (Sections 2.2 and 2.3, respectively). The main achievements for each platform are summarized in the tables at the end of the chapter (Section 2.4).

2.1 Introduction

The cross section of a waveguide is schematized in Fig. 2.1 for a generic conventional integrated platform. The structure comprises four layers: upper cladding, core, bottom cladding (under-cladding), and thick substrate. The first three layers enable waveguiding; the substrate is optional, supports the whole structure, and should not affect the propagating mode. The materials forming the platform determine the guiding capabilities.

Materials have different physical properties (e.g., absorption loss, refractive index, dispersion, or optical nonlinearities) that are suitable for a given application or wavelength range and unsuitable for others. In the MIR band, conventional waveguide platforms, such as silicon on insulator, can only be used in a very limited wavelength range because of the absorption loss. Figure 2.2 shows the transparency windows of some Group IV materials. Silicon dioxide and sapphire, typical under-cladding materials, are low-loss up to wavelengths around 3.6 μm and 4.3 μm , respectively. Silicon nitride supports low-loss propagation up to $\sim 6.6 \mu\text{m}$. Silicon, the most common core material, has prohibitive absorption beyond $\sim 8 \mu\text{m}$. Germanium seems appropriate for the entire MIR

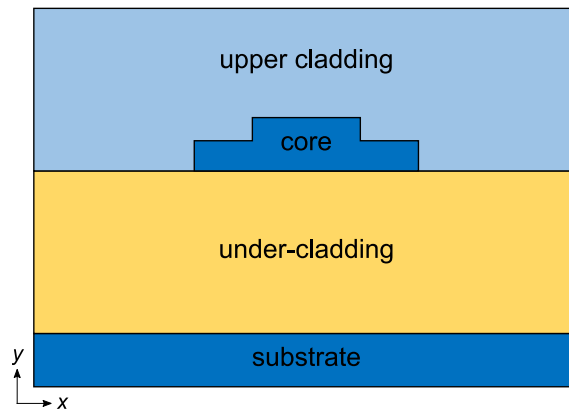


Figure 2.1: Schematic representation of a conventional integrated platform.

range, but the use of silicon is more extended, and hence preferred, for passive devices. No material is optimal in all cases. For this reason, many research groups have devoted the last decade to the pursuit of the best waveguide platform.

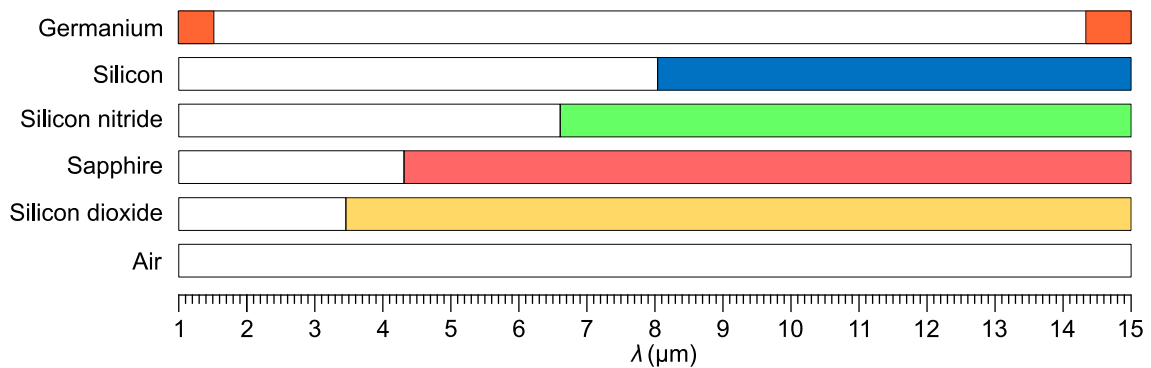


Figure 2.2: Transparency (white) and opaqueness (colored) windows of several materials used in Group IV photonics. Transparency is considered for losses smaller than 2 dB cm^{-1} . Depending on the waveguide geometry, the wavelength range over which the fundamental mode has a loss smaller than 2 dB cm^{-1} can be wider. Figure adapted from [66].

For a given platform, the operating range can be extended by reducing the interaction between the propagating mode and the absorptive medium. For a lossy under-cladding, this reduction can be achieved by engineering the waveguide cross-section; for example, by increasing the thickness and width of the waveguide core [83]. However, this solution can make the waveguide support high-order modes and can reduce the performance for sensing applications.

An alternative is to replace the absorptive layers by other materials, or to completely remove them. Thus, according to the under-cladding material, the platforms found in the literature can be grouped into two different categories:

- *Conventional platforms*, those with a solid underlying cladding that is low-loss at the operating wavelength. In Fig. 2.3a, the under-cladding of the waveguide in Fig. 2.1 is substituted with a new material. The transparency range of the platform will depend on the materials and the geometry of the waveguide. The guiding layer can be

made of (i) silicon, (ii) germanium or silicon-germanium alloys, or (iii) alternative materials.

- *Suspended platforms*, those in which the bottom layer is removed or, equivalently, the underlying cladding is substituted with air. Several variations have been proposed, among which suspended membranes and SWG-cladding suspended platforms stand out. Figure 2.3b schematizes a suspended waveguide.

In the literature, several articles can be found that review the principal silicon- and germanium-based waveguides and devices for the MIR band [62, 67, 68]. In the next sections, the most relevant platforms are studied in detail, emphasizing their propagation losses.

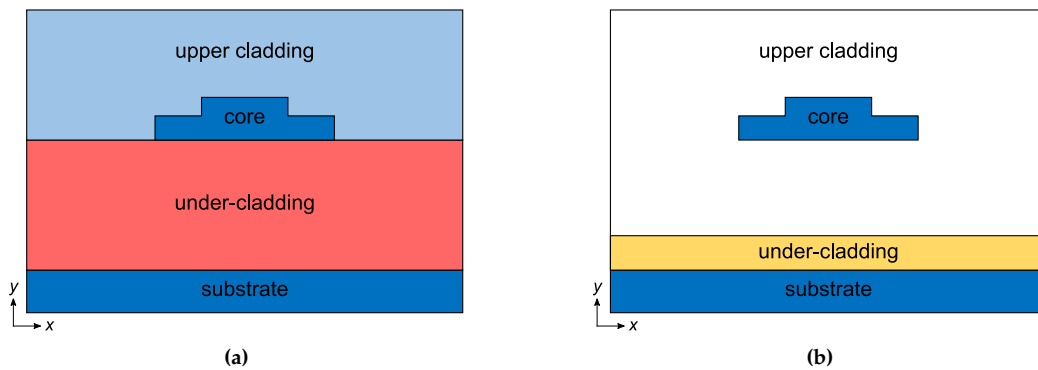


Figure 2.3: Types of photonic integrated platforms for the mid-infrared band: (a) conventional and (b) suspended waveguides.

2.2 Conventional Platforms

2.2.1 Silicon-Core Platforms

Silicon on Insulator

Silicon on insulator (SOI) is leading Group IV photonics at $\lambda = 1.55 \mu\text{m}$, as it is compatible with current CMOS manufacturing processes and allows the massive, cost-effective fabrication of highly compact devices [49]. The SOI platform comprises a crystalline silicon layer (refractive index of ~ 3.42 [84]) on top of an insulator or buried oxide (BOX) under-cladding, typically of silicon dioxide¹ (refractive index of ~ 1.42 [85]). Different materials, such as polymers or oxides, can cover the silicon layer as an upper cladding. Schematic representations of conventional strip and rib SOI waveguides are shown in Fig. 2.4.

Due to its vast popularity in the NIR band, SOI is the first technology that comes to mind for the development of optical integrated circuits in the MIR range [3]. Indeed, the maturity of SOI makes it the best choice for MIR photonics up to $\lambda \sim 4 \mu\text{m}$. The SiO_2 under-cladding exhibits increasing intrinsic loss that prevents the use of SOI at longer

¹In practical use, the term *silicon on insulator* is reserved for the silicon-on-silica platform. When other insulators are used, alternative denominations are more common (e.g., *silicon on sapphire* when the insulator is sapphire).

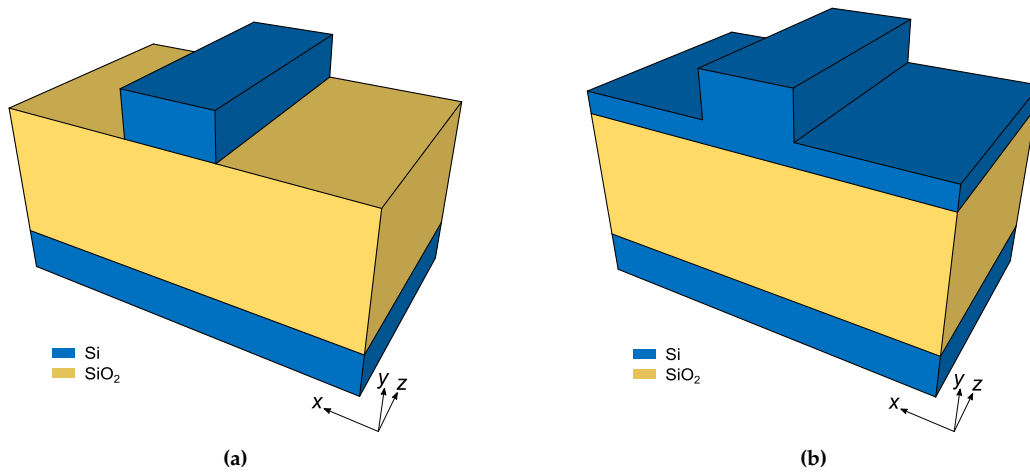


Figure 2.4: Schematic representation of (a) strip and (b) rib silicon-on-insulator waveguides.

MIR wavelengths. Theoretically, a judicious cross-section design can push this limit towards $\lambda \sim 6 \mu\text{m}$ [83, 86].

Up to $\lambda \sim 4 \mu\text{m}$, the dominance of SOI is evidenced by the number of devices that have been proposed until now, including waveguides with propagation losses (α) below 1 dB cm^{-1} [83, 87, 88], ring resonators [71, 83, 88–90], MMIs [89, 91, 92], MZIs [71, 90, 92], spectrometers [60, 93, 94], and (de)multiplexors [92], to name a few.

A variant of the SOI platform incorporates a polycrystalline silicon (poly-Si) overlayer. The main advantage relies on the fabrication, which offers selective deposition of poly-Si and hence the possibility of having different thicknesses along the chip [94, 95]. As MIR devices usually require thick guiding layers, selective overlayer deposition can be exploited to integrate both NIR and MIR optical circuits on the same SOI chip [91]. Waveguides with propagation losses in the range of 3 dB cm^{-1} to 6 dB cm^{-1} have been reported at a wavelength of $\sim 3.8 \mu\text{m}$ [94], as well as MMI splitters [91] and grating couplers [95].

Silicon on Sapphire

By substituting silicon dioxide with another insulator, the operating range of the SOI platform can be extended. Sapphire (refractive index of ~ 1.71 [96]) is used in the silicon-on-sapphire (SOS) platform [97], enabling transparency up to $\lambda \sim 4.3 \mu\text{m}$ [3, 66]. Strip and slot waveguides are schematized in Fig. 2.5. Like SOI, SOS wafers have been widely employed in the microelectronics industry, so that this high-contrast platform inherits the simplicity of fabrication and the feasibility of optoelectronic integration. As a drawback, sapphire is more expensive and more difficult to manipulate and polish [91].

This platform was very prolific in the years following the first experimental demonstration [69], but recently it has lost popularity. This reduced interest is probably due to the low transparency improvement SOS offers compared to the ubiquitous SOI. Propagation losses smaller than 1 dB cm^{-1} were achieved at $\lambda = 4.5 \mu\text{m}$ [98]. Other passive devices, such as ring resonators [98–101] and mode converters [102], have been characterized.

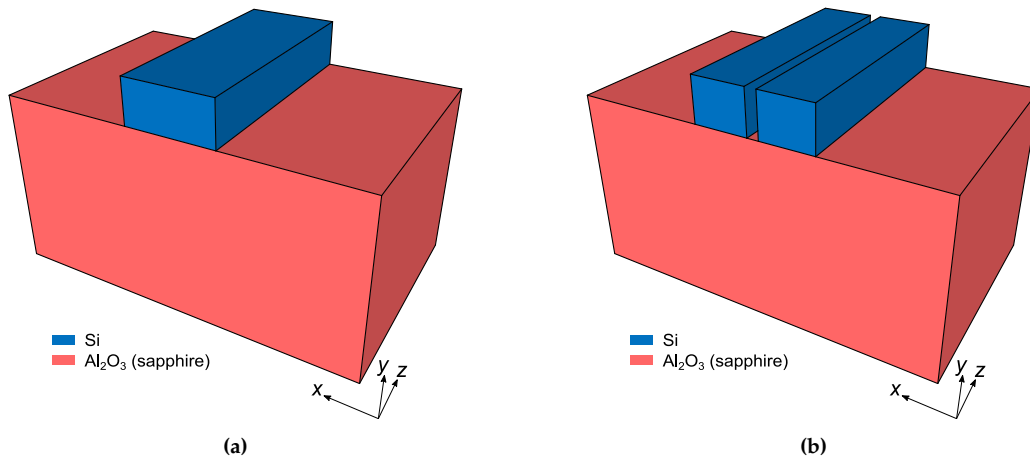


Figure 2.5: Schematic representation of (a) strip and (b) slot silicon-on-sapphire waveguides.

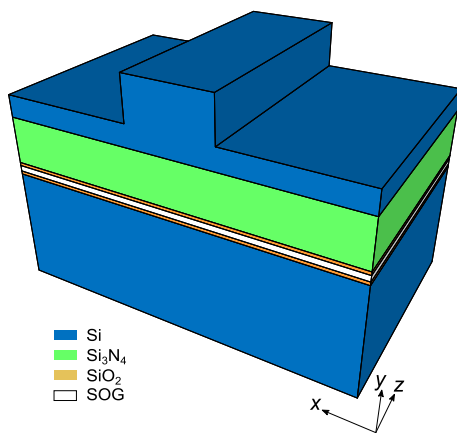


Figure 2.6: Schematic representation of a silicon-on-nitride waveguide. A thin stack of SiO_2 , spin-on glass (SOG), and SiO_2 layers are used to bond the silicon nitride cladding to the silicon substrate.

Silicon on Nitride

Silicon nitride (SiN) can be used as an under-cladding to push the operating wavelength up to $\lambda \sim 6.7 \mu\text{m}$ [3,66,103]. Figure 2.6 depicts a silicon-on-nitride (SON) rib waveguide, as demonstrated in [70]. In the Si_3N_4 form, this CMOS-compatible material has a refractive index of ~ 2 at MIR wavelengths that defines an index contrast comparatively lower than in SOI and SOS platforms. Higher refractive indices can be engineered by silicon enrichment [104]. Thus, SON waveguides can be used when tailorable and relatively low index contrast is needed (e.g., to couple light via the chip edge). A major disadvantage of this platform is its complex fabrication process, which is based on wafer bonding.

At $\lambda \sim 3.39 \mu\text{m}$, a measured propagation loss of $\sim 5 \text{ dB cm}^{-1}$ was reported for both quasi-TE and quasi-TM polarizations².

Air-Clad Pedestal

Although the air-clad pedestal platform has not been very successful, it is worth mentioning in this thesis because it falls halfway between suspended and non-suspended platforms. Silicon is partially removed from an all-silicon substrate and a pedestal is

²For the sake of simplicity, hereafter quasi-TE and quasi-TM polarizations of 3D waveguides will be referred as TE (transverse electric) and TM (transverse magnetic), respectively.

defined to support the waveguide core, as shown in Fig. 2.7. The air cladding creates the index contrast for waveguiding. Because of the large dimensions of the waveguide core, the structure possibly supports high-order modes. In [105], a propagation loss of 2.7 dB cm^{-1} was reported at a wavelength of $3.7 \mu\text{m}$. Bends and 3-dB splitters were also demonstrated.

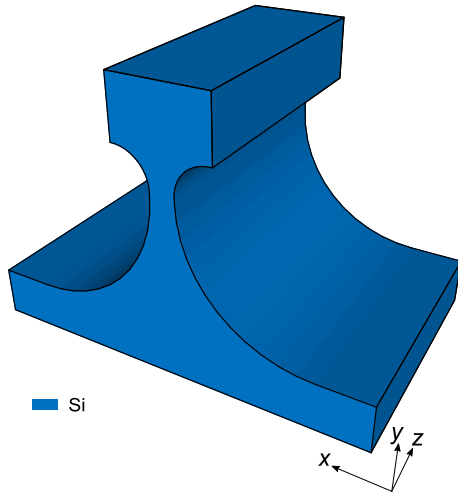


Figure 2.7: Schematic representation of an air-clad pedestal waveguide.

Other Platforms

Other silicon-based platforms with lower scientific impact can be found in the literature. Usually, they are helpful for niche applications, but not for general purpose. Some of these platforms are succinctly reviewed in this section:

- *Silicon on porous silicon.* Silicon-on-porous-silicon (SiPSi) waveguides were demonstrated in [87]. SiPSi wafers are not commercially available. The porous silicon under-cladding is formed from a silicon bulk substrate by irradiation and electro-chemical etching steps. The porosity determines the refractive index of the substrate (~ 1.4 in [87]). Although this platform was proposed to work at long MIR wavelengths, no information is provided in [87] about the transparency of porous silicon. A propagation loss of $3.9 \pm 0.2 \text{ dB cm}^{-1}$ was measured at $\lambda = 3.39 \mu\text{m}$.
- *Silicon on lithium niobate.* Lithium niobate (LiNbO_3) is transparent up to $\sim 5 \mu\text{m}$ and has a relatively low refractive index of ~ 2.5 . LiNbO_3 exhibits higher second-order optical nonlinearity and electro-optic coefficient than Si, thus making this compound very suitable for nonlinear applications and active devices in the MIR band. In [106], silicon-on-lithium-niobate (SOLN) waveguides were fabricated following a wafer bonding approach. A propagation loss of $2.5 \pm 0.7 \text{ dB cm}^{-1}$ was achieved at a wavelength of $3.39 \mu\text{m}$. This platform can be used to develop integrated electro-optic modulators in the MIR range.
- *Silicon on calcium fluoride.* In [107], a fabrication technique to transfer the upper silicon layer of SOI wafers onto virtually any material was proposed. As a proof of concept, the authors demonstrated high-contrast silicon-on-calcium-fluoride (SOCF)

waveguides, which can be potentially used up to a wavelength of $\sim 8 \mu\text{m}$. A propagation loss of 3.8 dB cm^{-1} was achieved at $\lambda = 5.2 \mu\text{m}$. Ring resonators were used to measure the absorption spectra of ethanol, toluene, and isopropyl alcohol.

- *T-waveguides*. In [108], wafer-bonded T-shaped waveguides were proved to be single-mode and single-polarization in a broad range of wavelengths. A propagation loss of 1.75 dB cm^{-1} was reported at $\lambda \sim 3.6 \mu\text{m}$.

2.2.2 Germanium-Core Platforms

Germanium on Silicon

At wavelengths longer than $\sim 8 \mu\text{m}$, silicon cannot be utilized in the waveguide core. To overcome the high absorption of silicon, germanium-core platforms, in which germanium is the material of the guiding layer, have been proposed with great success [68]. Germanium on silicon (GOS) is one of the first and most promising candidates at long MIR wavelengths ($\lambda > 8 \mu\text{m}$). In this platform, a germanium guiding layer is on top of a silicon substrate. Schematic GOS strip and rib waveguides are represented in Fig. 2.8a and Fig. 2.8b, respectively.

Since silicon is present in the under-cladding, low-loss transmission of light can only be achieved provided the fundamental mode is well confined within the waveguide core. Unfortunately, the relatively low index contrast between germanium and silicon, $\Delta n = n_{\text{Ge}} - n_{\text{Si}} \sim 0.55$, benefits the interaction of light with the under-cladding. Moreover, the lattice mismatch between silicon and germanium crystals at the core-substrate interface increases threading dislocation density (TDD). In addition, germanium exhibits higher free-carrier absorption (FCA) than silicon, especially at long wavelengths. These inconveniences can be minimized with careful designs, as indicated in [109].

A propagation loss as low as $0.58 \pm 0.12 \text{ dB cm}^{-1}$ has been demonstrated for single-mode rib waveguides at $\lambda = 3.8 \mu\text{m}$ [110]. Strip waveguides with propagation losses smaller than $\sim 3 \text{ dB cm}^{-1}$ have also been reported in the range between $5.3 \mu\text{m}$ and $5.8 \mu\text{m}$ [111,112] and utilized to conduct sensing experiments (cocaine detection [61]). Note that, in these cases, the full potential of the GOS platform is not exploited, as the operating wavelengths are not longer than $\sim 8 \mu\text{m}$.

Recently, Gallacher et al. achieved a significant milestone [109]: the authors demonstrated rib waveguides with losses lower than 5 dB cm^{-1} in the wavelength range from $7.5 \mu\text{m}$ to $11 \mu\text{m}$ for both TE and TM polarizations. Above $\lambda = 10 \mu\text{m}$, losses were as low as $\sim 1 \text{ dB cm}^{-1}$. These results constitute the first experimental validation of GOS waveguides at such long wavelengths. Additionally, a number of passive devices can be found in the literature, including grating couplers [110], MZIs [110,111], and phase shifters [113].

In [113], a germanium-on-silicon-on-insulator (GOSOI) platform was utilized. The GOSOI platform includes a thin SiO_2 layer that acts as a thermal insulator for realizing efficient thermo-optic phase shifters.

Silicon-Germanium on Silicon

Silicon-germanium (SiGe) alloys, which are CMOS-compatible, offer attractive optical properties — such as the possibility of engineering the refractive index, the material dispersion, or the third-order non-linearity [65]. Depending on the concentration of silicon

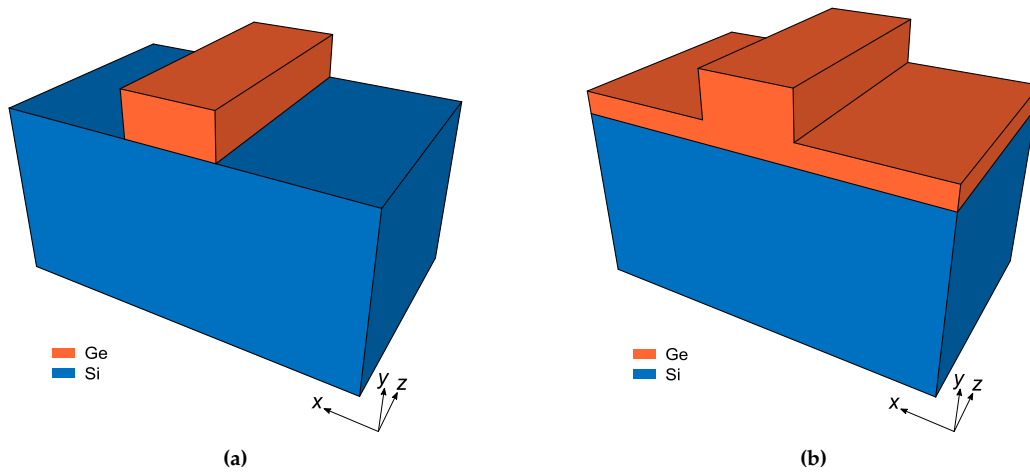


Figure 2.8: Schematic representation of (a) strip and (b) rib germanium-on-silicon waveguides.

and germanium, SiGe-based platforms can virtually cover the full transparency of germanium, making them one of the most significant platforms reported so far.

A silicon-germanium-on-silicon (SGOS) platform was demonstrated in [114]. A waveguide with a $\text{Si}_{0.6}\text{Ge}_{0.4}$ core buried in silicon yielded a loss of 0.5 dB cm^{-1} at $\lambda = 4.75 \mu\text{m}$. Interestingly, to couple light into this platform, a grating coupler was locally suspended to increase the core-cladding index contrast, thereby maximizing the radiation strength [115].

Instead of utilizing a uniform alloying, in [116] the authors proposed waveguides with graded $\text{Si}_{1-x}\text{Ge}_x$ cores that are buried in silicon, with x ranging from 0% to 40% (see Fig. 2.9). For a platform with $3\text{-}\mu\text{m}$ core thickness, low propagation losses of 1 dB cm^{-1} and 2 dB cm^{-1} were reported at $\lambda = 4.5 \mu\text{m}$ and $\lambda = 7.4 \mu\text{m}$, respectively. Y-junctions, directional couplers, s-bends, and crossings were also characterized at both central wavelengths. At $4.5 \mu\text{m}$, an AWG multiplexer was presented [117]. Experiments to measure the nonlinear optical response of these waveguides and supercontinuum generation, which are some of the prime reasons for exploring SiGe-based platforms, were carried out in [118] and [119], respectively.

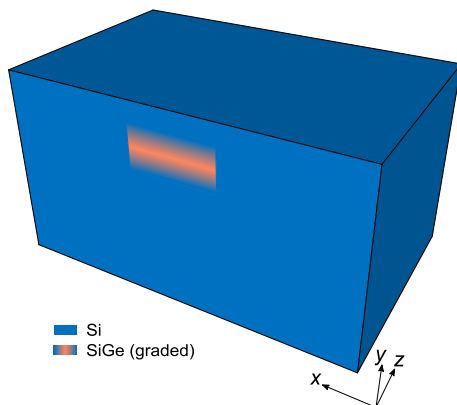


Figure 2.9: Schematic representation of a SiGe-on-Si waveguide. The core is buried in silicon and made of $\text{Si}_{1-x}\text{Ge}_x$, with x ranging from 0% to 40%, and from 40% to 0%.

Germanium-Rich (Graded) Silicon-Germanium on Graded Silicon-Germanium

Germanium-rich silicon-germanium alloys on a graded silicon-germanium layer improve the SGOS platforms of the previous section. In this case, the concentration of Ge is greater than that of Si ($x \geq 80\%$) in the homogeneous guiding layer, and the silicon substrate is substituted with a graded silicon-germanium alloy [72]. Propagation losses of $1.5 \pm 0.5 \text{ dB cm}^{-1}$ (TE) and $2 \pm 0.5 \text{ dB cm}^{-1}$ (TM) were achieved at $\lambda = 4.6 \mu\text{m}$.

Variants with graded SiGe in both the waveguide core and the under-cladding have also been reported in a wide spectral range [73], with propagation losses of $2\text{--}3 \text{ dB cm}^{-1}$ in the band from $\lambda = 5.5 \mu\text{m}$ to $\lambda = 8.5 \mu\text{m}$. Figure 2.10 depicts one of these SiGe-on-SiGe (SGOSG) waveguides, which enable index contrast tunability to virtually cover the entire MIR range up to $\lambda \sim 15 \mu\text{m}$.

Various high-performance devices have been demonstrated for this platform family, such as ultra-broadband MMIs [120] and racetrack resonators [121]. Theoretical designs of promising devices have been proposed, including ultra-wideband polarization rotators [122], polarization-insensitive MMIs [24], and grating couplers [123]. Sensing experiments have also been reported in the wavelength range spanning from $5.2 \mu\text{m}$ to $6.6 \mu\text{m}$ [64]. Recently, an integrated spatial heterodyne Fourier-transform spectrometer was proposed [78].

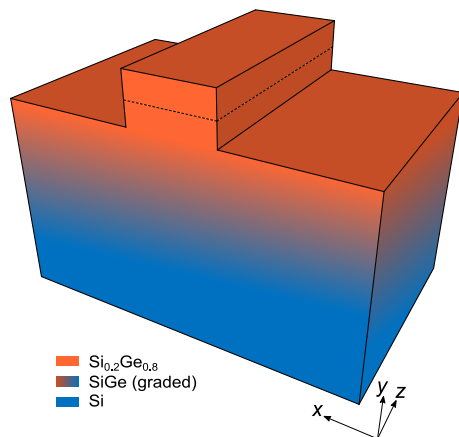


Figure 2.10: Schematic representation of a SiGe-on-graded-SiGe waveguide. In this example, the under-cladding layer of $\text{Si}_{1-x}\text{Ge}_x$ ranges from $x = 0$ up to $x = 79\%$, and the upper part of the core is homogeneous with $x = 80\%$.

Germanium on Nitride

A germanium-on-silicon-nitride (GON) platform is proposed in [124] (see Fig. 2.11). Due to the silicon nitride, the transparency window of this platform is comparable to that of SON. However, GON waveguides have a high core-cladding index contrast compared to SON and GOS platforms. This contrast benefits the development of more compact devices, with reduced cross-section and smaller bend radii. While this platform does not offer the advantages of GOS or silicon-germanium alloys, it can be useful for specific applications in which small footprints are required.

For TE-polarized single-mode strip waveguides, a propagation loss of 3.35 dB cm^{-1} was demonstrated at $\lambda = 3.8 \mu\text{m}$.

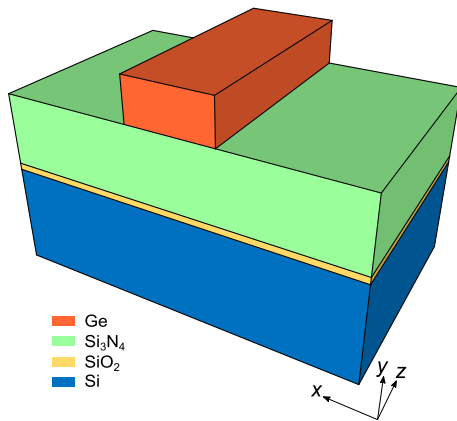


Figure 2.11: Schematic representation of a germanium-on-nitride waveguide. An SiO_2 bonding layer is between the nitride cladding and the silicon substrate.

Germanium on Insulator

The utilization of silicon dioxide as the under-cladding material vastly limits the transparency window of germanium. Therefore, the joint use of germanium and silicon dioxide is only helpful for applications where specific properties of germanium (e.g., high thermo-optic coefficient) are needed, or when very compact chips are required at short MIR wavelengths (below $\sim 4 \mu\text{m}$).

A high-contrast GOI platform was proposed in [125–127]. Rib and strip waveguides, with high propagation losses of $\sim 14 \text{ dB cm}^{-1}$ and $\sim 12 \text{ dB cm}^{-1}$, respectively, were characterized at $\lambda = 1.95 \mu\text{m}$, which is near the lower bound of the MIR range. The authors attribute the high losses to sidewall roughness caused by the fabrication process. Other passive devices, such as grating couplers, MMIs, ring resonator, and Vernier filters, were also reported [127, 128].

2.2.3 Alternative Platforms

While the most significant platforms are silicon- and germanium-based, other solutions can be found in the literature. Some of them are briefly reviewed in this section:

- *Silicon nitride on insulator.* In [129, 130], strip silicon-nitride-on-insulator (SiNOI) waveguides were presented. The core material of this CMOS-compatible platform is silicon nitride, which rests on a thick silicon dioxide layer on top of a silicon substrate. Silicon nitride can be useful for sensing in harsh environments because of its chemical stability and mechanical hardness [130]. Propagation losses of 0.16 dB cm^{-1} and 2.1 dB cm^{-1} were reported at $\lambda = 2.65 \mu\text{m}$ and $\lambda = 3.7 \mu\text{m}$, respectively.
- *Silicon carbide on insulator*
Silicon carbide is an excellent material for nonlinear applications in the MIR band because of its large second- and third-order nonlinearity coefficients. This compound appears in different crystalline structures or polytypes. 4H-SiC and oxidized silicon wafers are bonded to form a silicon-carbide-on-insulator (SiCOI) platform in [131]. Waveguides with a propagation loss of 7 dB cm^{-1} were demonstrated at $\lambda = 2.36 \mu\text{m}$.
- *Aluminum nitride on insulator.* Although this work deals exclusively with Group IV materials, it is worth mentioning MIR integrated platforms that are based on other

semiconductors. Aluminum nitride on insulator (AlNOI) is an especially promising III-V platform. Aluminum nitride has interesting properties for MIR applications in integrated photonics, such as broad transparency window ranging from 200 nm to 13.6 μm , CMOS compatibility, and thermochemical resistance. As for the SON platform, the latter can be helpful for sensing applications. The AlNOI platform was firstly utilized for the MIR in [132]. Strip waveguides with reduced propagation loss ($\alpha = 0.83 \text{ dB cm}^{-1}$) were demonstrated at the short wavelength of 2.5 μm , together with bends and 3-dB splitters. Recently, Dong et al. extended the operating wavelength up to 3.8 μm , but a high loss of 17.4 dB cm^{-1} was reported. Passive devices, such as directional couplers, MMIs, and add/drop filters, were also demonstrated [133].

- *Other non-Group IV semiconductors*

Other platforms not based on Group IV materials include silver halides [134, 135], chalcogenide crystals [136–139], mercury-cadmium-telluride [140, 141], and III-V semiconductors [142, 143]. Some of these platforms might lack the benefits of silicon photonics (e.g., large-scale production or compatibility with microelectronic manufacturing procedures), but can be useful for (bio)chemical sensing or nonlinear applications, for example.

2.3 Suspended Platforms

2.3.1 Suspended Membranes

The use of undercut SOI was proposed first by Soref et al. [3]. By replacing solid materials such as silicon dioxide or sapphire with air, suspended waveguides can take advantage of the entire transparency windows of silicon and germanium. In addition, these waveguides are especially appropriate for absorption-based detection of analytes, as a gas or liquid sample can fill the whole surrounding cladding.

Cheng et al. demonstrated suspended rib SOI waveguides, also known as suspended membranes, for the first time [74]. The rib creates the lateral silicon-air index contrast required for waveguiding. A set of holes is etched at both sides of the silicon core. The lateral holes do not interact with the fundamental mode propagating through the silicon core. These holes enable the flow of a hydrofluoric (HF) solution to reach and remove the silicon dioxide. Therefore, two dry-etch steps and one wet-etch step are necessary: (i) for defining the rib and (ii) for etching the holes. Figure 2.12 shows a schematic diagram of this suspended membrane. At $\lambda = 2.75 \mu\text{m}$, a propagation loss as low as 3.0 dB cm^{-1} was achieved. Ring resonators and grating couplers were also developed [74, 144].

Suspended membranes based on germanium have also been proposed, yielding propagation losses of 5.4 dB cm^{-1} , 2.9 dB cm^{-1} , and 2.6 dB cm^{-1} at wavelengths of 2.15 μm [145], 3.8 μm [146], and 7.67 μm [77], respectively. These germanium-based waveguides can potentially cover the full MIR band.

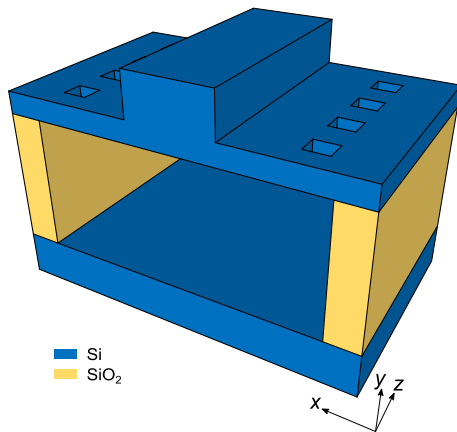


Figure 2.12: Schematic representation of a suspended silicon membrane waveguide.

2.3.2 SWG-Cladding Suspended Platforms

A suspended silicon platform based on strip waveguides with lateral subwavelength grating (SWG) cladding,³ schematically represented in Fig. 2.13, was presented for the first time in [75]. Unlike in suspended membranes, only one dry etch step is needed, which simultaneously defines the waveguide core and an SWG lattice of holes. This SWG cladding has a three-fold function: (i) to mechanically support the waveguide core, (ii) to synthesize a cladding-core index contrast that enables light guiding for a fundamental mode, and (iii) to allow the flow of the HF acid solution that removes the BOX. A propagation loss as low as 0.82 dB cm^{-1} was achieved at $\lambda = 3.8 \mu\text{m}$. Suspended silicon waveguides with a loss of 3.1 dB cm^{-1} at $\lambda = 7.67 \mu\text{m}$ constitute one of the main contributions of this thesis [79]. At this central wavelength, other devices, such as bends and MMIs, were also reported [79, 80, 147].

Zhou et al. demonstrated an SWG-cladding suspended silicon slot platform in [76], including slot waveguides, bends, racetrack resonators, and slot-to-strip mode converters. Owing to the high field concentration within the slot, these waveguides can offer high sensitivity for sensing applications up to $\sim 8 \mu\text{m}$.

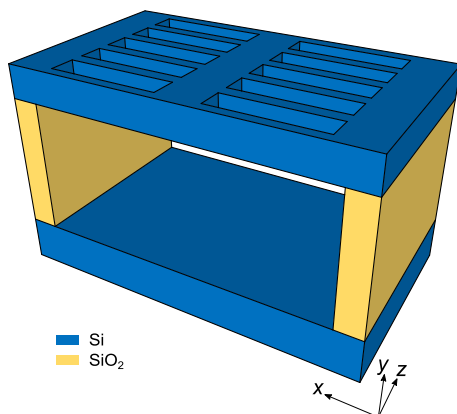


Figure 2.13: Schematic representation of a suspended silicon strip waveguide (with lateral SWG cladding).

SWG-cladding suspended silicon and germanium strip waveguide platforms constitute the backbone of this thesis. Suspended strip waveguides, devices, and surface fiber-

³From now on, waveguides based on this platform will be simply denoted as *suspended waveguides*. In this work, the denomination *suspended membrane* is reserved for the suspended rib waveguides of Section 2.3.1.

chip couplers have been developed at various MIR wavelengths. An in-depth study of the platform will be provided in Chapter 3.

2.3.3 Other Suspended Platforms

Alternative methods to suspend the guiding layer have been reported. Although these results are interesting in theory, they involve much more complex fabrication processes than the previous suspended structures and have not gained much popularity:

- *Fusion-bonded suspended silicon membrane.* In suspended membranes, venting holes are far from the waveguide core. Consequently, the suspended area is too wide and the membrane stability can be compromised. Narrower, more mechanically robust suspended membranes are demonstrated in [148], where a silicon layer with etched waveguides is fusion-bonded to a silicon substrate with pre-patterned air trenches. Thus, while the fabrication process is more difficult than that of conventional suspended membranes, the necessity of holes is removed. Figure 2.14a shows a schematic of a fusion-bonded suspended membrane. At $\lambda = 3.39 \mu\text{m}$, the propagation loss is 2.8 dB cm^{-1} .
- *Air-gap silicon rib.* In this platform, rib structures are etched at one side of a silicon wafer and a large gap is etched at the other side, as shown in Fig. 2.14b [149]. Waveguides with a propagation loss of 11 dB cm^{-1} , bends, and 1×2 MMIs were developed at $\lambda = 10.6 \mu\text{m}$.

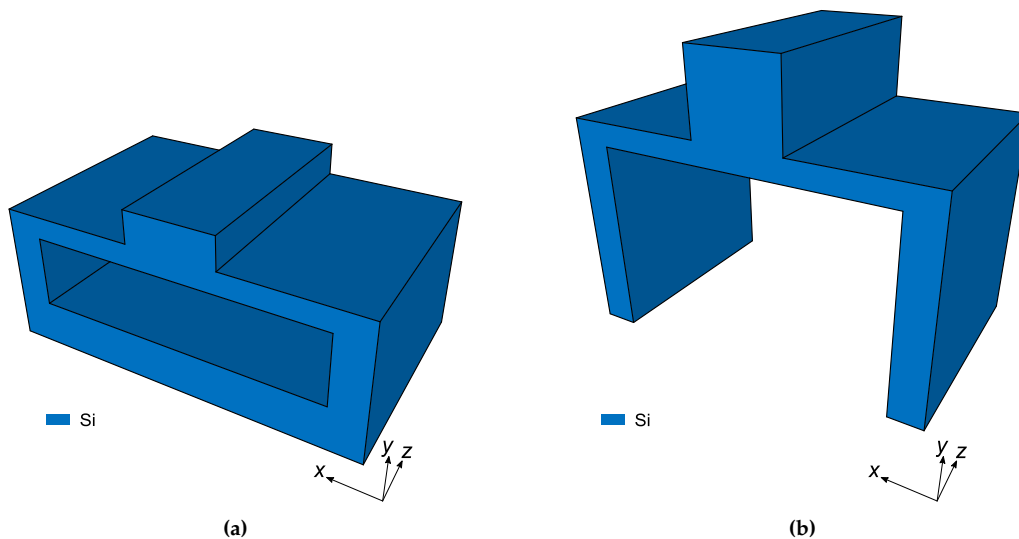


Figure 2.14: Schematic representation of alternative suspended waveguides: (a) a fusion-bonded suspended silicon membrane and (b) an air-gap silicon rib waveguide.

2.4 Summary of Platforms

In this section the most relevant MIR platforms that have been demonstrated so far in the literature are summarized. Conventional waveguides are reviewed in tables 2.1–2.3; and

suspended platforms, in table 2.4. For each platform, waveguide type, and wavelength, only the waveguides with lowest propagation losses are considered. The symbol “–” is used when a parameter is not applicable to a specific structure, whereas empty spaces are left when data is not explicitly available in the referenced articles. The nominal propagation loss α is indicated at the central wavelength λ . Platforms are sorted according to the order followed in this chapter, the type of waveguide (rib, strip, and slot), and the wavelength (from short to longer). The meaning of the geometrical parameters used in the tables is shown in Fig. 2.15 for the different waveguide configurations.

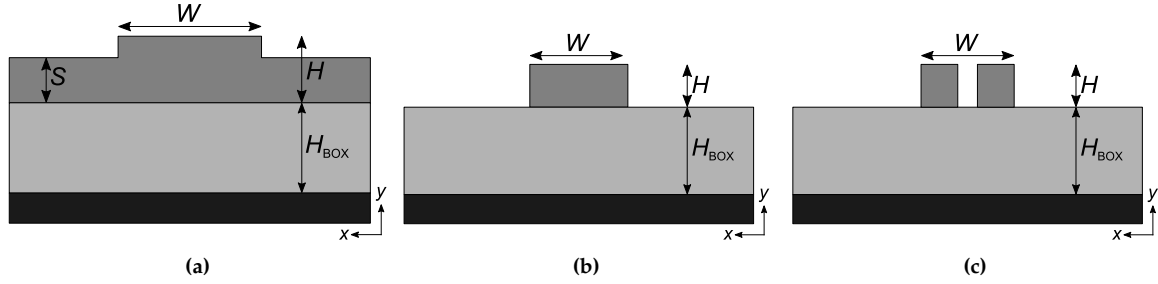


Figure 2.15: Geometrical parameters of (a) rib, (b) strip and (c) slot waveguides.

Table 2.1: Review of non-suspended platforms based on silicon. All dimensions and the wavelength are given in microns. Propagation losses are given in decibels per centimeter.

Plat.	Type	H	W	S	H_{BOX}	λ	Pol.	α	Ref.
SOI	Rib	0.8	2	1.2	2	3.4	TE / TM	0.6 / 0.7	[87]
SOI	Rib	0.22	1.35	0.18	2	3.8	TE	1.5	[91]
SOI	Strip	0.22	0.9	–	2	2.1	TE	0.6	[95]
SOI	Strip	0.5	1.3	–	3	3.8		1.3	[71]
SOI	Slot	0.5	1.38	0.08	3	3.8	TE	1.4	[150]
SOS	Strip	0.28	0.8	–	–	2.1	TE	1.1	[151]
SOS	Strip	0.28	1	–	–	2.1	TM	1.4	[151]
SOS	Strip	0.6	1	–	–	3.4	TE	2.1	[102]
SOS	Strip	0.8	1.5	–	–	4.5		0.7	[98]
SOS	Strip	0.28	1	–	–	5.2	TE	1.9	[151]
SOS	Strip	0.6	1.8	–	–	5.5	TE	4	[99]
SOS	Slot	0.6	0.6	0.13	–	3.4	TE	11	[102]
SON	Rib	0.8	2	1.2	1.3	3.4	TE / TM	5.2 / 5.1	[70]
Si	Pedestal	5	8	2	14	3.7		2.7	[105]

Table 2.2: Review of non-suspended platforms based on germanium. All dimensions and the wavelength are given in microns. Propagation losses are given in decibels per centimeter.

Plat.	Type	H	W	S	H_{BOX}	λ	Pol.	α	Ref.
GOS	Strip	1	2	–	–	3.7	TE	7.8	[111]
GOS	Strip	2	2.25	–	–	5.3	TE	3	[111]
GOS	Strip	2	2.9	–	–	5.8	TM	2.5	[112]
GOS	Rib	1.2	2.25	0.8	–	3.8	TE	2.5	[152]
GOS	Rib	1.7	2.7	1.2	–	3.8	TE	0.58	[110]
GOS	Rib	1.8	4.3	1.2	–	7.6	TE	2.5	[153]
GOS	Rib	1	4	1	–	10	TE	~ 1	[109]
GOSOI	Strip	0.85	6.5	–	2.22*	3.7	TE	~ 8	[154]
GOSOI	Strip	2	2.2	–	5*	5.3	TM	7	[113]
GOI	Strip	0.24	0.35	–	2	2	TE	20	[127]
GOI	Rib	0.2	0.6	0.1	2	2	TE	14	[126]
GON	Strip	1	2	–	1	3.8	TE	3.35	[124]
SGOS	Strip	2.7	3.75	–	–	4	TE	0.38	[119]
SGOS	Strip	4.2	6	–	–	4.2	TM	0.28	[119]
SGOS	Strip	1.4	2	–	–	4.8	TE	0.5	[114, 118]
SGOS	Strip	3	3.3	–	–	4.5	TM	< 1	[116]
SGOS	Strip	3	3.3	–	–	5.7	TM	< 1.5	[116]
SGOS	Strip	3	7	–	–	7.4	TM	< 2	[116]
SGOSG	Rib	2	7	0.5	–	4.6	TE	1.5	[72]
SGOSG	Rib	2	7	0.5	–	4.6	TM	2	[72]
SGOSG	Rib	–	4	9	–	5.5 – 8.5	TE / TM	2-3	[73]
SGOSG	Rib	–	4	2	–	5.5 – 8.5	TE / TM	2-3	[73]

* This value includes the thicknesses of both the silicon and the silicon dioxide layers.

Table 2.3: Review of non-suspended platforms based on other materials different from silicon or germanium. All dimensions and the wavelength are given in microns. Propagation losses are given in decibels per centimeter.

Plat.	Type	H	W	S	H_{BOX}	λ	Pol.	α	Ref.
SiNOI	Strip	2.5	4	–	4	3.7	TM	2.1	[130]
SiNOI	Strip	4	2.5	–	2.5	2.7		0.16	[129]
AlNOI	Strip	1	10	–	3	2.5	TM	0.83	[132]
AlNOI	Strip	1.2	2.25	–	3	3.8		17.4	[133]
SiCOI	Strip	0.6	2.7	–	3	2.36	TE	7	[131]

Table 2.4: Review of suspended platforms. All dimensions and the wavelength are given in microns. Propagation losses are given in decibels per centimeter.

Plat.	Type	H	W	S	H_{BOX}	λ	Pol.	α	Ref.
Si	Membrane	0.24	1	0.1	2	2.75	TE	3	[144]
Si	Air-gap	4	5	5	–	10.6	TE	11	[149]
Si	Wafer bonded	1.07	2.4	1.07	2	3.4	TE	4	[148]
Si	Wafer bonded	1.07	2.4	1.07	2	3.4	TM	2.8	[148]
Si	SWG (strip)	0.5	1.3	–	3	3.8	TE	0.82	[147]
Si	SWG (strip)	1.5	2.9	–	3	7.67	TE	3.1	This work [79]
Si	SWG (slot)	0.34	1	–	2	2.25	TE	2.8	[76]
Ge	Membrane	0.3	0.9	0.15	2	2.15	TE	5.4	[145]
Ge	Membrane	0.25	1.1	0.15	3.22	3.8	TE	2.9	[146]
Ge	Membrane	0.3	3.5	0.7	3.06	7.67	TE	2.6	[77]
Ge	SWG (strip)	0.5	1.3	–	3.06	3.8	TE	4.5	This work
Ge	SWG (strip)	1	2.9	–	3.06	7.67	TE	5.2	This work

CHAPTER THREE

SUSPENDED PLATFORMS FOR THE MID-INFRARED BAND

Of all the aforementioned platforms, suspended silicon and suspended germanium seem to arise as excellent choices for the MIR band. Both platforms have the potential to offer low-loss propagation of light and can be fabricated by using well-established manufacturing techniques. Suspended silicon waveguides can operate up to $\lambda \sim 8 \mu\text{m}$, whereas suspended germanium waveguides can cover even longer wavelengths, up to $\sim 15 \mu\text{m}$.

The aim of this chapter is to prove the viability of suspended platforms for light guiding. It begins by showing the geometry of suspended waveguides and their guiding principle (Section 3.1). Then, the modeling approaches for simulating suspended waveguides are proposed. These models are applied to design suspended silicon and suspended germanium waveguides (Section 3.2). Next, the definition of masks and the lithographic manufacturing process are described (Section 3.3), and experimental results are discussed (Section 3.4). For the suspended silicon platform, the design of some building blocks is provided (Section 3.5). These results validate the presented suspended waveguides and devices as an effective integrated platform for MIR applications. The chapter ends with concluding remarks (Section 3.6).

3.1 Introduction

The suspended silicon and suspended germanium platforms are based on SOI and GO-SOI wafers, respectively. Cross-sections of both wafers are illustrated in Fig. 3.1. The thickness H of the guiding layers can be customized when the wafers are purchased. The BOX thickness is fixed to $3 \mu\text{m}$. GOSOI wafers have a 60-nm-thick silicon film between the germanium layer and the BOX. This thin film will not affect the guiding capabilities of the designed waveguides and, thus, will be ignored from now on.

The suspended platforms are fabricated from these wafers in two steps: firstly, the waveguide core and lateral cladding are patterned and dry-etched; secondly, the BOX is removed using an acid solution (wet etching). A generic suspended waveguide is illustrated in Fig. 3.2. The core, of width W and thickness H , is anchored to lateral unetched silicon or germanium areas by a periodic cladding. This cladding, of width W_{clad} , com-

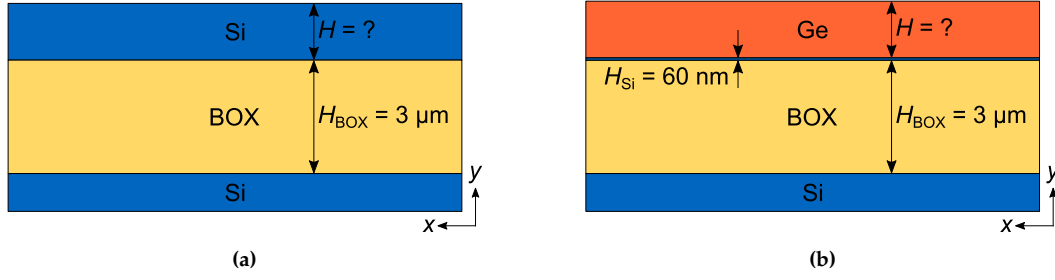


Figure 3.1: Cross-sections of the (a) SOI and (b) GOSOI wafers used for suspended silicon and suspended germanium platforms, respectively. The guiding layer thickness (H) must be designed. The BOX thickness is fixed to $3 \mu\text{m}$. The GOSOI wafer has a thin silicon layer of thickness $H_{\text{Si}} = 60 \text{ nm}$ that is removed when the suspended germanium waveguide is wet-etched.

prises strips of length L_{strip} and holes of length L_{hole} . An air gap of thickness $H_{\text{BOX}} = 3 \mu\text{m}$ separates the guiding layer from the silicon substrate.

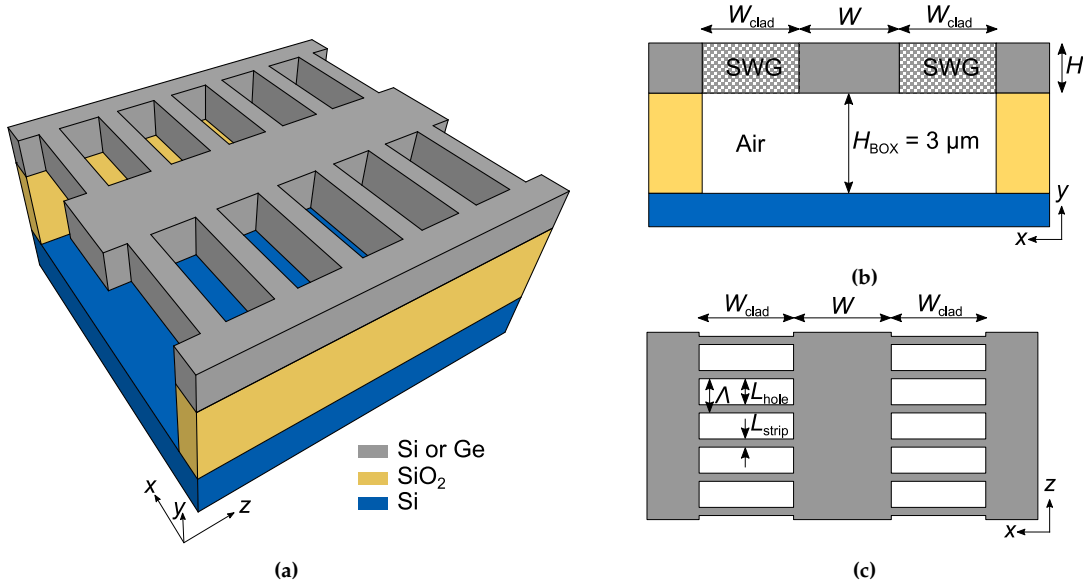


Figure 3.2: Schematic representation of a suspended silicon or suspended germanium waveguide. (a) 3D view. (b) Front view. (c) Top view of the guiding layer. In the front view the lateral cladding is replaced by a homogeneous SWG metamaterial.

The periodic cladding of a suspended waveguide operates in the subwavelength grating (SWG) regime.¹ Subwavelength gratings are arrangements of structures with a periodicity Λ smaller than half the guided wavelength, i.e.,

$$L_{\text{strip}} + L_{\text{hole}} = \Lambda < \Lambda_{\text{Bragg}} = \frac{\lambda}{2 \text{Re}(n_{\text{B}})}, \quad (3.1)$$

where Λ_{Bragg} is the Bragg period and n_{B} is the effective index of the fundamental Bloch-Floquet mode traveling along the waveguide [155]. In the SWG regime, radiation and Bragg reflection effects are suppressed and the periodic structure can be modeled as a homogeneous non-diffractive metamaterial whose refractive index depends on the ratio

¹A description of the different operating regimes of periodic structures will be provided in Chapter 4.

Λ/λ and the duty cycle ($DC = L_{\text{strip}}/\Lambda$) [155–157]. In suspended waveguides, the SWG cladding has three different functions:

- (i) *To support the waveguide core.* The strips of the cladding support the suspended core and prevent it from collapsing.
- (ii) *To allow BOX removal.* An acid solution flows through the periodically distributed holes that are etched in the cladding and removes the silicon dioxide under the guiding layer.
- (iii) *To provide refractive index contrast.* By conveniently choosing the pitch and the duty cycle, the lateral refractive index contrast that is required for waveguiding can be controlled.

If the suspended waveguide is properly designed and fabricated, the fundamental mode is strongly confined within the core and propagates through the structure as shown in Fig. 3.3.

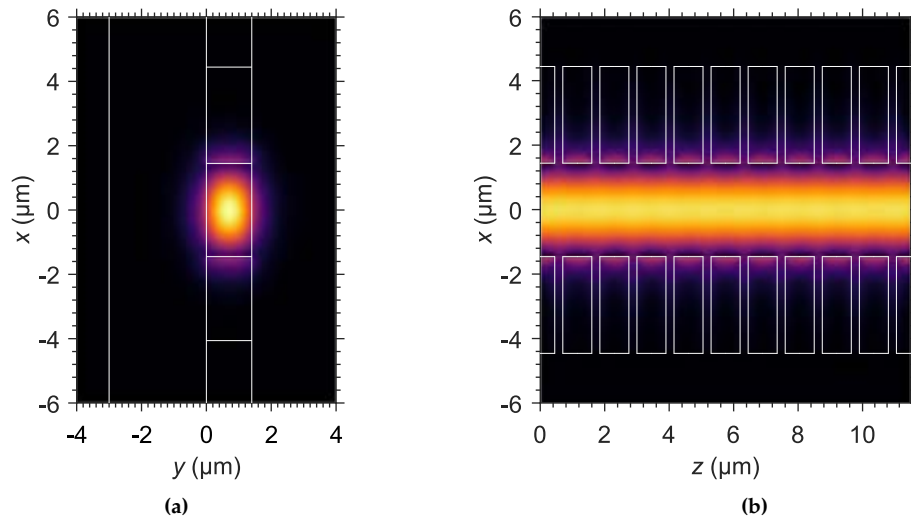


Figure 3.3: (a) Transverse field distribution and (b) propagation of the fundamental mode (TE polarization) of a suspended waveguide. The structure is outlined.

Simulations were carried out at UMA using a workstation with Intel Xeon ES-2697 v3 processor at 2.6 GHz. The fabrication and characterization processes were performed in the ORC. Currently, ORC's *Mid-Infrared Group IV Photonics* laboratory has three QCL lasers, whose central wavelengths are 3.8 μm , 7.67 μm , and 9.6 μm . The suspended waveguides should be realized at these wavelengths.

The upper bound of the transparency window of silicon is $\lambda \sim 8 \mu\text{m}$. Therefore, the useful wavelengths are 3.8 μm and 7.67 μm . In 2014 and 2016, suspended silicon waveguides were demonstrated at $\lambda = 3.8 \mu\text{m}$ [75, 147]. Thus, regarding the suspended silicon platform, this thesis is only focused on the development of waveguides at $\lambda = 7.67 \mu\text{m}$. At this wavelength, waveguides have been designed, fabricated, and characterized for TE polarization, yielding a propagation loss of $\sim 3 \text{ dB cm}^{-1}$, of which $\sim 2 \text{ dB cm}^{-1}$ are attributed to silicon loss. The remaining loss ($\sim 1 \text{ dB cm}^{-1}$), which can be attributed to roughness, is comparable to that reported in [147] at $\lambda = 3.8 \mu\text{m}$.

From the point of view of propagation losses, suspended germanium waveguides are not necessary at $\lambda = 3.8 \mu\text{m}$, since suspended silicon is low-loss and preferable. However, the measurement setup of the ORC at $3.8 \mu\text{m}$ is more mature (the available source is tunable and the optical fibers are less fragile) than at longer wavelengths. As a consequence, suspended germanium waveguides were realized at $3.8 \mu\text{m}$ to test the concept. At $7.67 \mu\text{m}$ and $9.6 \mu\text{m}$, suspended germanium waveguides are interesting per se because they can potentially offer low-loss propagation. They have been designed at both wavelengths. The first experimental losses, which have been measured only at $7.67 \mu\text{m}$, are promising ($\sim 5 \text{ dB cm}^{-1}$), but there is still room for improvement. At the time of writing this thesis, new chips are being fabricated to operate at $\lambda = 7.67 \mu\text{m}$ and $\lambda = 9.6 \mu\text{m}$.

In the following sections, the development cycle of suspended silicon and suspended germanium waveguides will be covered. The diagram in Fig. 3.4 summarizes the specific objectives of this chapter and the results obtained so far.

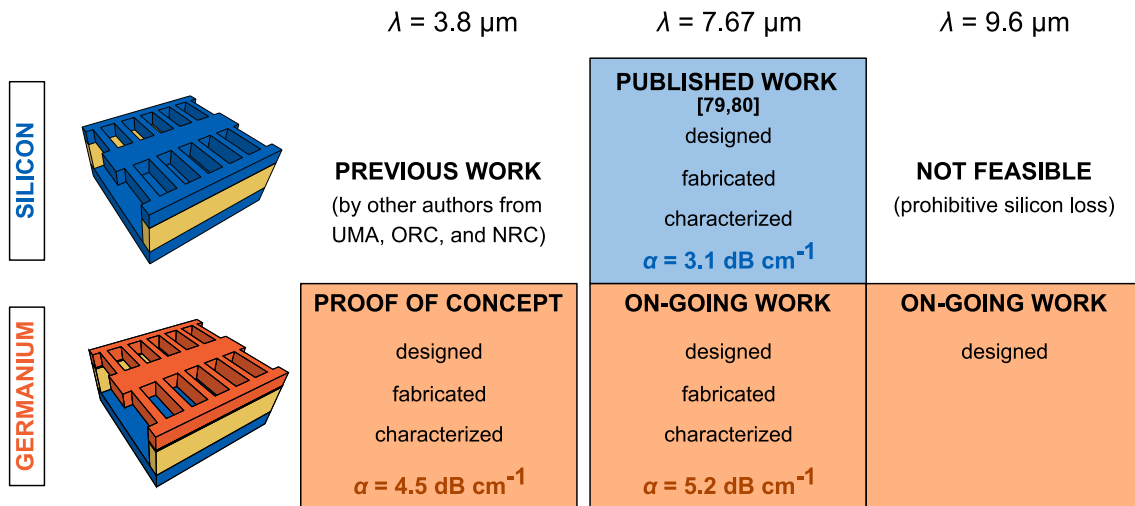


Figure 3.4: Overview of the designed suspended silicon and suspended germanium waveguides. The indicated propagation losses (α) correspond to measured data.

3.2 Waveguide Design

3.2.1 Waveguiding Requirements

To ensure single-mode operation with low propagation loss, suspended waveguides must be designed to meet the following requirements:

- (i) *Mechanical requirements.* The SWG cladding must be mechanically robust and the torque must be low enough to prevent collapse. Even small breaks in the cladding strips can increase the propagation loss.
- (ii) *Fabrication requirements.* The cladding holes must be sufficiently large to allow the flow of the acid liquid that suspends the structure. If silicon dioxide is not fully removed, remnants can vastly increase the propagation loss. Besides, the fabrication process and the thickness of the guiding layer impose a minimum feature size.
- (iii) *Optical requirements.*

- *SWG operation.* To avoid radiation or Bragg reflections, the periodic cladding must satisfy the SWG condition [see Eq. (3.1)].
- *Leakage minimization.* The modes supported by the waveguide can suffer from power leakage to the substrate (vertical leakage) and to the lateral unetched silicon or germanium (lateral leakage). Therefore, to enable practical single-mode operation, the fundamental mode must propagate with negligible vertical and lateral leakage losses, while high-order modes, if guided, must be leaked. As an example, Fig. 3.5 shows a cut of the fundamental (TE_{00}) and second-order (TE_{10}) modes at the middle of the waveguide core ($y = H/2$) for several core widths. In Fig. 3.5a the width is narrow enough to cut off the high-order mode, but at the expense of high leakage loss for the fundamental mode. The opposite case is shown in Fig. 3.5c, in which the core is so wide that both modes are strongly guided. A compromise solution is observed in Fig. 3.5b. Variations in H , W_{clad} , L_{strip} , and L_{hole} similarly affect the modal confinement.

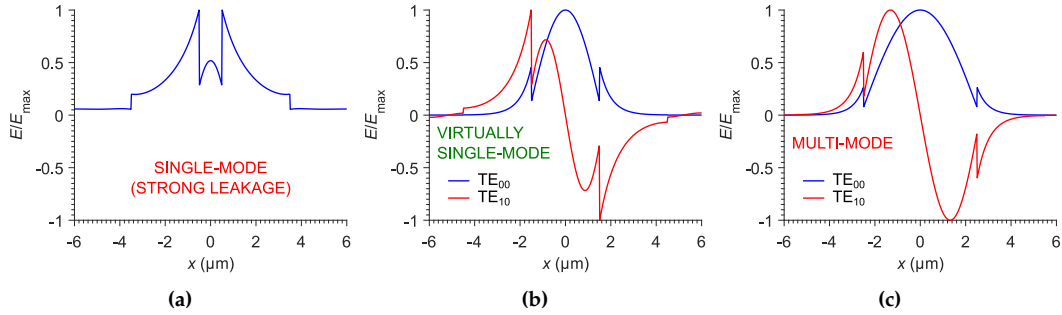


Figure 3.5: Influence of the core width on the TE_{00} and TE_{10} modes of a suspended waveguide. The transverse distribution of the electric field is cut at the middle of the waveguide core ($y = H/2$) for (a) $W = 1 \mu\text{m}$, (b) $W = 3 \mu\text{m}$, and (c) $W = 5 \mu\text{m}$.

All these requirements should be fulfilled simultaneously. Table 3.1 indicates whether high (\uparrow) or low (\downarrow) values are needed in practical waveguides for suspension and mechanical stability. Single-mode operation is examined in Table 3.2. A comparative analysis of both tables shows that most of the parameters require high values for some requirements and low values for others. Therefore, in order to meet the requirements, a trade-off between the different dimensions is necessary.

Table 3.1: Design requirements for suspension and mechanical stability in suspended waveguides.

Requirement	H	W	W_{clad}	L_{strip}^*	L_{hole}^*
Flow of HF acid solution	\downarrow			\downarrow	\uparrow
Lightweight waveguide core	\downarrow	\downarrow			
Robust cladding			\downarrow	\uparrow	\downarrow

* $L_{\text{strip}} + L_{\text{hole}} < \Lambda_{\text{Bragg}}$ according to Eq. (3.1).

H_{BOX} is fixed to $3 \mu\text{m}$ and cannot be designed.

3.2.2 Design Methodology and Modeling

The ultimate design goal is to minimize the propagation loss (α) of the fundamental mode supported by the suspended waveguide. The propagation loss is proportional to

Table 3.2: Design requirements for single-mode operation in suspended waveguides. Blue arrows highlight the most critical parameters for each requirement.

Requirement	H	W	W_{clad}	L_{strip}^*	L_{hole}^*
Reduced vertical leakage for TE ₀₀ mode	↑	↑		↑	↓
Increased vertical leakage for TE ₀₁ mode	↓	↓		↓	↑
Reduced lateral leakage for TE ₀₀ mode	↑	↑	↑	↓	↑
Increased lateral leakage for TE ₁₀ mode	↓	↓	↓	↑	↓

* $L_{\text{strip}} + L_{\text{hole}} < \Lambda_{\text{Bragg}}$ according to Eq. (3.1).
 H_{BOX} is fixed to 3 μm and cannot be designed.

the imaginary part of the effective index (n_B) of the mode and is due to the intrinsic loss of the core material (α_{material}) and the power leakage (α_{leakage}) as follows:

$$\alpha = \frac{2\pi}{\lambda} \text{Im}(n_B) \sim \Gamma \alpha_{\text{material}} + \alpha_{\text{leakage}}, \quad (3.2)$$

where Γ is the confinement factor within the core as defined in [158].²

The term $\Gamma \alpha_{\text{material}}$ of Eq. (3.2) is only relevant if the core material exhibits high loss at the operating wavelength. For example, $\alpha_{\text{Si}} \sim 2 \text{ dB cm}^{-1}$ at $\lambda = 7.67 \mu\text{m}$. In such a case, the influence of the material loss could be reduced by decreasing the confinement factor. The leakage term can be expressed as the sum of vertical and lateral leakage losses:

$$\alpha_{\text{leakage}} = \alpha_{\text{vertical}} + \alpha_{\text{lateral}}. \quad (3.3)$$

Both the confinement factor and the leakage depend on the dimensions of the waveguide. In practical designs, the confinement factor cannot be reduced without substantially increasing the leakage, so that only the latter can be minimized.

For conventional, non-suspended waveguides, the power leakage can be computed with commercial photonic simulators such as Photon Design's FIMMWAVE [159] or Synopsys' RSoft FemSIM [160]. As suspended waveguides are periodic structures, guided modes are Bloch–Floquet solutions of Maxwell's equations. In most of the mode solvers, Bloch–Floquet modes cannot be calculated easily and workarounds are required. In this thesis, three different approaches, which are summarized in Fig. 3.6, are proposed for modeling and simulating the suspended waveguides:

- *Isotropic approach.* This is the simplest approach. The SWG cladding is modeled as a homogeneous isotropic metamaterial with an equivalent refractive index $n_{\text{SWG}} = n_{xx}$, which can be approximated by Rytov's formula [161]:

$$n_{xx} \sim \left[\text{DC} \cdot n_{\text{strip}}^2 + (1 - \text{DC}) \cdot n_{\text{hole}}^2 \right]^{1/2}, \quad (3.4)$$

where n_{strip} is the refractive index of the cladding strips (silicon or germanium) and n_{hole} is the refractive index of the material that fills the cladding holes (air). Simulations can be carried out with any mode solver. In this work, RSoft FemSIM is employed, taking less than 10 s per effective index calculation.³ Vertical leakage simulations are highly accurate, yet lateral leakage losses are underestimated for narrow cladding widths.

²In Eq. (3.2), the influence of the material loss of the SWG cladding strips has not been considered.

³Using a uniform mesh of 50 nm (x direction) and 100 nm (y direction).

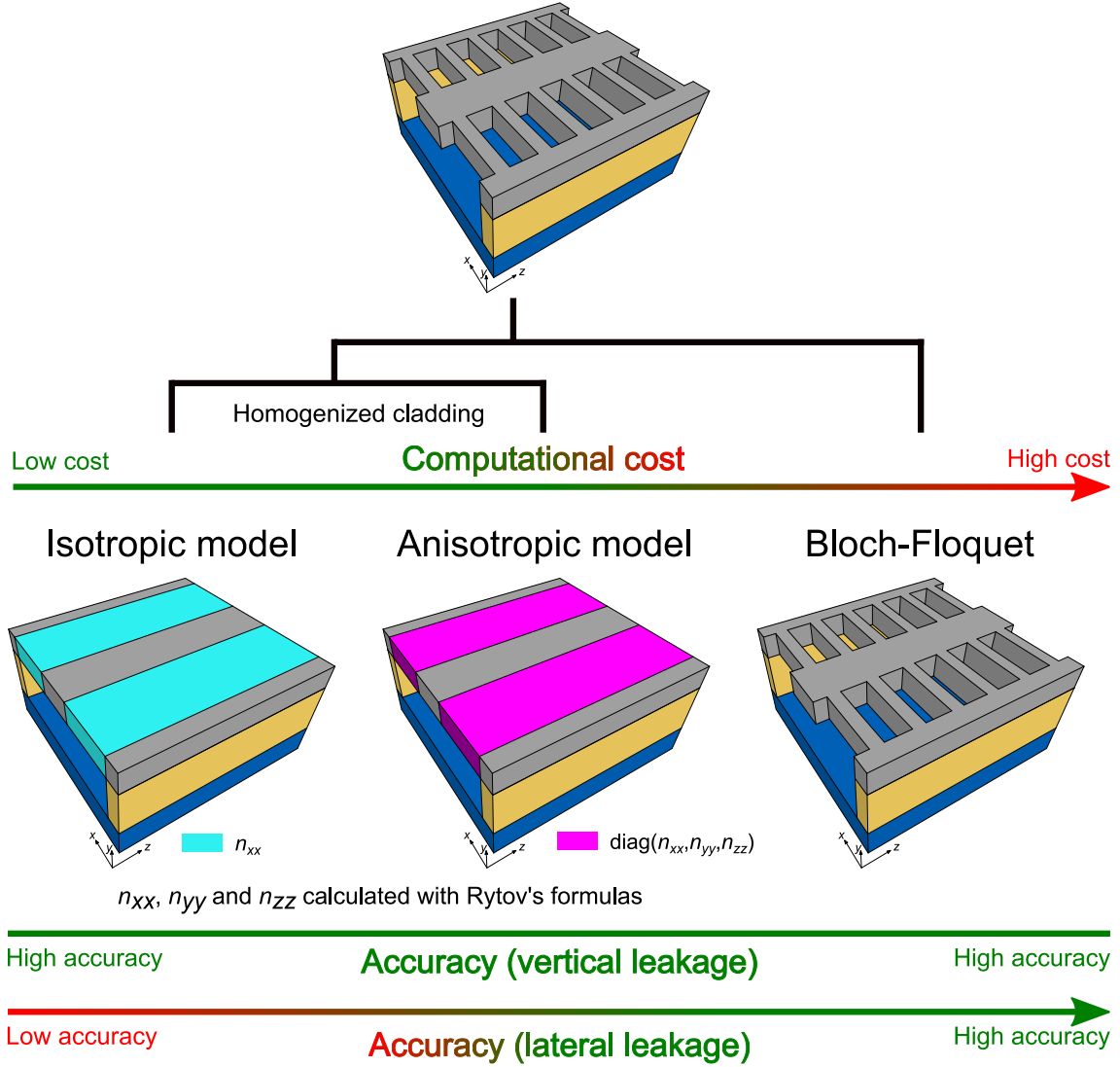


Figure 3.6: Modeling approaches of an SWG-cladding suspended waveguide.

- *Anisotropic approach.* The SWG cladding is modeled as a homogeneous anisotropic equivalent material (uniaxial crystal) with a permittivity tensor as follows [162]:

$$n_{\text{SWG}}^2 = \begin{bmatrix} n_{xx}^2 & 0 & 0 \\ 0 & n_{yy}^2 & 0 \\ 0 & 0 & n_{zz}^2 \end{bmatrix}, \quad (3.5)$$

where n_{xx} , n_{yy} , and n_{zz} can be calculated by Rytov's formulas [161]. Specifically, n_{xx} ($= n_{yy}$) can be estimated with Eq. (3.4), and

$$n_{zz} \sim \left[\text{DC} \cdot n_{\text{strip}}^{-2} + (1 - \text{DC}) \cdot n_{\text{hole}}^{-2} \right]^{-1/2}. \quad (3.6)$$

Simulations can be performed using FIMMWAVE, whose finite-element method (FEM) and finite-difference method (FDM) solvers support anisotropic homogeneous materials. While the computation time is only slightly increased with respect

to the isotropic model (~ 20 s per simulation⁴), lateral leakage results are much more accurate if the numerical parameters of the simulator are conveniently adjusted.

- *Bloch–Floquet approach.* The suspended waveguide is simulated by Bloch–Floquet modal analysis without homogenizing the SWG cladding. Effective indices can be calculated, for example, with RSoft FullWAVE (3D finite-difference time-domain method, 3D FDTD) [163] using a resonant method similar to that described in [164] in conjunction to signal-processing techniques [165–167]. This model is the most accurate, but the simulation time is substantially increased with respect to the previous approaches (~ 20 min per simulation point⁵).

The three models are compared in Fig. 3.7. The real part of the effective index of the fundamental mode of a suspended silicon waveguide is plotted versus the core thickness in Fig. 3.7a. In the depicted range of thicknesses, the maximum absolute error between the effective indices that are calculated for the isotropic and Bloch–Floquet models is 0.032, and half that value between the anisotropic and Bloch–Floquet approaches. These results suggest that simulations based on both the isotropic and the anisotropic models provide satisfactory mode solutions, which agree well with the Bloch–Floquet analysis.

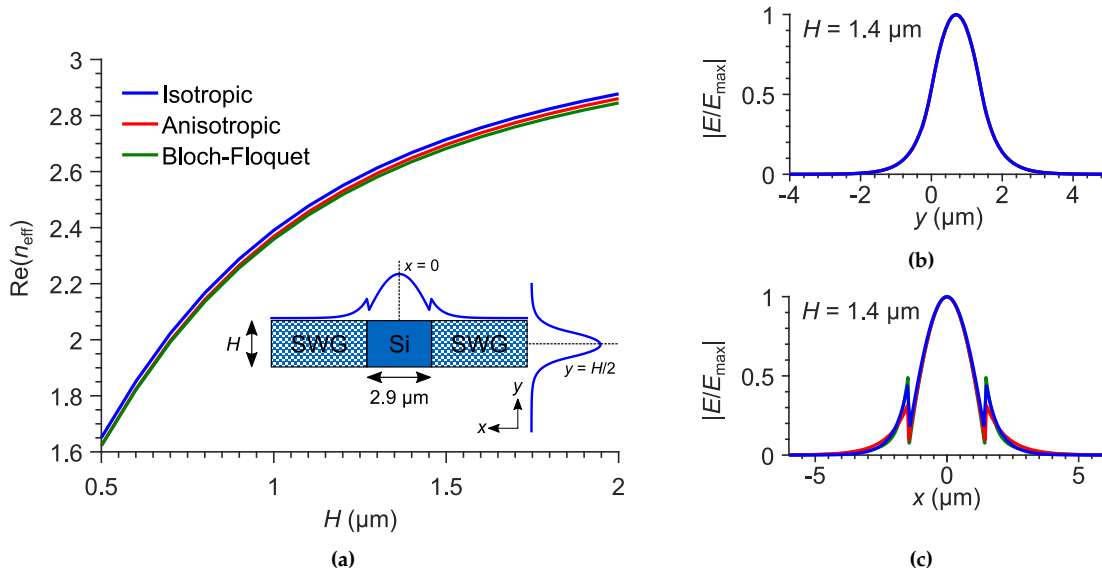


Figure 3.7: Comparison between isotropic, anisotropic, and Bloch–Floquet approaches. (a) Real part of the effective index of the fundamental mode of the suspended structure that is shown in the inset as a function of the thickness H . (b) Cut of the fundamental mode at the middle of the waveguide with $H = 1.4 \mu\text{m}$ ($x = 0$). (c) Cut of the fundamental mode at the middle of the waveguide with $H = 1.4 \mu\text{m}$ ($y = 0.7 \mu\text{m}$). Parameters: $\lambda = 7.67 \mu\text{m}$, $W = 2.9 \mu\text{m}$, $L_{\text{strip}} = 0.25 \mu\text{m}$, $L_{\text{hole}} = 0.9 \mu\text{m}$, $W_{\text{clad}} \rightarrow \infty$, $H_{\text{BOX}} \rightarrow \infty$. TE polarization.

The vertical and lateral confinements of the fundamental mode are examined when $H = 1.4 \mu\text{m}$. An x cut of the mode at the middle of the waveguide confirms that the mode field profiles, which are shown in Fig. 3.7b, are virtually identical in the vertical direction regardless of the model. This is due to the fact that the SWG cladding has low influence

⁴Using the FEM solver with a uniform mesh of 50 nm (x direction) and 100 nm (y direction).

⁵Using a uniform mesh of 50 nm (x direction), 100 nm (y direction) and 30 nm (z direction).

on the vertical confinement of the modes. Consequently, the isotropic model leads to the fastest simulations without compromising the accuracy of vertical leakage calculations.

An y cut of the mode at the middle of the guiding layer is shown in Fig. 3.7c. The mode profiles within the waveguide core are practically the same independent of the model. However, the evanescent tails of the modes are slightly different for each model, as they interact with the SWG medium. Thus, the isotropic model may not provide sufficiently accurate results for the lateral leakage.

Taking into account the constraints in Tables 3.1 and 3.2, and the modeling approaches of suspended waveguides, the following two-step design strategy is proposed:

- (i) *Thickness selection.* This is the most important step because it determines the wafer that must be purchased. The thickness H is chosen to guarantee vertical single-mode operation (negligible leakage for the fundamental mode; high leakage for the TE_{01} mode, if supported) regardless of the other possible dimensions of core and lateral cladding. The waveguide can be modeled using only the isotropic approximation.
- (ii) *Waveguide selection.* The core width (W) and the SWG cladding (W_{clad} , L_{strip} , and L_{hole}) are chosen to ensure single-mode operation (negligible lateral leakage for the fundamental mode; high lateral leakage for the TE_{10} mode, if supported) and meet fabrication and mechanical requirements. If the isotropic model were used, actual leakage losses could be higher than simulated. For this reason, in this work lateral leakage losses are well estimated using the anisotropic model, as it is much more accurate than the isotropic model, but also much faster than the Bloch–Floquet analysis.

3.2.3 Design of a Suspended Silicon Waveguide

Here, the entire design process of a suspended silicon waveguide for TE-polarized light at a wavelength of $7.67 \mu\text{m}$ is described in detail.

Influence of Silicon Loss

Since silicon has a material loss $\alpha_{\text{material}} = \alpha_{\text{Si}} \sim 2.1 \text{ dB cm}^{-1}$ at $\lambda = 7.67 \mu\text{m}$ [84], Eq. (3.2) indicates that the designed suspended silicon waveguides will have a minimum achievable propagation loss through the term $\Gamma\alpha_{\text{material}}$. The influence of this term on the final propagation loss can be low if the confinement factor is sufficiently reduced.

The mode confinement mainly depends on the cross-section of the waveguide core (H and W) and the lateral index contrast. For a reasonable equivalent refractive index of 1.8, the effective index of the fundamental mode of a suspended silicon waveguide is computed as a function of the core width for several thicknesses. Figure 3.8a shows the real part of the effective index, whose relatively high value indicates that the mode is well confined within the waveguide core for the considered H and W values. Additionally, Fig. 3.8b shows the propagation loss. In the depicted curves, infinite BOX thickness and cladding width are assumed, so that the estimated propagation losses are only due to the influence of silicon in the waveguide core ($\alpha = \Gamma\alpha_{\text{Si}}$). In practical waveguides, an intrinsic loss of $\sim 2.3 \text{ dB cm}^{-1}$ cannot be avoided. In consequence, the design stage must focus on minimizing the leakage term of Eq. (3.2).

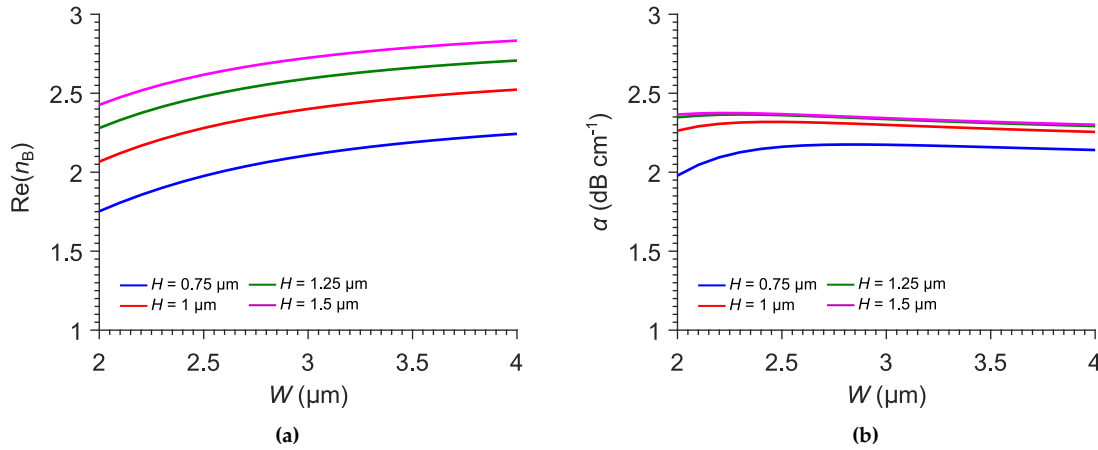


Figure 3.8: Study of the intrinsic loss of a suspended silicon waveguide considering the silicon loss, but not leakage losses. (a) Real part of the effective index and (b) propagation loss of the fundamental mode of a waveguide as a function of the core width for several thicknesses of the guiding layer. Parameters: $H_{\text{BOX}} \rightarrow \infty$, $W_{\text{clad}} \rightarrow \infty$, and $n_{\text{SWG}} = 1.8$ (isotropic model).

Thickness Selection

In this design step, the thickness of the guiding layer (H) is selected. The vertical leakage is primarily affected by this parameter, and to a lesser extent by the width of the waveguide core and the lateral index contrast.

First, a range of suitable thicknesses is chosen that guarantees high leakage losses for the undesired second-order vertical mode. As an extreme case, the real part of the effective index of the TE_{01} mode is calculated as a function of the core thickness for the slab waveguide in Fig. 3.9a. This structure can be interpreted as a suspended waveguide with an infinitely wide core or with a homogeneous lateral cladding of silicon. In real waveguides with finite core width or with SWG cladding, the vertical leakage will always be higher. As shown in Fig. 3.9b, the TE_{01} mode is cut off for $H < 1.2 \mu\text{m}$ and weakly guided for $1.2 \mu\text{m} < H < 1.5 \mu\text{m}$, thus yielding high vertical leakage, as required. Consequently, the presence of high-order modes can be ignored at least up to $H = 1.5 \mu\text{m}$.

Next, the geometry of the suspended silicon waveguide that was presented in [147] for a wavelength of $3.8 \mu\text{m}$ is used as a starting point for the new design at $7.67 \mu\text{m}$. Two parameters are preliminary chosen: (i) an equivalent refractive index n_{SWG} of 1.8, which approximately produces the same index contrast as at a wavelength of $3.8 \mu\text{m}$; and (ii) a core width W of $2.6 \mu\text{m}$, which corresponds to a scaling from $\lambda = 3.8 \mu\text{m}$ to $\lambda = 7.67 \mu\text{m}$. Note that if the silicon thickness H were scaled accordingly, a BOX thickness of $\sim 6 \mu\text{m}$ would be needed to maintain a negligible vertical leakage at a wavelength of $7.67 \mu\text{m}$. As $H_{\text{BOX}} = 3 \mu\text{m}$ in the utilized SOI wafers, H cannot be simply scaled up.

To choose the exact H value, the vertical leakage of the fundamental (TE_{00}) mode is examined using the isotropic model. To isolate vertical leakage from lateral leakage losses, the width of the lateral cladding is considered infinite (i.e., the unetched lateral silicon regions are not included within the simulation window, as illustrated in Fig. 3.10a). The vertical leakage loss of the fundamental mode as a function of the core thickness is shown in Fig. 3.10b. A thickness of $1 \mu\text{m}$, corresponding to the scaled value of the core thickness at $\lambda = 3.8 \mu\text{m}$ [147], is not sufficient for realistic waveguides at $\lambda = 7.67 \mu\text{m}$. For the

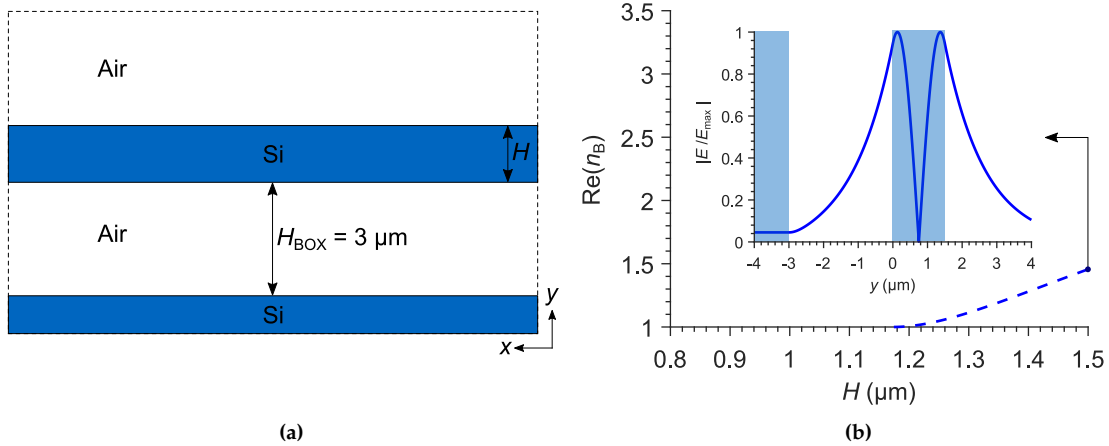


Figure 3.9: (a) Schematic representation of the slab waveguide used to analyze the vertical second-order (TE_{01}) mode. (b) Effective index of the TE_{01} mode of the slab waveguide as a function of the core thickness. The normalized magnitude of the transverse field distribution of the TE_{01} mode of the slab is shown for $H = 1.5 \mu\text{m}$.

considered $n_{\text{SWG}}, \alpha_{\text{vertical}} < 0.1 \text{ dB cm}^{-1}$ for any waveguide with $H > 1.4 \mu\text{m}$. Since an overetching during the fabrication process can reduce the core thickness, H was set to $1.5 \mu\text{m}$ to guarantee a vertical leakage lower than or equal to 0.1 dB cm^{-1} . This thickness would be valid even if n_{SWG} were higher, because the fundamental mode would be more vertically confined, resulting in a reduced power leakage toward the substrate.

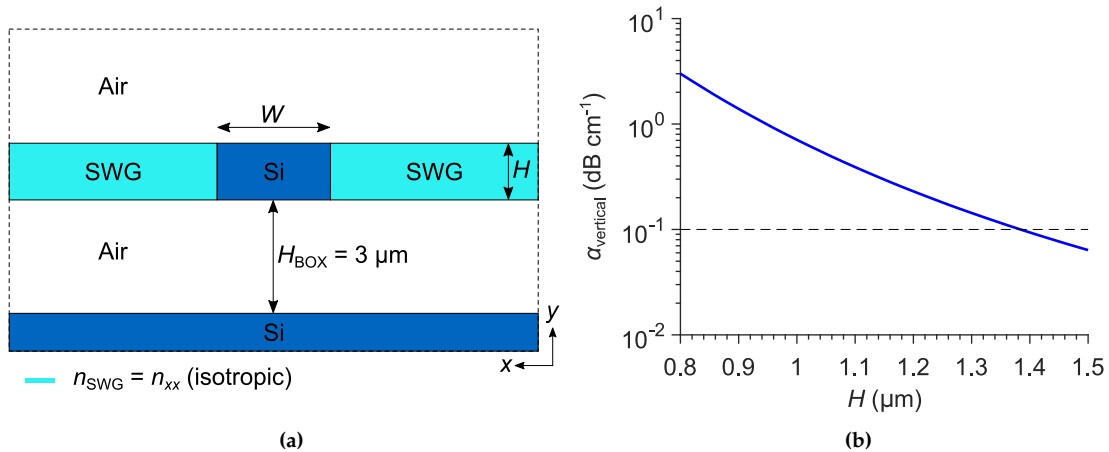


Figure 3.10: (a) Schematic representation of the structure that is simulated to calculate vertical leakage losses. (b) Estimated vertical leakage for the fundamental mode (TE_{00}) of the suspended silicon waveguide as a function of the core thickness. A vertical leakage loss of 0.1 dB cm^{-1} is marked with a dashed line. Parameters: $n_{\text{SWG}} = 1.8, W = 2.6 \mu\text{m}, H_{\text{BOX}} = 3 \mu\text{m}, W_{\text{clad}} \rightarrow \infty$.

Waveguide Selection

Once the nominal thickness (H) is chosen, the width of the core (W) and the dimensions of the SWG cladding ($W_{\text{clad}}, L_{\text{strip}},$ and L_{hole}) are selected to minimize the lateral leakage of the fundamental (TE_{00}) mode while ensuring mechanical robustness.

For a thick core of $1.5 \mu\text{m}$, fabrication tests have shown that cladding holes with $L_{\text{hole}} \geq 800 \text{ nm}$ are required to facilitate the flow of HF. Likewise, silicon strips with $L_{\text{strip}} \geq 200 \text{ nm}$ provide sufficient mechanical stability. The lengths L_{hole} and L_{strip} were set to 900 nm and 250 nm , respectively. These values were chosen because (i) they satisfy the SWG condition of Eq. (3.1), in which Λ_{Bragg} was estimated to be $\sim 1.3 \mu\text{m}$ using FEXEN⁶; and (ii) they synthesize an equivalent refractive index n_{SWG} of ~ 1.8 , which defines a lateral index contrast that is similar to that used in [147] and in Fig. 3.10b.

The waveguide core was widened from $2.6 \mu\text{m}$ to $2.9 \mu\text{m}$, in order to slightly increase the lateral modal confinement, thereby enabling the utilization of a narrower, more stable SWG cladding without affecting the lateral leakage. As a side effect, this variation in W reduces the vertical leakage, so that the thickness H that was selected previously can remain unchanged.

For the selected parameters, the lateral leakage is calculated in Fig. 3.11b as a function of the cladding width using the anisotropic model. The simulations are carried out by removing the silicon substrate, as schematized in Fig. 3.11a. The lateral leakage is below 0.1 dB cm^{-1} for $W_{\text{clad}} \sim 3.65 \mu\text{m}$. The second-order mode is leaked with a loss of $\sim 250 \text{ dB cm}^{-1}$ for such a cladding width, and of more than 150 dB cm^{-1} for $W_{\text{clad}} < 4 \mu\text{m}$. Thus, a cladding width of $3.65 \mu\text{m}$ was chosen.

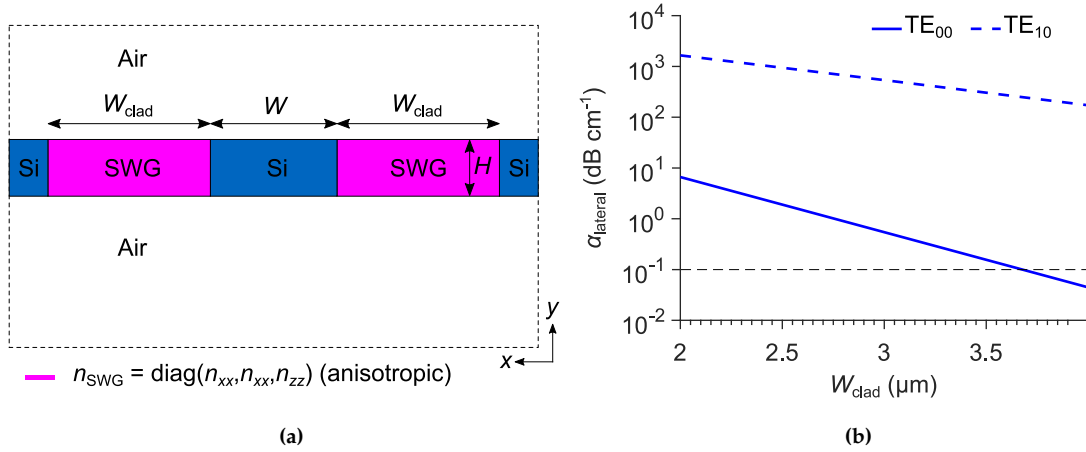


Figure 3.11: (a) Schematic representation of the structure that is simulated to calculate lateral leakage losses. (b) Estimated lateral leakage for the TE_{00} and TE_{10} modes of the suspended silicon waveguide as a function of the cladding width. Lateral leakage losses of 0.1 dB cm^{-1} are marked with dashed lines. Parameters: $n_{xx} = 1.8$, $n_{zz} = 1.1$, $H = 1.5 \mu\text{m}$, $W = 2.9 \mu\text{m}$, $H_{\text{BOX}} \rightarrow \infty$.

Table 3.3 summarizes the selected dimensions for the suspended silicon waveguide at $\lambda = 7.67 \mu\text{m}$.

3.2.4 Design of Suspended Germanium Waveguides

As an alternative to the suspended silicon platform, suspended germanium waveguides were designed at the following wavelengths:

⁶FEXEN (Fourier EXpansion simulation ENvironment) is the 2D electromagnetic simulator developed by the researchers of the Photonics & RF Lab at the Universidad de Málaga. FEXEN is based on the Fourier eigenmode expansion method (Fourier-EEM) and is especially optimized for the simulation of periodic structures [168].

Table 3.3: Nominal dimensions of the suspended silicon waveguide at a wavelength of 7.67 μm .

H (μm)	W (μm)	W_{clad} (μm)	L_{strip} (μm)	L_{hole} (μm)	H_{BOX}^* (μm)
1.50	2.90	3.65	0.25	0.90	3.00

*For reference. The thickness H_{BOX} is not a design parameter.

- (i) $\lambda = 3.8 \mu\text{m}$. The characterization of waveguides at 3.8 μm is simpler than at longer wavelengths because of the available experimental setup for the former (see Section 3.4.1 for a description of the setups). Thus, even though suspended silicon waveguides work well at 3.8 μm , the design of suspended germanium waveguides was proposed firstly at this wavelength to prove the concept more easily than at 7.67 μm . Of course, just as at other MIR wavelengths, the suspended germanium platform at 3.8 μm could be helpful for applications that can benefit from the specific characteristics of germanium, such as higher nonlinearity or refractive index.
- (ii) $\lambda = 7.67 \mu\text{m}$. As shown in Section 3.2.3, the suspended silicon waveguides designed at this wavelength would have a minimum achievable loss of $\sim 2.3 \text{ dB cm}^{-1}$ that is caused by the intrinsic loss of silicon. Suspended germanium waveguides do not suffer from high material loss, potentially outperforming their suspended silicon counterparts.
- (iii) $\lambda = 9.6 \mu\text{m}$. Suspended silicon waveguides have not been designed at 9.6 μm because of the prohibitive material loss. At 9.6 μm , as well as at longer MIR wavelengths, the suspended germanium platform could reach its fullest potential.

In this section, the design of suspended germanium waveguides for TE-polarized light at the aforementioned wavelengths is summarized and final results are provided.

Thickness Selection

GOSOI wafers with thicknesses of 0.5 μm , 1 μm , and 2 μm were available in the ORC. The process of selecting the platform was simplified with respect to the suspended silicon case. Now, instead of choosing exact H values, the goal was to find which of the three available thicknesses were the most appropriate for the suspended germanium waveguides at each wavelength.

Because the refractive index of germanium ($n_{\text{Ge}} \sim 4$) is higher than that of silicon ($n_{\text{Si}} \sim 3.42$), suspended germanium waveguides have stronger vertical index contrast than their silicon counterparts. Furthermore, if the same duty cycle as in the suspended silicon waveguides is used (DC $\sim 20\%$), the equivalent refractive index n_{SWG} will be increased (from ~ 1.8 to ~ 2), and hence the lateral index contrast.

Isotropic simulations were performed assuming $n_{\text{SWG}} \sim 2$. At each wavelength, the following conclusions are drawn:

- (i) $\lambda = 3.8 \mu\text{m}$. A negligible vertical leakage can be achieved with a thickness of 0.5 μm and a core width of 1.3 μm . These parameters are the same as in suspended silicon waveguides at this wavelength [147], so that the guided modes will be more confined within the germanium core.

- (ii) $\lambda = 7.67 \mu\text{m}$. A negligible vertical leakage can be achieved with a thickness of $1 \mu\text{m}$ and a core width of $2.9 \mu\text{m}$. In this case, the guiding layer is thinner than in the suspended silicon waveguides because of the stronger vertical index contrast.
- (iii) $\lambda = 9.6 \mu\text{m}$. If H and W were scaled from the $7.67\text{-}\mu\text{m}$ germanium design, a thickness of $1.25 \mu\text{m}$ and a width of $3.6 \mu\text{m}$ would be required. For a thickness of $1 \mu\text{m}$, the vertical leakage is relatively high ($\alpha_{\text{vertical}} \sim 0.8 \text{ dB cm}^{-1}$), but it could be slightly reduced by using a wider core (e.g., $\alpha_{\text{vertical}} \sim 0.5 \text{ dB cm}^{-1}$ if $W = 5 \mu\text{m}$). Alternatively, the power leakage is negligible regardless of the core width when $H = 2 \mu\text{m}$.

Finally, in order to study the vertical leakage of the second-order (TE_{01}) mode, a slab waveguide was analyzed. The TE_{01} mode is cut off at wavelengths of $3.8 \mu\text{m}$ and $7.67 \mu\text{m}$, as well as $9.6 \mu\text{m}$ when $H = 1 \mu\text{m}$. In contrast, the high-order mode is well guided at $9.6 \mu\text{m}$ for a core thickness of $2 \mu\text{m}$.

Waveguide Selection

Using the anisotropic model, the waveguides were completely designed at the three operating wavelengths. As an example, the lateral leakage of the suspended germanium waveguide at $7.67 \mu\text{m}$ is shown as a function of the cladding width in Fig. 3.12.

Table 3.4 indicates the final dimensions. Some considerations are given as follows:

- At wavelengths of $3.8 \mu\text{m}$ and $7.67 \mu\text{m}$, the SWG claddings are slightly narrower than in the corresponding suspended silicon waveguides (see [147] and Section 3.2.3). This reduction is due to the increased index contrast of the germanium-based platforms.
- If the dimensions simply were scaled, suspended germanium waveguides at $9.6\text{-}\mu\text{m}$ wavelength would require a core width of $3.6 \mu\text{m}$. For the design with $H = 1 \mu\text{m}$, a core width of $4.2 \mu\text{m}$ was selected instead. The rationale is that the chosen W value leads to a slightly reduced vertical leakage ($\alpha_{\text{vertical}} \sim 0.6 \text{ dB cm}^{-1}$) while lateral leakage is $\sim 0.1 \text{ dB cm}^{-1}$ for the fundamental mode and higher than 25 dB cm^{-1} for the second-order mode. A wider core would have decreased the vertical leakage marginally, but at the expense of increasing the confinement of the TE_{10} mode.
- A suspended germanium waveguide was designed at a wavelength of $9.6 \mu\text{m}$ for the $2\text{-}\mu\text{m}$ -thick platform. To facilitate the HF flow, the hole length was increased to $1.05 \mu\text{m}$, yet the duty cycle of $\sim 20\%$ was kept to maintain the same lateral index contrast as in the other designs. In this case, although the fundamental mode is low-loss and the second-order lateral mode is leaked with $\sim 25 \text{ dB cm}^{-1}$, the second-order vertical mode is supported because of the excessive guiding layer thickness. An optimum design could have been proposed for $H = 1.5 \mu\text{m}$, but a GOSOI wafer with such a thickness was not available in the ORC's laboratory.

3.3 Fabrication

The suspended silicon and suspended germanium structures were fabricated by using electron-beam (e-beam) lithography. A photosensitive resist is spun onto the guiding layer of the wafer. Then, electron beams are properly focused to pattern the layout of

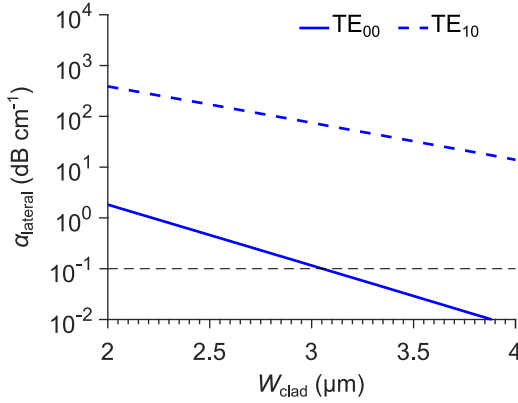


Figure 3.12: Lateral leakage of the fundamental and second-order lateral modes supported by the suspended germanium waveguide designed at $\lambda = 7.67 \mu\text{m}$ as a function of the cladding. Lateral leakage losses of 0.1 dB cm^{-1} are marked with dashed lines. Parameters: $H = 1 \mu\text{m}$, $W = 2.9 \mu\text{m}$, $L_{\text{strip}} = 200 \text{ nm}$, $L_{\text{hole}} = 800 \text{ nm}$, $H_{\text{BOX}} \rightarrow \infty$.

Table 3.4: Nominal dimensions of the suspended germanium waveguides.

λ (μm)	H (μm)	W (μm)	W_{clad} (μm)	L_{strip} (μm)	L_{hole} (μm)	H_{BOX}^* (μm)
3.80	0.50	1.30	2.00	0.10	0.45	3.00
7.67	1.00	2.90	3.10	0.20	0.80	3.00
9.60	1.00	4.20	3.60	0.20	0.80	3.00
9.60	2.00	3.60	3.40	0.25	1.05	3.00

*For reference. The thickness H_{BOX} is not a design parameter.

the optical circuit that will be etched. In this section, the procedures for mask definition and e-beam lithography will be described.

3.3.1 Mask Definition

The first step of the fabrication process is drawing the layout, which is afterward converted into a GDSII file that feeds the e-beam machine. Although e-beam lithography does not require the layout to be written on a mask plate, the stream file is typically called *mask*. The masks for the suspended waveguides were created with Mentor's Tanner L-Edit IC Layout [169]. A set of C++ functions, which are property of the ORC, were called from L-Edit to automatize the drawing.

The masks for both suspended silicon and suspended germanium comprise several sets of waveguides. Each set or cell is composed of waveguides with different lengths that are accessed by fiber-chip surface couplers, as illustrated in Fig. 3.13. Except for the length, all of the structures of a cell have the same dimensions. With this arrangement of waveguides, propagation losses can be calculated by using the effective cut-back method [170], which will be described in more detail in Section 3.4.

The dimensions of the waveguides are changed from one cell to another. Variations in W_{clad} , W , or L_{strip} have these two objectives:

1. *To compensate for fabrication errors.* The dimensions of fabricated structures typically suffer from positive or negative deviations caused by the combined effect of non-ideal e-beam patterning and dry etching. Additionally, the acid solution can affect the silicon or germanium layers and overetch the suspended waveguides, producing negative biasing (i.e., structures are narrower and thinner than desired). The overall effect of fabrication errors can be as high as $\pm 150 \text{ nm}$. When a mask is defined, dimensional variations are applied to compensate for these undesired effects.

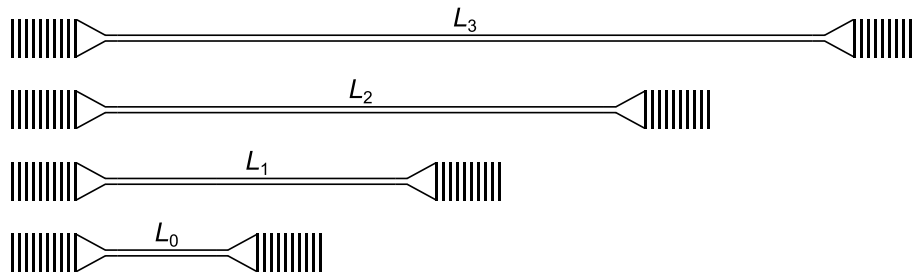


Figure 3.13: Layout of waveguides used to measure propagation losses with the effective cut-back method. Light is coupled to waveguides of different lengths by using fiber-chip surface couplers.

2. *To provide mechanical stability.* As the mechanical behavior of the suspended waveguides is not simulated, the fabricated structures may be unstable and can collapse. Even if the nominal design is sufficiently robust, an overetching caused by the acid solution can weaken and break the waveguides. A chip with all structures broken is useless. For these reasons, a variety of waveguides was considered.

An example of a mask to characterize suspended waveguides is shown in Fig. 3.14. Note that suspended structures are defined by their cladding holes. Since the cladding holes are too small, a metrology box, which is a hole of $1\text{ mm} \times 1\text{ mm}$, is drawn to be used as a target for an ellipsometer, to probe the thickness of the dry-etched areas during the fabrication process.

Some suspended 90° - and s-bends were also drawn in the mask for suspended silicon waveguides. A cascaded configuration, similar to that used for straight waveguides, was chosen to characterize the propagation loss per bend. These structures had not been designed. Instead, they were overdimensioned to ensure low loss.

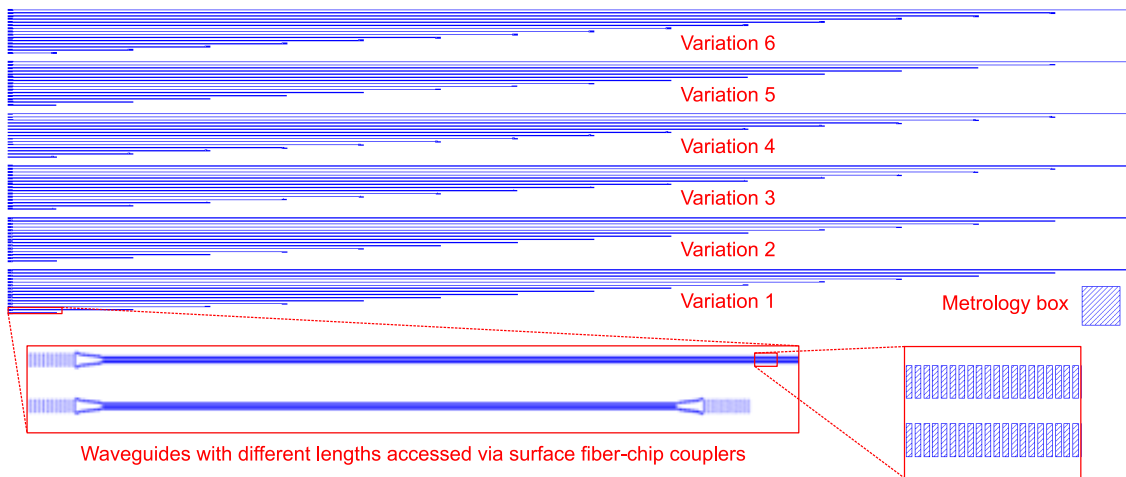


Figure 3.14: Example of a layout for the characterization of suspended waveguides. Sets of waveguides of different lengths are distributed along the chip area. Each set corresponds to a variation in the core width, cladding width, or cladding duty cycle. Fiber-chip surface couplers were used to couple the light. The suspended structures are defined by their holes. A metrology box is drawn to be used as a target for an ellipsometer and facilitate the measurement of the dry-etched layer thickness during the fabrication process.

3.3.2 Lithography Procedure

The fabrication of the designed structures was performed in the Southampton Nanofabrication Centre (SNC) by researchers from the ORC. The fabrication procedure, which is compatible for both suspended silicon and germanium waveguides, is briefly described as follows.⁷

- (i) *Moisture removal.* The sample — namely, the portion of the wafer where the circuit is fabricated — is baked at 220 °C to remove any moisture.
- (ii) *Photoresist application.* A ZEP520-A photoresist is deposited on the guiding layer, spin-coated, and baked. The final thickness of the photoresist layer should be carefully chosen and depends on the duration of the subsequent dry etch: if the photoresist layer is too thin, it can be fully etched, leaving undesired silicon/germanium areas unprotected; on the other hand, if the layer is too thick, electron scattering can increase the minimum feature size. For suspended silicon structures at $\lambda = 7.67 \mu\text{m}$ ($H = 1.5 \mu\text{m}$), a thickness of $\sim 700 \text{ nm}$ is used, whereas for suspended germanium waveguides at $\lambda = 3.8 \mu\text{m}$ and $\lambda = 7.67 \mu\text{m}$, whose waveguide core is thinner ($H = 0.5 \mu\text{m}$ and $H = 1 \mu\text{m}$, respectively), the photoresist is $\sim 500 \text{ nm}$ thick.
- (iii) *Electron-beam lithography.* The mask layout (GDSII file) is transferred into the photoresist by using a JEOL JBX-9300 e-beam machine. With this process, some regions of the photoresist become soluble in a chemical developer after electron irradiation.
- (iv) *Developing.* The sample is dipped into a ZED-N50 developing solution. Photoresist areas attacked by the electron beams are then removed, thereby leaving the underneath silicon/germanium exposed. The sample is washed off in isopropyl alcohol (IPA) and deionized (DI) water.
- (v) *Dry etch.* An inductively coupled plasma (ICP) etches the silicon/germanium areas that are not protected by the photoresist (i.e., the holes of the suspended structures). First, a conditioning silicon wafer is etched during 20 min to stabilize the etch rate. Then, by using a plain wafer as a carrier, the chip sample is loaded in an Oxford Instruments' ICP 380 system. After a short initial etching, the etch rate is estimated by measuring the thickness of the silicon/germanium layer of the metrology box with an ellipsometer. An iterative process (loading the sample in the ICP tool, etching, removing the sample from the ICP system, and checking the thickness) is followed until the silicon/germanium layer is totally etched. If the holes are not completely opened, the waveguides might not be successfully suspended.
- (vi) *Photoresist removal.* Remnants of the photoresist are ashed with oxygen plasma for $\sim 10 \text{ min}$ (silicon) and $\sim 5 \text{ min}$ (germanium). Germanium waveguides are less time in the asher to prevent oxidation.
- (vii) *Wet etch.* The sample is dipped into a 1:7 HF:H₂O solution, which suspends the waveguides. The duration of the dipping is critical: if the sample is not submerged for sufficient time, some devices may not be fully suspended, potentially increasing propagation loss; on the contrary, if the submersion time is excessive, the HF acid can negatively affect the thickness and widths of silicon and germanium structures.

⁷A detailed description can be found in [171].

This situation is illustrated in Fig. 3.15, in which narrow and wide waveguides are attacked by the acid. The figure shows that sufficient HF etching time for the narrow waveguide is not enough for the wider structure. To suspend all the structures, the sample must be dipped into the acid for longer time, which reduces the thickness of the guiding layer. Thus, masks should be defined so that wide structures (e.g., tapers), which require long etch times, become fully suspended, while interconnecting waveguides are not dramatically overetched. A dip time of 2–2.5 h was required to suspend the widest structures.

The silicon etch rate of the acid solution has been measured to be $\sim 0.4 \text{ nm min}^{-1}$ (see Fig. 3.16). After the indicated dipping time, a reduction of 50–60 nm can be expected in all dimensions. Additionally, this etch rate should be enough to remove the thin silicon film underneath the germanium layer of GOSOI wafers without requiring other chemical agents (see Fig. 3.1b).

(viii) *Rinse*. The sample is rinsed in a DI water weir to eliminate the remaining acid.

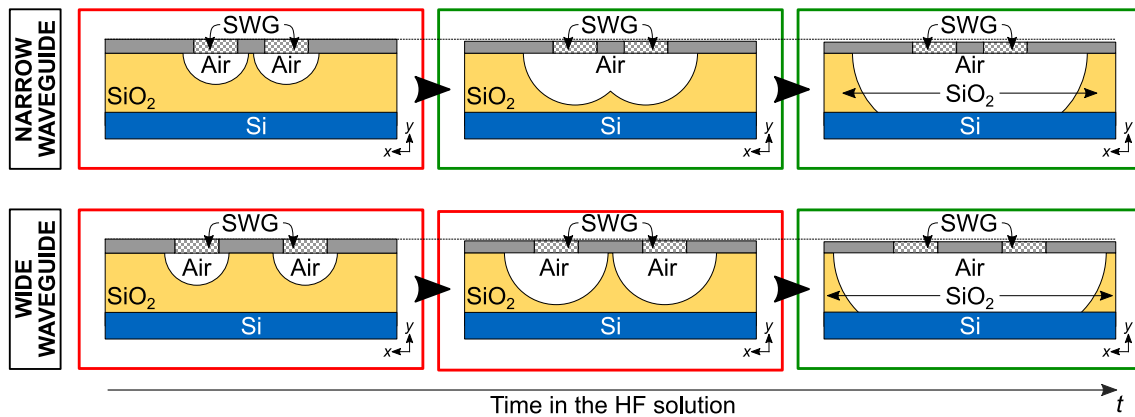


Figure 3.15: Illustration of the wet etch process used to suspend the structures. A sufficient HF etch time required for a narrow waveguide (central column) is not enough to suspend a wide structure such as an MMI or the input taper of a grating coupler.

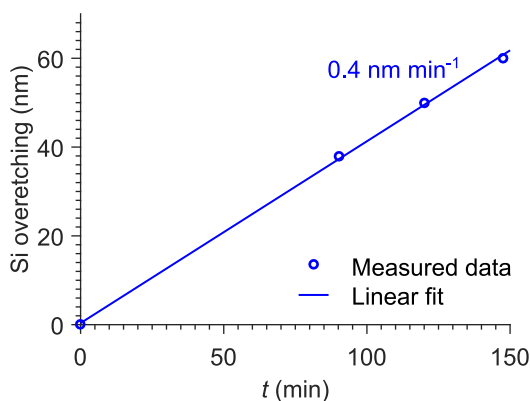


Figure 3.16: Silicon etch rate of 1:7 HF solution at the environmental conditions of the wet room of the Southampton Nanofabrication Centre. The measurements were taken with an ellipsometer. For an etch time of 2.5 h, this curve indicates an approximate silicon overetching of 60 nm.

3.3.3 Fabricated Structures

Suspended Silicon

Figure 3.17 shows some of the fabricated suspended waveguides and bends. The images were taken with a scanning electron microscope (SEM). To observe whether the silicon dioxide was properly removed, the chip was cleaved manually and the holding stage was tilted. All structures were fully suspended without showing signs of collapsing or bending. The breaks near the facets were caused by the cleaving. Roughness on the chip surface can be attributed to the silicon overetching. The measured thickness of the silicon guiding layer was of $1.42\ \mu\text{m}$, which indicates that the thickness was overetched $80\ \text{nm}$, in reasonably good agreement with the $\sim 60\ \text{nm}$ predicted in Fig. 3.16.

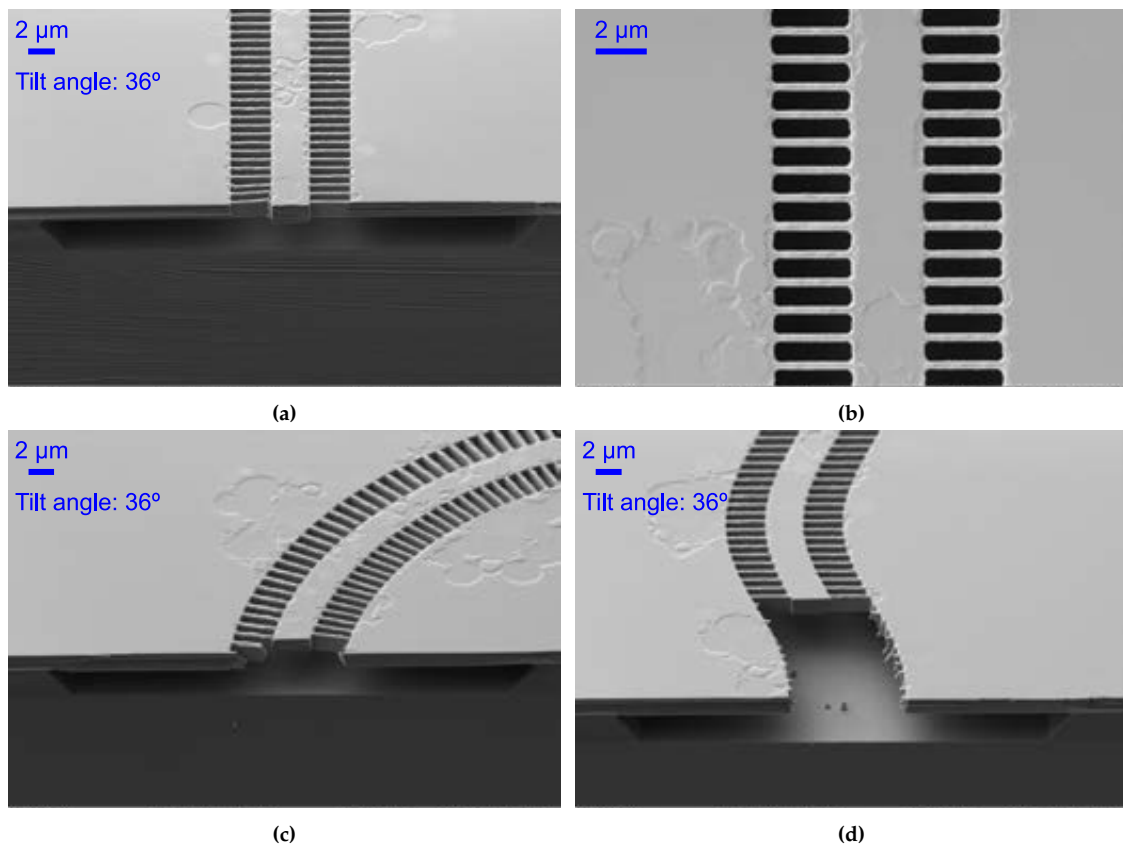


Figure 3.17: SEM images of fabricated suspended silicon (a,b) waveguides, (c) 90° -bend, and (d) s-bend. The structures of figures (a), (c) and (d) were cleaved and tilted to examine the undercut. Breaks at the facet and first periods were caused by the cleaving process. The chip surface is affected by undesired roughness, which was probably created by the HF solution.

Suspended Germanium

The structures of the first sample fabricated to test the suspended germanium waveguides at $\lambda = 3.8\ \mu\text{m}$ were mostly collapsed and broken. In general, the structures suffered from a negative fabrication bias of $\sim 50\ \text{nm}$, resulting in too narrow germanium strips of $L_{\text{strip}} \sim 40\text{--}60\ \text{nm}$. Some of the broken germanium strips are shown in Fig. 3.18.

The mask was redrawn to include new variations with positive bias (i.e., widened structures). Since only one more fabrication run for suspended germanium waveguides at $3.8\ \mu\text{m}$ was scheduled in the SNC, the new chip was left in the HF weir for only ~ 30 min, in order to ensure stability. This time was sufficient for suspending the waveguides, yet silicon dioxide probably remained underneath the wider input tapers that are used to access the fiber-chip surface couplers. The loss introduced by the remnants of BOX is removed with the cutback method. Measurements of this chip will be provided in Section 3.4.4.

Similarly, various chips were fabricated to characterize suspended germanium waveguides at $\lambda = 7.67\ \mu\text{m}$. Because the fabrication bias for $1\text{-}\mu\text{m}$ -thick germanium layers was unknown, variations with positive biases up to $+150\ \text{nm}$ were included in the first mask. A visual inspection of the chip under a microscope showed that only those variations with positive bias larger than $100\ \text{nm}$ did not collapse. A new chip with more positive variations was fabricated successfully. SEM images (see Fig. 3.19) showed that an overetching of $\sim 150\ \text{nm}$ was affecting all dimensions. This biasing could explain the massive breaks of the first sample. A focused ion beam (FIB) workstation was employed to etch a precise area of the chip and examine the removed BOX. The waveguides were fully suspended. Waveguide propagation losses measured with this chip will be analyzed in Section 3.4.4.

3.4 Characterization of Suspended Waveguides

3.4.1 Measurement Setup

The characterization of the suspended waveguides was performed using the measurement setups from the *Mid-IR Group IV Photonics* laboratory of the ORC. Fiber-chip surface couplers, whose design is addressed in Chapter 4, were used to couple light between the MIR fibers and the chip. After traveling through the structures, the light is extracted from the output coupler to another optical fiber, which carries the light toward the detector. In this section, these setups are described thoroughly.

Setup for 7.67- μm and 9.6- μm Wavelengths

The setup used to characterize suspended silicon and germanium waveguides at a wavelength of $7.67\ \mu\text{m}$ is illustrated in Fig. 3.20. The different parts of this measurement setup are:

- *Light sources.*

A continuous-wave distributed feedback (DFB) QCL (Thorlabs QD7500CM1) was employed to inject light into the samples. The maximum emitted power is $106\ \text{mW}$. The operating wavelength is fixed to $7.67\ \mu\text{m}$. The laser is held in a thermoelectrically cooled (TEC) mount (Thorlabs LDMC20/M) connected to a combined current/temperature controller (Thorlabs ITC4002QCL). A black diamond-2 lens with a focal length of $1.9\ \text{mm}$ collimates the output beam of the laser.

A laser source by Daylight Solutions was also available in the wavelength range of $9.25\text{--}10.0\ \mu\text{m}$, so that this setup could also be employed for characterization at $\lambda = 9.6\ \mu\text{m}$. The power output for this laser was lower than $100\ \text{mW}$.

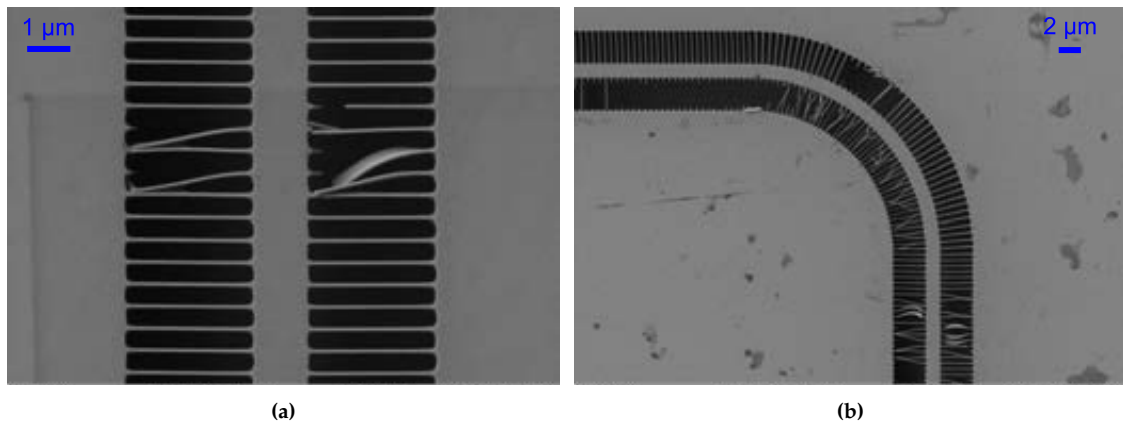


Figure 3.18: SEM images of fabricated suspended germanium (a) waveguides and (b) bends for 3.8- μm wavelength (first chip, broken). The bends are part of the grating couplers, which will be covered in Chapter 4.

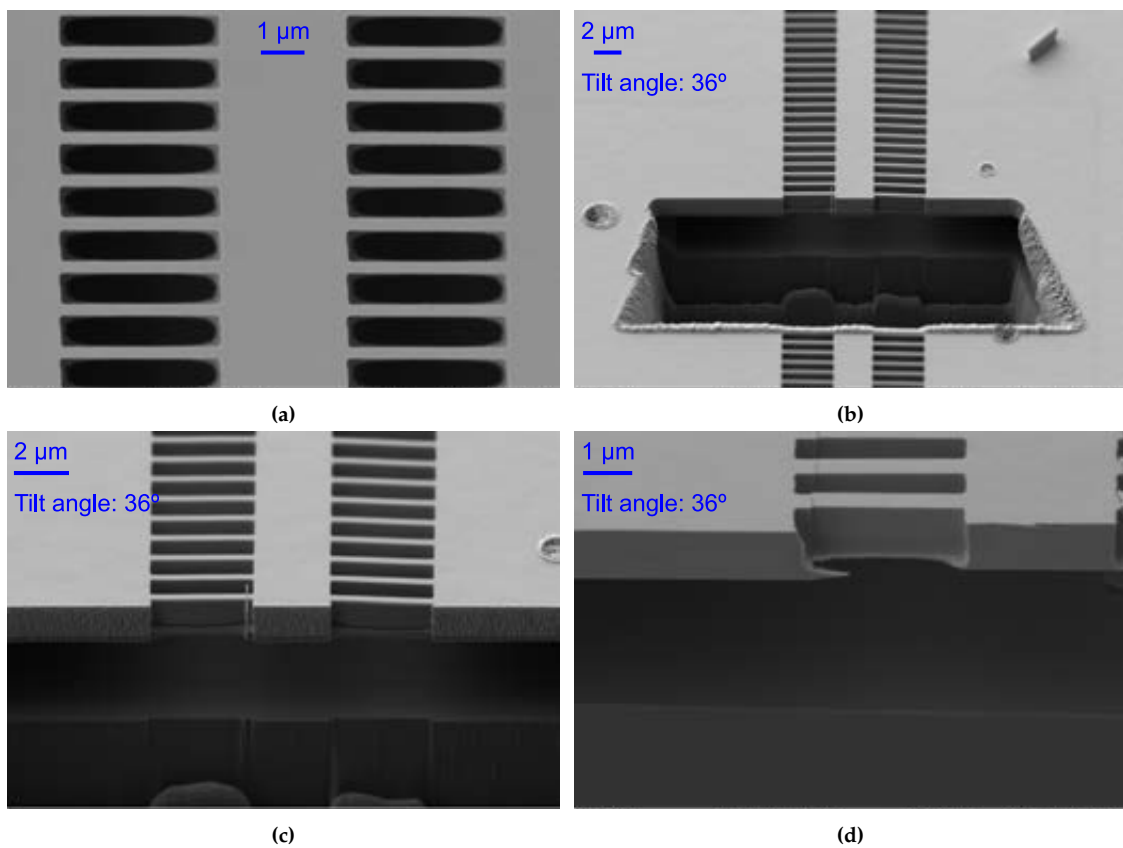


Figure 3.19: SEM images of fabricated suspended germanium waveguides for 7.67- μm wavelength. (a) Suspended waveguide. (b) FIB etched area to examine the undercut of the suspended waveguides. (c) Close look of a waveguide. (d) Close look of a waveguide hole.

- *Devices to control the light path.*

As optical fibers cannot be directly connected to the laser output, a set of conveniently located mirrors carries the light toward the input optical fiber. A final black diamond-2 lens (Thorlabs C028TME) is utilized to focus the collimated light onto the input optical fiber, whose tip is positioned at the focal distance of the lens (5.95 mm). Some of the mirrors in the beam path could be flipped 90° to set the 9.6- μm laser source.

- *Optical fibers.*

Mid-infrared fibers are fragile. Suspended silicon waveguides were characterized using a custom-made single-mode As_2Se_3 optical fiber (Coractive's IRT-SE-28/170) with a core diameter of 27 μm and a numerical aperture of 0.22. At $\lambda = 7.67 \mu\text{m}$, a mode field diameter of 29.44 μm was estimated using Marcuse's formula [172].

Later, another chalcogenide fiber (IRFlex's IRF-Se-12 fiber) was installed. It has a core diameter of 12 μm and a numerical aperture of 0.47 (estimated mode field diameter of 13.56 μm at the operating wavelength). The high core refractive index and the reduced mode field diameter have implications for the design of fiber-chip surface couplers (see Chapter 4).

The optical fibers are supported by a set of proprietary fiber holders that are designed and fabricated in the ORC.

- *Nanopositioning stages.*

A set of xyz -axis nanopositioners from Thorlabs and Newport are used to move the optical fibers along the chip surface. Nanopositioning stages are also used to move the lens and the input fiber in which light is coupled from the laser, and to place the output fiber in the right position to maximize the power that excites the photodetector.

- *Signal processing stages.*

At MIR wavelengths the noise level is high, as all heated bodies emit infrared radiation. Illumination lamps or even human radiation can disturb the measured data. A slotted chopper wheel modulates the laser beam before being focused onto the input optical fiber. The turning frequency of the chopper blade, 300–400 Hz, is set with a chopper controller (Stanford Research Systems SR540). This instrument is connected to the reference frequency input of a lock-in amplifier (AMETEK Signal Recovery DSP 7265). The detected power is demodulated, thereby improving the signal-to-noise ratio. This lock-in amplifier is managed via a computer with a LabView program.

- *Detector.*

Light from the output fiber excited a HgCdTe detector (Infrared Associates' MCT-13-1.00) that must be cooled with liquid nitrogen. A pre-amplifier is used to increase the signal level from the detector. This pre-amplifier is connected to the lock-in amplifier that filters the signal.

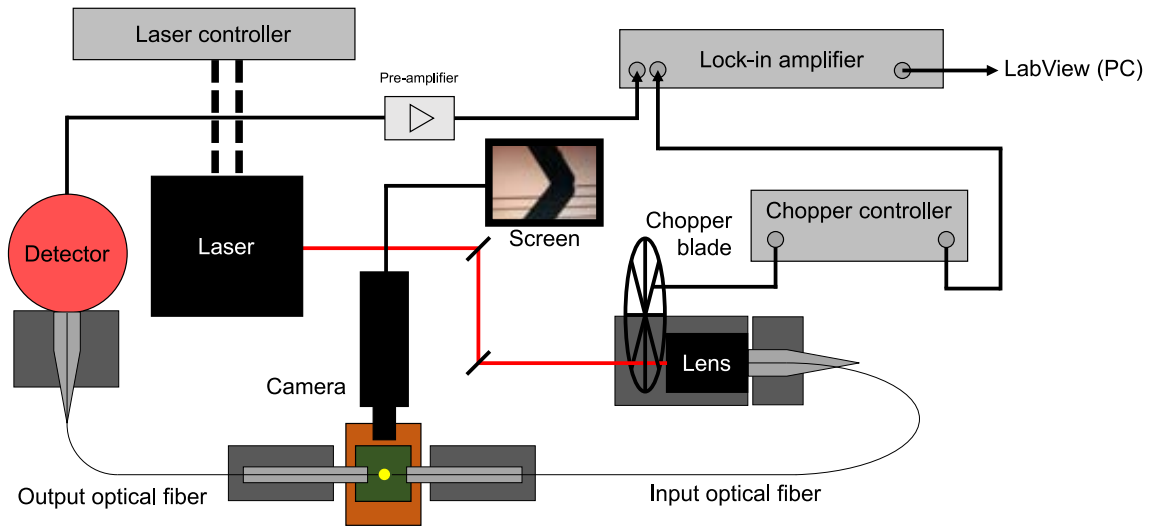


Figure 3.20: Schematic of the MIR measurement setup.

Setup for 3.8- μm Wavelength

This setup was employed to characterize suspended germanium waveguides at $\lambda = 3.8 \mu\text{m}$. The relevant differences with the 7.6- μm setup, which make the 3.8- μm setup more user-friendly than the previous one, are briefly noted as follows:

- A custom-made Daylight Solutions QCL that is tunable from 3.71 μm to 3.89 μm was used. The source can operate in either continuous-wave or pulsed modes. A maximum output power of $\sim 150 \text{ mW}$ is emitted at a nominal wavelength of 3.8 μm . The laser is cooled by an external chiller.
- A single-mode ZrF_4 (ZBLAN) optical fiber by Thorlabs was used. The specifications are: core refractive index of 1.48, core diameter of 9 μm and numerical aperture of 0.19. At $\lambda = 3.8 \mu\text{m}$, a mode field diameter of 17.8 μm is estimated. These fibers are protected by a plastic jacket.
- A thermoelectrically cooled MCT photodetector (Vigo System PVI-4TE-4) was used.

3.4.2 Measurement Procedure

The propagation loss of the suspended waveguides was determined with the effective cut-back method [170]. Waveguides with different lengths were distributed along the chip, as already shown in Fig. 3.13. Light was coupled using fiber-chip surface couplers (see Chapter 4). The loss per unit length can be estimated by measuring the power transmitted through each waveguide:

$$\alpha \text{ (dB cm}^{-1}\text{)} = -\frac{10 \log_{10} \left(\frac{P_i}{P_0} \right)}{L_i - L_0} = -\frac{10 \log_{10} \left(\frac{V_i}{V_0} \right)}{L_i - L_0}, \quad (3.7)$$

where P_0 is the measured power at the output of the shortest (reference) waveguide, whose length is L_0 ; and P_i is the measured power of a longer waveguide with length L_i . The symbols V_0 and V_i denote the output voltages of the photodetector, which are respectively proportional to P_0 and P_i through its responsivity. With this method, measured

transmissions are normalized with respect to P_0 (V_0) and then linearly fitted, thereby isolating the waveguide propagation loss from other sources of loss — such as grating couplers, tapers, or bends. A similar approach can be followed to estimate bend losses.

This characterization method requires that the fiber-chip surface couplers be identical for all the waveguides. Furthermore, the position of the fibers relative to each coupler must be maintained. Otherwise, measured transmission points cannot be properly normalized and fitted. Further details about the position of the optical fibers will be provided in Chapter 4.

At $\lambda = 3.8 \mu\text{m}$, the transmission spectrum over a range from 3715 nm–3888 nm was post-processed by sliding-window filtering or polynomial fitting, thereby reducing or removing the noise in the measurement. However, since the laser is not tunable at $\lambda = 7.67 \mu\text{m}$, measured transmissions at this wavelength cannot be filtered. Instead, they were averaged over 10 s to get rid of random time-dependent noise in the signal.

3.4.3 Results (Suspended Silicon)

Figure 3.21 shows the normalized measured transmission at $\lambda = 7.67 \mu\text{m}$. Before the HF attack, the waveguides were characterized, yielding a propagation loss of $62.3 \pm 9.6 \text{ dB cm}^{-1}$, as estimated in Fig. 3.21. This prohibitive loss is obviously due to the effect of silicon dioxide. Then, after removing the BOX, a propagation loss of $3.1 \pm 0.2 \text{ dB cm}^{-1}$ was achieved. According to the simulations in Section 3.2.3, the material loss of silicon contributes by $\sim 2.3 \text{ dB cm}^{-1}$. This loss is intrinsic to the structure and, thus, cannot be removed in practice. The remaining $\sim 0.8 \text{ dB cm}^{-1}$ are attributed to surface and sidewall roughness, as well as increased lateral leakage. This result practically coincides with that reported in [147], where the authors presented suspended silicon waveguides with a propagation loss of 0.82 dB cm^{-1} at the wavelength of $3.8 \mu\text{m}$ at which silicon is low-loss. Furthermore, this propagation loss is comparable to the propagation losses of state-of-the-art waveguides available in other long-wavelength MIR platforms (see Chapter 2).

Losses of $0.08 \pm 0.02 \text{ dB bend}^{-1}$ and $0.06 \pm 0.02 \text{ dB bend}^{-1}$ were measured for 90° - and s-bends, respectively.

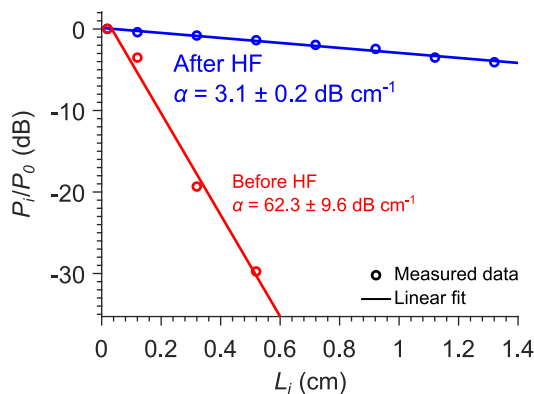


Figure 3.21: Propagation loss measurements for silicon waveguides with the BOX still present (red curve) and suspended silicon waveguides (blue curve) at 7.67- μm wavelength (TE polarization).

3.4.4 Results (Suspended Germanium)

As a proof of concept, suspended germanium waveguides were firstly characterized at $\lambda = 3.8 \mu\text{m}$. Figure 3.22a shows the measured voltage, which is normalized and fitted

following the effective cut-back method. Propagation losses of $6.7 \pm 0.2 \text{ dB cm}^{-1}$ and $4.5 \pm 0.3 \text{ dB cm}^{-1}$ were attained before and after HF attack, respectively. The loss reduction due to the HF etching is only $\sim 2.2 \text{ dB cm}^{-1}$, as silicon dioxide loss is relatively low at $\lambda = 3.8 \mu\text{m}$.

The principal goal was the characterization of the suspended germanium waveguides at $\lambda = 7.67 \mu\text{m}$ since, at this wavelength, germanium is transparent. Propagation losses before HF etching were presumably high ($> 60 \text{ dB cm}^{-1}$), but could not be calculated precisely because the measured power fell below the noise floor of the photodetector. A propagation loss of $5.2 \pm 0.3 \text{ dB cm}^{-1}$ was measured after removing the BOX, as shown in Fig. 3.22b.

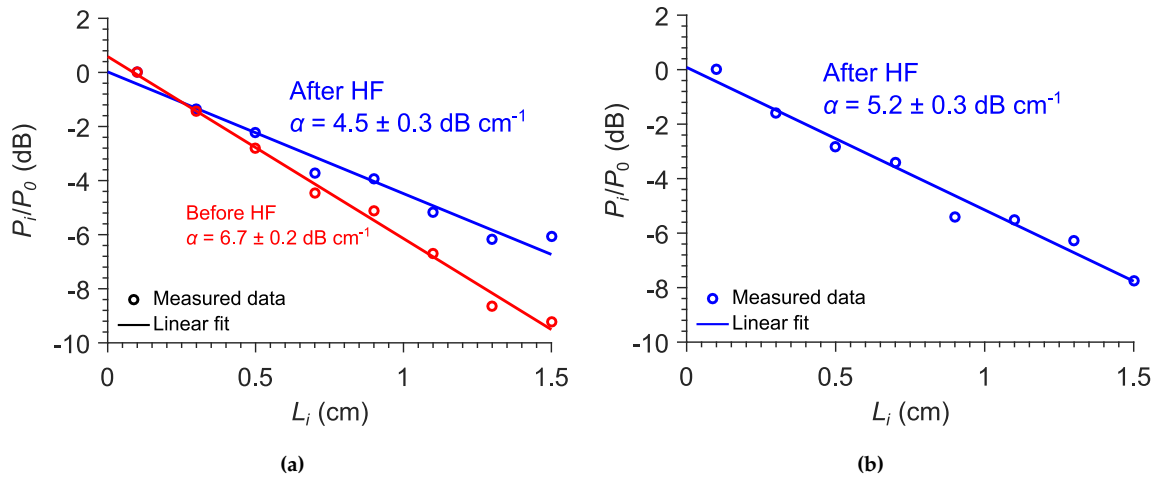


Figure 3.22: (a) Propagation loss measurements for germanium waveguides with the BOX still present (red curve) and for suspended germanium waveguides (blue curve) at $3.8\text{-}\mu\text{m}$ wavelength. (b) Propagation loss measurements for suspended germanium waveguides at $7.67\text{-}\mu\text{m}$ wavelength. The injected light is TE-polarized in both cases.

The high losses compared to suspended silicon waveguides — with $\alpha = 0.8 \text{ dB cm}^{-1}$ at $\lambda = 3.8 \mu\text{m}$ [147], and $\alpha = 3.1 \text{ dB cm}^{-1}$ at $\lambda = 7.67 \mu\text{m}$ — can be caused potentially by the following reasons:

- *Germanium layer impurities.* It was known that the GOSOI wafers that had been recently acquired by the MIR group of the ORC were contaminated. A defect map provided by the manufacturer of the wafers is shown in Fig. 3.23, indicating the distribution, diameter, and number of light point defects in the wafer, as well as the area, marked in red, of larger problematic regions.
- *Sidewall roughness and fabrication errors.* Although roughness was not clearly observable on the SEM images, this is the most typical source of loss in photonic integrated devices. The HF attack could deteriorate the chip surface.

SEM images did not reveal the 60-nm silicon film under the germanium layer. Anyhow, its presence could not explain an increased loss due to silicon absorption. According to isotropic simulations, this silicon layer would produce an increase of only 0.06 dB cm^{-1} in the mode loss.

Although the suspended germanium membranes presented by Osman et al. in [77] exhibit a lower propagation loss of 2.6 dB cm^{-1} at $\lambda = 7.67 \mu\text{m}$, they have two main dis-

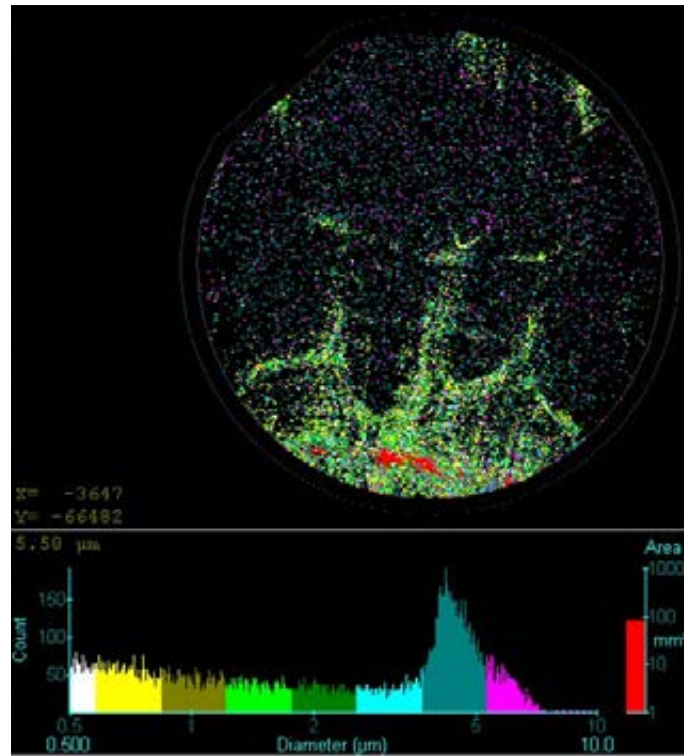


Figure 3.23: Defect map and histogram for one of the GOSOI wafers that were used to fabricate the suspended germanium samples. The defect map shows the distribution of light point defects (LPDs) and defect areas that were found on the wafer surface. The different colors correspond to the size of the defects. The histogram counts the number of LPDs as a function of their diameter.

advantages compared to the suspended waveguides proposed in this section: (i) they require a more complicated fabrication process with two dry etch steps, and (ii) they have a larger suspended area, which might jeopardize the mechanical stability of the structure.

The propagation losses reported in this thesis for the suspended germanium waveguides, albeit higher than those of suspended silicon waveguides, constitute the first experimental demonstrations of suspended germanium platforms with lateral SWG cladding in the MIR band.

3.5 Suspended Silicon Beamsplitters

After demonstrating the suspended silicon waveguides, various devices were designed for the new platform. In this section, suspended silicon multimode interference couplers and 3-dB splitters will be analyzed succinctly. Fiber-chip surface couplers will be covered in Chapter 4.

3.5.1 Multimode Interference Couplers

Multimode interference couplers (MMIs) are essential building blocks in integrated photonics, as they can be used as power splitters and combiners. These couplers typically exhibit more compactness, bandwidth, and relaxed fabrication tolerances than conventional directional couplers. MMIs can be part of Mach-Zehnder interferometers (MZIs),

which, for example, can be used to build FTIR spectrometers, as in [60] and [78]. In this work, suspended silicon 1×2 and 2×2 MMIs were designed at $\lambda = 7.67 \mu\text{m}$.

Suspended silicon MMIs comprise (i) a multimode waveguide of width W_{MMI} and length L_{MMI} , (ii) M input and N output waveguides of width W_a and separation W_s , and (iii) conventional adiabatic tapers of length L_{taper} to adapt the width W of the interconnecting waveguides to W_a . Because of the high modal confinement in the MMI core, the SWG cladding width can be reduced to $W_{\text{clad,MMI}}$ in the multimode region to improve the mechanical stability of the suspended structure. Figure 3.24 schematically illustrates the top views of suspended 1×2 ($M = 1, N = 2$) and 2×2 ($M = 2, N = 2$) MMIs. The former behaves as a 3-dB splitter, while the latter is an optical 90° 3-dB hybrid, which equally divides the input power and introduces a 90° phase shift between both output ports.

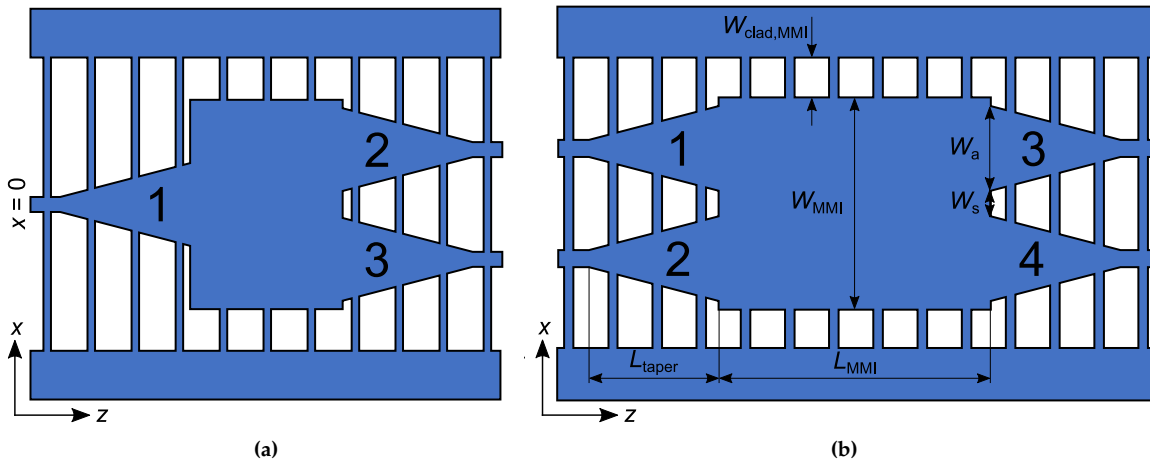


Figure 3.24: Schematic representations of suspended silicon (a) 1×2 and (b) 2×2 MMIs. Access ports are numbered. For simplicity, the geometrical parameters are indicated only in subfigure (b).

The working principle is based on the self-imaging phenomenon: when the light is injected into the wide multimode waveguide through one of the access ports, labeled from 1 to 4 in the figure, the interference between the supported modes produces several replicas or self-images of the input field at different positions along the propagation direction. A further discussion of the operation of MMIs can be found in [173].

The key parameters of MMIs are the (i) excess loss, (ii) the power imbalance, and (iii) the phase error. For a 1×2 MMI, the excess loss can be calculated as

$$\text{EL} = -10 \log \left(|S_{21}|^2 + |S_{31}|^2 \right), \quad (3.8)$$

where S_{21} and S_{31} are the S-parameters associated to the input port 1 and the output ports 2 and 3, respectively. The power imbalance and the phase error are zero because the structure is symmetrical with respect to $x = 0$ (see Fig. 3.24). On the other hand, the performance metrics of 2×2 MMIs can be calculated as follows:

$$\text{EL} = -10 \log \left(|S_{31}|^2 + |S_{41}|^2 \right), \quad (3.9)$$

$$\text{IB} = -10 \log \left(|S_{31}|^2 / |S_{41}|^2 \right), \quad (3.10)$$

$$PE = \angle (S_{31}/S_{41}) - 90^\circ, \quad (3.11)$$

where S_{31} and S_{41} are the S-parameters associated to the input port 1 and the output ports 3 and 4, respectively.

Suspended MMIs can be designed, as usual, following the guidelines by Soldano and Pennings [173]. First, after applying the effective index method (EIM) [174], the structure was preliminary designed with FEXEN, UMA's 2D in-house simulator [168]; afterward, 3D FDTD simulations of the original structure, including the SWG cladding, were carried out using RSoft FullWAVE to refine the geometry and double check the results.

Figure 3.25 shows the simulated performance of the designed 1×2 and 2×2 MMIs, whose dimensions are summarized in Table 3.5, as a function of the wavelength. At $\lambda = 7.67 \mu\text{m}$, $EL < 0.2 \text{ dB}$, $|IB| \sim 0 \text{ dB}$, and $|PE| < 1^\circ$.

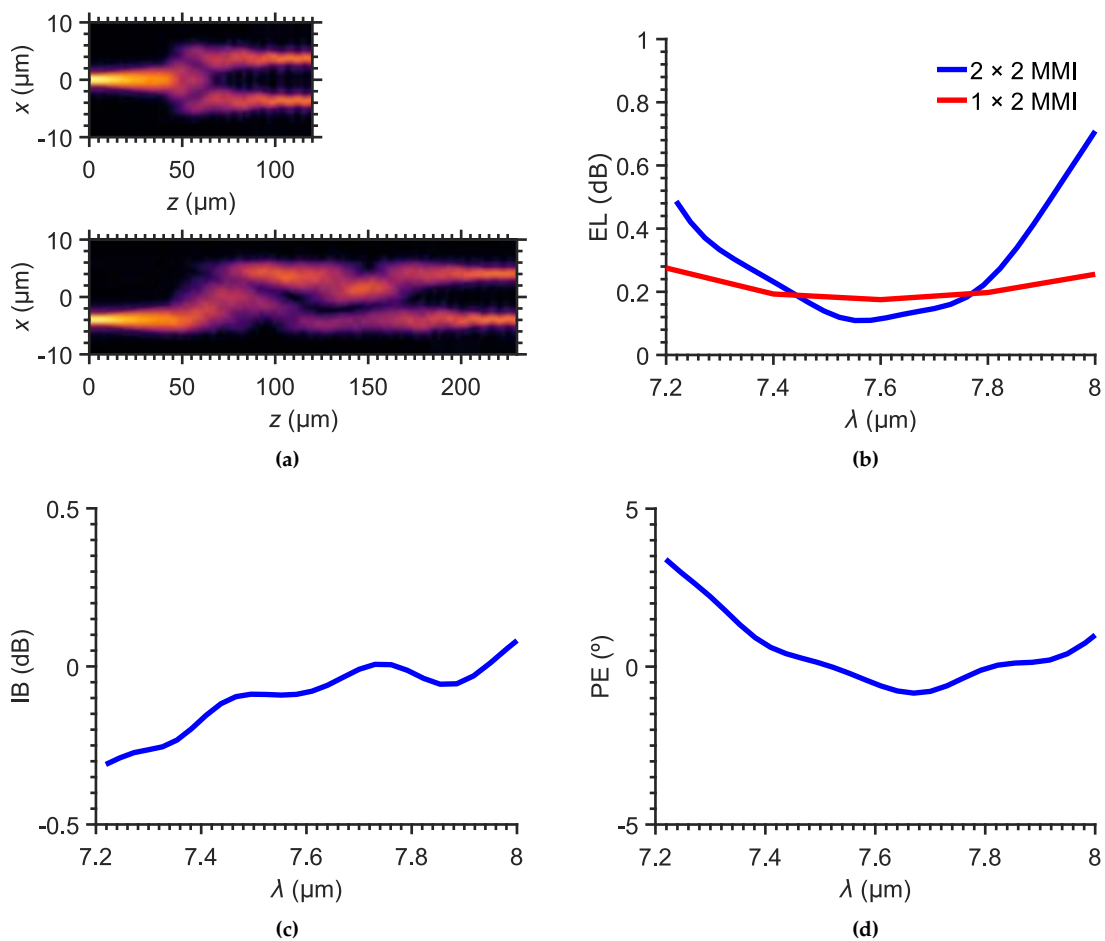


Figure 3.25: Performance of the 1×2 and 2×2 MMIs. (a) 3D FDTD propagation of the TE-polarized electric field (magnitude) for the 1×2 (top) and 2×2 (bottom) MMIs when the fundamental modes of the input waveguides are excited at a wavelength of $7.67 \mu\text{m}$. The simulated (b) excess losses, (c) power imbalance, and (d) phase error are shown as a function of the wavelength. The power imbalance and the phase error of the 1×2 MMI are zero because of the symmetry of the structure, so that the corresponding curves are not included in (c) and (d).

Several sets of cascaded MMIs were fabricated in the SNC using the same lithography procedure that was described in Section 3.3.2. Each set had i MMIs, in order to calculate the excess loss as the slope of the transmitted power as a function of the number of MMIs,

Table 3.5: Designed dimensions of the 1×2 and 2×2 MMI couplers for the suspended silicon platform at $\lambda = 7.67 \mu\text{m}$ (TE polarization). All dimensions are given in microns.

M	N	W_a	W_s	$W_{\text{clad,MMI}}$	W_{MMI}	L_{MMI}	L_{taper}
1	2	5.9	1.25	2	13.05	32.2	30
2	2	5.9	1.84	2	13.38	136.9	30

i. SEM images of the fabricated structures are shown in Fig. 3.26. For the 1×2 MMI, the first measurements done by the researchers of the ORC indicate excess losses as low as $0.47 \pm 0.05 \text{ dB MMI}^{-1}$ at $\lambda = 7.67 \mu\text{m}$ (see Fig. 3.27). The characterization of the 2×2 MMI is still in progress at the time of writing.

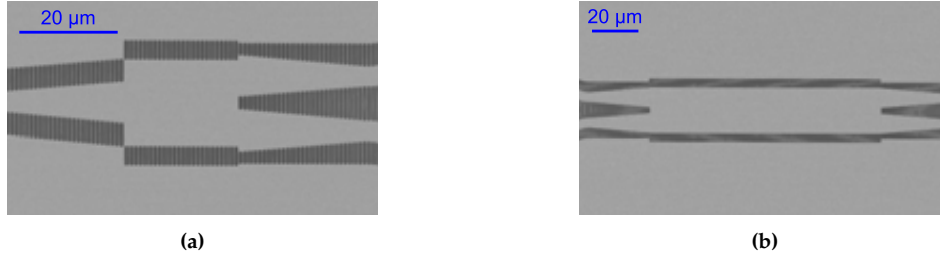


Figure 3.26: SEM images of the fabricated (a) 1×2 and (b) 2×2 MMIs for the suspended silicon platform at $\lambda = 7.67 \mu\text{m}$ and TE polarization.

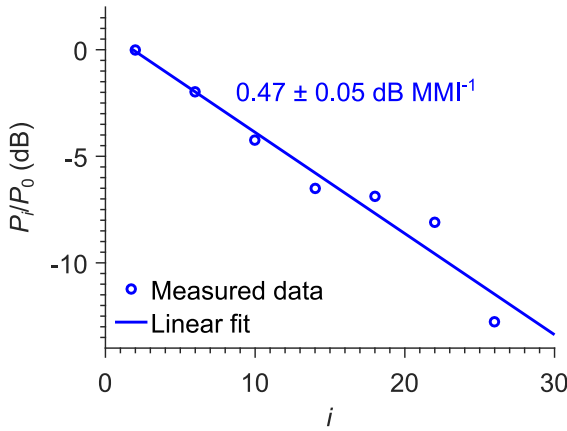


Figure 3.27: Measured excess loss of the 1×2 MMI fabricated for the suspended silicon platform at $\lambda = 7.67 \mu\text{m}$ (TE polarization). The transmitted power through each set of i MMIs is normalized to the transmission of the shortest set ($i = 2$); the excess loss is calculated as the slope of the linearly fitted curve.

3.5.2 Mode-Evolution-Based 3-dB Splitter

As an alternative to suspended silicon 1×2 MMIs, the 3-dB splitter illustrated in Fig. 3.28 is proposed. This structure comprises an input waveguide of length L_c that reduces its width along the propagation direction. The input mode is symmetrically coupled into the two output tapered waveguides, which are separate a distance W_s from the central, input waveguide. To reduce the length L_c of the interaction region, the duty cycle of the SWG cladding between the tapers is linearly apodized from DC_0 to DC_{final} . This variation in the duty cycle gradually increases the coupling strength, leading to reduced excess loss compared to non-apodized designs with the same length. Since the splitter's working principle is based on mode evolution, a wide bandwidth is expected.

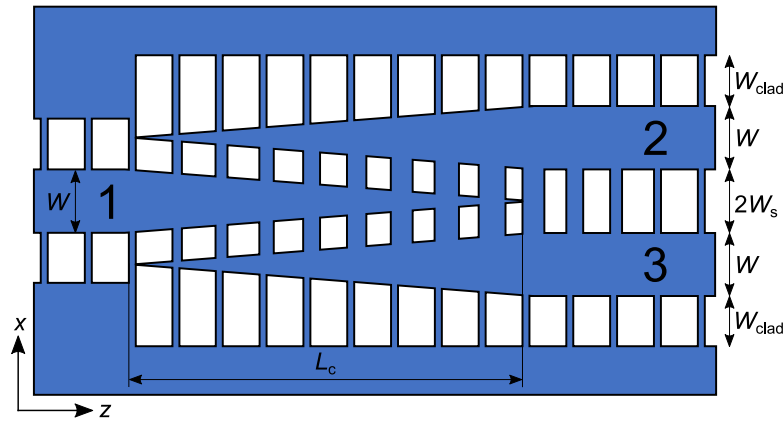


Figure 3.28: Schematic representation of the mode-evolution-based 3-dB splitter designed for the suspended silicon platform at a wavelength of $7.67 \mu\text{m}$ (TE polarization). Access ports are numbered.

As a first approximation, the SWG regions of the structure were substituted with isotropic equivalent media. The duty cycle variation was modeled as a gradual equivalent refractive index. Once the dimensions were chosen, 3D FDTD simulations were carried out including the actual SWG cladding.

The final geometrical parameters of the splitter are presented in Table 3.6. The TE-polarized field propagation and the excess loss, simulated with RSoft FullWAVE (3D FDTD), are shown in Fig. 3.29. At $\lambda = 7.67 \mu\text{m}$, an excess loss smaller of 0.07 dB is achieved in a coupling length of $\sim 31 \mu\text{m}$, which is smaller than the length of the 1×2 MMI that was designed in the previous section.

Table 3.6: Designed dimensions of the 3-dB splitter for the suspended silicon platform at $\lambda = 7.67 \mu\text{m}$ (TE polarization).

W_s (μm)	L_c (μm)	Λ (μm)	DC_0 (%)	DC_{final} (%)
1.10	31.05	1.15	21.74	56.52

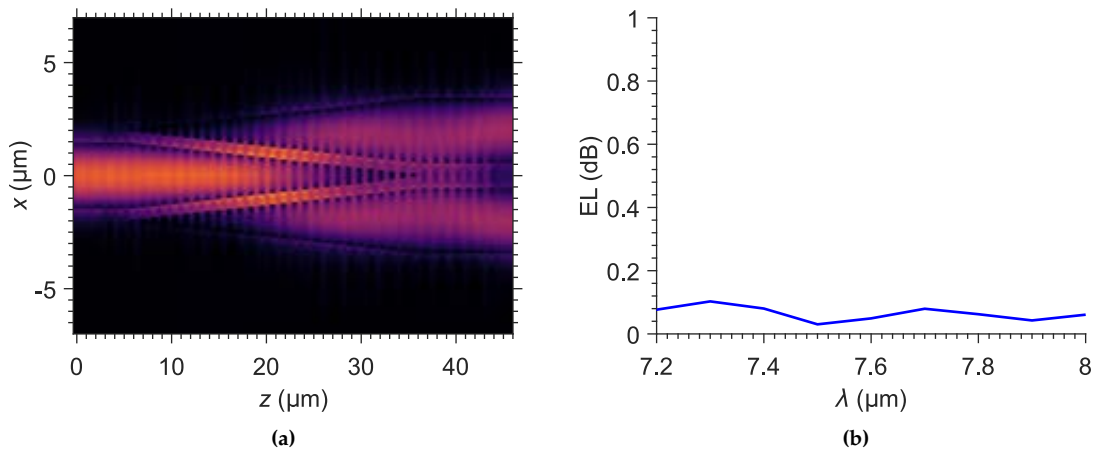


Figure 3.29: Performance of the suspended silicon 3-dB splitter. (a) 3D FDTD propagation of the TE-polarized electric field (magnitude) when the fundamental mode of the input waveguide is excited at a wavelength of $7.67 \mu\text{m}$. (b) Simulated excess loss as a function of the wavelength.

Although the device was fabricated, as shown in the SEM image in Fig. 3.30, its performance could not be demonstrated, because the duty cycle variation was not correctly defined in the mask. A new fabrication run is planned to characterize this splitter.

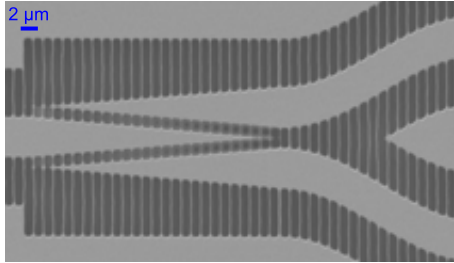


Figure 3.30: SEM image of the fabricated 3-dB splitter for the suspended silicon platform at $\lambda = 7.67 \mu\text{m}$ (TE polarization). S-bends are included to separate the output ports. The duty cycle variation was not correctly defined in the mask used to fabricate the structure, so that the characterization of this device has not yet been possible.

3.6 Conclusions

In this chapter, suspended waveguides with lateral SWG cladding have been comprehensively analyzed, covering the design, fabrication, and characterization of the developed structures.

Suspended waveguides must be designed according to mechanical, fabrication, and optical requirements. Specifically, the dimensions of the waveguides must guarantee low loss for the fundamental mode and high loss for the high-order modes (if supported), while a sufficient mechanical integrity is provided. Three models for modeling and simulating this kind of suspended structures have been proposed: isotropic, anisotropic, and rigorous Bloch–Floquet. While the isotropic approach is appropriate for estimating the vertical leakage to the silicon substrate, it is not well suited for the lateral leakage toward the unetched silicon or germanium lateral areas. Instead, for the latter, the anisotropic model and the Bloch–Floquet analysis are much more accurate. Using the isotropic and the anisotropic models, suspended silicon waveguides were designed to operate at a wavelength of $7.67 \mu\text{m}$; suspended germanium waveguides, at $3.8 \mu\text{m}$, $7.67 \mu\text{m}$, and $9.6 \mu\text{m}$.

Suspended silicon waveguides have been demonstrated at $7.67\text{-}\mu\text{m}$ wavelength with an excellent propagation loss of 3.1 dB cm^{-1} , of which $\sim 2.3 \text{ dB cm}^{-1}$ are due to the unavoidable silicon loss. Suspended silicon 90° - and s-bends also have been characterized with negligible loss. Additionally, suspended silicon multimode interference couplers and mode-evolution-based 3-dB splitters have been designed, with 1×2 MMIs exhibiting a demonstrated excess loss of 0.47 dB MMI^{-1} .

On the other hand, suspended germanium waveguides, characterized at wavelengths of $3.8 \mu\text{m}$ and $7.67 \mu\text{m}$, have yielded losses of $\sim 5 \text{ dB cm}^{-1}$, which is a promising value at such a long wavelength. The comparatively high loss value is mainly attributed to a contamination of the wafer utilized to fabricate the structures.

The proposed suspended platforms can play a decisive role in the development of miniaturized optical devices for spectroscopic applications and communications in the MIR band.

CHAPTER FOUR

FIBER-CHIP SURFACE COUPLERS

The coupling of light between optical fibers and integrated waveguides is one of the most challenging problems in Group IV photonics. In the NIR band, standard optical fibers have mode field diameters (MFD) of $\sim 10\ \mu\text{m}$, a size that is much larger than the width and thickness of typical single-mode photonic wires ($\sim 500\ \text{nm} \times 220\ \text{nm}$). In the MIR band, although the available optical fibers are different (e.g., MFD $\sim 14\ \mu\text{m}$ at $\lambda = 7.67\ \mu\text{m}$) and the required waveguides have larger cross-section dimensions than in the NIR range, the size mismatch still hinders direct butt-coupling of light through chip facets. In this context, fiber-chip couplers, used to efficiently couple light between the optical fiber and the chip, have become essential devices for any photonic integrated platform.

The most common fiber-chip couplers that are currently used in Group IV photonics can be grouped into two categories:

- (i) *Edge couplers*. Light is coupled through the chip facet. An edge coupler is an integrated structure that expands or delocalizes the propagating mode field in order that the mode size of the optical fiber and the waveguide become similar near the chip facet. This mode size adaptation improves the coupling efficiency with respect to direct butt-coupling. Although edge couplers offer high coupling efficiency and broad bandwidth, they require the dicing or polishing of the chip facets through which the light is coupled. Typically, edge couplers are optimized for non-standard, lensed optical fibers with small mode field diameters, which demand precise fiber alignment. Different types of edge couplers have been proposed in the literature, including SWG tapers [175], inverse tapers [176, 177], and multi-layered structures [177, 178]. An inverse-taper-based edge coupler is illustrated in Fig. 4.1a.
- (ii) *Surface grating couplers*. Light is coupled vertically in or out of the chip. A surface grating coupler (or, simply, a grating coupler) is a diffractive (periodic or quasi-periodic) structure, formed in a planar waveguide, that couples the waveguide mode to an off-chip free-propagating plane wave. The diffracted light can be intercepted by an optical fiber positioned above the grating at a specific angle [179]. Surface grating couplers offer some obvious advantages for prototyping — such as the tolerance to fiber-grating misalignments or the possibility of being located at any point along the chip surface, which enables wafer-scale testing [180]. Their drawbacks are the narrow bandwidth, which is caused by the intrinsic wavelength

dependence of the radiation angle, and the comparatively low coupling efficiency. A 3D representation of a surface grating coupler is shown in Fig. 4.1b.

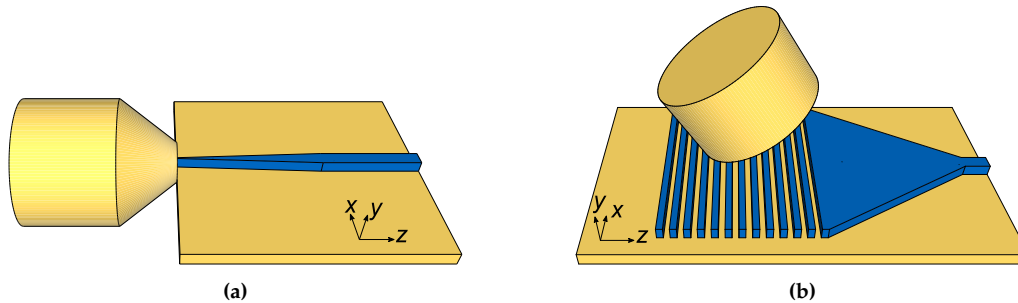


Figure 4.1: (a) Coupling from a lensed optical fiber into a conventional SOI waveguide using an inverse-taper-based edge coupler. (b) Coupling from a standard optical fiber into a conventional SOI waveguide using a surface grating coupler.

Although less used today, a third type of fiber-chip surface coupler is worth mentioning: the prism-film coupler. A high-refractive-index prism is placed above the planar waveguide maintaining a thin coupling gap with low refractive index. The light is coupled between the waveguide and the prism owing to evanescent-wave interaction. These couplers were proposed back in the seventies for low-index-contrast integrated platforms [181–183], in order to measure the optical properties of thin dielectric films [184]. In this thesis, the prism-film coupler concept will be revisited.

This chapter is devoted to the development of fiber-chip surface couplers. First, the fundamentals of surface grating couplers are explained, including their working principle and performance metrics (Section 4.1). Then, the design of conventional grating couplers for the suspended silicon ($\lambda = 7.67 \mu\text{m}$) and suspended germanium ($\lambda = 3.8 \mu\text{m}$) platforms, which was postponed in Chapter 3, is summarized (Section 4.2). Once the general procedure for designing grating couplers is shown, the first main contribution of this chapter is presented: the suspended germanium micro-antenna (Section 4.3). Next, the second major contribution, the zero-order grating coupler, is proposed with the aim of reducing the wavelength dependence of conventional grating couplers (Section 4.4). Finally, the conclusions are drawn (Section 4.5).

4.1 Fundamentals of Surface Grating Couplers

4.1.1 Introduction

Surface grating couplers are planar devices used to couple light from the chip into the optical fiber, or from the optical fiber into the chip. The working principle and the performance of the device are identical in both ways, in virtue of the reciprocity principle. Thus, hereafter, only the chip-to-fiber coupling will be studied.

The top and side views of a conventional surface grating coupler are schematized in Fig. 4.2. The device, which is etched into a guiding layer of thickness H , consists of scatterers that are periodically¹ distributed along the propagation direction. Each scatterer

¹Surface grating couplers with quasi-periodic perturbations have been proposed and are extensively used [185, 186]. By judiciously varying the perturbation, the coupling efficiency can be enhanced. Since the

comprises a segment of refractive index n_1 and length $a = \text{DC} \cdot \Lambda$ that is followed by a segment of refractive index n_2 and length $b = (1 - \text{DC}) \cdot \Lambda$, where DC is the duty cycle, Λ is the period length or pitch, and $n_1 > n_2$. The light diffracted by all the grating periods interferes constructively at a given angle θ , thereby forming a plane wave that propagates freely through the upper medium.² An optical fiber with a tilt angle $\theta_{\text{fiber}} (= \theta)$ is positioned above the chip to collect the radiated light. The length (L_g) and width (W_g) of the grating are chosen in order that the size of the radiated field matches that of the optical fiber mode. A taper of length L_{taper} is typically used to increase the width W of an interconnecting waveguide to W_g .

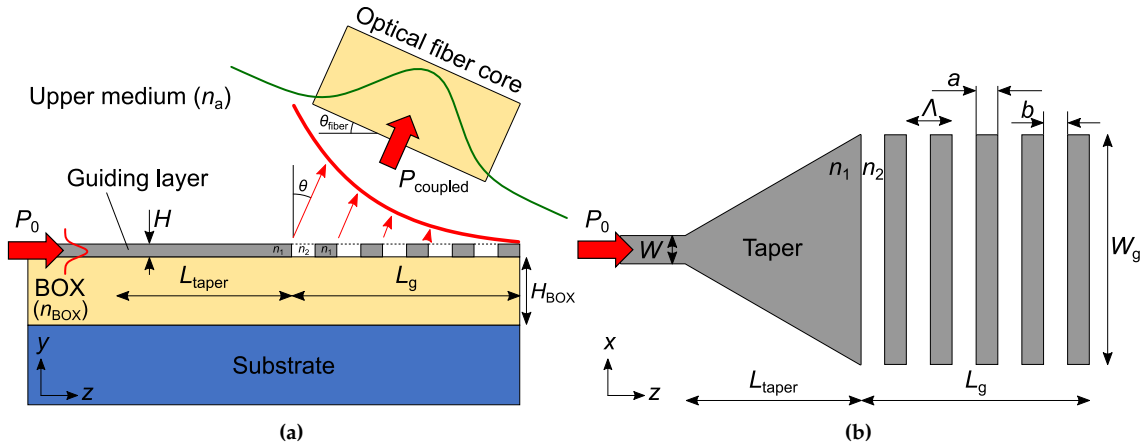


Figure 4.2: Schematic representation of a conventional surface grating coupler. (a) Side view, including the optical fiber. (b) Top view. An input interconnecting waveguide and a linear taper are shown in both subfigures.

4.1.2 Working Principle of Periodic Waveguides

In this section, in order to facilitate the understanding of the fundamentals of surface grating couplers, the working principle of generic periodic waveguides is explained.

For simplicity, a periodic waveguide will be modeled as a 2D structure that corresponds to the side view in Fig. 4.2. Since the width of a surface grating coupler is typically much larger than the wavelength ($W_g \gg \lambda$), the grating can be seen as invariant in the x direction, so that the 2D model can be considered valid.

Under this approximation, the function that defines the refractive index of the grating waveguide is periodic and independent of the x coordinate, that is,

$$n(y, z + \Lambda) = n(y, z). \quad (4.1)$$

Hence, according to the Bloch–Floquet theory [187, 188], the grating supports a Bloch–Floquet mode with an electric or magnetic field component that can be expressed generically by

$$\Phi(y, z) = \phi(y, z) e^{-\gamma_B z}, \quad (4.2)$$

working principle is fundamentally the same for both periodic and apodized (non-periodic) grating couplers, only the former, which are simpler, are covered in this section.

²A plane wave can also be radiated downward. This case, which usually is not desired, will not be considered.

where ϕ is the mode profile and γ_B is the complex propagation constant. The mode profile is also a periodic function, i.e.,

$$\phi(y, z + \Lambda) = \phi(y, z). \quad (4.3)$$

The complex propagation constant can be written as

$$\gamma_B = jk_0 n_B = \alpha_B + j\beta_B. \quad (4.4)$$

Here, $k_0 = 2\pi/\lambda$ is the vacuum wavenumber, n_B is the effective index of the Bloch–Floquet mode, α_B is the attenuation constant, and β_B is the phase constant. The attenuation constant accounts for the power loss, such as leakage or reflection, as the mode travels through the periodic waveguide. Specifically, the remaining power at the output of a grating of length L_g is given by

$$P(L_g) = P_0 e^{-2\alpha_B L_g}, \quad (4.5)$$

where P_0 is the input power. On the other hand, the constant β_B corresponds to the z component of the wavevector of the guided Bloch–Floquet mode, and indicates the phase change of the mode as it propagates along the grating.

Because the mode profile ϕ is a spatially periodic function [Eq. (4.3)], it can be expanded as a Fourier series:

$$\phi(y, z) = \sum_m \phi_m(y) e^{jm \frac{2\pi}{\Lambda} z}, \quad (4.6)$$

where $\phi_m(y)$ is the coefficient of the spatial harmonic of order m . Taking Eqs. (4.2) and (4.6), the mode field component can be rewritten as

$$\Phi(y, z) = \sum_m \phi_m(y) e^{\gamma_{B,m} z}, \quad (4.7)$$

where $\gamma_{B,m}$, the propagation constant of the $|m|^{\text{th}}$ -order harmonic, is

$$\gamma_{B,m} = jk_0 n_{B,m} = \alpha_B + j\beta_{B,m}. \quad (4.8)$$

Although α_B is the same for all of the harmonics, the phase constant is different [179]:

$$\beta_{B,m} = k_0 \text{Re}(n_{B,m}) = k_0 \text{Re}(n_B) + m \frac{2\pi}{\Lambda}. \quad (4.9)$$

Note that, since m is an integer, a discrete set of phase constants exists for each Bloch–Floquet mode within the grating region.

The upper medium supports a continuous spectrum of plane waves, which can propagate with an angle θ (defined with respect to the vertical) and a wavevector

$$\mathbf{k} = \mathbf{k}(\theta) = \hat{y} k_0 n_a \cos(\theta) + \hat{z} k_0 n_a \sin(\theta), \quad (4.10)$$

where \hat{y} and \hat{z} are the unity vectors in the y and z directions, respectively. When the Bloch–Floquet mode propagates through the grating, the phase constants of some harmonics can match the z component of the \mathbf{k} vector, thereby enabling the upward radiation of a discrete set of inhomogeneous plane waves

$$U_m(y, z) = u_m(z) e^{-j(k_{m,y} y + k_{m,z} z)}, \quad (4.11)$$

where $u_m(z)$ is the amplitude of the plane wave, and $k_{m,y}$ and $k_{m,z}$ are, respectively, the y and z components of the wavevector

$$\mathbf{k}_m = \mathbf{k}(\theta = \theta_m) = \hat{\mathbf{y}}k_0n_a \cos(\theta_m) + \hat{\mathbf{z}}k_0n_a \sin(\theta_m), \quad (4.12)$$

where θ_m denotes the radiation angle of the diffracted harmonic. The graphical representation in Fig. 4.3 shows the satisfaction of the phase matching condition that enables diffraction ($k_{m,z} = \beta_{B,m}$), resulting in the grating momentum conservation equation (or grating equation):

$$k_0n_a \sin(\theta_m) = k_0 \operatorname{Re}(n_B) + m \frac{2\pi}{\Lambda}. \quad (4.13)$$

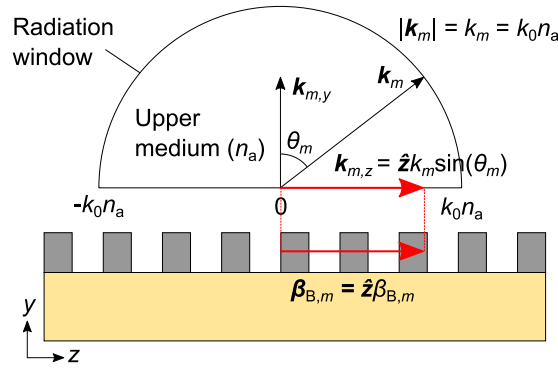


Figure 4.3: Graphical representation of the phase matching condition ($k_{m,z} = \beta_{B,m}$). The grating-propagating harmonic with phase constant $\beta_{B,m}$ is radiated upwards as a plane wave with wavevector $\mathbf{k}(\theta = \theta_m) = \mathbf{k}_m$.

This equation governs the diffractive behavior of periodic waveguides, and can be represented graphically using wavevector diagrams or k -diagrams. In Fig. 4.3, a generic k -diagram for upward³ radiation is shown, indicating the diffraction angle θ_m of the radiated order m . The semicircle, of radius k_0n_a , defines the radiation window: those orders whose refractive indices are contained within the window, i.e., those harmonics with $|\operatorname{Re}(n_{B,m})| < n_a$, are radiated. Thus, when $\operatorname{Re}(n_B)$ is known for the fundamental Bloch–Floquet mode of a periodic waveguide, these diagrams help identify the number of diffracted orders and their radiation angles.

By normalizing all of the wavevectors by k_0 , Eq. (4.13) becomes

$$n_a \sin(\theta_m) = \operatorname{Re}(n_B) + m \frac{\lambda}{\Lambda}. \quad (4.14)$$

and k -diagrams can be expressed in terms of effective index, as in Fig. 4.4.

Depending on the wavelength and the geometry, Eq. (4.14) determines three different regimes or zones in which a periodic waveguide can operate. These regimes and their properties are described as follows:

- (i) *Diffraction-less.* No real radiation angle meets Eq. (4.14) or, equivalently, no effective index falls within the radiation window. Consequently, all diffraction orders are

³Another k -diagram could be drawn to show the downward radiation orders. As previously noted, downward radiation is not considered here for simplicity.

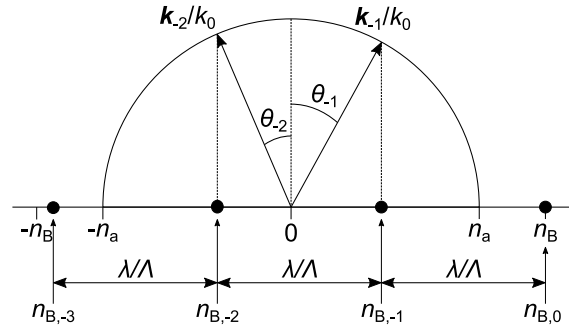


Figure 4.4: Example of normalized k -diagram. The real part operator $\text{Re}(\cdot)$ is assumed implicit when the real part of the effective indices is written. The harmonics or orders whose effective indices fall within the radiation window are diffracted with the indicated angles. The distance between the effective indices of two consecutive harmonics is λ/Λ .

frustrated. This is the typical scenario for subwavelength grating (SWG) operation, which occurs when Eq. (3.1), repeated here for the reader's convenience, is fulfilled:

$$\Lambda < \frac{\lambda}{2 \text{Re}(n_B)}. \quad (3.1)$$

Although the SWG propagation is the most common diffraction-less case, waveguiding can also occur beyond the first Bragg regime [189].

- (ii) *Bragg*. The harmonic of order p , where $p < 0$, satisfies that $n_{B,p} = -n_B$. In this case, which can be clearly identified in a k -diagram, the Bragg condition is fulfilled, i.e.,

$$\Lambda = \frac{|p| \lambda}{2 \text{Re}(n_B)}. \quad (4.15)$$

In this situation, the grating is said to operate in the $|p|^{\text{th}}$ Bragg regime or within the $|p|^{\text{th}}$ photonic bandgap (according to photonic crystal theory [190]). The light is partially reflected back at each discontinuity, and the reflected waves superimpose constructively. Thus, the propagation of light is forbidden and the power transmitted by the $|p|^{\text{th}}$ harmonic decays exponentially. Furthermore, in the Bragg regime some real radiation angles can meet Eq. (4.14), thereby enabling radiation.

- (iii) *Radiation*. Equation (4.14) is satisfied for one or more diffraction orders ($m < 0$).⁴ As a result, the grating radiates one or more plane waves with an amplitude profile

$$u_m(z) = C_m e^{-2\alpha_B z}, \quad (4.16)$$

where C_m is a complex constant that depends on the geometry of the grating and is different for each order. Note that, in contrast, all diffracted waves share the same Bloch–Floquet attenuation constant or radiation strength (α_B). Radiation zones are numbered according to the order p of the preceding Bragg regime: for instance, a grating in the fourth radiation zone operates between the fourth and fifth bandgaps.

⁴The zero-order grating coupler that will be proposed in Section 4.4 diffracts light for $m = 0$. This coupler, which uses non-standard techniques for radiating the light, is an exception.

Conventional surface grating couplers operate in the radiation zones and can diffract light in various diffraction orders, each radiating at a different angle. The optical fiber is positioned above the grating with a specific tilt angle to intercept the radiated power. Since the optical fiber can only be aligned to collect light from one order, grating couplers are usually designed with a pitch Λ that meets Eq. (4.14) for only one diffraction order, which is typically $m = -1$ [179]. Single-beam operation has also been demonstrated for the second diffraction order ($m = -2$) in [123,191,192]. Moreover, if a surface grating coupler fulfills Eq. (4.14) for several angles, the grating can be designed to mitigate undesired radiation orders ($C_m \sim 0$), as will be shown in Section 4.3.

To provide a better understanding of the working principle of surface grating couplers, thorough examples are given in Fig. 4.5. This figure shows the k -diagrams that are associated to a periodic waveguide as the λ/Λ ratio is decreased. Although the effective index n_B could change in actual gratings when λ/Λ is varied, in these examples n_B is considered constant for simplicity. Moreover, the real part operator $\text{Re}(\cdot)$ is assumed implicit, for visual clarity. Each k -diagram in Fig. 4.5 is described in the following list, whose items are labeled using the same letters as in the figure:

- (a) The pitch is much smaller than the wavelength, so that the periodic structure works in the SWG regime. The grating behaves as a non-diffractive waveguide.
- (b) Equation (4.15) is satisfied for $p = -1$. The fulfillment of this condition can be identified easily because $\text{Re}(n_{B,-1}) = -\text{Re}(n_B)$. Hence, the structure operates in the first Bragg regime and acts as a reflector.
- (c) Above the first bandgap and before starting to radiate, the guided mode can propagate without diffracting, yet the SWG condition is not satisfied. Even though this regime could be useful (e.g., better tolerance to fabrication errors could be achieved as a result of the increased pitch), diffraction-less grating waveguides are not usually designed in this regime because of the proximity to both the first bandgap and the first radiation zone.⁵
- (d) The grating enters the first radiation zone. In the range where $-n_a < \text{Re}(n_{B,-1}) < 0$, a single radiation order is supported. A plane wave is radiated backward ($-90^\circ < \theta_{-1} < 0^\circ$). Many surface grating couplers operate in this zone.
- (e) When $\text{Re}(n_{B,-2}) = -\text{Re}(n_B)$, and therefore $\text{Re}(n_{B,-1}) = 0$ ($\theta_{-1} = 0^\circ$), the structure enters the second Bragg regime. This is an interesting scenario: when the Bragg order (p) is even, the harmonic whose order is $p/2$ is always radiated at 0° . Even though fully vertical radiation allows for compact chip packaging and easy optical fiber placement for measuring, high back-reflections may arise due to the photonic bandgap. Thus, to reduce back-reflections, surface grating couplers are typically designed with off-vertical radiation angles.
- (f) In the second radiation zone (i.e., the radiation regime that is between the first and second bandgaps), the first-order ($m = -1$) harmonic can radiate forward ($\theta_{-1} > 0^\circ$). Unfortunately, single-beam operation can only be achieved for a relatively small

⁵A higher wavelength dispersion than in the deep SWG regime can be expected. Moreover, fabrication fluctuations could change the operation regime and make the grating reflect or diffract. In addition, while the grating behaves in the diffraction-less regime for the upper medium, downward radiation can occur if the refractive index of the bottom medium is greater than that of the upper medium.

range of radiation angles before the second-order ($m = -2$) harmonic starts radiating. Many surface grating couplers radiate only the order -1 in this zone. Because of this limited range of angles for single-beam forward radiation, designing surface grating couplers with single-beam backward (Fig. 4.5d) radiation typically is easier.

- (g) The effective index of the second-order ($m = -2$) harmonic enters the radiation window, so that two beams ($m = -1$ and $m = -2$) are radiated. This situation is usually undesired, unless most of the power that propagates through the grating is coupled to only one of the orders.
- (h) The third harmonic fulfills $\text{Re}(n_{B,-3}) = -\text{Re}(n_B)$, that is, the grating enters the third Bragg regime. Since $\lambda/\Lambda = 2n_B/3$ [Eq. (4.15) for $p = -3$], four harmonics fit exactly in the range between $-n_B$ and n_B . As a result, the two supported radiation orders ($m = -1$ and $m = -2$) are symmetrically distributed around the center of the radiation window.
- (i) In the third radiation zone, three-beam radiation is theoretically possible (potential diffractive orders: $m = -1$, $m = -2$, and $m = -3$). However, this scenario cannot happen in the example that is shown in the figure. Instead, the effective index of the first-order harmonic exits the radiation window before the third-order harmonic starts radiating, thereby enabling single-beam radiation with only the second-order harmonic. This case has been exploited, for example, in [123, 191, 192].
- (j) The grating enters the fourth Bragg regime. Hence, the second-order harmonic radiates at 0° . Additionally, the effective indices of the first five harmonics are contained between $-n_B$ (which corresponds to $n_{B,-4}$) and n_B (which always equals $n_{B,0}$). For higher λ/Λ values, the grating will operate in radiation and Bragg regimes alternately, and the number and order of the radiating harmonics will increase.

4.1.3 Performance Metrics of Surface Grating Couplers

The main performance metrics of surface grating couplers are the back-reflections (R), the coupling efficiency (CE), and the bandwidth (BW). Other parameters, such as the radiation angle or the tolerance to fiber tilt misalignments, can be considered to be figures of merit for specific applications.

Coupling Efficiency

Coupling efficiency is defined as the fraction of incident power that is coupled from the chip into the optical fiber and vice versa [155]. This parameter can be estimated as

$$\text{CE} = \text{OL} \cdot D \cdot (1 - R), \quad (4.17)$$

where R denotes back-reflections; D is the directionality, defined as the fraction of input power that is radiated upward; and OL is the scalar overlap integral between the radiated field and the mode field of the optical fiber. To achieve the maximum value of CE ($= 1$), back-reflections must be suppressed ($R = 0$) and all power must be radiated upward ($D = 1$) with a near-field profile that perfectly matches that of the Gaussian-like mode of the optical fiber ($\text{OL} = 1$). Next, these parameters are briefly discussed:

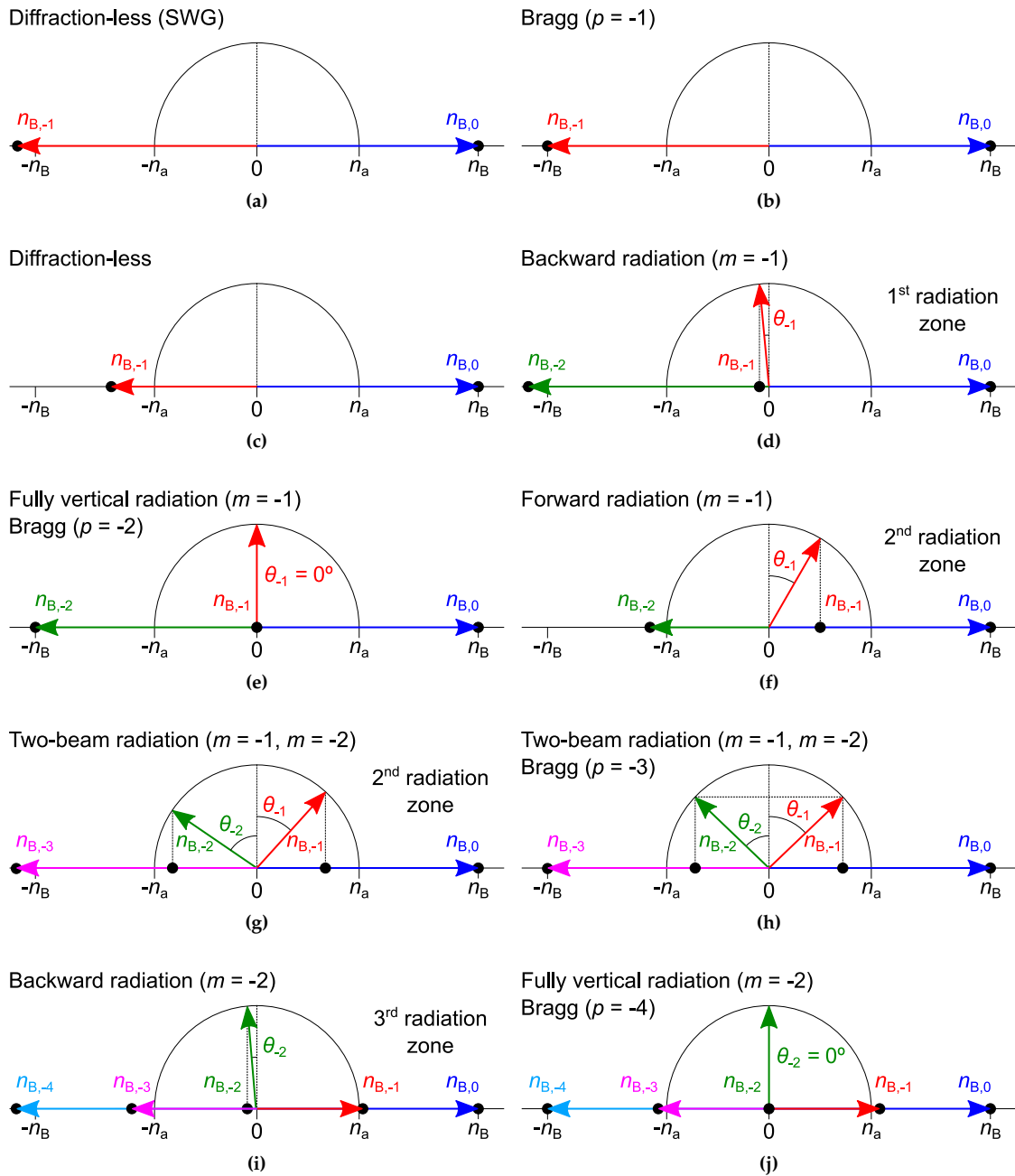


Figure 4.5: Examples of normalized k -diagrams, which show the different operation regimes of a periodic waveguide as the λ/Λ ratio is decreased. The effective index n_B is considered constant. The real part operator $\text{Re}(\cdot)$ is assumed implicit when the real part of the effective indices is written. (a) Diffraction-less [SWG]. (b) First Bragg regime. (c) Diffraction-less. (d) Backward single-beam radiation with $m = -1$ [first radiation zone]. (e) Fully vertical single-beam radiation with $m = -1$ + second Bragg regime. (f) Forward single-beam radiation with $m = -1$ [second radiation zone]. (g) Backward [$m = -2$] and forward [$m = -1$] two-beam radiation. (h) Backward [$m = -2$] and forward [$m = -1$] two-beam radiation + third Bragg regime. (i) Backward single-beam radiation with $m = -2$ [third radiation zone]. (j) Fully vertical single-beam radiation with $m = -2$ + fourth Bragg regime.

- *Overlap integral.* The overlap integral can be calculated as

$$\text{OL} = \frac{\int_{z'} E_{\text{radiated}} E_{\text{fiber}}^* dz'}{\int_{z'} E_{\text{radiated}} E_{\text{radiated}}^* dz' \int_{z'} E_{\text{fiber}} E_{\text{fiber}}^* dz'}, \quad (4.18)$$

where * symbolizes complex conjugate, E_{radiated} is the radiated field, E_{fiber} is the mode field of the optical fiber, and z' is the axis parallel to the facet of the optical fiber. This integral limits the coupling efficiency in uniformly periodic grating couplers, as the theoretical maximum overlap between an exponential and a Gaussian function is 80% [180]. In the literature, apodized surface grating couplers with non-periodic perturbations have been proposed to ensure a near-Gaussian diffracted field profile, thereby improving the coupling efficiency [185].

- *Directionality.* Although only upward radiation has been considered so far, the grating equation can also enable outgoing beams toward the bottom medium. The directionality is given by

$$D = \frac{P_{\text{up}}}{T + P_{\text{up}} + P_{\text{down}}}, \quad (4.19)$$

where P_{up} is the power radiated upward, P_{down} is the power radiated downward, and T is the transmitted power that remains at the end of the grating waveguide. If the number of periods in the grating is sufficiently high, all input power can be radiated (i.e., $T \sim 0$). In vertically symmetrical surface grating couplers ($n_a = n_{\text{BOX}}$ and $H_{\text{BOX}} \rightarrow \infty$), the guided mode is equally diffracted upward and downward ($P_{\text{up}} = P_{\text{down}}$), yielding $D = 0.5$. In typical platforms in which the refractive indices of the upper and bottom media are similar but not equal, such as SOI with air cladding, the directionality can be slightly improved by leveraging the vertical asymmetry. To optimize the directionality, various techniques can be found in the literature, including the use of bottom mirrors [193,194] and of non-rectangular grating teeth (blazed gratings) [195–197].

- *Back-reflections.* Because back-reflections are, together with the coupling efficiency and the bandwidth, one of the main performance metrics, this parameter is described in the next section.

It is worth noting that, at a given wavelength, the coupling efficiency of conventional surface grating couplers is polarization dependent. The rationale of this dependency is that, in general, the effective indices of TE and TM guided modes are different. According to Eq. (4.14), the radiation angles strongly depend on the Bloch–Floquet effective index of the grating. Thus, the coupling efficiency cannot be maximized for both TE and TM polarizations simultaneously (unless specific techniques are employed [198]).

Back-Reflections

When a Bloch–Floquet mode is excited and guided through a surface grating coupler, an amount of power can be reflected back to the input waveguide. Even when operation in the Bragg regimes is avoided, the discontinuity between the input waveguide and the grating can make conventional grating couplers exhibit back-reflections above 30%. This

value can enable the formation of optical cavities between the input and output grating couplers in a photonic circuit. Back-reflections smaller than 1% are typically required [199].

The influence of optical fibers can degrade back-reflections, because a Fresnel loss can occur at the air-fiber interface. This reflected power can couple back into the grating, thereby increasing the effective back-reflections to values higher than 1% and hence reducing the coupling efficiency. This inconvenience is especially serious at long MIR wavelengths ($\lambda > 7.5 \mu\text{m}$), as the optical fibers that are commercially available in the MIR band have high refractive indices. For example, IRFlex's IRF-Se-12 fiber has a core refractive index of 2.7 at $\lambda = 7.67 \mu\text{m}$ [200], whereas a standard SMF-28 fiber at $\lambda = 1.55 \mu\text{m}$ has a core refractive index of only ~ 1.45 [201].

Several techniques have been proposed to reduce back-reflections, including the use of waveguide-to-grating transitions [195, 202, 203], SWG structures [195, 203, 204], and focusing gratings [205].

Spectral Bandwidth

Equation (4.14) shows that the radiation angles of surface grating couplers depend on the wavelength. Therefore, the optical fiber, which is positioned above the grating with a fixed tilt angle, cannot efficiently collect the radiated light in a wide range of wavelengths. The 1-dB bandwidth, defined as the wavelength range for which the coupling efficiency drops by 1 dB with respect to its peak value, is proportional to the derivative of the wavelength with respect to the radiation angle [206]:

$$\text{BW}_{1\text{dB}} = \eta_{1\text{dB}} \left| \frac{\partial \lambda}{\partial \theta} \right| = \eta_{1\text{dB}} \left| \frac{n_a \cos \theta}{\frac{m}{\Lambda} + \frac{\partial \text{Re}(n_B)}{\partial \lambda} - \frac{\partial n_a}{\partial \lambda} \sin \theta} \right|, \quad (4.20)$$

where $\eta_{1\text{dB}}$ is a factor solely determined by the optical fiber and θ is the radiation angle of the dominant order⁶.

In conventional surface grating couplers, the radiation order is -1 and the upper cladding is air, a non-dispersive medium ($\partial n_a / \partial \lambda = 0$). Taking these considerations into account, Eq. (4.20) becomes

$$\text{BW}_{1\text{dB}} = \eta_{1\text{dB}} \left| \frac{n_a \cos \theta}{-\frac{1}{\Lambda} + \frac{\partial \text{Re}(n_B)}{\partial \lambda}} \right|. \quad (4.21)$$

These equations indicate that the bandwidth of surface grating couplers that are designed with a pitch Λ for a specific optical fiber is given mainly by the following sources:

- *The wavelength dependence of the Bloch–Floquet effective index.* Clearly, since grating couplers are designed to maximize the coupling efficiency at a single wavelength, broadband grating couplers require a low variation of $\text{Re}(n_B)$ with λ . Surface grating couplers using SWG structures and low-refractive-index materials to increase the bandwidth have been reported in the literature [204, 207].
- *The radiation angle.* Grating couplers that radiate close to the vertical direction ($\theta = 0^\circ$) are preferable for broadband operation.

⁶Equation (4.20) assumes that the surface grating coupler diffracts only one order, m . Thus, $\theta = \theta_m$.

- *The characteristics of the optical fiber*, which are enclosed in the $\eta_{1\text{ dB}}$ parameter [204, 208, 209]. For example, the bandwidth can be enlarged when the grating coupler is designed to operate with optical fibers with narrow MFDs. This consideration was exploited in the design of the suspended germanium micro-antenna that will be covered in Section 4.3.
- *The diffraction order*. This parameter typically cannot be utilized to enhance the bandwidth because conventional grating couplers radiate the -1 order [Eq. (4.21)]. However, in Section 4.4, an ultra-broadband grating coupler will be presented that radiate the zeroth order.

4.2 Suspended Grating Couplers

Conventional grating couplers were designed to characterize the suspended waveguides that were demonstrated in Chapter 3. In this section, the general strategy followed to design such grating couplers is presented. Then, the development of suspended silicon grating couplers at $\lambda = 7.67\ \mu\text{m}$ and suspended germanium grating couplers at $\lambda = 3.8\ \mu\text{m}$ is briefly explained.

4.2.1 General Design Approach

The geometrical parameters that define the performance of conventional grating couplers are the pitch and the duty cycle. The overall design procedure that has been followed in this work is summarized in the following steps:

- Values of Λ and DC are selected that produce fabricable structures having low back-reflections and operating far from Bragg regimes. Typically, only those structures that radiate the $m = -1$ order are studied. At this step, the calculations are performed efficiently with UMA's in-house simulator, FEXEN [168], by exciting the fundamental mode of a homogeneous input waveguide that is followed by only one grating period, and imposing Bloch–Floquet boundary conditions on the other side, thus emulating a semi-infinite periodic structure (see Fig. 4.6a).
- For the selected structures with comparatively low back-reflections, the coupling efficiency and the radiation angle are estimated from the radiated field and power. The simulations are carried out with FEXEN, now including the input waveguide, grating with enough number of periods to radiate most of the input power, and output waveguide (see Fig. 4.6b).
- The best design is selected according to three figures of merit: high coupling efficiency, small radiation angle, and tolerance to fabrication imperfections.
- For the best design, back-reflections are further reduced with an adaptation section that is placed between the input access waveguide and the first radiative element (see Fig. 4.6c).

Once this procedure is finished, lateral tapers are designed to adapt the width of the interconnecting waveguides and the gratings, which are wider than the former. In this work, since adiabatic tapers would be hundreds-of-microns-long and hence more prone

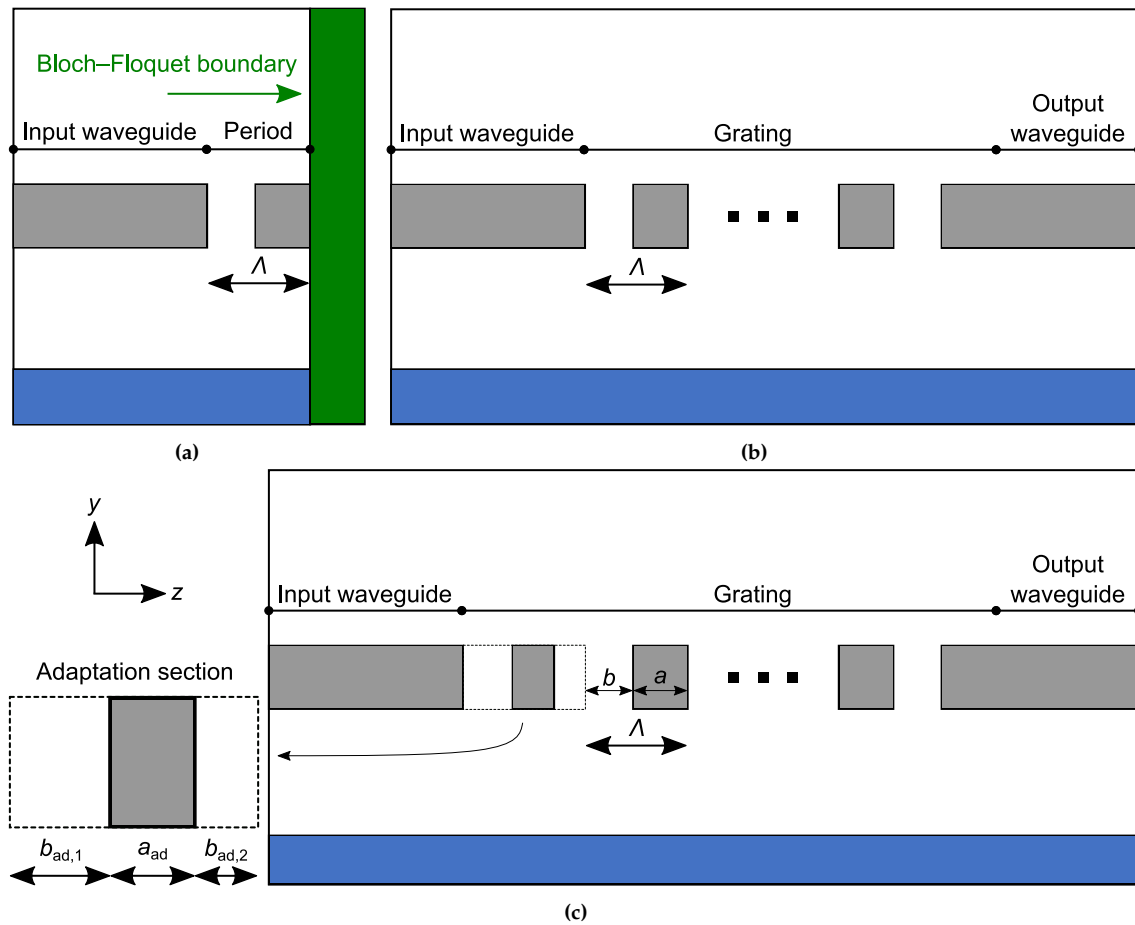


Figure 4.6: Simulation procedure followed to design suspended grating couplers. (a) Back-reflections are calculated by including only one grating period and imposing Bloch-Floquet boundary conditions. (b) The coupling efficiency and the radiation angle are estimated from the radiated field, which is calculated by simulating the complete structure. (c) Back-reflections are calculated again after adding an adaptation section.

to collapse when suspended, shorter three-stage non-adiabatic tapers were developed. Heuristic approaches based on the designer's experience were employed to maximize the transmitted power. Alternatively, to avoid tapers and thus reduce the footprint of the device, focusing grating couplers can be designed by applying the equations in [205].

4.2.2 Design of a Suspended Silicon Grating Coupler

When suspended silicon waveguides were designed at $\lambda = 7.67 \mu\text{m}$, a custom-made chalcogenide optical fiber by CorActive, with a MFD of $\sim 29.5 \mu\text{m}$ and a core refractive index of 2.7, was available in the MIR laboratory of the ORC [210].

Following the approach described in Section 4.2.1, a conventional grating coupler radiating the first ($m = -1$) order was designed with a respectable coupling efficiency of 58%. Low intrinsic back-reflections smaller than 0.8% were also achieved by including a simple adaptation section at the beginning of the grating. When the optical fiber is included within the simulation window, the Fresnel reflection at the fiber-air interface worsens the performance of the device, leading to $R \sim 4.7\%$ and $\text{CE} \sim 50\%$. The 1-dB bandwidth of $\sim 230 \text{ nm}$ corresponds to a fractional bandwidth $\text{BW}_{1\text{dB}}/\lambda = 3.00\%$, which

is slightly smaller than the values exhibited by typical NIR grating couplers ($BW_{1\text{dB}}/\lambda = 3.23\%$) [208]. The radiation angle is $\sim 19^\circ$.

The geometrical parameters of this grating coupler are summarized in Table 4.1 and a SEM image of a fabricated focusing coupler is shown in Fig. 4.7a. Although the device was not characterized, it was employed to couple light into the chips used to demonstrate suspended silicon structures at a wavelength of $7.67\ \mu\text{m}$.

4.2.3 Design of a Suspended Germanium Grating Coupler

Thorlabs' ZBLAN optical fiber available at $\lambda = 3.8\ \mu\text{m}$ has a MFD of $\sim 17.8\ \mu\text{m}$ and a core refractive index of ~ 1.48 [211]. For the characterization of suspended germanium waveguides, a conventional grating coupler ($m = -1$) with a coupling efficiency of $\sim 44\%$ was designed. The calculated back-reflections are lower than 0.5% . After including the optical fiber in the simulation window, the latter increases up to 1.7% . Despite the increased wavelength compared to NIR grating couplers, a narrow bandwidth of $\sim 57\ \text{nm}$ ($BW_{1\text{dB}}/\lambda = 1.5\%$) was achieved. The radiation angle is approximately -19° . The geometrical parameters of this design can be found in Table 4.1. A SEM image of the fabricated coupler is included in Fig. 4.7b.

While suspended germanium waveguides were being designed, CorActive's optical fiber for the $7.67\text{-}\mu\text{m}$ setup was replaced with a non-custom IRFlex's IRF-Se-12 optical fiber [200] (MFD = $13.56\ \mu\text{m}$ according to Marcuse's formula [172]). A suspended germanium grating coupler was designed at $\lambda = 7.67\ \mu\text{m}$ for the new optical fiber, resulting in a satisfactory coupling efficiency of $\sim 45\%$, but a narrow bandwidth of $98\ \text{nm}$ ($BW_{1\text{dB}}/\lambda \sim 1.3\%$) and low tolerance to fabrication errors ($\Delta \sim \pm 25\ \text{nm}$) due to the proximity of the second-order Bragg regime. Owing to its poor overall performance, this grating coupler is not recommended for practical applications. The search for efficient, broadband, and tolerant fiber-chip surface couplers for long MIR wavelengths motivated the design of a suspended germanium micro-antenna, which is covered in Section 4.3.

Table 4.1: Dimensions of the designed suspended grating couplers.

Platform	$\lambda\ (\mu\text{m})$	$a\ (\mu\text{m})$	$b\ (\mu\text{m})$	$a_{\text{ad}}\ (\mu\text{m})$	$b_{\text{ad},1}\ (\mu\text{m})$	$b_{\text{ad},2}\ (\mu\text{m})$
Suspended Si	7.67	2.75	1	1.6	0.5	0
Suspended Ge	3.8	0.7	0.88	0.7	0.47	1.09

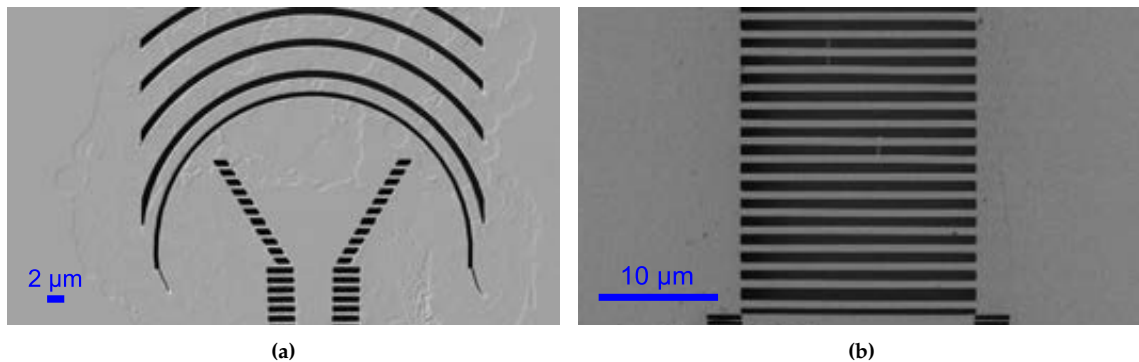


Figure 4.7: SEM images of (a) the suspended silicon and (b) the suspended germanium grating couplers at wavelengths of $7.67\ \mu\text{m}$ and $3.8\ \mu\text{m}$, respectively.

4.3 Suspended Germanium Micro-antenna

4.3.1 Motivation

The design of suspended grating couplers in Section 4.2 showed that the fractional bandwidth is smaller at MIR wavelengths than at $\lambda = 1.55 \mu\text{m}$ when non-custom MIR optical fibers are used. The bandwidth is not increased proportionally when the wavelength is scaled up. At wavelengths beyond $\sim 7.5 \mu\text{m}$, this phenomenon is even more pronounced, and designs with acceptable bandwidth are difficult to achieve.

Most research in MIR integrated photonics has mainly focused on the development of low-loss waveguides. Fiber-chip couplers have primarily been used to characterize new platforms (that is, to couple light to measure propagation losses), but have not been optimized specifically for high coupling efficiency or broad bandwidth [77].

The main difficulty for designing efficient grating couplers for long MIR wavelengths arises from (i) the materials of the platforms used in the MIR band and (ii) the optical properties of commercially available optical fibers. These particularities are detailed as follows:

- (i) *Platforms with high index contrast.* As the intrinsic loss of silicon is high for $\lambda > 8 \mu\text{m}$, other materials — e.g., germanium ($n_{\text{Ge}} \sim 4$) — are required for this wavelength range. Germanium-based platforms provide higher index contrasts than their silicon counterparts ($n_{\text{Ge}}^2 \sim 16 > n_{\text{Si}}^2 \sim 12$). Because the photonic bandgap in periodic structures is larger for higher index contrasts [190], the range of Λ values within the Bragg regime is increased for germanium gratings compared to silicon gratings. As a consequence, diffraction occurs for a narrow range of periods Λ . Typical grating coupler designs may operate near Bragg regimes, thus suffering from narrow bandwidth and reduced tolerance to fabrication imperfections.
- (ii) *Optical fibers with small mode field diameter relative to the wavelength.* A standard NIR optical fiber (SMF-28) has a MFD of $10.4 \mu\text{m}$ at $\lambda = 1.55 \mu\text{m}$, so that the MFD-to-wavelength ratio ($\overline{\text{MFD}} = \text{MFD}/\lambda$) is ~ 6.7 . In contrast, IRFlex's IRF-Se-12 fiber has a core diameter of $12 \mu\text{m}$ and a numerical aperture of 0.47 [200], yielding $\overline{\text{MFD}} \sim 1.8$ at $\lambda = 7.67 \mu\text{m}$. As the length of the coupling structure is in close relation to the MFD of the fiber, the optimum electrical length of the grating, $\overline{L_g} = L_g/\lambda$, will be $6.7/1.8 \sim 4$ times shorter at $\lambda = 7.67 \mu\text{m}$ than at $\lambda = 1.55 \mu\text{m}$. If MIR optical fibers had a $\overline{\text{MFD}}$ value comparable to that at NIR wavelengths, MIR grating couplers with the same radiation strength as in the NIR band could be designed. However, single-mode MIR optical fibers have smaller $\overline{\text{MFD}}$. In consequence, grating couplers with substantially higher radiation strengths are required at long MIR wavelengths.

This need for high radiation strength has implications for grating design. Since grating couplers in the NIR band typically radiate most power in ~ 20 periods to efficiently couple light into an optical fiber [180], an efficient MIR coupler will require only $\sim 20/4 \sim 5$ periods — assuming the pitch Λ is scaled; if Λ were further increased, the number of periods could be even smaller. Furthermore, a fiber-chip surface coupler designed for the MIR band with a short electrical length will radiate a narrow diverging outgoing beam with cylindrical wavefront, which will provide for broad bandwidth and fiber tilt tolerance. Because of these fundamental differences with NIR surface couplers, it can be argued that efficient long-wavelength

MIR surface couplers for non-custom optical fibers should operate more like micro-antennas rather than conventional grating couplers.

In the following sections, the development of a suspended germanium micro-antenna at $\lambda = 7.67 \mu\text{m}$ that addresses the previous considerations will be analyzed. This micro-antenna design was published in [81].

4.3.2 Design

A schematic of the proposed micro-antenna is represented in Fig. 4.8. Note that, although the structure is similar to a conventional suspended grating coupler, here the pitch is much larger.

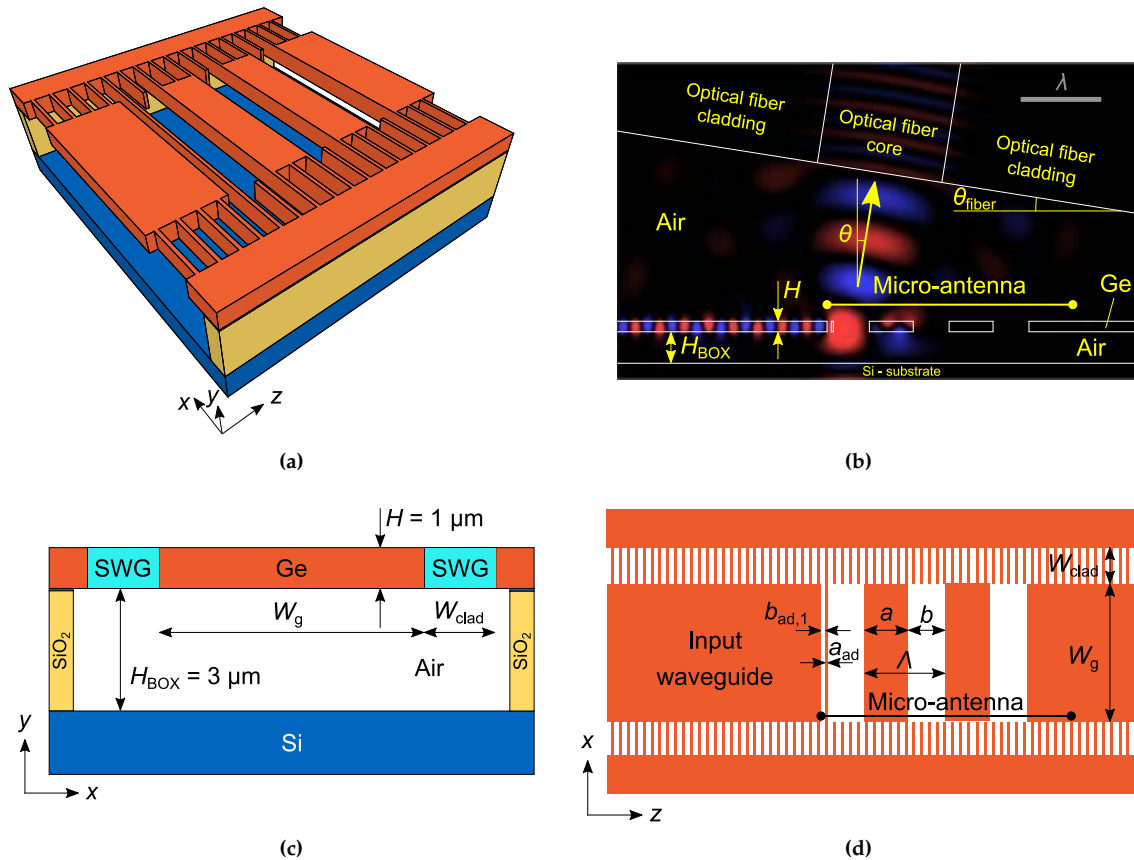


Figure 4.8: Schematic representation of the suspended germanium micro-antenna. (a) 3D view. (b) Side view with 2D FDTD propagation. (c) Front view. (d) Top view.

As indicated in Section 4.2.1, the typical grating coupler design approach consists in scanning the pitch and the duty cycle, in order to maximize the coupling efficiency and minimize back-reflections. The search space is usually restricted to those (Λ, DC) pairs that enable single-beam radiation. Because of the design difficulties mentioned in Section 4.3.1, the single-beam condition limits the number of potential efficient micro-antennas with broad bandwidth and high tolerance to fabrication imperfections. To overcome this limitation, in this work the single-beam constraint has been relaxed.

High coupling efficiency can be achieved even if several diffraction orders are supported, provided the grating is designed such that most of the optical power is radiated

into a single beam. Thus, to expand the search space, a simple condition for “no more than two orders” can be derived from Eq. (4.14). Figure 4.9a shows the normalized k -diagram of a grating coupler that supports three arbitrary diffraction orders (in red). The distance, in effective index units, between two consecutive harmonics is λ/Λ . Then, $2\lambda/\Lambda$ is the distance between the effective indices of the harmonics that are closer to the boundaries of the radiation window. To guarantee that at least one of the three orders is pushed out of the diffraction window, $2\lambda/\Lambda$ must be greater than $2n_a$ (see Fig. 4.9b). Therefore, no more than two orders will be radiated if

$$\Lambda < \frac{\lambda}{n_a}. \quad (4.22)$$

This bound can be used to define the pitch range to be explored in the design process.

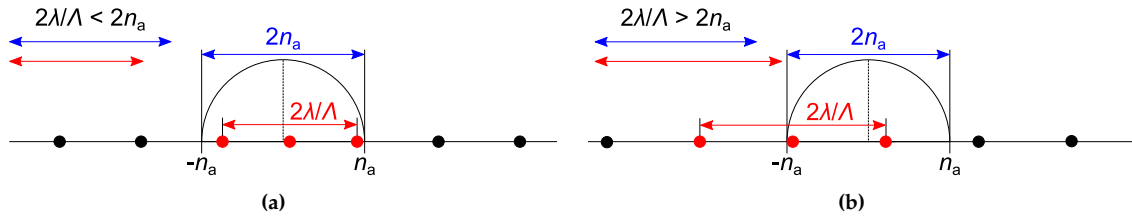


Figure 4.9: Normalized k -diagram utilized to demonstrate “no more than two radiated beams”-condition. (a) Three radiated orders are supported. (b) A maximum of two radiated orders are supported when the condition is fulfilled.

Back-reflections were calculated for a complete set of (Λ, DC) pairs. Figure 4.10 shows the map of back-reflections for all possible gratings with periods ranging from $1\ \mu\text{m}$ up to $10\ \mu\text{m}$. Below $\Lambda \sim 1\ \mu\text{m}$, the periodic waveguide is working in the SWG regime. The upper bound for Λ was chosen to cover all periods that meet condition (4.22), $\Lambda < \lambda = 7.67\ \mu\text{m}$. Since good designs could still be found for longer periods, additional values (up to $\Lambda \sim 10\ \mu\text{m}$) were also evaluated. Bragg and radiation regimes can be recognized visually in this contour map of R . Reddish areas where $R > 70\%$ correspond to the different Bragg regimes. On the other hand, dark blue areas with $R \leq 30\%$,⁷ delimited with solid lines in Fig. 4.10, are candidates for good coupler designs. However, not all zones with low back-reflections are useful in practice. Those with high DC values (i.e., small hole sizes) could prevent HF from successfully removing the BOX beneath the wide micro-antenna, while those with low DC values (i.e., thin germanium strips) could compromise the mechanical stability of the suspended coupler. Furthermore, designs located in narrow zones between two Bragg regions can exhibit low tolerance to fabrication errors, as small variations in Λ or DC can translate into huge variations in the radiation angle or can push the working point into the Bragg regime, leading to excessive back-reflections and hence low coupling efficiency. With all of these considerations taken into account, seven regions of interest (ROIs) were designated and labeled with numbers (1–7). These ROIs can potentially contain the best possible designs. Note that most of these ROIs (3–7) do not meet single beam condition [123, 191, 192], and therefore they would not be evaluated following a conventional grating coupler design approach.

⁷Back-reflections of 30% can be suppressed by using simple adaptation sections, as will be shown later in this section.

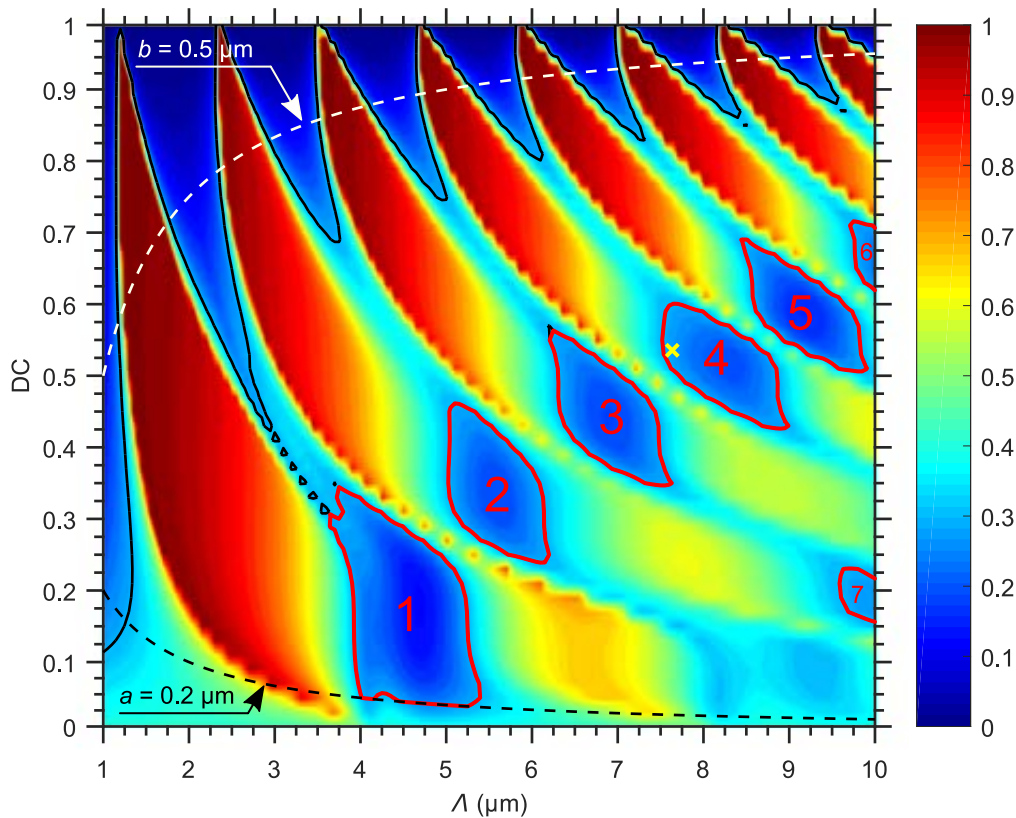


Figure 4.10: Simulated back-reflections as a function of the pitch (Λ) and duty cycle (DC). Areas with back-reflections smaller than 30% are delimited with solid lines. Unpractical zones due to fabrication restrictions are demarcated with dashed curves. Regions of interest (feasible gratings, exhibiting low back-reflections and operating far enough from Bragg regimes) are labeled with numbers and enclosed in red lines. Final design point, in ROI 4, is marked with a yellow cross.

The coupling efficiency and radiation angle were estimated exclusively for the reduced parameter space determined by the ROIs. For a mode field diameter of $13.56 \mu\text{m}$, the structures with highest CE values can be found in ROIs 3 (bottom part), 4, and 7, as shown in Fig. 4.11. Nonetheless, ROIs 3 and 7 were discarded, because their associated radiation angles are greater than the maximum value accepted by typical measurement set-ups, about 30° (see Fig. 4.11b). In ROI 4, the design with $\Lambda = 7.6 \mu\text{m}$ and $\text{DC} = 0.55$ was chosen, resulting in a coupling efficiency of 29% and a radiation angle of $\sim 9^\circ$. Despite its proximity to the ROI edge, this design is tolerant to fabrication imperfections, as reasonable errors of $\pm 150 \text{ nm}$ do not push the structure outside the ROI.

To reduce back-reflections, an adaptation section was introduced before the first radiative element, as schematized in Fig. 4.8. The lengths of the germanium strip ($a_{\text{ad}} = 200 \text{ nm}$) and the air trenches ($b_{\text{ad},1} = 400 \text{ nm}$ and $b_{\text{ad},2} = 0$) were chosen to minimize back-reflections down to $R < 0.2\%$ (around -30 dB). As a result of the enhanced matching between the waveguide and the grating region, the amount of power radiated upwards is increased, yielding a coupling efficiency of $\sim 40\%$.

The final geometric parameters are summarized in Table 4.2.

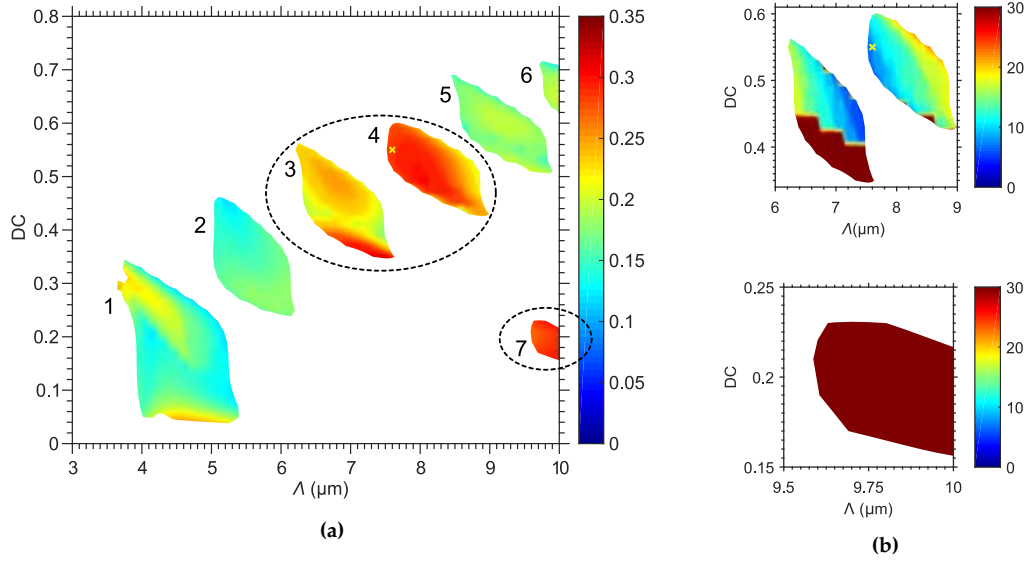


Figure 4.11: (a) Simulated coupling efficiency (CE) and (b) absolute value of the simulated radiation angle ($|\theta|$) as a function of the pitch (Λ) and duty cycle (DC) for designs contained in the ROIs delimited in Fig. 4.10. The final design point is marked with a yellow cross.

Table 4.2: Dimensions of the designed suspended germanium micro-antenna at $\lambda = 7.67 \mu\text{m}$.

H (μm)	a (μm)	b (μm)	a_{ad} (μm)	$b_{\text{ad},1}$ (μm)	$b_{\text{ad},2}$ (μm)
1.00	4.18	3.42	0.20	0.40	0.00

4.3.3 Discussion

Analysis of the Micro-antenna without Optical Fiber

The Bloch–Floquet effective index of the designed micro-antenna is $n_B = 2.18$, calculated with FEXEN. The corresponding k -diagram is represented in Fig. 4.12. Only two radiation orders are excited, $m = -2$ and $m = -3$, as condition (4.22) anticipated. By Eq. (4.14), the radiation angle associated to the $m = -2$ order is $\theta_{-2} = \arcsin(0.16) = 9.2^\circ$. Furthermore, the design is located in the fourth radiation zone (between the fourth- and fifth-order Bragg regimes). This is, as far as this author knows, the first time an efficient surface chip-fiber coupler is designed to operate with high-order diffraction beams in the fourth radiation zone.

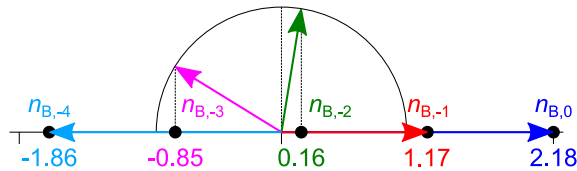


Figure 4.12: Normalized k -diagram of the proposed micro-antenna. The real part operator $\text{Re}(\cdot)$ is assumed implicit when the real part of the effective indices is written.

The micro-antenna, including its adaptation section and an input waveguide, is analyzed with 2D FDTD using RSoft FullWAVE. Figure 4.13a shows the simulated electric field distribution when the fundamental TE mode of the input waveguide is excited from the left. Because of the high radiation strength, most of the input power is radiated in the first radiative element and the wavefront is cylindrical instead of being flat. Although Fig. 4.12 indicates that the third ($m = -3$) order is also supported, only one radiated beam can be seen in Fig. 4.13a. The radiation angle, $\theta \sim 9^\circ$, is in good agreement with that predicted by Bloch–Floquet simulations.

The far-field radiation pattern of the micro-antenna, calculated with FullWAVE from a near-field cut 500 nm above the chip plane, is shown in Fig. 4.13b. The diagram reveals that two radiation orders are effectively supported, and one of them ($\theta = 8.6^\circ \sim \theta_{-2}$) noticeably prevails over the other ($\theta = -63.6^\circ$). The predominant radiation angle predicted by this far-field approximation confirms the inclination of the fiber estimated from the Bloch–Floquet analysis. Also, as a consequence of the strong exponential decay, the full width at half maximum of the fundamental beam is $\text{FWHM} \sim 25^\circ$, more than twice that of conventional grating couplers with comparable coupling efficiency in the NIR band [212].

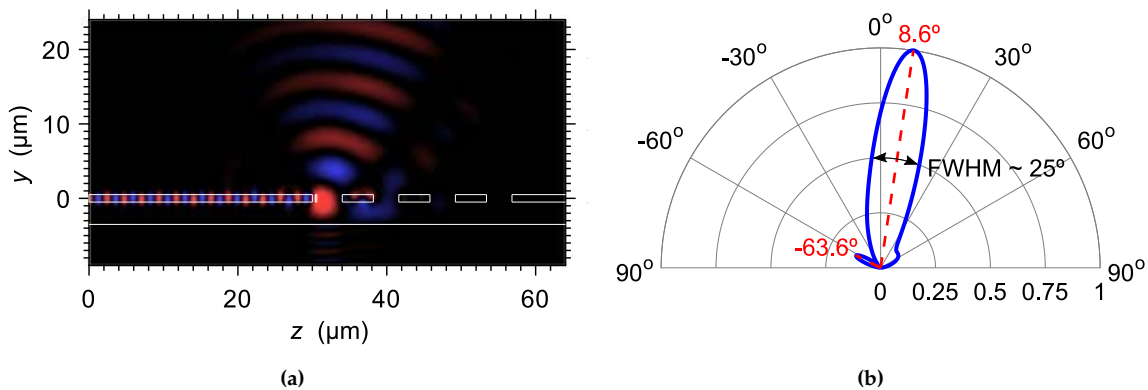


Figure 4.13: (a) 2D FDTD propagation of the electric field (TE polarization). In these simulations the optical fiber has not yet been included. The input waveguide, micro-antenna with three radiative elements, output waveguide and silicon substrate are outlined. Only one radiated beam is observable. (b) Far-field radiation pattern (normalized intensity) derived from a field cut 500 nm above the grating surface.

Analysis of the Micro-antenna with Optical Fiber

A 2D slab model of an IRFlex’s IRF-Se-12 optical fiber⁸ was introduced in the simulation window. The fiber was tilted $\theta_{\text{fiber}} = 9^\circ$ with respect to the vertical. The high refractive index of the fiber core produces reflections at the fiber facet. Note that these reflections would affect not only the proposed micro-antenna, but any fiber-chip coupler designed to operate with this optical fiber. To maximize the coupling efficiency, the height of the optical fiber above the chip must be chosen carefully. Figure 4.14 shows the simulated coupling efficiency as a function of the fiber distance d_{fiber} . A standing wave pattern is observed in the air gap between the micro-antenna and the fiber. The distance between

⁸Core diameter: $D_{\text{core}} = 12 \mu\text{m}$; cladding diameter: $D_{\text{clad}} = 170 \mu\text{m}$; core refractive index: $n_{\text{core}} = 2.7$; numerical aperture: $\text{NA} = 0.47$ [200].

maxima is approximately $\lambda/2 \sim 3.8 \mu\text{m}$. In practice, this separation provides enough margin to accurately align an optical fiber using nanopositioning stages. A fiber distance of $14.46 \mu\text{m}$ (central maximum in Fig. 4.14) was selected, because it is the minimum value of d_{fiber} that could be used maintaining clearance between the chip surface and the fiber cladding.

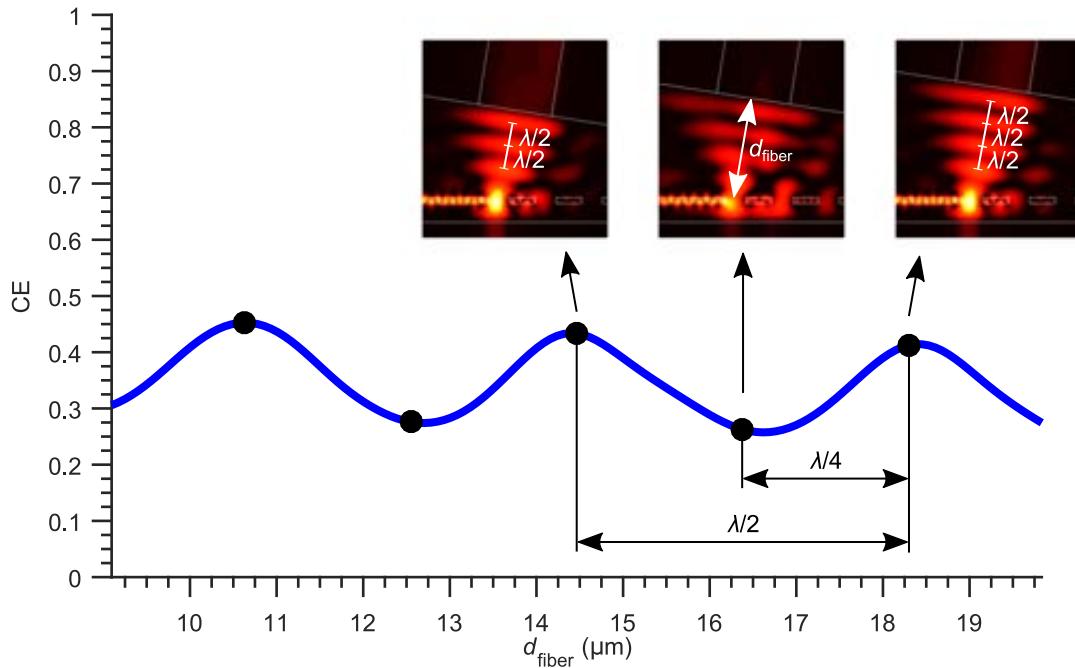


Figure 4.14: Simulated coupling efficiency as a function of distance d_{fiber} of the optical fiber with respect to the chip plane. A standing wave pattern is formed in the air gap between the grating and the fiber, with a difference between consecutive maxima or minima of half wavelength. Magnitudes of the electric field (TE polarization) are also included for several points.

Table 4.3 provides the coupling efficiency, back-reflections, and non-coupled transmitted power to the output waveguide for several micro-antennas with a different number (N) of diffractive elements. For each micro-antenna, these parameters are calculated with FullWAVE by monitoring the fields inside (i) the optical fiber, (ii) the input waveguide, and (iii) the output waveguide, and by computing the overlap of such fields with the modes of the corresponding structures. The 2D FDTD field distribution of each micro-antenna is shown in Fig. 4.15. As transmitted power (T) drops from 32.6% ($N = 1$) to 2.4% ($N = 2$), it is apparent that most of the power is radiated in the first two radiative elements, the first one being the strongest. For $N > 2$, micro-antenna performances are virtually indistinguishable. From now on, three radiative elements ($N = 3$) are chosen. The simulated coupling efficiency is $\text{CE} = 43\%$, in good agreement with the value estimated without the optical fiber during the design process. Reflections at the input waveguide are $R < 5\%$, higher than those initially designed because of the reflections at the air-fiber interface.

Table 4.3: Simulated coupling efficiency (CE), back-reflections (R) and transmitted power to the output waveguide (T) for the designed micro-antenna as a function of the number of diffractive elements (N).

N	CE (%)	R (%)	T (%)
1	16	0.31	32.59
2	40	4.10	2.40
3	43	4.65	0.48
4	43	4.54	0.14

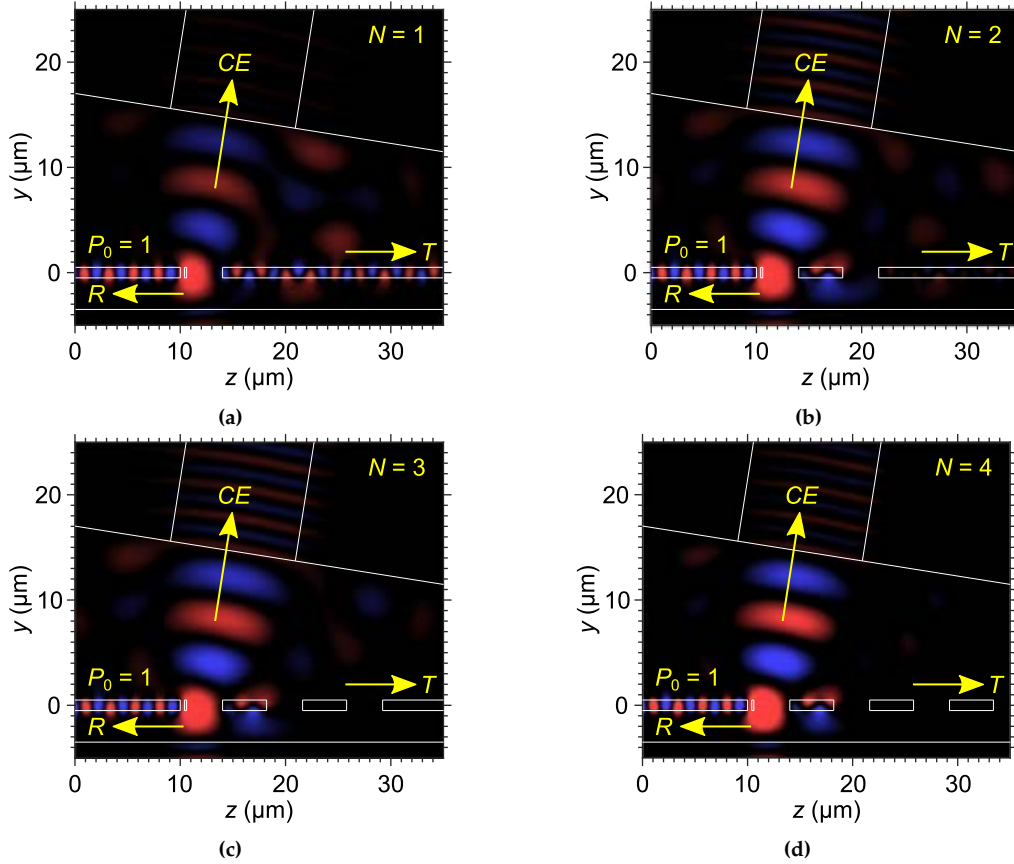


Figure 4.15: Influence of the number of periods N on the radiation of the micro-antenna. 2D FDTD propagations of the electric field (TE polarization) are calculated with the fiber included in the simulation window. Device geometry and optical fiber are outlined.

The coupling efficiency as a function of the wavelength is shown in Fig. 4.16a (blue line). The simulation of the reciprocal case, i.e., coupling light from the fiber into the chip, resulted in the same efficiency in virtue of the reciprocity principle [213]. A 1-dB bandwidth of 465 nm is achieved. This corresponds to a fractional bandwidth ($BW_{1\text{dB}}/\lambda$) of 6.06%, which is almost twice the ratio of standard grating couplers at $\lambda = 1.55 \mu\text{m}$ ($BW_{1\text{dB}}/\lambda = 3.23\%$ assuming $BW_{1\text{dB}} = 50 \text{ nm}$) [208]. Such a broad bandwidth was anticipated because the micro-antenna has been designed to efficiently couple light to an optical fiber with reduced core width and large numerical aperture [208, 209]. Additionally, Fig. 4.16b represents the coupling efficiency as a function of the fiber angle misalignments ($\Delta\theta_{\text{fiber}} = \theta_{\text{fiber}} - 9^\circ$). The coupling efficiency is very tolerant to fiber tilt, with a 1-dB an-

angular bandwidth of 19.3° (about $\pm 10^\circ$ with respect to the nominal tilt angle of 9°), which approximately constitutes a threefold enhancement compared to the angular bandwidth of conventional grating couplers in the NIR (around $\pm 3^\circ$) [214]. This improvement arises from the broad angular width of the outgoing beam (see Fig. 4.13b) and is consistent with the broad 1-dB bandwidth of Fig. 4.16a.

The proposed micro-antenna is very robust against fabrication errors. Figure 4.16a shows the calculated coupling efficiency when a deviation $\Delta = \pm 150$ nm is introduced in the length of the germanium segments a and a_{ad} (see Fig. 4.8). The penalty in coupling efficiency, maintaining the same fiber tilt angle of the nominal case (i.e., 9°), is less than 10% at the central wavelength. The rationale of this small penalty is that the absolute error $\Delta = \pm 150$ nm (a typical value for the fabrication process of suspended structures) corresponds to a relative error $\Delta DC \sim 2\%$ as a consequence of the large pitch.

Finally, 3D FDTD simulations are carried out to double-check the design. The width of the micro-antenna, which was not needed for the 2D approximation, was chosen to maximize the overlap between the radiated field and the optical fiber mode in the fiber facet plane, resulting in $W_g \sim 20$ μm . Figure 4.16a (blue dashed line) depicts the coupling efficiency as a function of the wavelength, yielding $CE = 39.6\%$ and $BW_{1\text{dB}} = 436$ nm. Figure 4.16b shows an angular bandwidth of 19.6° . These results agree well with the 2D simulations.

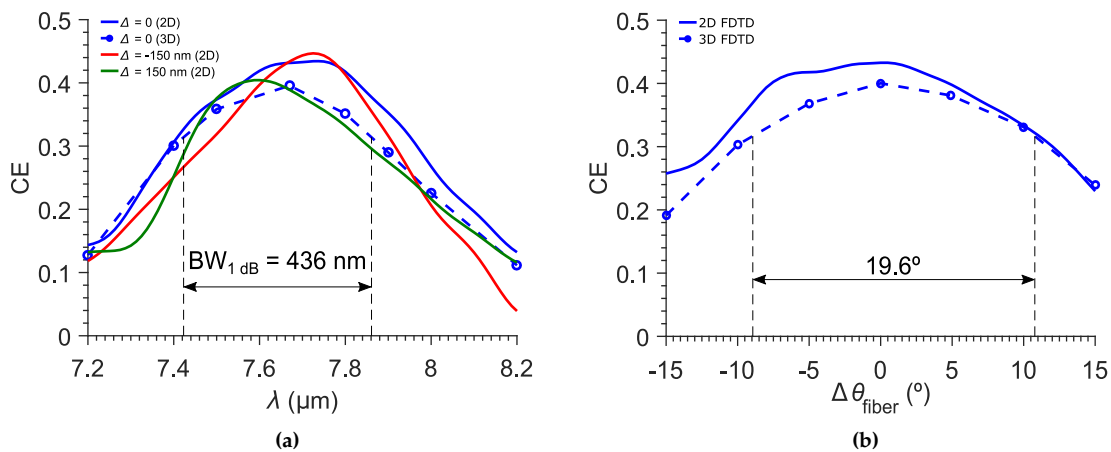


Figure 4.16: (a) Simulated coupling efficiency as a function of the wavelength when dimension errors $\Delta = 0$ (blue line), 150 nm (green line) and -150 nm (red line) affect the length of the germanium strips of the structure. 3D FDTD simulation results are also included (blue dashed line) for the nominal design. The radiation angle is 9° in all cases. (b) Simulated coupling efficiency as a function of fiber tilt misaligned angle.

4.3.4 Fabrication and Characterization

Straight and focusing micro-antennas were fabricated for the suspended germanium platform at 7.67 μm . Straight micro-antennas were accessed via three-step tapers with a total length of 25 μm . Focusing micro-antennas were designed from the straight version by applying the equations in [205]. More than three diffractive elements were added to guarantee that back-reflections were minimum, although the structure should work with only two or three periods. To increase the mechanical stability, the cladding was not etched. As most of the power is diffracted at the beginning of the structure, the lack of

lateral index contrast should not affect the light propagation and radiation, which was checked via 3D FDTD simulation.

SEM images of the fabricated micro-antenna are shown in Fig. 4.17. In some cases, the adaptation tooth was broken (see Fig. 4.18). As a result, back-reflections would increase up to $\sim 30\%$. These higher back-reflections can produce Fabry-Pérot fringes in the measured power transmission.

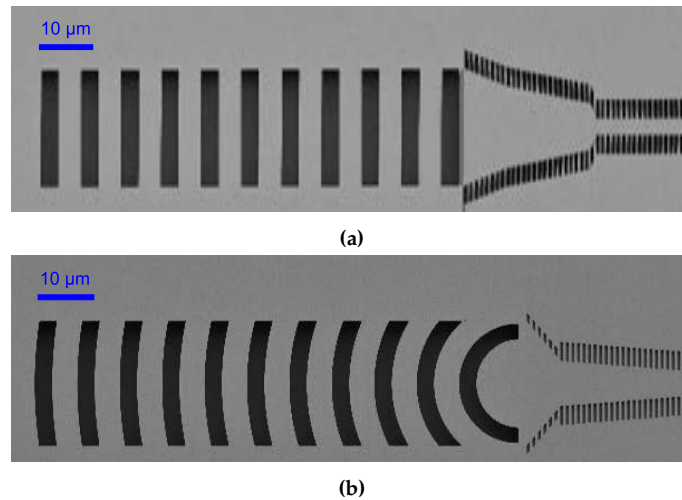


Figure 4.17: SEM images of the fabricated (a) straight and (b) focusing suspended germanium micro-antennas.

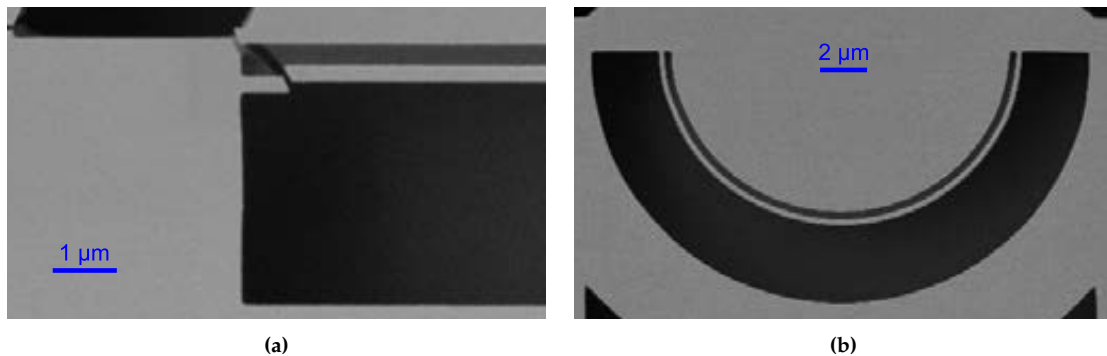


Figure 4.18: Zoom of the adaptation section of the fabricated (a) straight and (b) focusing suspended germanium micro-antennas.

It was not possible to experimentally determine the coupling efficiency of the micro-antenna because the loss of the measurement setup of the ORC's MIR laboratory was not characterized. However, the fiber tilt tolerance was studied. For an input optical fiber with a tilt angle of $\sim 10^\circ$, the tilt angle of the output fiber was scanned manually. Figure 4.19 shows the measured voltage at the output of the photodetector. The micro-antenna couples an indefinite, but high enough, amount of power regardless of the angle. This result confirms the considerably broad angular bandwidth predicted by the simulations.

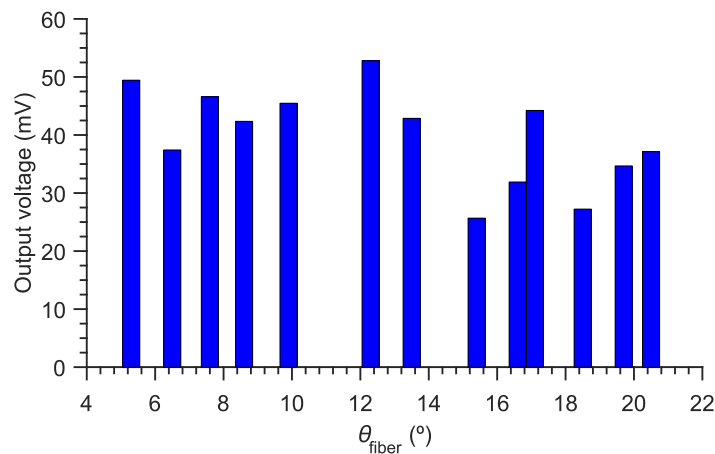


Figure 4.19: Measured power as a function of the fiber tilt angle. Light was coupled into/out of a suspended germanium waveguide using input and output micro-antennas. The tilt angle of the input waveguide was fixed to $\sim 10^\circ$, while the tilt angle of the output waveguide was changed.

4.4 Zero-Order Grating Coupler

4.4.1 Motivation

Although this thesis is focused on the MIR band, the zero-order grating coupler (ZGC) was initially designed at $\lambda = 1.55 \mu\text{m}$ to facilitate the fabrication and characterization of the device. The design was started at UMA and finished in the NRC, where the experimental demonstration is being carried out at the time of writing by researchers from this center. Later in this section, the ZGC concept is migrated to $\lambda = 3.8 \mu\text{m}$. The ZGC concept was presented for the first time in [82].

In the NIR band, the efficiency of SOI-based surface grating couplers has been enhanced using several techniques, e.g., mitigating back-reflections [202–204], maximizing the directionality [193,215], or optimizing the overlap between the radiated field and the near-Gaussian fiber mode [185]. In [194], a sub-decibel grating coupler was reported that, making use of a bottom mirror and a SWG structure, achieves an excellent experimental coupling efficiency of 85.7% (-0.67 dB) and a 1-dB bandwidth of 22 nm. A grating with a simulated coupling efficiency of 89% (-0.51 dB) and a 1-dB bandwidth of 33 nm was reported in [186]. Blazed grating couplers with asymmetric teeth shape have been utilized to maximize the directionality and hence the coupling efficiency [195–197, 216, 217]. To increase the bandwidth of grating couplers, some encouraging results have been demonstrated, but at the expense of the coupling efficiency. For instance, in [218] a triangular SWG structure is utilized to achieve a large simulated 1-dB bandwidth of 290 nm, but its coupling efficiency is moderate (-2.18 dB) and requires the use of a non-standard BOX thickness. In [204], SWG engineering is used to increase the coupler bandwidth while minimizing back reflections, achieving a 1-dB bandwidth of 90 nm with a coupling efficiency of -3.8 dB .

ZGCs are fiber-chip surface couplers designed to simultaneously maximize both coupling efficiency and bandwidth. These characteristics are not only useful in the NIR, but also for sensing in the MIR band, since broadband couplers with good efficiency can be needed, for example, to measure the transmission spectra of substances in a wide range of wavelengths.

4.4.2 Geometry

A ZGC is schematically shown in Fig. 4.20. For the initial design in the NIR range, the ZGC is based on a SOI wafer with 220-nm-thick silicon guiding layer and 3- μm -thick BOX. The dimensions of the grating (a and b , or Λ and DC) are the same as in conventional surface grating couplers. An input taper section (not shown in the figure) is used to laterally expand the silicon wire mode to the wider SWG radiating region. A silicon prism, with angle ϕ_{prism} , is placed on top of the structure. The prism can be taped by an optical epoxy that also acts as the upper cladding ($n_e = 1.50$, [219]), or can be attached using nanopositioning stages ($n_e = 1$, air). The cladding layer has a linearly varying thickness, starting from $t_{\text{clad},0}$ at the beginning of the grating and vanishing at its end. A quarter-wave anti-reflection (AR) coating is included on the upper surface of the prism to avoid reflections at the silicon-air interface. An SMF-28 optical fiber with a mode field diameter of 10.4 μm is positioned perpendicularly to the upper surface of the prism [201].

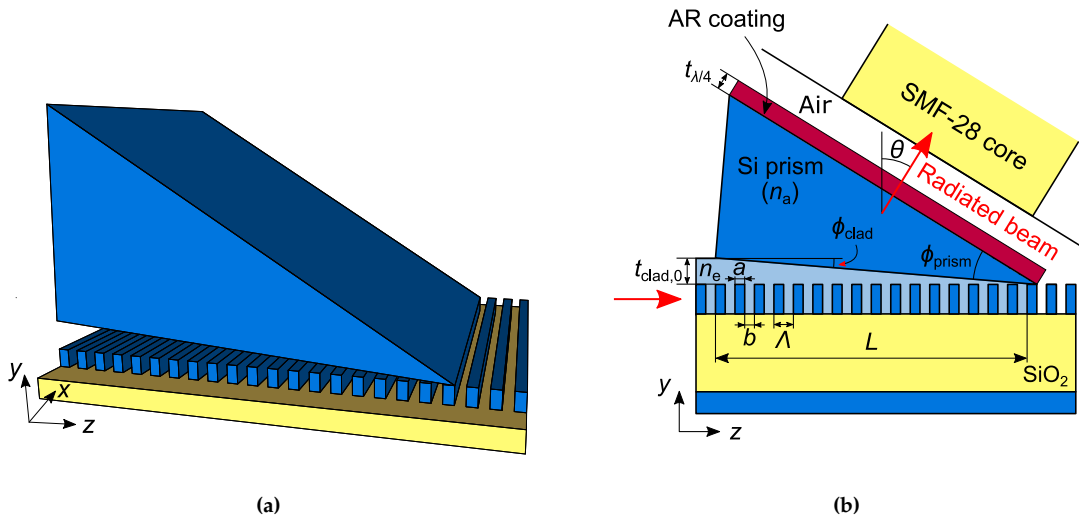


Figure 4.20: Schematic representation (not to scale) of a zero-order grating coupler. (a) 3D view. (b) Side view. In the 3D view, the upper cladding (refractive index n_e in the side view) is transparent for visualization simplicity.

4.4.3 Working Principle

As mentioned in Section 4.1.2, the bandwidth limitation of surface grating couplers primarily arises from the variation of the radiation angle with the wavelength [204, 207]. From Eq. (4.14), it follows that, for $m = 0$, the wavelength dependence is eliminated (apart from the effect of the refractive index dispersion), and Eq. (4.14) becomes

$$n_a \sin(\theta_0) = \text{Re}(n_B). \quad (4.23)$$

This relation governs the radiation angle dependence of a zero-order ($m = 0$) surface grating coupler. To make the grating radiate the zeroth order, the steps schematized in Fig. 4.21 are followed:

- (i) *SWG operation.* The grating period Λ is chosen so that the structure operates in the SWG regime. Then, the waveguide core effectively behaves as a homogeneous

equivalent medium with a refractive index (n_{SWG}) determined by the grating pitch and duty cycle. In this case, no order fulfills Eq. (4.14), and the propagating wave is not diffracted.

- (ii) *Zero-order radiation.* A high-index material is placed on top of the grating making $n_a > \text{Re}(n_B)$. In this situation, the zeroth order propagates from the waveguide to the superstrate, with a radiation angle given by Eq. (4.23).

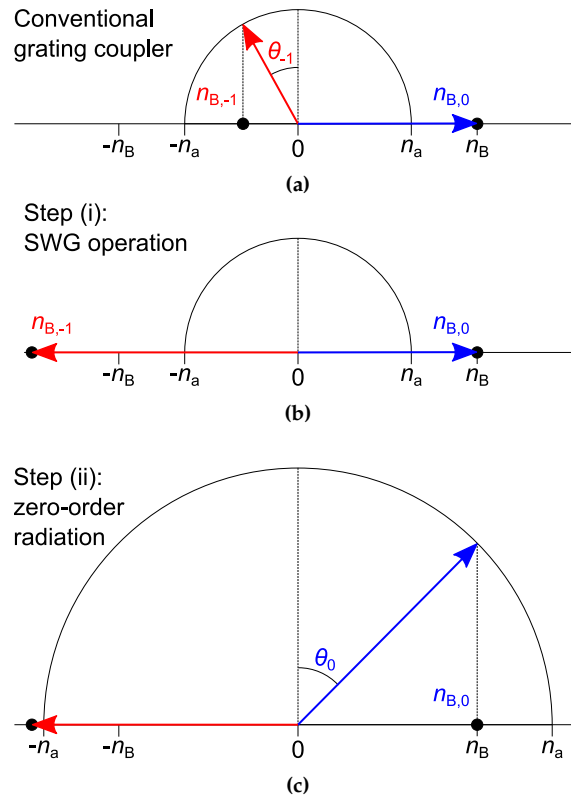


Figure 4.21: Working principle of a zero-order grating coupler. (a) Normalized k -diagram of a conventional grating coupler with $m = -1$ radiation. (b) Normalized k -diagram of a SWG waveguide. All radiation orders are frustrated. (c) Normalized k -diagram of a zero-order grating coupler. By increasing the upper material refractive index, the zeroth order is diffracted. The real part operator $\text{Re}(\cdot)$ is assumed implicit when the real part of the effective indices is written.

The ZGC is assisted by a prism and can be described by the formulation originally developed in [181, 182, 220] for conventional prism-film couplers. However, unlike the latter, ZGCs enable index engineering to enlarge the operation bandwidth.

4.4.4 Design of a Longitudinal Zero-Order Grating Coupler

The design of a ZGC at a wavelength of $1.55 \mu\text{m}$ is described in this section. The goal is to simultaneously maximize the 1-dB bandwidth and the coupling efficiency.

In order to define a design strategy, the ZGC is modeled as the 2D slab waveguide illustrated in Fig. 4.22. The structure is composed of four layers, which account for the prism, the epoxy gel ($n_e = 1.5$),⁹ the SWG core, and the BOX. The SWG core is replaced by

⁹The ZGC could be designed with an air gap ($n_e = 1$) instead.

a homogeneous isotropic medium with equivalent refractive index n_{SWG} . Note that the wavelength dependence of n_{SWG} is not taken into account in this model (i.e., $\partial n_{\text{SWG}}/\partial\lambda = 0$).

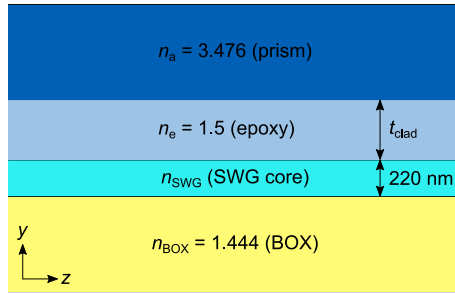


Figure 4.22: 2D slab model of a zero-order grating coupler.

The effective index of the fundamental mode of the equivalent slab waveguide is calculated for different cladding thicknesses t_{clad} and equivalent refractive indices n_{SWG} . The real part of the effective index is related to the radiation angle through Eq. (4.23). The imaginary part governs the radiation strength of the coupler, which, in turn, determines the radiated field matching with the optical fiber mode. Figure 4.23 shows the variation of the radiation angle and the radiation strength as a function of t_{clad} for several n_{SWG} values.

The radiation angle depends strongly on n_{SWG} , while its variation with t_{clad} is comparatively smaller. On the other hand, the radiation strength is almost independent on n_{SWG} , but changes noticeably with t_{clad} . Consequently, the design can be accomplished in two almost decoupled steps: (i) an optimal n_{SWG} can be chosen to achieve broad bandwidth; (ii) t_{clad} can be adjusted to match the radiated field to the Gaussian-like profile of the SMF-28 optical fiber, thereby increasing the coupling efficiency.

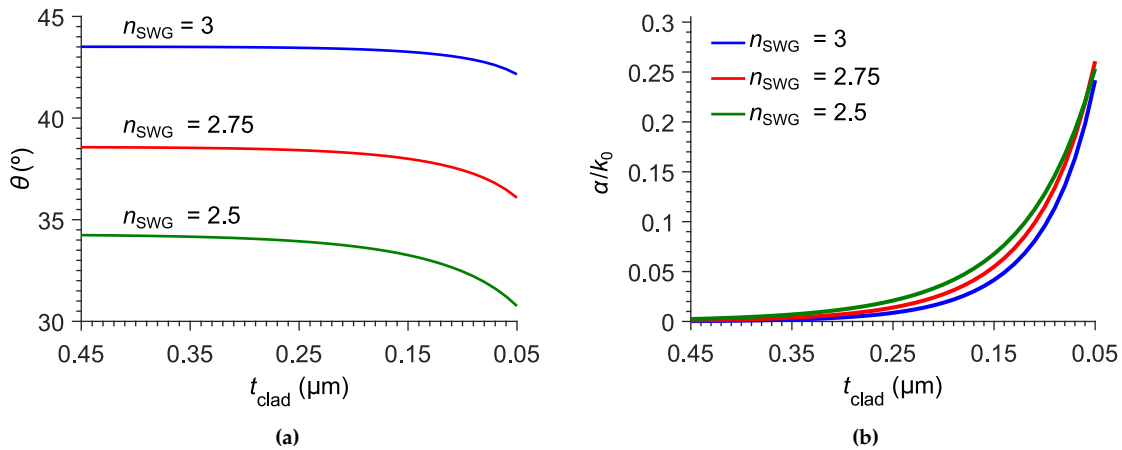


Figure 4.23: (a) Real part (radiation angle) and (b) imaginary part of the effective index of the fundamental mode supported by the zero-order grating coupler (slab model in Fig. 4.22) as a function of the cladding thickness and the equivalent refractive index of the waveguide core.

Bandwidth Enhancement

The bandwidth of a grating coupler is proportional to $|\partial\lambda/\partial\theta|$ (see *Bandwidth* in Section 4.1.3) [204]. While the bandwidth of a ZGC is inherently broader than that of a conventional grating coupler, it can be further enlarged by leveraging the subwavelength nature of the ZGC core. From Eq. (4.20) and making $m = 0$,

$$\text{BW}_{1\text{ dB}} \propto \left| \frac{\partial\lambda}{\partial\theta} \right| = \underbrace{\frac{1}{\tan(\theta)}}_{\text{Factor A}} \cdot \underbrace{\frac{1}{\left[\frac{1}{\text{Re}(n_B)} \frac{\partial \text{Re}(n_B)}{\partial\lambda} - \frac{1}{n_a} \frac{\partial n_a}{\partial\lambda} \right]}}_{\text{Factor B}}. \quad (4.24)$$

Figure 4.24a shows the variation of $|\partial\lambda/\partial\theta|$ with n_{SWG} , as well as the factors A and B, for the slab waveguide model with a cladding thickness t_{clad} of 250 nm, an epoxy refractive index n_e of 1.5, and a silicon prism ($n_a = 3.476$), at a nominal wavelength of 1.55 μm . For a given upper material (e.g., silicon), Factor A is increased for low n_{SWG} values (low radiation angles), while Factor B is increased as the wavelength dispersion of the effective index of the propagating mode decreases. As shown in Fig. 4.24a, low n_{SWG} are required to maximize the product of both factors and hence the bandwidth, which can be achieved by reducing the duty cycle of the ZGC core. These conclusions assume that $\partial n_{\text{SWG}}/\partial\lambda = 0$, which is valid only for the slab model.

However, $\partial n_{\text{SWG}}/\partial\lambda \neq 0$ in actual SWGs. Because $\partial n_{\text{SWG}}/\partial\lambda$ affects $\partial \text{Re}(n_B)/\partial\lambda$, low SWG dispersion (ideally zero) is desired. To illustrate the dispersion effect, an SWG stratified medium composed of two transversally infinite layers of silicon and epoxy (see the inset in Fig. 4.24b) is analyzed at $\lambda = 1.55 \mu\text{m}$. Figure 4.24b shows the wavelength dispersion of the synthesized refractive index n_{SWG} as a function of the pitch Λ for a fixed minimum feature size (MFS) of 100 nm. While the SWG material is virtually non-dispersive for short periods, the wavelength dependence substantially grows as the wave propagating through the structure approaches the photonic bandgap ($\Lambda \rightarrow \Lambda_{\text{Bragg}}$). For this reason, the practical values of Λ in a ZGC are limited by the intrinsic wavelength dispersion of the SWG core, which was not considered in the slab model. Therefore, the conclusions drawn from Fig. 4.24a are only valid for low Λ values.

Thus, the bandwidth of a ZGC can be improved by using low duty cycles and small periods. For a given MFS, the lowest feasible duty cycle is $\text{DC} = \text{MFS}/\Lambda$, with $\Lambda \geq 2 \cdot \text{MFS}$. As short pitches are preferred, in practice making $\Lambda = 2 \cdot \text{MFS}$ and $\text{DC} = 0.5$ is the best choice for bandwidth enhancement.

For a typical minimum feature size of 100 nm, the SWG waveguide core has $a = 100 \text{ nm}$ and $b = 100 \text{ nm}$ ($\Lambda = 200 \text{ nm}$, $\text{DC} = 0.5$), which corresponds to $n_{\text{SWG}} \sim 2.75$.

Coupling Efficiency Optimization

Once the bandwidth is enlarged, the coupling efficiency is optimized. Since virtually no power is radiated toward the substrate, $D \sim 1$. Using an appropriate injection stage (i.e., adiabatic taper to convert the narrow input waveguide into a wide SWG), back-reflections can be minimized ($R \sim 0$). Hence, the coupling efficiency practically corresponds to the overlap between the radiated field and the mode field of the optical fiber ($\text{CE} \sim \text{OL}$).

The cladding layer is apodized to increase the overlap. From prism-film coupling theory [183], it is known that a theoretical coupling efficiency up to $\sim 96\%$ can be achieved

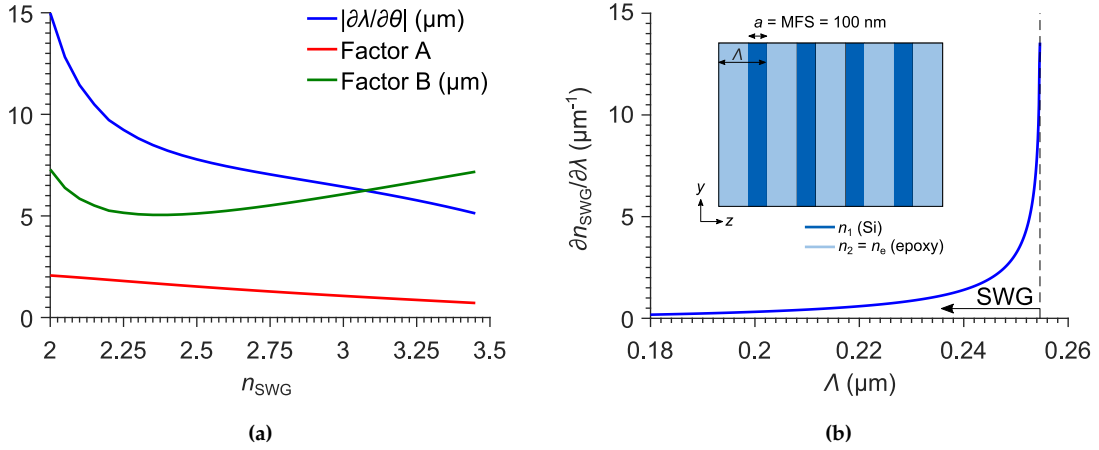


Figure 4.24: (a) Angle sensitivity of the slab model of the zero-order grating coupler, which does not include SWG dispersion effects. (b) SWG dispersion of the laminar periodic structure shown in the inset as a function of the pitch when the length of the silicon layers is fixed to the minimum feature size (at $\lambda = 1.55 \mu\text{m}$).

by linearly tapering the cladding thickness:

$$t_{\text{clad}}(z) = \frac{t_{\text{clad},L} - t_{\text{clad},0}}{L}z + t_{\text{clad},0}, \quad (4.25)$$

where $t_{\text{clad},L}$ and $t_{\text{clad},0}$ are the cladding thicknesses at the beginning and the end of the grating waveguide, respectively. For simplicity, $t_{\text{clad},L}$ is set to 0. Since the radiation angle is primarily determined by n_{SWG} (see Fig. 4.23), the bandwidth is minimally affected by the cladding apodization.

For a specific platform, the radiated field profile depends on the initial cladding thickness $t_{\text{clad},0}$ and the coupling length L . Both parameters are firstly scanned for a ZGC with an equivalent refractive index n_{SWG} . Once the design is complete, the homogenized waveguide core is replaced by the actual SWG structure and simulated with FEXEN.

Using this design approach, an optimum overlap of $\sim 95\%$ was achieved for $L = 20.3 \mu\text{m}$ and $t_{\text{clad},0} = 355 \text{ nm}$. Those values correspond to a cladding inclination of $\phi_{\text{clad}} = \tan(t_{\text{clad},0}/L) = 1^\circ$. The radiation angle is $\theta = 39.3^\circ$.

Results

Figure 4.25a shows the coupling efficiency of the ZGC simulated with FEXEN. The design is then verified with 2D FDTD simulation using RSoft FullWAVE, including the effect of the silicon prism, the anti-reflection (AR) coating, and the optical fiber. The calculated back-reflection is 3.3%, primarily due to Fresnel loss at the fiber facet. The quarter-wave AR layer (refractive index: $n_{\lambda/4} = \sqrt{3.476} = 1.864$; thickness: $t_{\lambda/4} = 0.208 \mu\text{m}$) was located on the prism surface facing the fiber. The fiber was nominally separated from the prism surface by a 10- μm air gap. The prism angle was $\phi_{\text{prism}} = 38.3^\circ$. This apodized design yields a coupling efficiency of $\sim 91\%$ at the nominal wavelength of $1.55 \mu\text{m}$ and a 1-dB bandwidth of 126 nm. The simulated electric field propagation (TE polarization) in the complete structure is shown in Fig. 4.25b.

For comparison purposes, a non-apodized ZGC was also designed with a cladding thickness of 200 nm, achieving a coupling efficiency higher than 75% and a 1-dB bandwidth of $\sim 130 \text{ nm}$ (see Fig. 4.25a). While the coupling efficiency is noticeably improved

by cladding apodization, the bandwidth is only marginally affected, in good agreement with the modal analysis in Fig. 4.23.

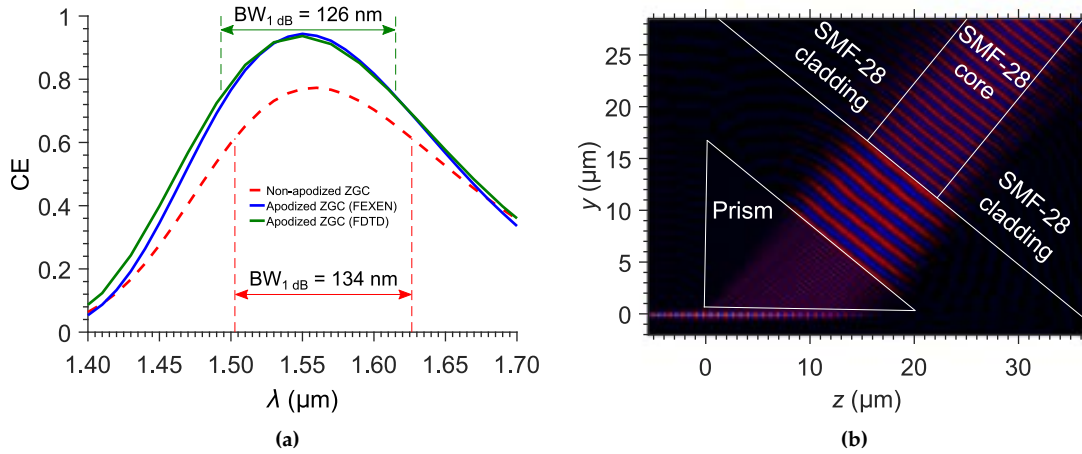


Figure 4.25: (a) Calculated fiber-chip coupling efficiency as a function of wavelength for the designed zero-order grating couplers. (b) Simulated (FDTD) field propagation of the TE-polarized wave through the zero-order grating coupler at $\lambda = 1.55\ \mu\text{m}$.

Finally, the ZGC was redesigned to substitute the epoxy cladding with air ($n_e = 1$). To maintain approximately the same performance as with $n_e = 1.5$, the prism angle was simply readjusted to $\phi_{\text{prism}} = 35.67^\circ$.

Access Taper

To complete the analysis, a lateral taper to connect the narrow single-mode input photonic wire with the wider SWG waveguide of the ZGC was studied. In this section, the adiabatic taper that was originally designed is detailed, as reported in [82].

The proposed taper is composed of two parts (see Fig. 4.26):

- (i) A linear transition to transform the input silicon wire into a SWG waveguide, while increasing the waveguide width from the initial width $W = 500\text{ nm}$ to $W_{\text{int}} = 6\ \mu\text{m}$.
- (ii) A linear periodic taper to achieve the final waveguide width W_g of $\sim 15\ \mu\text{m}$. This width corresponds to the maximum overlap (99%) between the lateral (x direction) of the fundamental Bloch–Floquet mode of the grating waveguide and the optical fiber mode.

For the taper, the SWG pitch of 200 nm is always below the Bragg threshold [see Eq. (4.15)] along the propagation direction. The taper lengths ($L_{\text{taper},1} = 60\ \mu\text{m}$ and $L_{\text{taper},2} = 120\ \mu\text{m}$) assure the structure operates in the adiabatic regime.

4.4.5 Design of a Transverse Zero-Order Grating Coupler

As shown in the previous section, low synthesized refractive indices n_{SWG} improve the ZGC bandwidth. Since the lowest n_{SWG} values can be achieved by using a transverse (x -periodic) SWG configuration, a transverse ZGC also was designed.

Figure 4.27a shows a 3D schematic of this device. In this case, n_{SWG} is calculated with RSoft FemSIM as the refractive index of the homogeneous waveguide that supports a

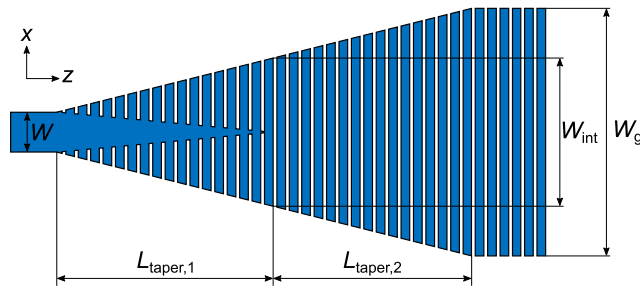


Figure 4.26: Schematic representation of a longitudinal access taper (not to scale) used for longitudinal zero-order grating couplers.

guided mode whose effective index coincides with the effective index of the mode of the actual SWG. The chosen n_{SWG} value was 2 at $\lambda = 1.55 \mu\text{m}$. Lower values are not allowed because the fundamental mode is weakly guided, hence increasing substrate leakage loss [221]. In order to avoid the need for 3D simulations of the periodic structure, which are time-consuming because of the prism, the SWG dispersion was taken into account when calculating n_{SWG} .

Assuming an air cladding, a coupling efficiency of 85% and a 1-dB bandwidth of 139 nm was achieved for $t_{\text{clad},0} = 370 \text{ nm}$ and $L = 14.5 \mu\text{m}$. The transverse SWG core comprises strips of 206 nm and trenches of 100 nm.

To adapt the fundamental mode of the input waveguide to the fundamental mode of the transverse SWG structure, the taper shown in Fig. 4.27b was designed using FDTD simulations. A first transition of length $L_{\text{taper},1} = 40 \mu\text{m}$ converts the input homogeneous waveguide into a 2D SWG grating of intermediate width $W_{\text{int}} = 5 \mu\text{m}$. A length $L_{\text{taper},2} = 90 \mu\text{m}$ is chosen to adiabatically achieve the final width.

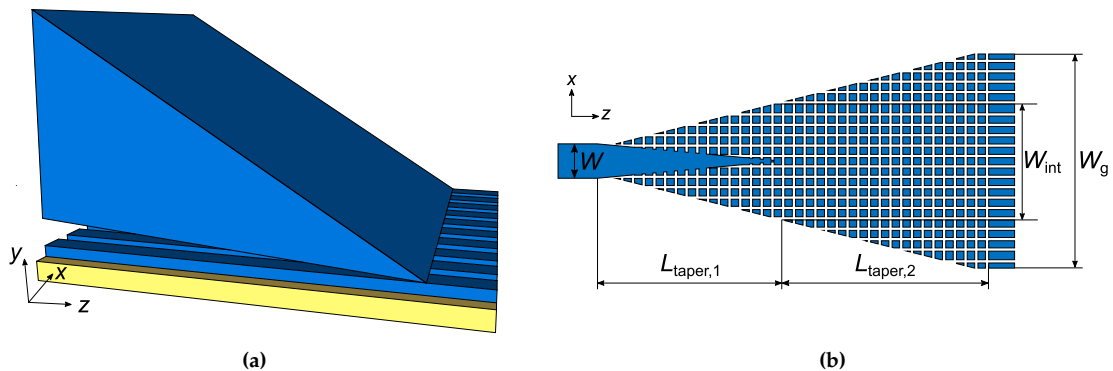


Figure 4.27: (a) Schematic representation of a transverse zero-order grating coupler and (b) access taper. The schematics are not to scale.

4.4.6 Fabrication and Characterization

At the time of writing, the coupling efficiency of the ZGCs has not yet been estimated and only preliminary results are available. In this section, a summary of the efforts that have been devoted to the demonstration of this structure is presented.

Before carrying out the fabrication of the structures, one crucial choice was made: the silicon prism would not be taped to the chip surface. Instead, it would either be held with

a special holder or taped to the fiber tip. This decision had four important advantages for characterization purposes:

- (i) No adhesive bonding should be applied. Thus, only designs with $n_e = 1$ would be fabricated.
- (ii) The prism could be removed when off-chip coupling is not required.
- (iii) One single prism could be used to test many ZGC variations.
- (iv) Fresnel reflections at the prism-fiber can be negligible if an appropriate AR coating is deposited. Hence, the prism-air AR coating should be replaced by a prism-fiber AR coating.

The masks were drawn using Autodesk's AutoCAD. To generate variations in the geometry of the gratings, a library of Visual Basic functions, which had been developed by researchers from UMA, was used. Sets of waveguides of different lengths and series of tapers in back-to-back configuration were included in the mask to measure the propagation and insertion losses, respectively, using conventional grating couplers or direct butt-coupling to access the chips. After characterizing the waveguides and tapers, the performance of the ZGCs can be calculated by measuring their response.

Several samples for testing longitudinal and transverse ZGCs were fabricated in 220-nm SOI wafers with 3- μm -thick BOX. The first samples were patterned in the e-beam facilities of the University of Waterloo [222], and then etched and diced in the NRC. Subsequent samples were patterned and etched at University of Washington [223], then diced in the NRC.

The measured losses of the tapers were $\sim 1.5 \text{ dB taper}^{-1}$ for the longitudinal version and $\sim 5 \text{ dB taper}^{-1}$ for the transverse version. These values are attributed to the disorders effects (jitter) in the SWG patterns [224]. To reduce these high losses, a second taper configuration with reduced SWG area was proposed, as illustrated in Fig. 4.28. In this new case, the geometry is the following:

- (i) A homogeneous linear taper ($L_{\text{taper}} = 200 \mu\text{m}$) widens the interconnecting waveguide from 500 nm to 15 μm .
- (ii) A short adaptation section ($L_{\text{adapt}} = 3 \mu\text{m}$) converts the fundamental mode at the output of the taper into the fundamental mode of the SWG.

In the best case, the taper designed for the longitudinal ZGC exhibited a measured insertion loss of $\sim 0.5 \text{ dB taper}^{-1}$. A SEM image of one of these tapers is shown in Fig. 4.29.

By the time this thesis was written, the experimental ZGC performance has not yet been estimated, but the measurements are in progress.

4.4.7 Migration to the Mid-Infrared Band

The broad bandwidths of ZGCs are of great interest in the MIR band. A longitudinal ZGC was designed for a 500-nm-thick SOI platform at $\lambda = 3.8 \mu\text{m}$. At this wavelength, silicon dioxide loss is not too high and BOX removal of the grating couplers is not worth it.

The dimensions of the MIR ZGC are given in Table 4.4. Figure 4.30 shows the simulated coupling efficiency as a function of the wavelength. A coupling efficiency of $\sim 95\%$

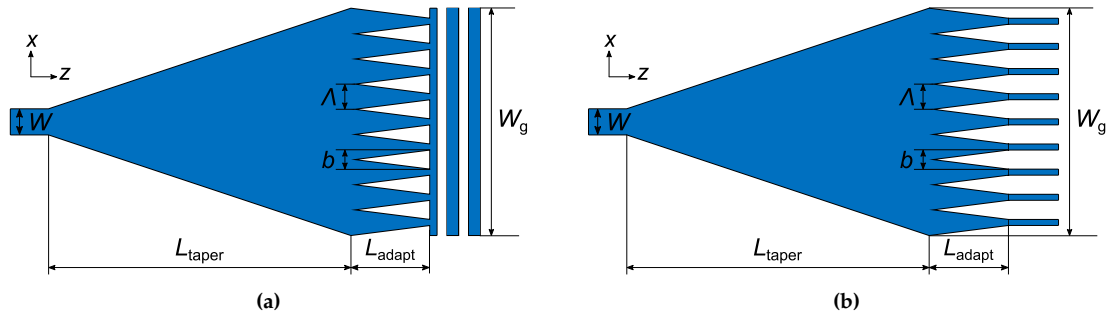


Figure 4.28: Schematic representation (not to scale) of the second-type tapers designed for (a) longitudinal and (b) transverse zero-order grating couplers.

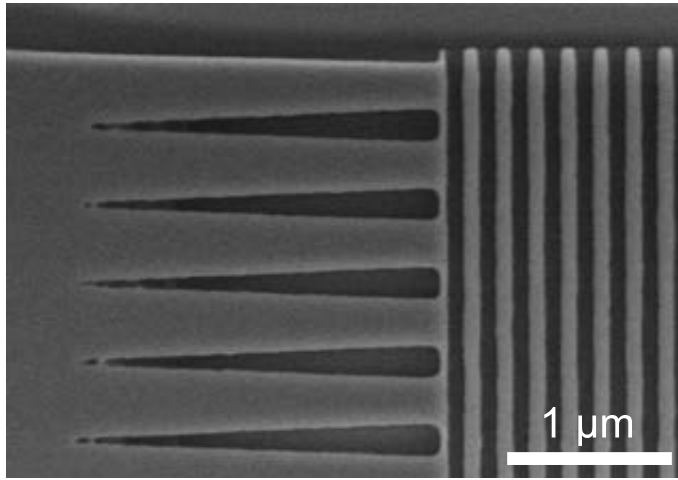


Figure 4.29: SEM image of the adaptation section of the longitudinal access taper (second type) that is used to transform the input, narrow silicon wire into a wide SWG. A part of the grating also is included in the image.

is predicted at the central wavelength, with a 1-dB bandwidth of 564 nm. This value corresponds to a fractional bandwidth of $\sim 14.8\%$, which constitutes an improvement of ~ 1.8 over the longitudinal NIR ZGC. The bandwidth enhancement is mainly due to the small $\overline{\text{MFD}}$ (MFD-to-wavelength ratio) of the optical fiber, which is $\overline{\text{MFD}} \sim 11.4$ at $\lambda = 3.8 \mu\text{m}$, and $\overline{\text{MFD}} \sim 6.7$ at $\lambda = 1.55 \mu\text{m}$, i.e., $11.4/6.7 \sim 1.7$. Since both the NIR ZGC and the MIR ZGC operate in the deep SWG regime (i.e., low SWG dispersion), the fractional bandwidth of the MIR ZGC is only marginally broadened with respect to the NIR design despite the reduced Λ/λ ratio.

Table 4.4: Dimensions of the designed longitudinal zero-order grating couplers at a wavelength of $3.8 \mu\text{m}$.

$t_{\text{clad},0}$ (μm)	L (μm)	a (μm)	b (μm)	ϕ_{prism} ($^\circ$)
1.0	30.0	0.1	0.1	32.8

4.5 Conclusions

The characteristic parameters of integrated platforms and commercial optical fibers complicate the design of fiber-chip surface couplers at long MIR wavelengths. In this chapter, a novel all-dielectric micro-antenna design for a suspended germanium platform has

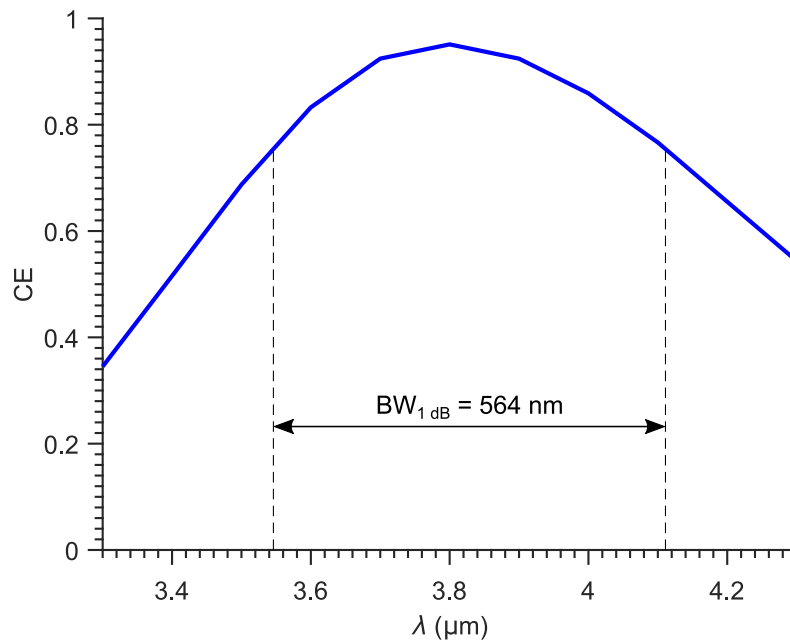


Figure 4.30: Coupling efficiency of the MIR zero-order grating coupler as a function of the wavelength (TE polarization).

been proposed with outstanding performance in terms of bandwidth and tolerance to fiber tilt misalignments. Together with the suspended germanium waveguides that were discussed in Chapter 3, this fiber-chip surface coupler constitutes another step toward the development of the suspended germanium platform with SWG lateral cladding.

To enhance the operating bandwidth of grating couplers, another new surface grating concept has been presented. Assisted by a silicon prism, the zero-order grating coupler achieves both broadband operation and high coupling efficiency simultaneously. Based on zero-order coupling and subwavelength refractive index engineering, this coupler overcomes the intrinsic bandwidth limitation of conventional surface grating couplers.

The results in this chapter open excellent prospects for the development of broadband and efficient input/output optical coupling interfaces for Group IV photonic circuits.

CHAPTER FIVE

CONCLUSIONS AND PROSPECTS

In this chapter, the main achievements of this thesis are summarized (Section 5.1), and ongoing work and research activities that can be continued in the future are outlined (Section 5.2).

5.1 Conclusions

This thesis has reported on the progress toward the development of Group IV-based photonic integrated platforms for mid-infrared (MIR) wavelengths. Specifically, suspended silicon and germanium waveguide platforms have been investigated, with the main focus on (i) the implementation and characterization of single-mode waveguides with low propagation losses, and (ii) the design of broadband, efficient fiber-chip surface couplers.

5.1.1 Suspended Platforms

Suspended Silicon Platform

A suspended silicon platform with lateral subwavelength grating (SWG) cladding has been proposed to operate at a wavelength of $7.67\ \mu\text{m}$, which is close to the upper bound of the transparency window of silicon in the MIR band. In particular, suspended waveguides, as well as bends and beamsplitters, have been developed for this platform.

In order to design the waveguides, three different approaches have been proposed to model the SWG lateral cladding: isotropic, anisotropic, and Bloch–Floquet. While the latter is the most rigorous, isotropic and anisotropic homogenization approaches are sufficiently reliable for practical design. To enable single-mode operation with low propagation loss, a two-stage systematic design methodology was followed: firstly, using the isotropic model, the thickness of the initial silicon-on-insulator (SOI) wafer was chosen to avoid power leakage to the substrate (vertical leakage); secondly, using the anisotropic homogenization, the remaining dimensions of the waveguide core and lateral cladding were determined to prevent power leakage toward the unsuspended lateral silicon (lateral leakage).

In addition to waveguides, whether straight or bent, any photonic integrated platform requires other passive structures to be fully functional. Two types of beamsplitters were designed for the suspended silicon platform: 1×2 and 2×2 multimode interference

couplers (MMIs), and a mode-evolution-based 3-dB splitter. These devices can be part of more complex blocks such as Mach-Zehnder interferometers, which could be used in the future, for instance, to build a suspended FTIR spectrometer for sensing applications.

The fabrication and the characterization were performed by researchers of the Optoelectronics Research Centre (ORC) of the University of Southampton, although the author of this thesis participated actively in the measurements during two short stays. At a wavelength of $7.67\ \mu\text{m}$, suspended silicon waveguides yielded a propagation loss of $3.1 \pm 0.2\ \text{dB cm}^{-1}$ (TE polarization), which is the lowest value that has been reported so far for a silicon-based waveguide at such a long wavelength. This propagation loss is expected to come from several sources: intrinsic silicon material loss, which contributes by $\sim 2.3\ \text{dB cm}^{-1}$; and scattering at the roughness that prolonged HF etching creates at the silicon/air interfaces. S-bends and 90° -bends also were demonstrated, with losses of $0.06 \pm 0.02\ \text{dB bend}^{-1}$ and $0.08 \pm 0.02\ \text{dB bend}^{-1}$, respectively. For the 1×2 MMI, preliminary measurements indicate excess losses as low as $0.47 \pm 0.05\ \text{dB MMI}^{-1}$.

These results, mostly published in [79,80], pave the way to a rich set of new systems operating in the MIR band with promising applications in communications and spectroscopy.

Suspended Germanium Platforms

Because of the high material loss of silicon, the suspended silicon platform becomes unsuitable for integrated photonics beyond $\sim 8\ \mu\text{m}$. At such long wavelengths, waveguide platforms that are based on germanium (low absorption up to $\sim 14\ \mu\text{m}$) arise as excellent candidates.

The germanium counterpart of the suspended silicon waveguides has been proposed at wavelengths of $3.8\ \mu\text{m}$ (as a proof of concept), $7.67\ \mu\text{m}$, and $9.6\ \mu\text{m}$. Many cycles of design, layout preparation, fabrication, scanning electron microscopy (SEM) inspection, and testing were carried out in the ORC. In particular, a number of fabrication runs were needed to fully suspend germanium waveguides, avoid collapsing, refine dimensions, and eventually enable waveguiding. Except for the fabrication in the Southampton Nanofabrication Centre cleanroom, all activities were performed by the author of this thesis at the Universidad de Málaga and, during two short research stays, in the ORC of the University of Southampton.

Propagation losses of $\sim 5\ \text{dB cm}^{-1}$ were measured at both $\lambda = 3.8\ \mu\text{m}$ and $\lambda = 7.67\ \mu\text{m}$ (TE polarization). The relatively high loss is attributed to a known contamination of the wafer that was used to fabricate the structures. These results constitute the first demonstration of a germanium-based suspended platform with SWG lateral cladding.

5.1.2 Fiber-Chip Surface Couplers

A significant part of this thesis is dedicated to the design of fiber-chip surface couplers. Apart from suspended conventional grating couplers for the suspended silicon platform at $\lambda = 7.67\ \mu\text{m}$ and the suspended germanium platform at $\lambda = 3.8\ \mu\text{m}$, novel coupling strategies have been proposed: the suspended germanium micro-antenna and the zero-order grating coupler.

Suspended Germanium Micro-antenna

In the MIR band, fiber-chip couplers with broad bandwidth and high coupling efficiency are critical for many applications, especially for absorption spectroscopy. Broad bandwidth is needed to cover the widest possible range of wavelengths when determining the absorption spectrum of a substance; high coupling efficiency, to increase the signal-to-noise ratio, that is, to have the required dynamic range to detect absorption peaks that otherwise could be masked by the noise floor.

The specifications of the single-mode MIR optical fibers that are commercially available at $\lambda = 7.67 \mu\text{m}$ (namely, small core diameters and large numerical apertures) drove the search for comparatively short grating couplers with high radiation strengths. The characteristics of these optical fibers, together with the high index contrast of the suspended germanium platform, which increases the size of the photonic bandgap of the gratings compared to silicon-based platforms, make conventional coupler designs suffer from narrow bandwidths and low fabrication tolerances.

To overcome such problems, a new grating coupling approach has been developed for the suspended germanium platform at $\lambda = 7.67 \mu\text{m}$. The design methodology was inspired by fundamental grating coupler equations, yet two diffractive orders were allowed rather than only one. This approach enables the design of diffractive structures with the high radiation strength that is required for long-wavelength single-mode fibers. The resulting structure, a suspended germanium micro-antenna, radiates most of the input power in just two or three radiation elements in a short electrical length. As a side effect of the narrow radiated field, the device bandwidth is broadened.

The proposed micro-antenna exhibits a coupling efficiency of $\sim 40\%$ (-4 dB) (TE polarization) with reduced back-reflections and a broad 1-dB bandwidth of $\sim 430 \text{ nm}$, which almost doubles the typical fractional bandwidth of conventional grating couplers in the near-infrared (NIR). The micro-antenna has an exceptional angular bandwidth of $\sim 20^\circ$, providing for a fiber tilt tolerance of $\pm 10^\circ$ with an efficiency penalty of only 1 dB. Moreover, coupling efficiency is tolerant to fabrication errors up to $\pm 150 \text{ nm}$.

The structure was fabricated at the University of Southampton to measure the propagation loss of the designed suspended germanium waveguides. While a complete characterization of the micro-antenna was not feasible in the MIR laboratory, the broad angular bandwidth was confirmed experimentally.

The suspended germanium micro-antenna is one of the most significant contributions of this thesis. It exceeds the coupling efficiencies and bandwidths of other reported grating couplers for the long-wavelength MIR range. Besides, the micro-antenna constitutes, to the best of this author's knowledge, the first time that an efficient surface fiber-chip coupler has been designed to operate in the fourth radiation zone (between fourth and fifth Bragg regimes). The micro-antenna approach can be readily extended to other MIR platforms.

The micro-antenna concept has been recently published in [81].

Zero-Order Grating Coupler

The primary bandwidth limitation of conventional grating couplers is the strong angle variation with the wavelength. Zero-order grating couplers (ZGCs) have been proposed specifically to suppress the angle-wavelength dependence. Initially, the ZGC was designed in the NIR band for the SOI platform, since the concept could be proved more

easily at this wavelength range. To enable zero-order radiation, the structure is assisted by a high-refractive-index prism. Unlike conventional prism-film couplers, the ZGC has a subwavelength-patterned waveguide core, which can be engineered to achieve approximately a threefold bandwidth enlargement compared to conventional grating couplers. The coupling efficiency is increased without degrading the bandwidth by tilting the prism by an angle of 1° . Thus, the ZGC achieves both broad bandwidth and high coupling efficiency simultaneously. Simulations predict an unprecedented coupler performance with a 1-dB bandwidth of 126 nm and a coupling efficiency of 91% (-0.41 dB) for the TE polarization.

Several alternative designs have been proposed using z - and x -periodic SWGs, each with respective silicon prism specifications. To minimize back-reflections, different types of injection stages (adiabatic tapers) were designed.

The design was completely done by the author of this thesis at the Universidad de Málaga and in the National Research Council Canada (NRC), during a short stay there. Various fabrication runs were carried out in the NRC, at the University of Waterloo, and at the University of Washington. The experimental characterization in the NIR band is still in progress by the researchers of the NRC. So far, the first measurements also indicate losses of ~ 0.5 dB taper $^{-1}$ for the adiabatic tapers, but the bandwidth and the coupling efficiency of the ZGCs have not yet been rigorously confirmed.

The concept proposal and theoretical design of the z -periodic ZGC has been published in [82].

5.2 Prospects

The main results of this thesis set the basis for a series of attractive lines of investigation. Ongoing work and several possible directions for future research activities are listed here.

5.2.1 Suspended Silicon Platform

Now that state-of-the-art suspended silicon waveguides have been demonstrated at a wavelength of 7.67 μm , the focus should be shifted to the development of other fundamental building blocks. Even though preliminary experimental results for the 1×2 MMI have been reported, the demonstration of the already designed 2×2 MMI and mode-evolution-based 3-dB beamsplitter is not complete.

Once these components are characterized, other devices — such as directional couplers, Y-branches, ring and racetrack resonators, Mach-Zehnder interferometers, or Bragg grating filters — need to be implemented in order to build complex systems.

5.2.2 Suspended Germanium Platforms

For the suspended germanium platform, waveguides have been characterized at wavelengths of 3.8 μm and 7.67 μm , exhibiting propagation losses around 5 dB cm $^{-1}$. The attained results are promising, as they validate the platform for MIR waveguiding. Future work can include the following ambitious tasks:

- (i) *Refinement at 3.8- μm and 7.67- μm wavelengths.* Further improvements on design and, most importantly, fabrication are expected to reduce propagation losses to values even smaller than those for the suspended silicon platform.

- (ii) *Migration toward longer wavelengths.* Although the suspended germanium platform can potentially outperform suspended silicon at $\lambda = 7.67 \mu\text{m}$, the actual interest lies on pushing the operating wavelength toward longer values. At $\lambda = 9.6 \mu\text{m}$, several designs have been proposed in this thesis, and they are pending fabrication and characterization. Moreover, the platform could be further developed up to a wavelength of $\sim 15 \mu\text{m}$, thereby covering almost the entire MIR band. Preliminary designs at $\lambda = 12 \mu\text{m}$ suggest that a Ge-on-SOI wafer with a 2- μm -thick guiding layer would be sufficient for achieving low-loss single-mode propagation.
- (iii) *Development of passive devices.* As for the suspended silicon platform, a set of suspended germanium building blocks (e.g., beamsplitters and ring resonators) could also be realized in the long term.

5.2.3 Suspended Platforms with Tilted SWG Lateral Cladding

There are three options to reduce the lateral leakage in suspended waveguides: (i) increasing the cladding width, (ii) increasing the core width, and (iii) increasing the cladding-core index contrast. The latter can be done by reducing the duty cycle of the SWG cladding, as long as the structure remains sufficiently stable.

Recently, tilted SWGs have been reported as a way to control the properties of the anisotropic synthesized metamaterial [162]. Specifically, for the in-plane polarization, the equivalent refractive index of the tilted structure can be lower than that of conventional SWGs. By tilting the strips of the SWG lateral cladding, suspended waveguides with higher index contrast, and hence reduced lateral leakage, can be designed. Figure 5.1 shows SEM images of the very preliminary attempts to implement these structures in a suspended silicon platform at $\lambda = 7.67 \mu\text{m}$. Propagation losses of these waveguides have not yet been measured.

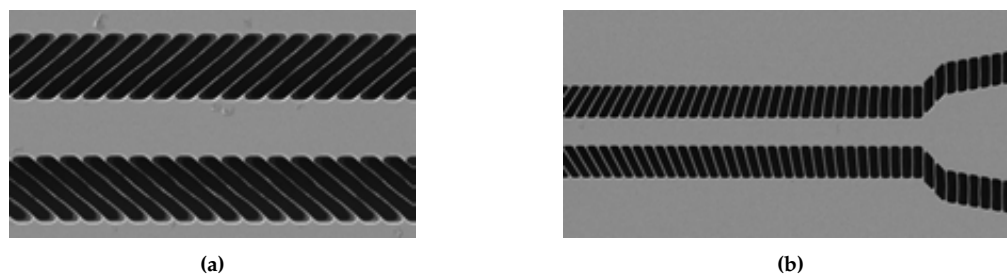


Figure 5.1: SEM images of (a) suspended silicon waveguide with tilted lateral SWG cladding and (b) transition from straight to tilted cladding.

5.2.4 Sensing Experiments with Suspended Waveguides

The prime potential application for MIR integrated photonics is sensing. In the literature, sensing experiments at different wavelengths and platforms have been reported (e.g., [61, 139]). At $\lambda = 7.67 \mu\text{m}$, experiments for detecting methane could be conducted with the suspended silicon and germanium platforms [19].

Suspended waveguides could be used for sensing applications in two different ways:

- (i) *For guiding and processing light.* As suspended waveguides were designed to minimize propagation losses, they could be employed to guide the light to the struc-

tures that interact with the substances under test or they could be integrated within complex systems (e.g., a spectrometer). The development of Mach-Zehnder interferometers and ring resonators, as mentioned in Section 5.2.1, could also benefit this objective.

- (ii) *For interacting with the sample.* As they are surrounded by air, suspended waveguides and bends (spirals) could be ideal for operating as the sensing element of an spectroscopy system if they were specifically designed for maximizing the light-matter interaction without increasing propagation losses. As a first approximation to the problem, some preliminary simulations have been carried out to study the sensing capabilities of the suspended silicon waveguides at $\lambda = 7.67 \mu\text{m}$ as designed in Chapter 3. Figure 5.2 shows the transverse field profiles of the fundamental TE and TM modes of waveguides. The electric field is substantially more vertically expanded for the TM mode than for the TE mode. As a figure of merit, the power confinement factor outside the waveguide core — or interaction factor (η) — was calculated, yielding ~ 0.1 and ~ 0.55 for TE_{00} and TM_{00} modes, respectively. Even though the light-cladding interaction for the TE polarization is low, the TM mode has a higher confinement factor in the upper and bottom claddings that could be useful for sensing. These results suggest that, if designed for enhanced light-matter interaction, these waveguides could be utilized for infrared spectroscopy.

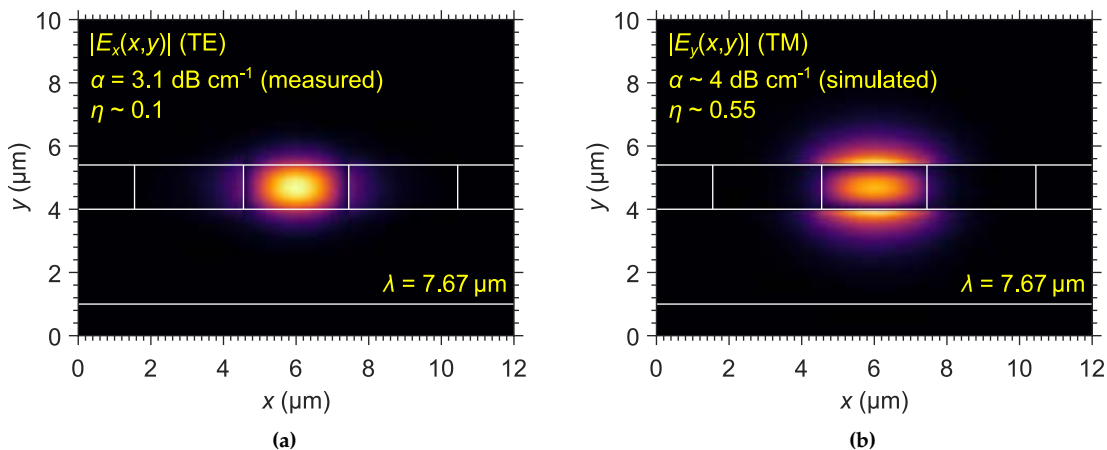


Figure 5.2: Transverse field distributions of the fundamental (a) TE and (b) TM modes supported by the suspended silicon waveguide designed in Chapter 3 ($\lambda = 7.67 \mu\text{m}$). Waveguide propagation losses (α) and waveguide sensitivities (η) are indicated. For the TE polarization, propagation loss values are experimental.

5.2.5 Micro-antennas

Regarding the micro-antenna couplers for the long-wavelength MIR region, three research activities can be proposed for the future:

- (i) *Full characterization at 7.67- μm wavelength.* Suspended germanium micro-antennas have been designed at $\lambda = 7.67 \mu\text{m}$, fabricated, and employed to couple light. Only the wide angular bandwidth of $\sim 20^\circ$ was experimentally confirmed. However, these structures need to be fully demonstrated. By characterizing the inherent

losses of the measurement setup, the actual coupling efficiency of the micro-antenna can be determined. A tunable laser will be required to analyze the spectral bandwidth.

- (ii) *Development at longer wavelengths.* Once suspended germanium waveguides are designed at long MIR wavelengths, new off-chip couplers will be needed. For example, at $9.6\ \mu\text{m}$, the central wavelength of one of the lasers in the ORC, the mode field diameter (MFD) of the IRFlex's IRF-Se-12 fiber is $\sim 16.4\ \mu\text{m}$ (i.e., $\overline{\text{MFD}} = \text{MFD}/\lambda \sim 1.7$). This $\overline{\text{MFD}}$ value is approximately the same as at a wavelength of $7.67\ \mu\text{m}$, so that the micro-antenna approach is still applicable at $9.6\ \mu\text{m}$.
- (iii) *High-efficiency designs.* So far, a coupling efficiency of $\sim 40\%$ has been achieved in simulation. A significant limitation is the relatively low directionality, of $\sim 60\%$. The micro-antenna performance could likely be improved by allowing two dry etch steps. By defining asymmetric teeth profiles, such as the L-shaped periods in [197], most of the power injected from the input waveguide into the coupler can be radiated only upwards (blaze effect).
- (iv) *Migration to other platforms.* Although the micro-antenna presented in this thesis was designed for the suspended germanium platform, other MIR platforms, such as those based on SiGe alloys, could benefit from the micro-antenna approach.

5.2.6 Zero-Order Grating Couplers

Zero-order grating couplers have been proposed theoretically for the NIR and MIR wavelength ranges, and the characterization is in progress in the NRC. The most obvious next steps on this topic are the following:

- (i) *Experimental demonstration at $1.55\text{-}\mu\text{m}$ wavelength.* Several chips with z -periodic and x -periodic structures were fabricated. Measurements are challenging even in the NIR band owing to the non-standard geometry, which requires a very accurate positioning of the optical fiber and the silicon prism on top of the grating. At the time, researchers in the NRC have preliminarily measured a spectral bandwidth of $\sim 100\ \text{nm}$ for the z -periodic ZGC at a central wavelength of $1.55\ \mu\text{m}$, but the coupling efficiency has not yet been estimated precisely. The full, rigorous demonstration of both z - and x -periodic ZGCs is a primary goal.
- (ii) *Experimental demonstration at $3.8\text{-}\mu\text{m}$ wavelength.* Once ZGCs at $1.55\ \mu\text{m}$ are experimentally confirmed, the structure designed to operate at $\lambda = 3.8\ \mu\text{m}$, with unprecedented performance in simulation, could be fabricated and measured.
- (iii) *Migration to longer wavelengths.* The ZGC concept could be migrated to longer MIR wavelengths for the suspended silicon and suspended germanium platforms, in order to provide both the broad bandwidth and the high efficiency for sensing experiments.

APPENDIX A

CURRICULUM VITAE

Alejandro Sánchez Postigo earned his MSc in Telecommunication Engineering from the Universidad de Málaga in January 2015. In the same year, he received a national scholarship from the Spanish Ministry of Science that funded his Ph.D. on the development of suspended waveguide platforms for mid-infrared Group IV photonics. This work was supervised by Prof. Dr. Gonzalo Wangüemert-Pérez and Dr. Alejandro Ortega-Moñux. While most of the research activities of this project involved design and simulation in the Photonics & RF Lab at the Universidad de Málaga, he has collaborated with the National Research Council Canada — which he visited for three months in order to work on the design of a ultra-broadband off-chip coupler under the supervision of Dr. Pavel Cheben — and the Optoelectronics Research Centre at the University of Southampton — in which he designed and experimentally characterized novel integrated platforms for the mid-infrared wavelength range, during two stays supervised by Prof. Goran Mashanovich.

A complete list of his publications is given below.

International journal papers

1. **A. Sánchez-Postigo**, A. Ortega-Moñux, D. Pereira-Martín, Í. Molina-Fernández, R. Halir, P. Cheben, J. Soler Penadés, M. Nedeljkovic, G. Mashanovich, J. G. Wangüemert Pérez, "Design of a suspended germanium micro-antenna for efficient fiber-chip coupling in the long-wavelength mid-infrared range," *Optics Express* 27, 22302–22315 (2019).
2. **A. Sánchez-Postigo**, J. G. Wangüemert-Pérez, J. Soler Penadés, A. Ortega-Moñux, M. Nedeljkovic, R. Halir, F. El Mokhtari Mimum, Y. Xu Cheng, Z. Qu, A. Khokhar, A. Osman, W. Cao, C. Littlejohns, G. Mashanovich, Í. Molina-Fernández, "Mid-infrared suspended waveguide platform and building blocks," *IET Optoelectronics* 13, 55–61 (2019).
3. J. Leuermann, A. Fernández-Gavela, A. Torres-Cubillo, S. Postigo, **A. Sánchez-Postigo**, L. M. Lechuga, R. Halir, Í. Molina-Fernández, "Optimizing the limit of detection of waveguide-based interferometric biosensor devices," *Sensors* 19, 3671 (2019).

4. J. Gonzalo Wangüemert-Pérez, A. Hadij-ElHouati, **A. Sánchez-Postigo**, J. Leuermann, D.-X. Xu, P. Cheben, A. Ortega-Moñux, R. Halir, Í. Molina-Fernández, "Sub-wavelength structures for silicon photonics biosensing," *Optics & Laser Technology* 109, 437–448 (2019) [INVITED].
5. D. Melati, Y. Grinberg, M. Kamandar Dezfouli, S. Janz, P. Cheben, J. H. Schmid, **A. Sánchez-Postigo**, and D.-X. Xu, "Mapping the global design space of nanophotonic components using machine learning pattern recognition," *Nature Communications* (2019). (Accepted.)
6. J. Soler Penadés, **A. Sánchez-Postigo**, M. Nedeljkovic, A. Ortega-Moñux, J. G. Wangüemert-Pérez, Y. Xu, R. Halir, Z. Qu, A. Z. Khokhar, A. Osman, W. Cao, C. G. Littlejohns, P. Cheben, Í. Molina-Fernández, G. Z. Mashanovich, "Suspended silicon waveguides for long-wave infrared wavelengths," *Optics Letters* 43, 795–798 (2018).
7. **A. Sánchez-Postigo**, J. Gonzalo Wangüemert-Pérez, J. M. Luque-González, Í. Molina Fernández, P. Cheben, C. A. Alonso-Ramos, R. Halir, J. H. Schmid, A. Ortega-Moñux, "Broadband fiber-chip zero-order surface grating coupler with 0.4 dB efficiency," *Optics Letters* 41, 3013–3016 (2016).

Conference proceedings

1. **A. Sánchez-Postigo**, G. Wangüemert-Pérez, J. Soler Penadés et al., "Suspended silicon integrated platform for the long-wavelength mid-infrared band," *ICTON* (2019) [INVITED].
2. J. Soler Penadés, **A. Sánchez-Postigo**, M. Nedeljkovic et al. "Suspended germanium waveguide for infrared wavelengths," *ICTON* (2019) [INVITED].
3. J. G. Wangüemert-Pérez, **A. Sánchez-Postigo**, A. Hadij-ElHouati et al., "Engineering sub-wavelength silicon waveguides for sensing applications in the near-infrared and mid-infrared band," *SPIE Photonics West* (2019) [INVITED].
4. J. G. Wangüemert-Pérez, **A. Sánchez-Postigo**, A. Hadij-ElHouati et al., "Subwavelength metamaterial for communications and sensing," *SPIE/COS Photonics Asia* (2019) [INVITED].
5. A. Ortega-Moñux, J. M. Luque-González, **A. Sánchez-Postigo** et al., "Subwavelength grating metamaterial engineering: a new tool for silicon photonics," *Advanced Photonics* (2018) [INVITED].
6. J. G. Wangüemert-Pérez, **A. Sánchez-Postigo**, J. Soler Penadés et al., "Mid-infrared suspended waveguide platform and building blocks," *ECIO* (2018) [INVITED].
7. D. Pereira-Martín, **A. Sánchez-Postigo**, A. Hadij-ElHouati et al., "Automatic design of high-performance fiber-chip surface grating couplers based on Floquet-Bloch mode analysis", *OWTNM* (2018).
8. **A. Sánchez-Postigo**, J. G. Wangüemert-Pérez, J. M. Luque-González et al., "Broadband high-efficiency zero-order surface grating coupler for the near- and mid-infrared wavelength ranges," *SPIE Optics + Optoelectronics* (2017).

9. A. Ortega-Moñux, R. Halir, **A. Sánchez-Postigo** et al., "Design of optical metamaterial waveguide structures," SPIE Optics + Optoelectronics (2017) [INVITED].
10. **A. Sánchez-Postigo**, J. G. Wangüemert-Pérez, J. M. Luque-González et al., "Design of broadband subwavelength-engineered metamaterial grating couplers with sub-decibel coupling efficiency in near- and mid-infrared," Photonics North (2017).
11. J. G. Wangüemert-Pérez, **A. Sánchez-Postigo**, J. M. Luque-González et al., "Subwavelength metamaterial structures for silicon photonics," Photonics North (2017) [INVITED].
12. **A. Sánchez-Postigo**, A. Ortega-Moñux, J. M. Luque-González et al., "High efficiency, ultra-broadband fiber-to-chip coupler based on subwavelength gratings," META (2016) [Poster presentation].
13. **A. Sánchez-Postigo**, J. M. Luque-González, R. Halir et al., "Design of ultra-broadband multimode interference devices for the mid-infrared wavelength range (3–4 μm)," OPTOEL (2015) [Poster presentation].
14. **A. Sánchez-Postigo**, J. G. Wangüemert-Pérez, R. Halir et al., "A subwavelength structured multimode interference coupler for the 3–4 micrometers mid-infrared band," SPIE Optics + Optoelectronics (2015).

APPENDIX B

RESUMEN EN ESPAÑOL

En las últimas décadas, la banda del infrarrojo medio ha despertado un gran interés en la comunidad científica dedicada a la fotónica del Grupo IV debido a las múltiples aplicaciones que pueden desarrollarse en este rango de longitudes de onda. Esta tesis se centra en el desarrollo de nuevas plataformas fotónicas integradas para la banda del infrarrojo medio, haciendo hincapié en la realización de guías de onda y de acopladores fibra-chip por superficie.

En este apéndice se ofrece un resumen en español de la tesis. Primero, se lleva a cabo una introducción a la banda del infrarrojo medio y a su relación con la fotónica del Grupo IV (Sección B.1). Seguidamente, se aborda el desarrollo (diseño, fabricación y caracterización experimental) de las guías suspendidas de silicio y de germanio, eje del trabajo efectuado (Sección B.2). Por último, se expone el diseño de los acopladores fibra-chip por superficie propuestos: una microantena de germanio suspendido y una rejilla de difracción de orden cero (Sección B.3).

B.1 Introducción

B.1.1 La banda del infrarrojo medio y la fotónica del Grupo IV

El infrarrojo medio (*mid-infrared*, MIR) es la banda del espectro electromagnético que abarca longitudes de onda de $2\ \mu\text{m}$ a $20\ \mu\text{m}^1$ [1]. La radiación infrarroja puede aprovecharse para una gran cantidad de aplicaciones. Entre las más relevantes, se pueden distinguir tres tipos, recogidos en la figura B.1:

- *Espectroscopia infrarroja*. Las moléculas de una gran cantidad de compuestos pueden absorber la radiación infrarroja que incide en ellas, aumentando sus movimientos de vibración y rotación [5]. Este fenómeno tiene lugar, sobre todo, a las frecuencias de la banda del MIR. El espectro de absorción de una sustancia da cuenta de la cantidad de energía absorbida por sus moléculas en función de la longitud de onda λ (o del número de onda k). Con el examen de los picos de absorción obtenidos mediante análisis espectroscópico, es posible identificar las sustancias que

¹Dependiendo del ámbito de aplicación, pueden asociarse otros conjuntos de longitudes de onda a esta banda del espectro electromagnético. Véase [2] para más información.

componen una muestra y determinar sus concentraciones. La espectroscopia infrarroja puede utilizarse para monitorización medioambiental [7, 8], desarrollo de sensores bioquímicos [9], diagnóstico médico [10–12], análisis de alimentos [13, 14] o astronomía [15–17], entre otras aplicaciones.

- *Comunicaciones ópticas por espacio libre.* En el infrarrojo medio existen dos ventanas de comunicaciones, de 3 μm a 5 μm y de 8 μm a 14 μm [21,22], en las que la atmósfera terrestre deja pasar la luz con escasa atenuación. A estas longitudes de onda es posible desarrollar enlaces de comunicaciones ópticas no guiadas con grandes anchos de banda.
- *Termografía.* Todo objeto, por encontrarse a una temperatura determinada, emite radiación infrarroja. Ésta puede medirse y visualizarse mediante cámaras, que suelen operar en las bandas de 3 μm a 5 μm y de 7 μm a 14 μm [23].

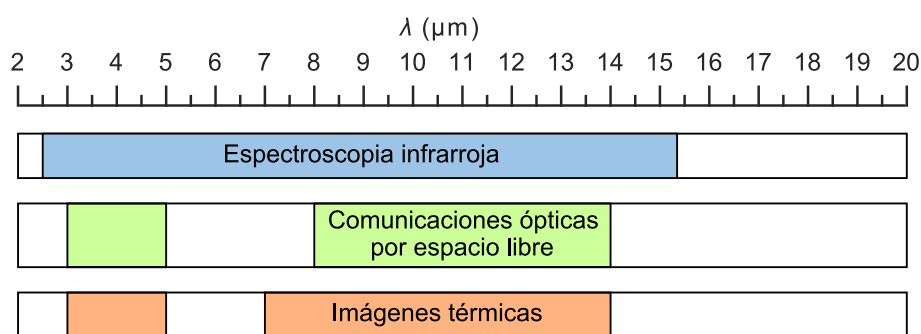


Figura B.1: La banda del infrarrojo medio y sus principales aplicaciones.

Las aplicaciones de espectroscopia infrarroja son, sin duda, las más destacables en la banda del MIR. En la mayoría de los sistemas ópticos empleados para llevar a cabo estudios espectroscópicos de muestras, pueden encontrarse los siguientes elementos: una fuente, que puede ser de banda ancha o sintonizable; una estructura, por ejemplo una cubeta o una pequeña cámara de gas, que permita la interacción de la luz de la fuente con la muestra; dispositivos para llevar la luz desde la fuente hasta las distintas partes del sistema y para el procesamiento óptico de la señal; y un fotodetector que mide el espectro.

La mayoría de los aparatos comerciales empleados para realizar espectroscopia infrarroja son voluminosos y pesados [42, 44]. Esto dificulta su empleo en situaciones donde se requieren análisis de sustancias en tiempo real o en condiciones peligrosas (piénsese en sistemas de detección de gases letales). Por este motivo, sería deseable disponer de dispositivos compactos, en miniatura, que pudiesen integrarse, por ejemplo, dentro de teléfonos móviles y relojes inteligentes. La fotónica integrada, y en especial la del Grupo IV, puede revolucionar este campo.

El principal problema de la migración desde la banda del infrarrojo cercano (*near-infrared*, NIR) ($\lambda \sim 1.55 \mu\text{m}$) al infrarrojo medio es que la plataforma habitual, la de silicio sobre aislante (*silicon on insulator*, SOI), presenta pérdidas inaceptables para longitudes de onda mayores de 4 μm a causa del dióxido de silicio, como se muestra en la figura B.2 [66]. Como consecuencia, deben buscarse alternativas que involucren nuevas estructuras de guiado o que combinen materiales con un mayor margen de transparencia en el MIR.

De esta forma, numerosos grupos de investigación han propuesto nuevas plataformas, como las de silicio sobre zafiro [69], silicio sobre nitruro de silicio [70] y germanio sobre silicio [71], o las basadas en aleaciones de silicio-germanio [72,73]. Otra forma de reducir las pérdidas consiste en la eliminación de la capa de dióxido de silicio de la plataforma SOI, lo que conduce a las estructuras suspendidas de silicio y de germanio, capaces, en teoría, de cubrir la banda completa del MIR [75,77,144].

El desarrollo de estas plataformas más novedosas conlleva notables esfuerzos de diseño, ya que, dependiendo de los materiales y de las estructuras de guiado, pueden necesitarse técnicas no convencionales de simulación. Por otro lado, la fabricación y la caracterización experimental de los dispositivos se torna más compleja en el MIR porque los procesos de fabricación y la instrumentación de laboratorio no tienen el mismo grado de madurez que a las longitudes de onda del NIR. Aunque ya se están presentando dispositivos complejos, como espectrómetros, en algunos casos concretos [60,78], el principal reto continúa siendo mucho más básico: encontrar la plataforma de propósito general óptima, esto es, aquella que ofrezca buenas prestaciones, que pueda desarrollarse fácilmente de manera masiva y que sea eficiente y económica.

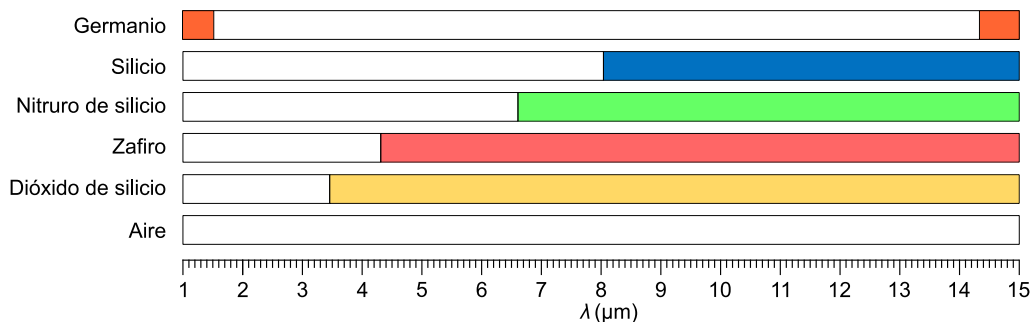


Figura B.2: Ventanas de transparencia (blanco) y opacidad (color) de varios materiales usados en la fotónica del Grupo IV. Se considera que un material es transparente cuando sus pérdidas son menores de 2 dB cm^{-1} . Figura adaptada de [66].

B.1.2 Objetivos y aportaciones

El objetivo general de esta tesis es avanzar en el desarrollo de la fotónica del Grupo IV en la banda del infrarrojo medio. Con este fin se han realizado aportaciones relevantes, con aplicaciones potenciales en comunicaciones y detección de sustancias.

En concreto, se han implementado plataformas suspendidas de silicio y de germanio que permiten superar la limitación fundamental de la tecnología SOI empleada en el NIR: las altas pérdidas del dióxido de silicio. De esta forma, la banda de operación puede extenderse hasta los límites de transparencia de ambos materiales ($\sim 8 \mu\text{m}$ en el caso del silicio y $\sim 15 \mu\text{m}$ en el del germanio). Se han demostrado guías de silicio suspendido a la longitud de onda de $7.67 \mu\text{m}$ con unas pérdidas de propagación de tan solo 3.1 dB cm^{-1} [79, 80], las más bajas, según la bibliografía consultada, que se han obtenido con una plataforma basada en silicio a una longitud de onda tan alta. Asimismo, se han demostrado guías de germanio suspendido a $3.8 \mu\text{m}$ y $7.67 \mu\text{m}$ con unas pérdidas de $\sim 5 \text{ dB cm}^{-1}$. Aunque son más altas que las obtenidas en silicio, estas pérdidas constituyen la primera validación experimental del concepto de guía suspendida en germanio.

Por otro lado, se han propuesto soluciones novedosas para el problema de la inyección eficiente de luz al chip, lo que ha dado lugar a nuevos dispositivos de acoplo, alternativos a los clásicos acopladores de rejilla, con extraordinarias prestaciones en términos de ancho de banda y eficiencia: la microantena de germanio suspendido [81] y el acoplador de rejilla de orden cero [82].

B.2 Plataformas suspendidas para el infrarrojo medio

B.2.1 Introducción

En la figura B.3 se muestra la geometría de una guía suspendida genérica (de silicio o de germanio). El núcleo de la guía, de altura H y anchura W , está anclado a los laterales sin suspender por medio de una rejilla compuesta por barras de silicio de longitud L_{strip} separadas entre sí una distancia L_{hole} . El espacio de aire entre la capa de guiado y el sustrato de silicio tiene una altura fija (H_{BOX}) de $3 \mu\text{m}$.

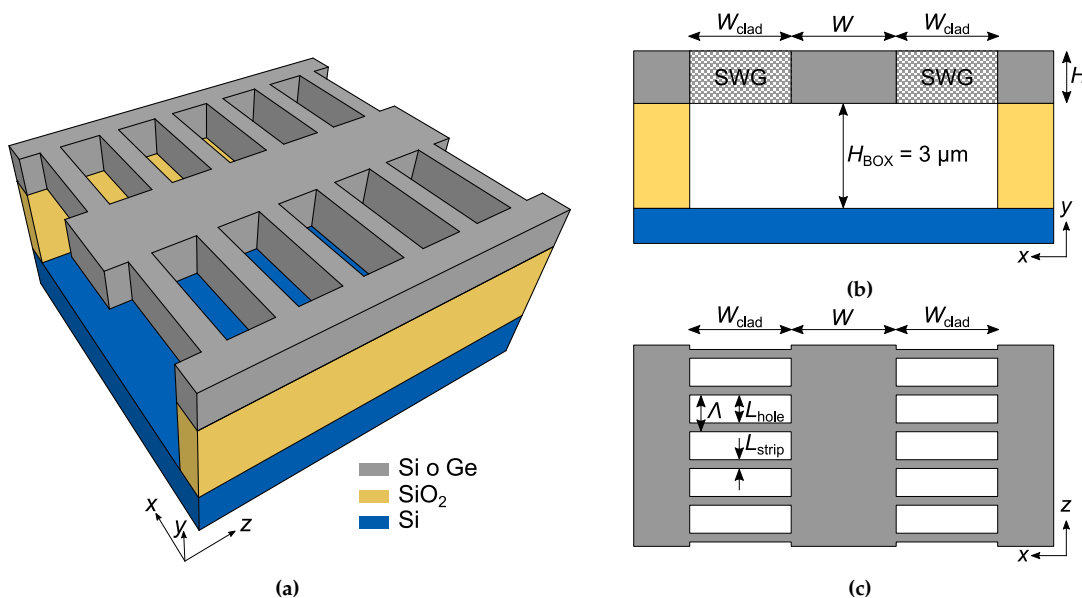


Figura B.3: Representación esquemática de una guía suspendida de silicio o de germanio. (a) Vista 3D. (b) Vista frontal. (c) Vista aérea de la capa de guiado. En la vista frontal la rejilla lateral se ha reemplazado por un medio homogéneo equivalente.

En las guías suspendidas, las rejillas laterales tienen tres funciones:

1. *Sostener el núcleo de la guía.* Las barras de silicio o de germanio laterales sujetan el núcleo, que está suspendido, impidiendo que se caiga.
2. *Permitir la eliminación del dióxido de silicio.* Para suspender las estructuras, es necesario hacer pasar una solución acuosa (ácido fluorhídrico, HF) a través de los agujeros grabados en la capa de guiado de la estructura. El ácido reacciona con el dióxido de silicio, eliminándolo.
3. *Proporcionar contraste de índice lateral.* Para que se produzca el guiado de luz, es preciso que exista un contraste de índice lateral en la estructura, de manera que el

índice de refracción del núcleo sea mayor que el de los laterales. La periodicidad de la rejilla es de menor tamaño que la longitud de onda, de tal forma que trabaja en el régimen sublongitud de onda (*subwavelength grating*, SWG) [155–157]. Así, la rejilla puede modelarse como un medio homogéneo equivalente, cuyo índice de refracción puede controlarse mediante el periodo Λ y el ciclo de trabajo (*duty cycle*, $DC = L_{\text{strip}}/\Lambda$).

Cuando una guía suspendida está convenientemente diseñada y fabricada, la luz se encuentra muy confinada dentro del núcleo y se propaga con bajas pérdidas. Como ejemplo, el perfil transversal y la propagación del modo fundamental de una guía puede verse en la figura B.4.

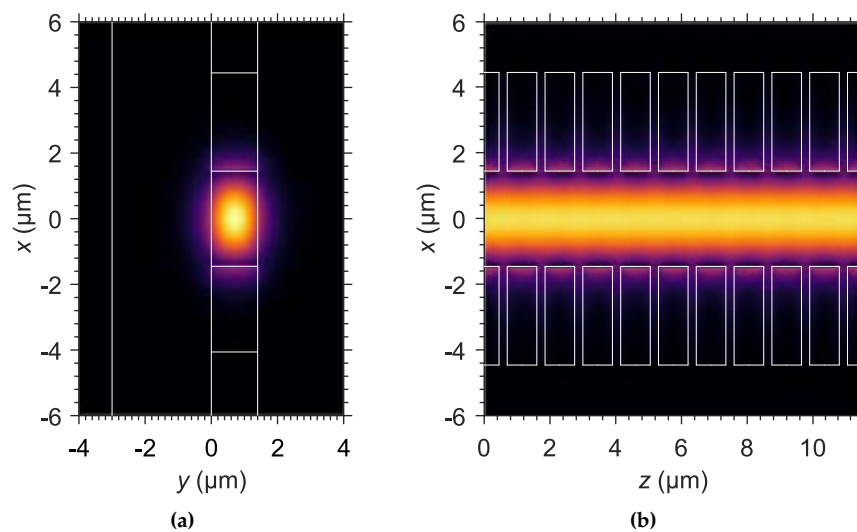


Figura B.4: (a) Distribución transversal y (b) propagación del modo fundamental (polarización TE) de una guía suspendida.

En este apartado se resume el diseño, la fabricación y la medida de las guías suspendidas de silicio y de germanio realizadas en esta tesis. Para la plataforma de silicio suspendido, se han demostrado guías para polarización transversal eléctrica (TE) y longitud de onda de $7.67 \mu\text{m}$, prácticamente en el límite de la banda de transparencia del silicio. Para la plataforma de germanio suspendido, se realizó una primera prueba de concepto a la longitud de onda de $3.8 \mu\text{m}$, para luego pasar a $7.67 \mu\text{m}$ y $9.6 \mu\text{m}$. Debido a la complejidad del diseño, que en todo momento debía nutrirse de la información suministrada por las fabricaciones previas de estructuras, el ciclo de desarrollo se extendió durante casi dos años, dando tiempo a validar experimentalmente las guías diseñadas para $3.8 \mu\text{m}$ y $7.67 \mu\text{m}$. (La fabricación de las guías de germanio suspendido para la longitud de onda de $9.6 \mu\text{m}$ no se había concluido en el momento de redactar esta tesis).

B.2.2 Diseño

Requisitos de las guías

Para diseñar guías suspendidas monomodo con bajas pérdidas deben satisfacerse los siguientes requisitos:

1. *Requisitos mecánicos.* Las rejillas laterales tiene que ser suficientemente robustas como para soportar el peso del núcleo de la guía. El par de fuerzas aplicado debe ser lo bastante bajo como para que la guía no se derrumbe o fracture. Incluso pequeñas roturas en las tiras de silicio o de germanio laterales son suficientes para aumentar las pérdidas de propagación de las guías.
2. *Requisitos de fabricación.* Los agujeros de aire de las rejillas laterales tienen que facilitar el flujo del agente químico que elimina el dióxido de silicio. Si la suspensión no es satisfactoria, las pérdidas pueden aumentar notablemente por efecto de los residuos de óxido. Asimismo, los procesos de fabricación y la altura de la capa de guiado imponen un tamaño mínimo de las estructuras que pueden grabarse.
3. *Requisitos ópticos o electromagnéticos.*

- *Funcionamiento en régimen SWG.* Para evitar que se produzca radiación o reflexión de Bragg, las rejillas laterales deben cumplir la condición SWG [155]:

$$L_{\text{strip}} + L_{\text{hole}} = \Lambda < \Lambda_{\text{Bragg}} = \frac{\lambda}{2n_B}, \quad (\text{B.1})$$

donde Λ_{Bragg} es el periodo de Bragg y n_B es el índice efectivo del modo Bloch-Floquet que se propaga por la estructura.

- *Funcionamiento monomodo.* Los modos soportados por la guía pueden sufrir pérdidas por fugas de potencia al sustrato (fugas verticales) o a los laterales de silicio o de germanio no suspendidos (fugas laterales). Por ello, para que el funcionamiento sea monomodo en la práctica, el modo fundamental de la estructura debe propagarse con mínimas fugas, tanto verticales como laterales, mientras que los modos superiores, en caso de que estén soportados, deberán extinguirse rápidamente.

En las tablas B.1 y B.2 se indican las tendencias necesarias de las dimensiones de las guías para que cada requisito se cumpla. Como puede observarse, es imposible que todos se satisfagan simultáneamente, por lo que el diseño óptimo de la guía será aquél que proporcione permita bajas pérdidas sin que la guía se derrumbe (solución de compromiso).

Tabla B.1: Requisitos de diseño para la suspensión y la estabilidad mecánica de las guías suspendidas.

Requisito	H	W	W_{clad}	L_{strip}^*	L_{hole}^*
Fluidez de la solución ácida	↓			↓	↑
Ligereza del núcleo	↓	↓			
Robustez de la rejilla lateral			↓	↑	↓

* $L_{\text{strip}} + L_{\text{hole}} < \Lambda_{\text{Bragg}}$ según la ecuación (B.1).
 $H_{\text{BOX}} = 3 \mu\text{m}$ y no puede diseñarse.

Modelado de las guías

Desde el punto de vista electromagnético, las guías suspendidas deben diseñarse para que el modo fundamental que se propaga por ellas no tenga fugas ni al sustrato ni a los

Tabla B.2: Requisitos de diseño de la guía suspendida para garantizar la operación en régimen monomodo. Las fechas azules indican cuáles son los parámetros más críticos para cada requisito.

Requisito	H	W	W_{clad}	L_{strip}^*	L_{hole}^*
Reducción de fugas verticales para el modo TE_{00}	↑	↑		↑	↓
Aumento de fugas verticales para el modo TE_{01}	↓	↓		↓	↑
Reducción de fugas laterales para el modo TE_{00}	↑	↑	↑	↓	↑
Aumento de fugas laterales para el modo TE_{10}	↓	↓	↓	↑	↓

* $L_{\text{strip}} + L_{\text{hole}} < \Lambda_{\text{Bragg}}$ según la ecuación (B.1).
 $H_{\text{BOX}} = 3 \mu\text{m}$ y no puede diseñarse.

laterales sin suspender. Al mismo tiempo, el segundo modo vertical (TE_{01}) y el segundo modo lateral (TE_{10}) deben tener fugas elevadas, a fin de que, en la práctica, pueda considerarse que la guía trabaja en régimen monomodo.

El cálculo de las pérdidas por fugas (*leakage*) puede realizarse mediante el análisis modal de la estructura. Si la guía no tiene pérdidas del material, el *leakage* puede calcularse a partir de la parte imaginaria del índice efectivo del modo:

$$\alpha = \frac{2\pi}{\lambda} \text{Im}(n_B) = \alpha_{\text{vertical}} + \alpha_{\text{lateral}}, \quad (\text{B.2})$$

donde α_{vertical} es el *leakage* vertical y α_{lateral} es el *leakage* lateral.

Las guías suspendidas son estructuras periódicas debido a las rejillas laterales SWG y, por tanto, soportan modos Bloch-Floquet. Los resolutores modales convencionales no suelen calcular modos Bloch-Floquet directamente. Por ello, en su lugar, hay que utilizar métodos alternativos de simulación. En esta tesis se plantean tres enfoques diferentes²:

1. *Modelo isótropo*. Es el caso más sencillo. La rejilla SWG se modela como un metamaterial homogéneo isótropo con un índice de refracción equivalente n_{SWG} de valor n_{xx} , que puede calcularse a partir de la fórmula de Rytov [161]:

$$n_{xx} \sim \left[\text{DC} \cdot n_{\text{strip}}^2 + (1 - \text{DC}) \cdot n_{\text{hole}}^2 \right]^{1/2}, \quad (\text{B.3})$$

donde n_{strip} es el índice de refracción de las barras de la rejilla (silicio o germanio) y n_{hole} es el índice de refracción del material que llena los huecos (aire). Las simulaciones pueden hacerse con cualquier resolutor modal. En esta tesis se empleó RSoft FemSIM, que puede proporcionar resultados en menos de 10s por punto de simulación³. Los valores simulados de pérdidas por fugas verticales son muy exactos, mientras que los de fugas laterales se subestiman para guías con rejillas estrechas (W_{clad} bajo).

2. *Modelo anisótropo*. La rejilla SWG se sustituye por un metamaterial homogéneo anisótropo (cristal uniaxial) con un tensor de permitividad [162]

$$n_{\text{SWG}}^2 = \begin{bmatrix} n_{xx}^2 & 0 & 0 \\ 0 & n_{yy}^2 & 0 \\ 0 & 0 & n_{zz}^2 \end{bmatrix}, \quad (\text{B.4})$$

²Todas las simulaciones descritas a continuación se realizaron en una estación de trabajo con procesador Intel Xeon ES-2697 v3 a una frecuencia de 2.6 GHz.

³Usando un mallado uniforme de 50 nm en la dirección x y de 100 nm en la dirección y .

donde n_{xx} , n_{yy} y n_{zz} pueden calcularse con las fórmulas de Rytov [161]. En concreto, n_{xx} ($= n_{yy}$) puede estimarse con la ecuación (B.3) y

$$n_{zz} \sim \left[\text{DC} \cdot n_{\text{strip}}^{-2} + (1 - \text{DC}) \cdot n_{\text{hole}}^{-2} \right]^{-1/2}. \quad (\text{B.5})$$

Estas simulaciones pueden realizarse con Photon Design FIMMWAVE, que cuenta con resolutores modales, de elementos finitos (*finite-element method*, FEM) y de diferencias finitas (*finite-difference method*, FDM), que soportan medios anisótropos. Con este enfoque el tiempo de simulación se incrementa ligeramente respecto del caso anterior (~ 20 s por punto de simulación⁴); a cambio, las fugas laterales pueden calcularse con mucha más exactitud.

3. *Modelo Bloch-Floquet*. En este caso, la guía suspendida se simula utilizando análisis Bloch-Floquet sin homogeneizar la rejilla SWG. Los índices efectivos de los modos pueden calcularse, por ejemplo, con Synopsys RSoft FullWAVE (3D *finite-difference time-domain*, FDTD), combinando los métodos descritos en [164–167]. Este modelo es el más exacto, pero los tiempos de simulación se incrementan notablemente con respecto de los de los enfoques anteriores (~ 20 min por punto de simulación⁵)

Un esquema de los métodos descritos se muestra en la figura B.5.

Considerando estos enfoques, las guías suspendidas pueden diseñarse en dos fases:

1. *Selección de la plataforma*. Usando el modelo isótropo, se obtiene con exactitud la altura H que minimiza las fugas verticales para el modo fundamental y las aumenta para el primer modo superior (TE_{01}).
2. *Selección del resto de dimensiones de la guía*. Usando el modelo anisótropo, se determinan la anchura del núcleo de la guía (W), la rejilla SWG (L_{strip} y L_{hole}) y su anchura (W_{clad}), de tal forma que se minimice el *leakage* lateral para el modo fundamental y se incremente para el primer modo superior (TE_{10}). La velocidad en las simulaciones del modelo anisótropo respecto del Bloch-Floquet favorece el uso de aquél, cuya exactitud es, en la práctica, suficiente para el diseño de las guías.

Teniendo en cuenta los requisitos impuestos a las guías en esta misma sección y los tres tipos de modelado propuestos, se diseñaron guías de silicio suspendido a la longitud de onda de $7.67 \mu\text{m}$ (tabla B.3) y guías de germanio suspendido a $3.8 \mu\text{m}$, $7.67 \mu\text{m}$ y $9.6 \mu\text{m}$ (tabla B.4).

Tabla B.3: Dimensiones de la guía de silicio suspendido diseñada para operar a la longitud de onda de $7.67 \mu\text{m}$.

H (μm)	W (μm)	W_{clad} (μm)	L_{strip} (μm)	L_{hole} (μm)	H_{BOX}^* (μm)
1.50	2.90	3.65	0.25	0.90	3.00

*Como referencia. La altura H_{BOX} no es un parámetro de diseño.

⁴Usando un mallado uniforme de 50 nm en la dirección x y de 100 nm en la dirección y con el resolutor modal FEM.

⁵Usando un mallado uniforme de 50 nm en la dirección x , de 100 nm en la dirección y y de 30 nm en la dirección z .

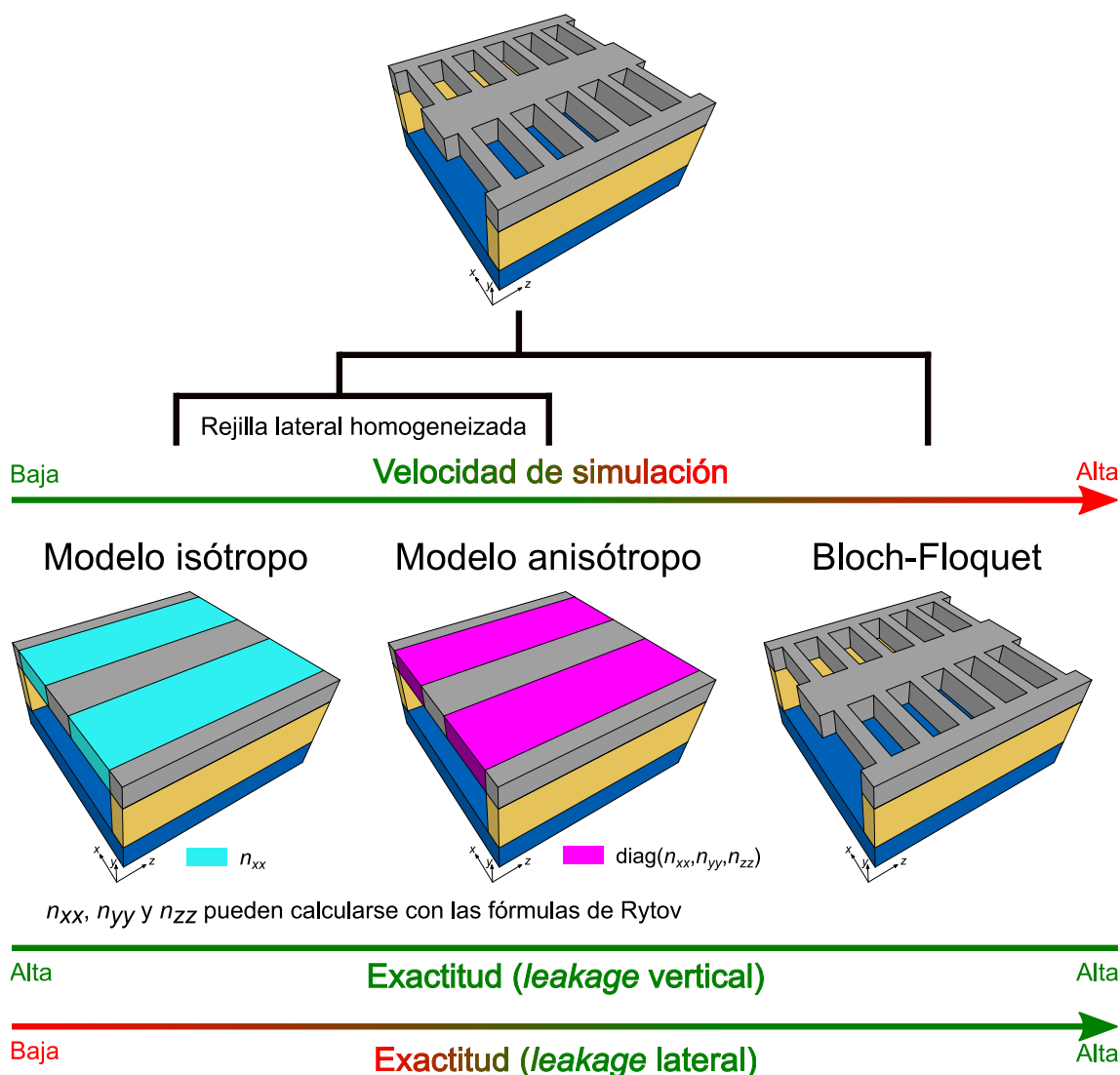


Figura B.5: Modelado de las guías suspendidas.

Tabla B.4: Dimensiones de las guías de germanio suspendido diseñadas.

λ (μm)	H (μm)	W (μm)	W_{clad} (μm)	L_{strip} (μm)	L_{hole} (μm)	H_{BOX}^* (μm)
3.80	0.50	1.30	2.00	0.10	0.45	3.00
7.67	1.00	2.90	3.10	0.20	0.80	3.00
9.60	1.00	4.20	3.60	0.20	0.80	3.00
9.60	2.00	3.60	3.40	0.25	1.05	3.00

*Como referencia. La altura H_{BOX} no es un parámetro de diseño.

B.2.3 Fabricación

Máscaras

En la figura B.6 se muestra una de las máscaras que se definieron para fabricar las guías suspendidas. Para dibujarlas se utilizó el programa Mentor Tanner L-Edit IC Layout

[169], con ayuda de unas rutinas en C++ escritas por los investigadores del Optoelectronics Research Centre (ORC) de la Universidad de Southampton.

En las distintas máscaras que se dibujaron, las guías se distribuyeron en distintos grupos por toda la superficie del chip. Cada conjunto de guías se corresponde con una variación en la anchura del núcleo, de las rejillas laterales o del ciclo de trabajo, con el objetivo de compensar posibles errores de fabricación, intentar que algunas estructuras no se derrumben y reducir posibles pérdidas por fugas a los laterales sin grabar. Se emplearon acopladores chip-fibra de superficie para acoplar la luz, cuyo diseño se resumirá en la sección B.3. Como puede advertirse en la figura, las estructuras suspendidas están definidas por los agujeros de las rejillas laterales. Se incluye una caja de medida en la máscara para servir de punto de sondeo con el que estimar con un elipsómetro el grosor de la capa de guiado durante el proceso de fabricación.

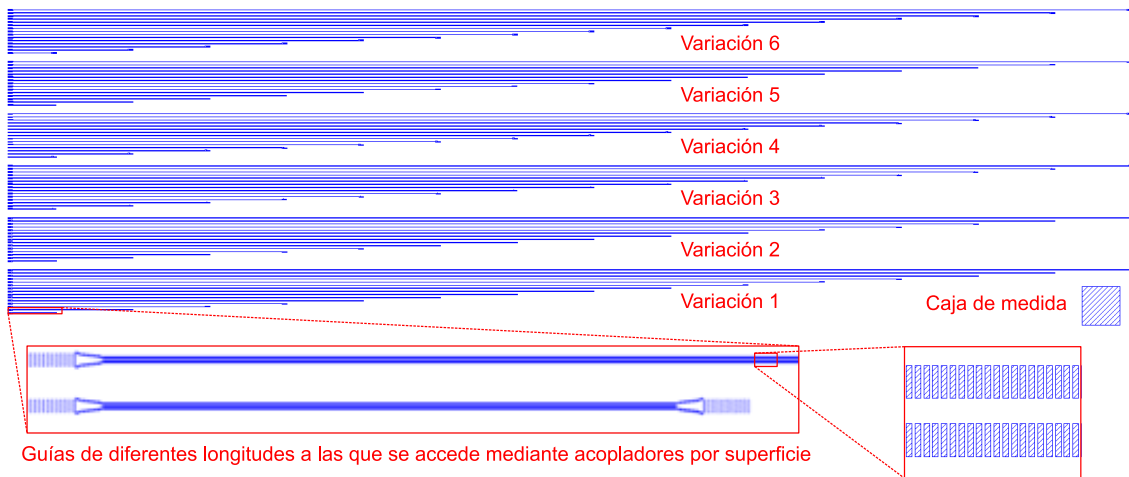


Figura B.6: Ejemplo de máscara para la caracterización de guías suspendidas.

Litografía

La fabricación de las guías suspendidas se llevó a cabo por los investigadores del Southampton Nanofabrication Centre (SNC) de la Universidad de Southampton.

El proceso de fabricación es esencialmente el mismo para las guías de silicio y las guías de germanio. Después de un horneado para eliminar humedad, se aplica una fotorresina ZEP520-A. Mediante litografía de haz de electrones (*e-beam*) se transfiere a la fotorresina el patrón de la máscara con las estructuras. Tras revelarla, se realiza un grabado seco (*inductively coupled plasma*, ICP), que define los agujeros de las rejillas laterales de la guía suspendida. El chip es entonces sumergido en un baño con una disolución de agua y fluoruro de hidrógeno (HF) en proporción 1 a 7, que ataca el dióxido de silicio y acaba suspendiendo la estructura. La duración del baño es crítica: si el chip no permanece suficiente tiempo en contacto con el ácido, pueden quedar restos de dióxido de silicio que aumenten las pérdidas; por el contrario, si el tiempo de inmersión es excesivo, las dimensiones de la estructura pueden verse afectadas por efecto del ácido sobre el silicio o el germanio.

La figura B.7 muestra imágenes de algunas de las guías suspendidas de silicio y de germanio fabricadas. Estas fotografías se sacaron con un microscopio electrónico de barrido (*scanning electron microscope, SEM*) del SNC.

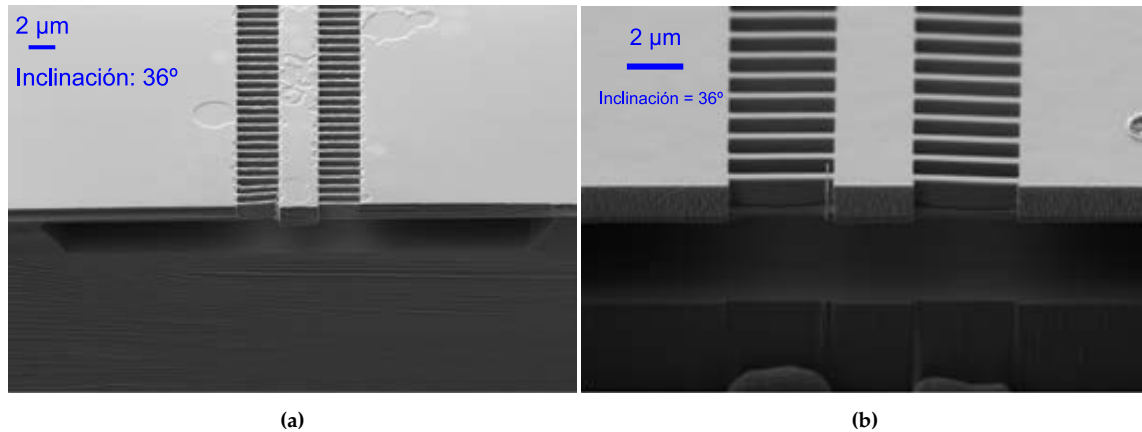


Figura B.7: Imágenes SEM de las guías suspendidas de (a) silicio y de (b) germanio diseñadas para operar a la longitud de onda de $7.67 \mu\text{m}$.

B.2.4 Caracterización experimental

Montaje de medida

En la figura B.8 se muestra esquemáticamente el montaje de medida empleado para la caracterización de las guías suspendidas a la longitud de onda de $7.67 \mu\text{m}$. Este montaje se encontraba en el laboratorio de fotónica del Grupo IV para el infrarrojo medio del ORC, al que el autor de esta tesis se desplazó en el marco de dos estancias breves supervisadas por el profesor Goran Mashanovich.

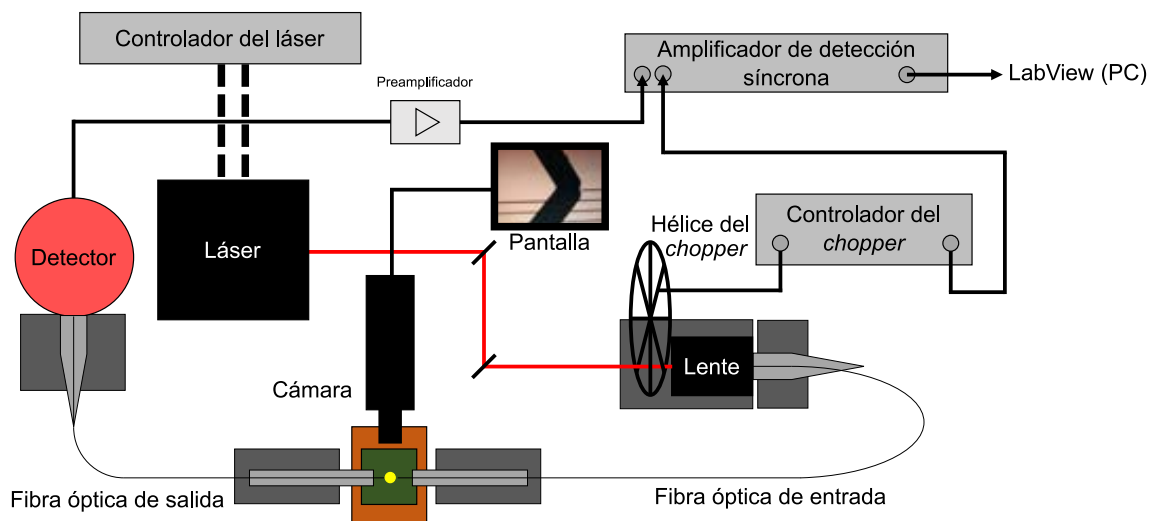


Figura B.8: Esquema del montaje de medida usado para caracterizar las guías suspendidas ($\lambda = 7.67 \mu\text{m}$).

Con este montaje, la luz de un láser de cascada cuántica (*quantum cascade laser, QCL*), tras ser modulada con un *chopper*, se inyecta en el chip a través de un acoplador por su-

perficie, cuyo diseño se explicará en la sección B.3. Después de propagarse por el chip, la luz se extrae mediante un acoplador análogo al de la entrada y es conducida con una delicada fibra óptica de calcogenuro hasta el detector, que previamente debe enfriarse con nitrógeno líquido. La señal eléctrica generada a la salida del fotodetector es preamplificada y, posteriormente, llevada hasta un amplificador de detección síncrona (*lock-in amplifier*) que permite reducir la relación señal a ruido usando la frecuencia del *chopper* para demodular la señal. La medida es posprocesada en un ordenador personal con el software LabView.

La caracterización de las guías de germanio a la longitud de onda de $3.8\ \mu\text{m}$ se realizó con un montaje similar del mismo laboratorio.

Resultados

Las guías se caracterizaron experimentalmente por medio de la técnica *cut-back* [170].

La figura B.9 muestra la potencia medida a la salida de las guías suspendidas de silicio después de normalizarla a la potencia medida a la salida de la guía más corta. La caracterización realizada antes de eliminar el dióxido de silicio devolvió unas pérdidas de propagación de $62.3 \pm 9.6\ \text{dB cm}^{-1}$, como se observa en la figura B.9. Tras sumergir el chip en HF, las pérdidas de propagación descendieron hasta $3.1 \pm 0.2\ \text{dB cm}^{-1}$. Estas pérdidas son, que se sepa, las más bajas que se han obtenido con guías de silicio a una longitud de onda tan alta, y son comparables a las guías más avanzadas desarrolladas para otras plataformas. De los $3.1\ \text{dB cm}^{-1}$, aproximadamente $2.3\ \text{dB cm}^{-1}$ se puede atribuir a las pérdidas intrínsecas del silicio a $7.67\ \mu\text{m}$. Los $0.8\ \text{dB cm}^{-1}$ restantes pueden deberse a rugosidades laterales y superficiales y, quizás, a unas pérdidas por fugas laterales mayores de las diseñadas. Este resultado, obviando las pérdidas propias del silicio, coincide prácticamente con el que se presenta en [147] para guías de silicio suspendido a una longitud de onda de $3.8\ \mu\text{m}$.

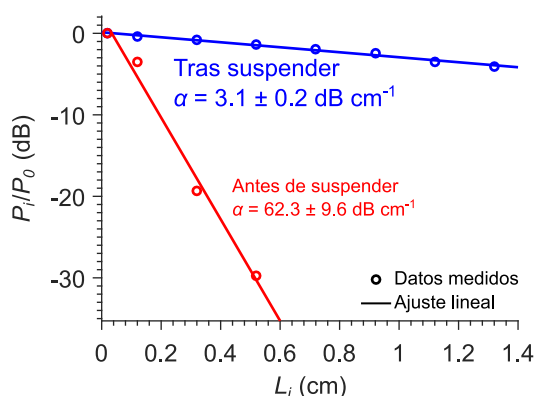


Figura B.9: Pérdidas de propagación medidas de las guías de silicio suspendido ($\lambda = 7.67\ \mu\text{m}$), con y sin dióxido de silicio.

Las guías de germanio suspendido se caracterizaron primero a $3.8\ \mu\text{m}$, como prueba de concepto. El montaje de medida para esta longitud de onda cuenta con un láser sintonizable y con fibras ópticas más robustas (de ZrF_4), lo que facilita la medición. Como se observa en la figura B.10a, se obtuvieron unas pérdidas de propagación de $6.7 \pm 0.2\ \text{dB cm}^{-1}$ antes de quitar el dióxido de silicio, y de $4.5 \pm 0.3\ \text{dB cm}^{-1}$ tras eliminarlo. Estas pérdidas eran suficientemente bajas como para considerar validada la estructura.

Seguidamente, se caracterizaron las guías suspendidas a $7.67 \mu\text{m}$, que sí tenían verdadero interés, ya que, como consecuencia de la transparencia del germanio a esta longitud de onda, podrían, en teoría, sufrir menos pérdidas que las guías de silicio suspendido. Antes de sumergir el chip en HF se midieron unas pérdidas mayores de 60 dB cm^{-1} . Tras la eliminación del dióxido de silicio, éstas se redujeron hasta $5.2 \pm 0.3 \text{ dB cm}^{-1}$ (ver figura B.10b). El hecho de que las pérdidas sean mayores que las de las guías suspendidas de silicio a la misma longitud de onda se atribuye a una conocida contaminación de las obleas de germanio empleadas para fabricar el chip. En cualquier caso, este resultado demuestra la viabilidad de la suspensión para las guías de germanio. Actualmente se está trabajando en nuevas fabricaciones con las que reducir las pérdidas obtenidas hasta ahora. Además, se tienen preparadas las máscaras para una próxima fabricación de guías suspendidas a $9.6 \mu\text{m}$.

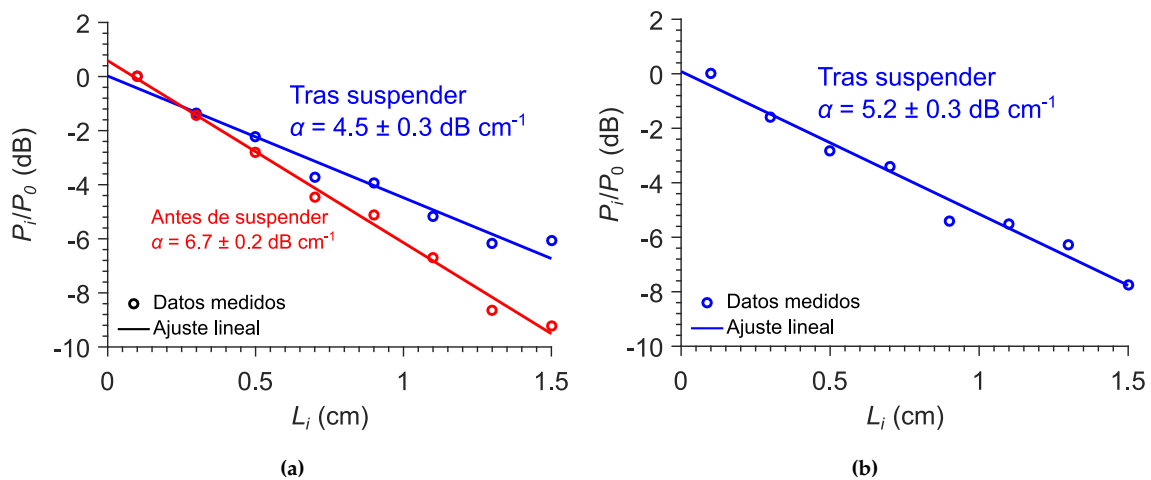


Figura B.10: Pérdidas de propagación medidas de las guías de germanio suspendido a las longitudes de onda de (a) $3.8 \mu\text{m}$ (con y sin dióxido de silicio) y de (b) $7.67 \mu\text{m}$.

B.3 Acopladores chip-fibra por superficie

B.3.1 Introducción

Las dimensiones de la sección transversal de los núcleos de las guías de onda fotónicas integradas son, por lo general, mucho más pequeñas que los diámetros de las fibras ópticas. Cuando se intenta inyectar luz de una fibra a una guía, esta diferencia de tamaños genera una incompatibilidad o desadaptación entre el modo fundamental de la fibra y el de la guía. Como consecuencia, la integral de solapamiento entre ambos modos es baja, lo que da lugar a pérdidas de potencia, que no se acopla en su totalidad de la fibra al chip. La misma situación desfavorable se tiene al intentar acoplar luz desde el chip hasta la fibra óptica. Para solventar este inconveniente, existen distintas alternativas [175,176,178,180], entre las que destacan los acopladores de rejilla por superficie.

Los acopladores de rejilla por superficie están formados por una estructura periódica o casi periódica que difracta la luz que se propaga por ella. Colocando la fibra en la posición adecuada sobre la estructura, con el ángulo de inclinación correcto, es posible recoger la luz radiada. Estas estructuras posibilitan el acoplo en cualquier punto de la

superficie del chip y son más robustas a desalineamientos que los acopladores por canto del chip. Como inconveniente, presentan de manera natural un ancho de banda limitado.

El escaso ancho de banda de los acopladores de rejilla convencionales puede entenderse si se examina la ecuación que gobierna la radiación en estos dispositivos [179]

$$n_a \sin(\theta) = \text{Re}(n_B) + m \frac{\lambda}{\Lambda}, \quad (\text{B.6})$$

donde n_a es el índice de refracción del medio en el que se encuentra la fibra óptica, θ es el ángulo de radiación, n_B es el índice efectivo del modo Bloch-Floquet que se propaga por la guía periódica, Λ es el periodo de la guía, λ es la longitud de onda de trabajo y m es un número entero que recibe el nombre de orden de radiación. Habitualmente $n_a = 1$ (aire) y $m = -1$. Como puede verse en la ecuación, existe una relación directa entre $\sin(\theta)$ y λ . Por tanto, para diferentes longitudes de onda se obtienen diferentes ángulos de radiación. Esto significa que, para una fibra colocada en un ángulo y una posición fijos, sólo a la longitud de onda nominal se podrá alcanzar la máxima eficiencia de acoplo.

En esta tesis se han diseñado acopladores de rejilla convencionales para caracterizar las plataformas de silicio suspendido ($\lambda = 7.67 \mu\text{m}$) y la de germanio suspendido ($\lambda = 3.8 \mu\text{m}$). Adicionalmente, con el objetivo de mejorar las prestaciones de los acopladores convencionales, se han realizado dos aportaciones muy significativas que se detallarán en los siguientes apartados: la microantena de germanio suspendido y el acoplador de rejilla de orden cero.

B.3.2 Microantena de germanio suspendido

Las fibras ópticas utilizadas en la banda del NIR tienen diámetros modales mayores que la longitud de onda [201]. Sin embargo, las pocas fibras de calcogenuro disponibles comercialmente para su uso a longitudes de onda altas del MIR tienen diámetros comparables a λ [200]. Este tamaño reducido de las fibras en términos de longitud de onda tiene un impacto directo en los acopladores, que deberán radiar con fuerzas de radiación elevadas.

En la figura B.11 se muestra una representación de la microantena, en la que, además de las distintas vistas, se proporciona la propagación del campo eléctrico (polarización TE). Como puede apreciarse, el incremento en la fuerza de radiación exige un acoplador muy corto en términos eléctricos, con un frente de onda radiado de tipo cilíndrico. Debido a estas características, claramente distintas de las de los acopladores de rejilla tradicionales, se considera que los acopladores eficientes para estas fibras estrechas de la banda del MIR se comportan como microantenas.

Para diseñar la estructura y alcanzar la fuerza de radiación requerida, se relajó la condición habitual que establece que un acoplador de rejilla debe radiar sólo un orden de difracción [179]. Así, se utilizaron las técnicas típicas de diseños de acopladores de rejilla, pero estudiando todos aquellos periodos que cumplieren la condición de “no más de dos órdenes de radiación”:

$$\Lambda < \frac{\lambda}{n_a}. \quad (\text{B.7})$$

La aplicación de esta condición permitió encontrar un diseño satisfactorio que radiaba los órdenes -2 y -3 en la zona de radiación 4 (entre el cuarto y el quinto régimen de

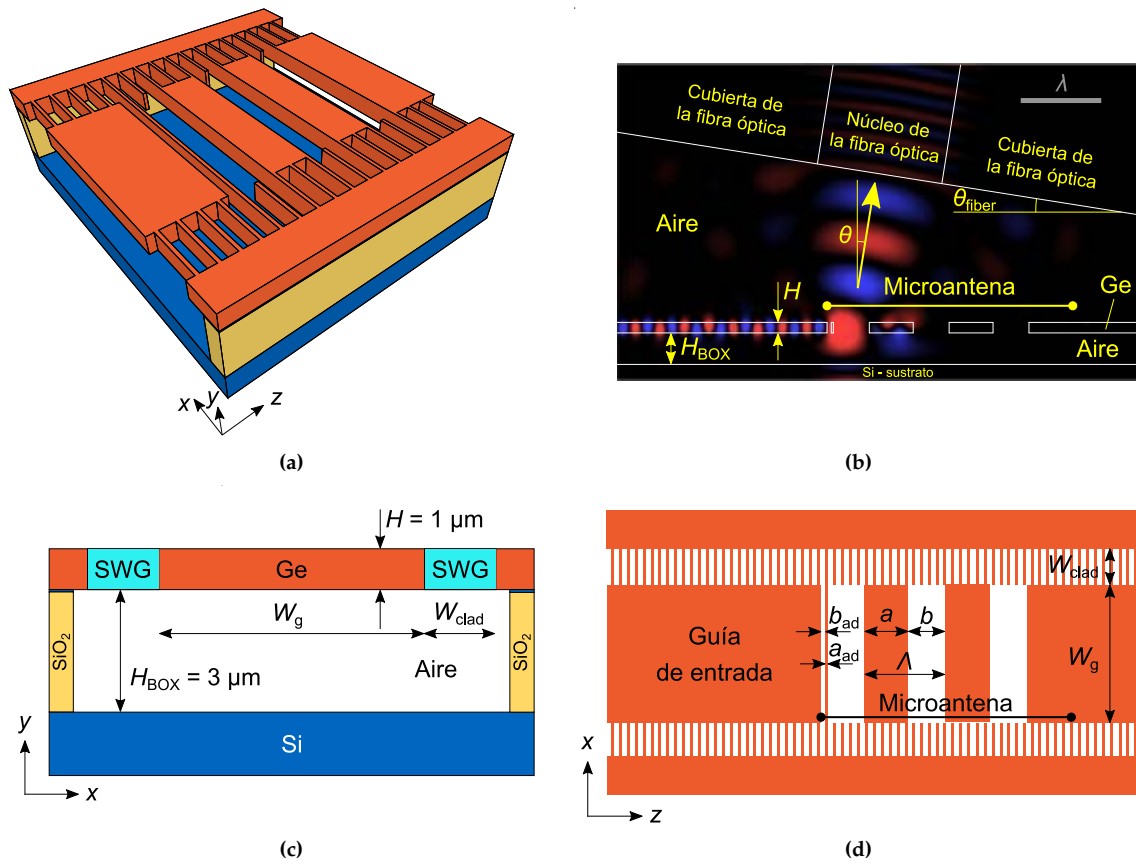


Figura B.11: Representación esquemática de una microantena de germanio suspendido. (a) Vista 3D. (b) Vista lateral superpuesta a una propagación 2D FDTD del campo. (c) Vista frontal. (d) Vista aérea de la capa de guiado.

Bragg). Este diseño es el primero, que se sepa, que opera con razonable eficiencia ($\sim 40\%$), soportando dos órdenes, en esta zona de radiación.

El diseño de la microantena de germanio suspendido proporciona, a la longitud de onda de $7.67\ \mu\text{m}$, una extraordinaria tolerancia a errores de inclinación de la fibra de $\pm 10^\circ$, así como un ancho de banda a 1 dB ($BW_{1\text{dB}}$) de $430\ \text{nm}$, que da lugar a un ancho de banda fraccional ($BW_{1\text{dB}}/\lambda$) de 5.68% . Este valor que casi dobla el ancho de banda fraccional de los acopladores de rejilla convencionales del infrarrojo cercano ($\sim 3.23\%$). En la figura B.12 se representa la eficiencia de acoplo en función de la longitud de onda y del ángulo de inclinación de la fibra (respecto del ángulo nominal de 9°).

La microantena se fabricó para caracterizar las guías de germanio suspendido a la longitud de onda de $7.67\ \mu\text{m}$ siguiendo el proceso descrito en la sección B.2.3. En la figura B.13 se muestran las imágenes SEM de la microantena. El diseño de esta microantena es una de las contribuciones más relevantes de esta tesis y se ha publicado en [81].

B.3.3 Acoplador de rejilla de orden cero

El diseño del acoplador de rejilla de orden cero (*zero-order grating coupler*, ZGC) se comenzó en la Universidad de Málaga (UMA) y se finalizó en el National Research Council Canada (NRC) durante una estancia breve bajo la supervisión del Dr. Pavel Cheben. La

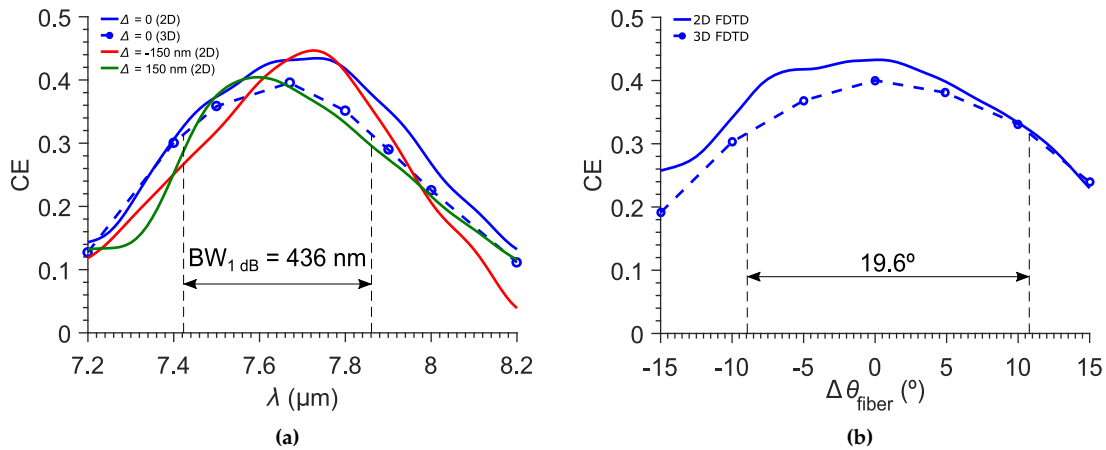


Figura B.12: (a) Eficiencia de acoplo simulada en función de la longitud de onda cuando las dimensiones tienen errores de $\Delta = 0$ (línea azul), $\Delta = 150$ nm (línea verde) y $\Delta = -150$ nm (línea roja) que afectan a la longitud de las tiras de germanio. Resultados de simulación 3D FDTD también se incluyen (línea discontinua azul) para el diseño nominal. (b) Eficiencia de acoplo simulada en función del ángulo de desalineamiento de la fibra respecto de su valor nominal de 9° .

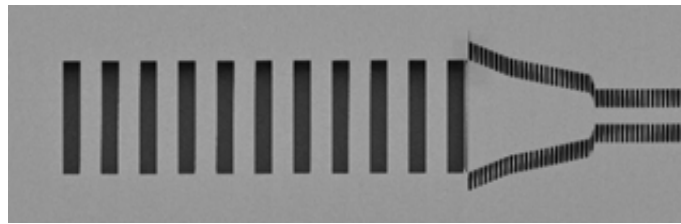


Figura B.13: Imagen SEM de la microantena de germanio suspendido para operar a la longitud de onda de 7.67 μm .

caracterización experimental de este dispositivo es muy compleja y se está realizando actualmente en el NRC. Aunque esta tesis está dedicada a la banda del MIR, el ZGC se diseñó inicialmente a una longitud de onda de 1.55 μm . Esta decisión se debió a la falta de disponibilidad de láseres y detectores para el MIR tanto en las instalaciones de la UMA como en las del NRC. En cualquier caso, el diseño teórico se migró a la banda del MIR y se simuló para comprobar su viabilidad en el contexto de esta tesis.

Habitualmente, al diseñar acopladores de rejilla sólo es posible maximizar una de las dos figuras de mérito fundamentales: la eficiencia de acoplo o el ancho de banda. Así, es posible tener altas eficiencias de acoplo sacrificando el ancho de banda y, al contrario, se puede aumentar el ancho de banda a costa de la eficiencia. El propósito del ZGC es optimizar, simultáneamente, tanto la eficiencia de acoplo como el ancho de banda de operación del acoplador.

En la figura B.14 se muestra la representación esquemática de un ZGC. Este acoplador está constituido por una guía periódica SWG de grosor H , longitud L y periodo Λ . Las longitudes de los segmentos de los materiales que conforman cada periodo son a y b , de tal forma que $\Lambda = a + b$. Sobre la guía se sitúa un prisma de alto índice de refracción n_a y ángulo ϕ_{prism} que se encuentra separado del núcleo de la guía periódica por una capa de índice de refracción n_e y altura variable $t_{\text{clad}}(z)$. En la figura B.14 se incluye también

el núcleo de una fibra óptica con un ángulo de orientación θ destinada a recibir la luz radiada por el acoplador.

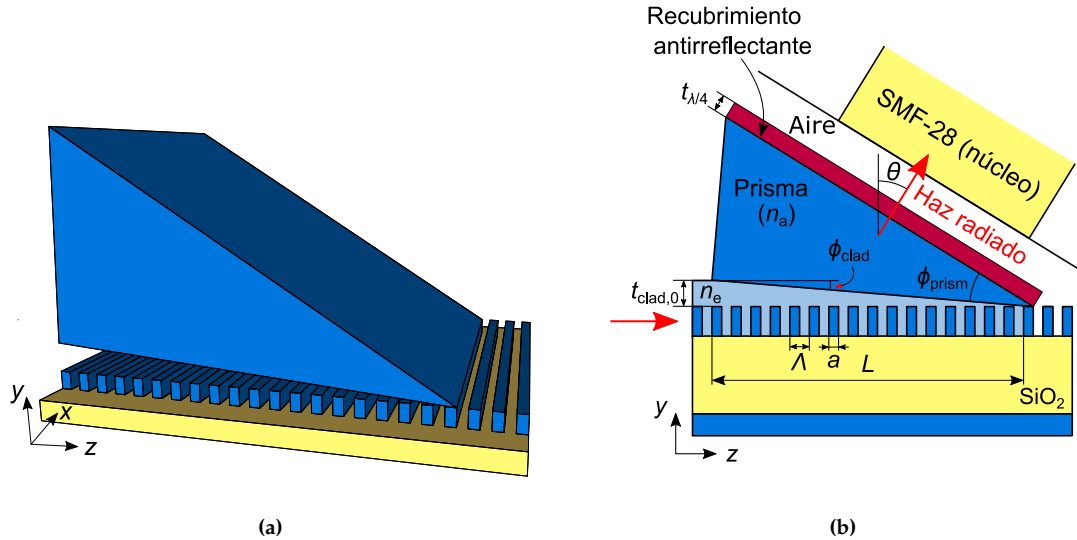


Figura B.14: Representación esquemática (no a escala) de un acoplador de rejilla de orden cero. (a) Vista 3D. (b) Vista lateral.

Los ZGC suprimen la dependencia explícita del ángulo de radiación θ con λ , dada por la ecuación B.6, haciendo que la guía periódica tenga un periodo suficientemente pequeño como para trabajar en régimen SWG. En ese caso no existe ningún orden de radiación. Para conseguir que se radie con el orden cero, se introduce un material superior con un índice de refracción que satisfaga

$$n_a > n_B. \tag{B.8}$$

De esta forma, el orden cero ($m = 0$) radia con un ángulo dado por

$$n_a \sin(\theta) = n_B. \tag{B.9}$$

La relación de proporcionalidad explícita entre $\sin(\theta)$ y λ desaparece en un ZGC, aumentándose automáticamente el ancho de banda. Para maximizar la eficiencia de acoplo se realiza una variación lineal en la separación entre el prisma y la guía, lo que permite alcanzar eficiencias de hasta el 95% [183]. Puede demostrarse que esta variación apenas tiene efecto en el índice efectivo del modo Bloch-Floquet que se propaga por la guía, por lo que el aumento de la eficiencia de acoplo no penaliza el ancho de banda de los ZGC.

En la figura B.15 se muestran los resultados de las simulaciones del ZGC diseñado a la longitud de onda de $1.55 \mu\text{m}$. Se obtuvo una eficiencia de $\sim 95\%$ y un ancho de banda a 1 dB de $\sim 130 \text{ nm}$ cuando $L = 20.3 \mu\text{m}$ y $t_{\text{clad},0} = 355 \text{ nm}$. Este mayor ancho de banda supone un incremento de $\sim 2.6\%$ respecto de acopladores de rejilla convencionales en la banda del NIR.

Posteriormente el diseño se migró a la banda del infrarrojo medio, a una longitud de onda de $3.8 \mu\text{m}$. Como las pérdidas del silicio son relativamente asumibles a esta longitud de onda, no es necesaria suspender la estructura. Para una longitud L de $30 \mu\text{m}$ y una altura inicial $t_{\text{clad},0}$ de $1 \mu\text{m}$, se mantuvo la eficiencia de acoplo en el 95%, mientras que el ancho de banda se expandió hasta $\sim 560 \text{ nm}$, como se muestra en la figura B.16.

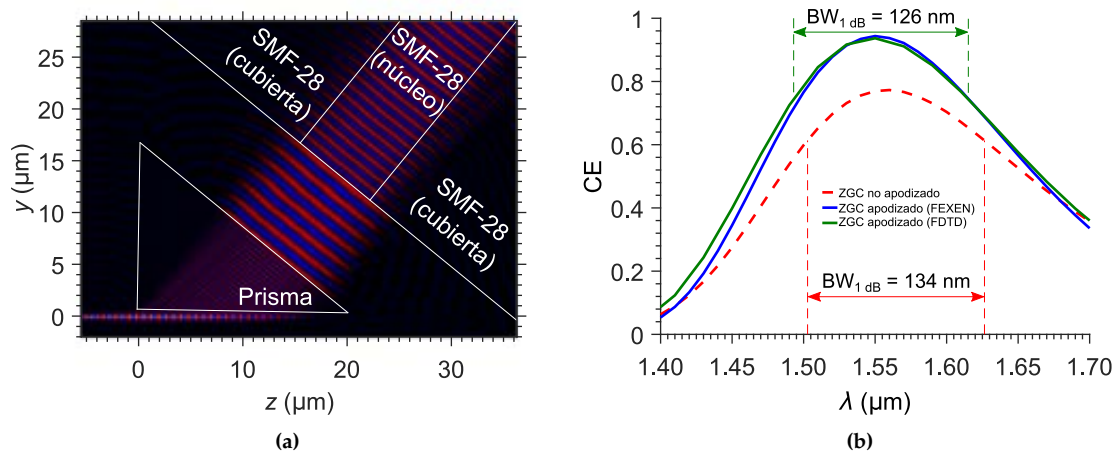


Figura B.15: Simulación del acoplador de rejilla de orden cero. (a) Propagación del campo (polarización TE) a la longitud de onda de $1.55 \mu\text{m}$. (b) Eficiencia de acoplo en función de la longitud de onda. Para poder comparar, se muestra también el diseño de un acoplador de rejilla sin inclinación del prisma.

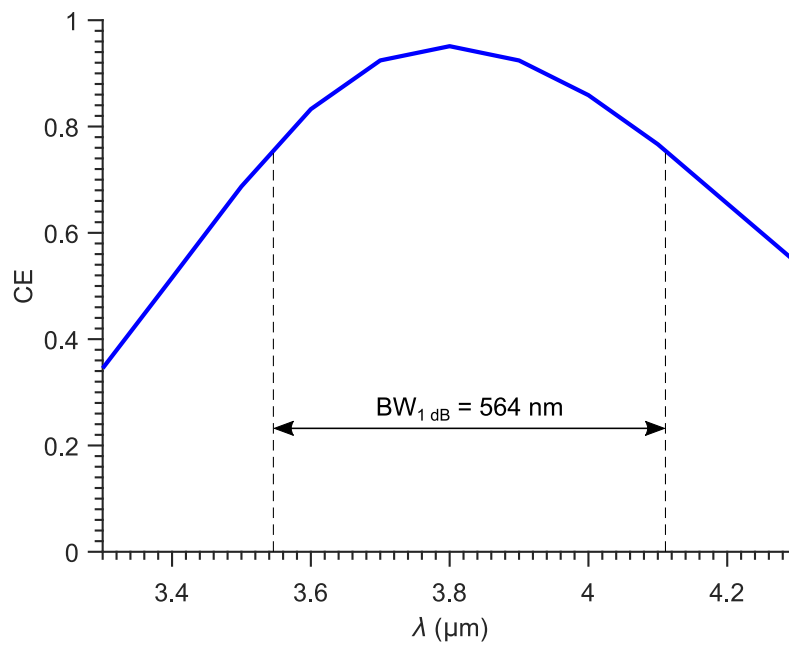


Figura B.16: Eficiencia de acoplo del acoplador de rejilla de orden cero diseñado para la banda del infrarrojo medio en función de la longitud de onda.

BIBLIOGRAPHY

- [1] B. E. A. Saleh and M. C. Teich, *Fundamentals of Photonics*, Wiley Series in Pure and Applied Optics (John Wiley & Sons, Inc., 2007).
- [2] J. Byrnes, ed., *Unexploded Ordnance Detection and Mitigation*, NATO Science for Peace and Security Series B: Physics and Biophysics (Springer Netherlands, 2009).
- [3] R. A. Soref, S. J. Emelett, and W. R. Buchwald, "Silicon waveguided components for the long-wave infrared region," *Journal of Optics A: Pure and Applied Optics* **8**, 840–848 (2006).
- [4] R. Soref, "Toward silicon-based longwave integrated optoelectronics (LIO)," in "Proc. SPIE 6898, Silicon Photonics III," (SPIE, 2008).
- [5] B. C. Smith, *Fundamentals of Fourier Transform Infrared Spectroscopy* (CRC Press, 2011).
- [6] B. Stuart, *Infrared Spectroscopy: Fundamentals and Applications* (John Wiley & Sons, Ltd, 2004).
- [7] R. Stach, B. Pejčić, E. Crooke, M. Myers, and B. Mizaikoff, "Mid-infrared spectroscopic method for the identification and quantification of dissolved oil components in marine environments," *Analytical Chemistry* **87**, 12306–12312 (2015).
- [8] L. Cunningham, J. Tibby, S. Forrester, C. Barr, and J. Skjemstad, "Mid-infrared spectroscopy as a potential tool for reconstructing lake salinity," *Water* **8**, 479 (2016).
- [9] S. De Bruyne, M. M. Speeckaert, and J. R. Delanghe, "Applications of mid-infrared spectroscopy in the clinical laboratory setting," *Critical Reviews in Clinical Laboratory Sciences* **55**, 1–20 (2018).
- [10] C. Hughes and M. J. Baker, "Can mid-infrared biomedical spectroscopy of cells, fluids and tissue aid improvements in cancer survival? A patient paradigm," *Analyst* **141**, 467–475 (2016).
- [11] M.-C. Yu, P. Rich, L. Foreman, J. Smith, M.-S. Yu, A. Tanna, V. Dibbur, R. Unwin, and F. W. K. Tam, "Label free detection of sensitive mid-infrared biomarkers of glomerulonephritis in urine using Fourier transform infrared spectroscopy," *Scientific Reports* **7**, 4601 (2017).
- [12] M. Paraskevaidi, C. L. M. Morais, K. M. G. Lima, K. M. Ashton, H. F. Stringfellow, P. L. Martin-Hirsch, and F. L. Martin, "Potential of mid-infrared spectroscopy as a non-invasive diagnostic test in urine for endometrial or ovarian cancer," *Analyst* **143**, 3156–3163 (2018).
- [13] B. Horn, S. Esslinger, M. Pfister, C. Fauhl-Hassek, and J. Riedl, "Non-targeted detection of paprika adulteration using mid-infrared spectroscopy and one-class classification – Is it data preprocessing that makes the performance?" *Food Chemistry* **257**, 112–119 (2018).
- [14] O. Uncu, B. Ozen, and F. Tokatli, "Mid-infrared spectroscopic detection of sunflower oil adulteration with safflower oil," *Grasas y Aceites* **70**, 290 (2019).
- [15] D. Farrah, J. Bernard-Salas, H. W. W. Spoon, B. T. Soifer, L. Armus, B. Brandl, V. Charmandaris, V. Desai, S. Higdon, D. Devost, and J. Houck, "High-resolution mid-infrared spectroscopy of ultraluminous infrared galaxies," *The Astrophysical Journal* **667**, 149–169 (2007).



- [16] H.-D. Kenchington Goldsmith, M. J. Ireland, P. Ma, B. Luther-Davies, R. Wang, B. Norris, P. Tuthill, and S. J. Madden, "Photonic mid-infrared nulling for exoplanet detection on a planar chalcogenide platform," in "Proc. SPIE 10701, Optical and Infrared Interferometry and Imaging VI," (SPIE, 2018).
- [17] C. Battersby, L. Armus, E. Bergin, T. Kataria, M. Meixner, A. Pope, K. B. Stevenson, A. Cooray, D. Leisawitz, D. Scott, J. Bauer, C. M. Bradford, K. Ennico, J. J. Fortney, L. Kaltenegger, G. J. Melnick, S. N. Milam, D. Narayanan, D. Padgett, K. Pontoppidan, T. Roellig, K. Sandstrom, K. Y. L. Su, J. Vieira, E. Wright, J. Zmuidzinas, J. Staguhn, K. Sheth, D. Benford, E. E. Mamajek, S. G. Neff, S. Carey, D. Burgarella, E. De Beck, M. Gerin, F. P. Helmich, S. H. Moseley, I. Sakon, and M. C. Wiedner, "The Origins Space Telescope," *Nature Astronomy* **2**, 596–599 (2018).
- [18] "Water," <https://webbook.nist.gov/cgi/cbook.cgi?ID=C7732185>.
- [19] "Methane," <https://webbook.nist.gov/cgi/cbook.cgi?ID=74-82-8>.
- [20] "Carbon monoxide," <https://webbook.nist.gov/cgi/cbook.cgi?ID=630-08-0>.
- [21] R. E. Roberts, J. E. A. Selby, and L. M. Biberman, "Infrared continuum absorption by atmospheric water vapor in the 8–12- μ m window," *Applied Optics* **15**, 2085–2090 (1976).
- [22] A. Soibel, M. Wright, W. Farr, S. Keo, C. Hill, R. Yang, and H. Liu, "High-speed operation of interband cascade lasers," *Electronics Letters* **45**, 264–265 (2009).
- [23] M. Vollmer and K.-P. Möllmann, *Infrared Thermal Imaging: Fundamentals, Research and Applications* (John Wiley & Sons, 2010).
- [24] V. Vakarin, J. Ramírez, J. Frigerio, Q. Liu, A. Ballabio, X. Le Roux, C. Alonso-Ramos, G. Isella, P. Cheben, W. N. Ye, L. Vivien, and D. Marris-Morini, "Wideband Ge-rich SiGe polarization-insensitive waveguides for mid-infrared free-space communications," *Applied Sciences* **8**, 1154 (2018).
- [25] E. Y.-k. Ng and R. U. Acharya, "Remote-sensing infrared thermography," *IEEE Engineering in Medicine and Biology Magazine* **28**, 76–83 (2009).
- [26] H. Manor and S. Arnon, "Performance of an optical wireless communication system as a function of wavelength," *Applied Optics* **42**, 4285–4294 (2003).
- [27] M. A. Khalighi and M. Uysal, "Survey on free space optical communication: A communication theory perspective," *IEEE Communications Surveys and Tutorials* (2014).
- [28] E. Leitgeb, T. Plank, M. S. Awan, P. Brandl, W. Popoola, Z. Ghassemlooy, F. Ozek, and M. Wittig, "Analysis and evaluation of optimum wavelengths for free-space optical transceivers," in "2010 12th International Conference on Transparent Optical Networks," (IEEE, 2010).
- [29] Y. Su, W. Wang, X. Hu, H. Hu, X. Huang, Y. Wang, J. Si, X. Xie, B. Han, H. Feng, Q. Hao, G. Zhu, T. Duan, and W. Zhao, "10 Gbps DPSK transmission over free-space link in the mid-infrared," *Optics Express* **26**, 34515–34528 (2018).
- [30] R. Furstenberg, C. A. Kendziora, J. Stepnowski, S. V. Stepnowski, M. Rake, M. R. Papantonakis, V. Nguyen, G. K. Hubler, and R. A. McGill, "Stand-off detection of trace explosives via resonant infrared photothermal imaging," *Applied Physics Letters* **93**, 224103 (2008).
- [31] J.-L. Gonzalez-Hernandez, A. N. Recinella, S. G. Kandlikar, D. Dabydeen, L. Medeiros, and P. Phatak, "Technology, application and potential of dynamic breast thermography for the detection of breast cancer," *International Journal of Heat and Mass Transfer* **131**, 558–573 (2019).
- [32] A. Lay-Ekuakille, P. Visconti, R. de Fazio, and D. Veneziano, "Quasi-real time acquisition and processing for biomedical IR and conventional imaging in surgery applications," *Journal of Instrumentation* **14**, P03011 (2019).

- [33] M. D. Peña and A. R. Muntaner, *Química Física* (Pearson Educación, 1989).
- [34] M. Gebhardt, C. Gaida, F. Stutzki, S. Hädrich, C. Jauregui, J. Limpert, and A. Tünnermann, "Impact of atmospheric molecular absorption on the temporal and spatial evolution of ultra-short optical pulses," *Optics Express* **23**, 13776–13787 (2015).
- [35] D. F. Swinehart, "The Beer-Lambert law," *Journal of Chemical Education* **39**, 333–335 (1962).
- [36] P. R. Griffiths, "Beer's law," in "Handbook of Vibrational Spectroscopy," P. R. Griffiths, ed. (John Wiley & Sons, Ltd, Chichester, UK, 2006).
- [37] "1-Propanol," <https://webbook.nist.gov/cgi/cbook.cgi?ID=71-23-8>.
- [38] "2-Propanol," <https://webbook.nist.gov/cgi/cbook.cgi?ID=C67630>.
- [39] J. Faist, F. Capasso, D. L. Sivco, C. Sirtori, A. L. Hutchinson, and A. Y. Cho, "Quantum cascade laser," *Science* **264**, 553–556 (1994).
- [40] R. Q. Yang, "Infrared laser based on intersubband transitions in quantum wells," *Superlattices and Microstructures* **17**, 77–83 (1995).
- [41] Z. Du, S. Zhang, J. Li, N. Gao, and K. Tong, "Mid-infrared tunable laser-based broadband fingerprint absorption spectroscopy for trace gas sensing: a review," *Applied Sciences* **9**, 338 (2019).
- [42] "ThermoFisher," <https://www.thermofisher.com>.
- [43] "4300 Handheld FTIR — Agilent," <https://www.agilent.com/en/products/ftir/ftir-compact-portable-systems/4300-handheld-ftir>.
- [44] "Ametek," <https://www.ametekpi.com/>.
- [45] G. T. Reed and A. P. Knights, *Silicon Photonics: An Introduction* (John Wiley & Sons, Ltd, 2004).
- [46] R. Soref, "The past, present, and future of silicon photonics," *IEEE Journal of Selected Topics in Quantum Electronics* **12**, 1678–1687 (2006).
- [47] G. T. Reed, ed., *Silicon Photonics: The State of the Art* (John Wiley & Sons, Ltd, 2008).
- [48] D. Thomson, A. Zilkie, J. E. Bowers, T. Komljenovic, G. T. Reed, L. Vivien, D. Marris-Morini, E. Cassan, L. Viroth, J.-M. Fédéli, J.-M. Hartmann, J. H. Schmid, D.-X. Xu, F. Boeuf, P. O'Brien, G. Z. Mashanovich, and M. Nedeljkovic, "Roadmap on silicon photonics," *Journal of Optics* **18**, 073003 (2016).
- [49] X. Chen, M. M. Milosevic, S. Stankovic, S. Reynolds, T. D. Bucio, K. Li, D. J. Thomson, F. Gardes, and G. T. Reed, "The emergence of silicon photonics as a flexible technology platform," *Proceedings of the IEEE* **106**, 2101–2116 (2018).
- [50] Y. Vlasov, "Silicon CMOS-integrated nano-photonics for computer and data communications beyond 100G," *IEEE Communications Magazine* **50**, s67–s72 (2012).
- [51] P. Yang, S. Nakamura, K. Yashiki, Z. Wang, L. H. K. Duong, Z. Wang, X. Chen, Y. Nakamura, and J. Xu, "Inter/intra-chip optical interconnection network: opportunities, challenges, and implementations," in "2016 Tenth IEEE/ACM International Symposium on Networks-on-Chip (NOCS)," (IEEE, 2016).
- [52] C. Minkenberg, N. Farrington, A. Zilkie, D. Nelson, C. P. Lai, D. Brunina, J. Byrd, B. Chowdhuri, N. Kucharewski, K. Muth, A. Nagra, G. Rodriguez, D. Rubi, T. Schrans, P. Srinivasan, Y. Wang, C. Yeh, and A. Rickman, "Reimagining datacenter topologies with integrated silicon photonics," *Journal of Optical Communications and Networking* **10**, 126–139 (2018).
- [53] E. El-Fiky, A. Samani, D. Patel, M. Jacques, M. Sowailam, and D. V. Plant, "400 Gb/s O-band silicon photonic transmitter for intra-datacenter optical interconnects," *Optics Express* **27**, 10258–10268 (2019).

- [54] D. Dai, "Advanced passive silicon photonic devices with asymmetric waveguide structures," *Proceedings of the IEEE* **106**, 2117–2143 (2018).
- [55] "Luxtera," <http://www.luxtera.com/>.
- [56] "Intel," <http://www.intel.com/>.
- [57] J. T. Robinson, L. Chen, and M. Lipson, "On-chip gas detection in silicon optical microcavities," *Optics Express* **16**, 4296–4301 (2008).
- [58] W.-C. Lai, S. Chakravarty, X. Wang, C. Lin, and R. T. Chen, "On-chip methane sensing by near-IR absorption signatures in a photonic crystal slot waveguide," *Optics Letters* **36**, 984–986 (2011).
- [59] K. Misiakos, I. Raptis, E. Makarona, A. Botsialas, A. Salapatas, P. Oikonomou, A. Psarouli, P. Petrou, S. Kakabakos, K. Tukkiniemi, M. Sapanen, and G. Jobst, "All-silicon monolithic Mach-Zehnder interferometer as a refractive index and bio-chemical sensor," *Optics Express* **22**, 26803–26813 (2014).
- [60] M. Nedeljkovic, A. V. Velasco, A. Z. Khokhar, A. Delage, P. Cheben, and G. Z. Mashanovich, "Mid-infrared silicon-on-insulator Fourier-transform spectrometer chip," *IEEE Photonics Technology Letters* **28**, 528–531 (2016).
- [61] Y.-C. Chang, P. Wägli, V. Paeder, A. Homsy, L. Hvozdar, P. van der Wal, J. Di Francesco, N. F. de Rooij, and H. Peter Herzig, "Cocaine detection by a mid-infrared waveguide integrated with a microfluidic chip," *Lab on a Chip* **12**, 3020–3023 (2012).
- [62] T. Hu, B. Dong, X. Luo, T.-Y. Liow, J. Song, C. Lee, and G.-Q. Lo, "Silicon photonic platforms for mid-infrared applications [Invited]," *Photonics Research* **5**, 417–430 (2017).
- [63] C. Ranacher, C. Consani, A. Tortschanoff, R. Jannesari, M. Bergmeister, T. Grille, and B. Jakoby, "Mid-infrared absorption gas sensing using a silicon strip waveguide," *Sensors and Actuators A: Physical* **277**, 117–123 (2018).
- [64] Q. Liu, J. M. Ramirez, V. Vakarín, X. Le Roux, A. Ballabio, J. Frigerio, D. Chrastina, G. Isella, D. Bouville, L. Vivien, C. A. Ramos, and D. Marris-Morini, "Mid-infrared sensing between 5.2 and 6.6 μm wavelengths using Ge-rich SiGe waveguides [Invited]," *Optical Materials Express* **8**, 1305–1312 (2018).
- [65] N. K. Hon, R. Soref, and B. Jalali, "The third-order nonlinear optical coefficients of Si, Ge, and $\text{Si}_{1-x}\text{Ge}_x$ in the midwave and longwave infrared," *Journal of Applied Physics* **110**, 011301 (2011).
- [66] R. Soref, "Mid-infrared photonics in silicon and germanium," *Nature Photonics* **4**, 495–497 (2010).
- [67] Y. Zou, S. Chakravarty, C.-J. Chung, X. Xu, and R. T. Chen, "Mid-infrared silicon photonic waveguides and devices [Invited]," *Photonics Research* **6**, 254–276 (2018).
- [68] D. Marris-Morini, V. Vakarín, J. M. Ramirez, Q. Liu, A. Ballabio, J. Frigerio, M. Montesinos, C. Alonso-Ramos, X. Le Roux, S. Serna, D. Benedikovic, D. Chrastina, L. Vivien, and G. Isella, "Germanium-based integrated photonics from near- to mid-infrared applications," *Nanophotonics* **7**, 1781–1793 (2018).
- [69] T. Baehr-Jones, A. Spott, R. Ilic, A. Spott, B. Penkov, W. Asher, and M. Hochberg, "Silicon-on-sapphire integrated waveguides for the mid-infrared," *Optics Express* **18**, 12127–12135 (2010).
- [70] S. Khan, J. Chiles, J. Ma, and S. Fathpour, "Silicon-on-nitride waveguides for mid- and near-infrared integrated photonics," *Applied Physics Letters* **102**, 121104 (2013).

- [71] G. Z. Mashanovich, F. Y. Gardes, D. J. Thomson, Y. Hu, K. Li, M. Nedeljkovic, J. Soler Penades, A. Z. Khokhar, C. J. Mitchell, S. Stankovic, R. Topley, S. A. Reynolds, Y. Wang, B. Troia, V. M. N. Passaro, C. G. Littlejohns, T. Dominguez Bucio, P. R. Wilson, and G. T. Reed, "Silicon photonic waveguides and devices for near- and mid-IR applications," *IEEE Journal of Selected Topics in Quantum Electronics* **21**, 8200112 (2015).
- [72] J. M. Ramirez, V. Vakarín, C. Gilles, J. Frigerio, A. Ballabio, P. Chaisakul, X. L. Roux, C. Alonso-Ramos, G. Maisons, L. Vivien, M. Carras, G. Isella, and D. Marris-Morini, "Low-loss Ge-rich $\text{Si}_{0.2}\text{Ge}_{0.8}$ waveguides for mid-infrared photonics," *Optics Letters* **42**, 105–108 (2017).
- [73] J. M. Ramirez, Q. Liu, V. Vakarín, J. Frigerio, A. Ballabio, X. Le Roux, D. Bouville, L. Vivien, G. Isella, and D. Marris-Morini, "Graded SiGe waveguides with broadband low-loss propagation in the mid infrared," *Optics Express* **26**, 870–877 (2018).
- [74] Z. Cheng, X. Chen, C. Y. Wong, K. Xu, and H. K. Tsang, "Mid-infrared suspended membrane waveguide and ring resonator on silicon-on-insulator," *IEEE Photonics Journal* **4**, 1510–1519 (2012).
- [75] J. Soler Penadés, C. Alonso-Ramos, A. Z. Khokhar, M. Nedeljkovic, L. A. Boodhoo, A. Ortega-Moñux, I. Molina-Fernández, P. Cheben, and G. Z. Mashanovich, "Suspended SOI waveguide with sub-wavelength grating cladding for mid-infrared," *Optics Letters* **39**, 5661–5664 (2014).
- [76] W. Zhou, Z. Cheng, X. Wu, X. Sun, and H. K. Tsang, "Fully suspended slot waveguide platform," *Journal of Applied Physics* **123**, 063103 (2018).
- [77] A. Osman, M. Nedeljkovic, J. Soler Penades, Y. Wu, Z. Qu, A. Z. Khokhar, K. Debnath, and G. Z. Mashanovich, "Suspended low-loss germanium waveguides for the longwave infrared," *Optics Letters* **43**, 5997–6000 (2018).
- [78] Q. Liu, J. M. Ramirez, V. Vakarín, X. Le Roux, C. Alonso-Ramos, J. Frigerio, A. Ballabio, E. Talamas Simola, D. Bouville, L. Vivien, G. Isella, and D. Marris-Morini, "Integrated broadband dual-polarization Ge-rich SiGe mid-infrared Fourier-transform spectrometer," *Optics Letters* **43**, 5021–5024 (2018).
- [79] J. Soler Penadés, A. Sánchez-Postigo, M. Nedeljkovic, A. Ortega-Moñux, J. G. Wangüemert-Pérez, Y. Xu, R. Halir, Z. Qu, A. Z. Khokhar, A. Osman, W. Cao, C. G. Littlejohns, P. Cheben, I. Molina-Fernández, and G. Z. Mashanovich, "Suspended silicon waveguides for long-wave infrared wavelengths," *Optics Letters* **43**, 795–798 (2018).
- [80] A. Sánchez-Postigo, J. G. Wangüemert-Pérez, J. Soler Penadés, A. Ortega-Moñux, M. Nedeljkovic, R. Halir, F. El Mokhtari Mimun, Y. Xu Cheng, Z. Qu, A. Z. Khokhar, A. Osman, W. Cao, C. G. Littlejohns, P. Cheben, G. Z. Mashanovich, and Í. Molina-Fernández, "Mid-infrared suspended waveguide platform and building blocks," *IET Optoelectronics* **13**, 55–61 (2019).
- [81] A. Sánchez-Postigo, A. Ortega-Moñux, D. Pereira-Martín, Í. Molina-Fernández, R. Halir, P. Cheben, J. Soler Penadés, M. Nedeljkovic, G. Z. Mashanovich, and J. G. Wangüemert-Pérez, "Design of a suspended germanium micro-antenna for efficient fiber-chip coupling in the long-wavelength mid-infrared range," *Optics Express* **27**, 22302–22315 (2019).
- [82] A. Sánchez-Postigo, J. Gonzalo Wangüemert-Pérez, J. M. Luque-González, Í. Molina-Fernández, P. Cheben, C. A. Alonso-Ramos, R. Halir, J. H. Schmid, and A. Ortega-Moñux, "Broadband fiber-chip zero-order surface grating coupler with 0.4 dB efficiency," *Optics Letters* **41**, 3013–3016 (2016).
- [83] S. A. Miller, M. Yu, X. Ji, A. G. Griffith, J. Cardenas, A. L. Gaeta, and M. Lipson, "Low-loss silicon platform for broadband mid-infrared photonics," *Optica* **4**, 707–712 (2017).

- [84] D. Chandler-Horowitz and P. M. Amirtharaj, "High-accuracy, midinfrared ($450 \text{ cm}^{-1} \leq \omega \leq 4000 \text{ cm}^{-1}$) refractive index values of silicon," *Journal of Applied Physics* **97**, 123526 (2005).
- [85] I. H. Malitson, "Interspecimen comparison of the refractive index of fused silica," *Journal of the Optical Society of America* **55**, 1205–1209 (1965).
- [86] M. Sobhy, M. Gad, Y. M. Sabry, and D. Khalil, "Optimization of silicon on silica waveguides for mid-infrared applications at $4.28 \mu\text{m}$," in "Proceedings Volume 10923, Silicon Photonics XIV," (SPIE, 2019).
- [87] G. Z. Mashanovich, M. M. Milošević, M. Nedeljkovic, N. Owens, B. Xiong, E. J. Teo, and Y. Hu, "Low loss silicon waveguides for the mid-infrared," *Optics Express* **19**, 7112–7119 (2011).
- [88] A. G. Griffith, R. K. Lau, J. Cardenas, Y. Okawachi, A. Mohanty, R. Fain, Y. H. D. Lee, M. Yu, C. T. Phare, C. B. Poitras, A. L. Gaeta, and M. Lipson, "Silicon-chip mid-infrared frequency comb generation," *Nature Communications* **6**, 6299 (2015).
- [89] M. M. Milošević, M. Nedeljkovic, T. M. Ben Masaud, E. Jaberansary, H. M. H. Chong, N. G. Emerson, G. T. Reed, and G. Z. Mashanovich, "Silicon waveguides and devices for the mid-infrared," *Applied Physics Letters* **101**, 121105 (2012).
- [90] B. Troia, J. Soler Penadés, Z. Qu, A. Z. Khokhar, A. Osman, Y. Wu, C. Stirling, M. Nedeljkovic, V. M. N. Passaro, and G. Z. Mashanovich, "Silicon ring resonator-coupled Mach–Zehnder interferometers for the Fano resonance in the mid-IR," *Applied Optics* **56**, 8769–8776 (2017).
- [91] M. Nedeljkovic, A. Z. Khokhar, Y. Hu, X. Chen, J. Soler Penadés, S. Stankovic, H. M. H. Chong, D. J. Thomson, F. Y. Gardes, G. T. Reed, and G. Z. Mashanovich, "Silicon photonic devices and platforms for the mid-infrared," *Optical Materials Express* **3**, 1205–1214 (2013).
- [92] Y. Hu, T. Li, D. J. Thomson, X. Chen, J. Soler Penadés, A. Z. Khokhar, C. J. Mitchell, G. T. Reed, and G. Z. Mashanovich, "Mid-infrared wavelength division (de)multiplexer using an interleaved angled multimode interferometer on the silicon-on-insulator platform," *Optics Letters* **39**, 1406–1409 (2014).
- [93] E. Ryckeboer, A. Gassenq, M. Muneeb, N. Hattasan, S. Pathak, L. Cerutti, J. Rodriguez, E. Tournié, W. Bogaerts, R. Baets, and G. Roelkens, "Silicon-on-insulator spectrometers with integrated GaInAsSb photodiodes for wide-band spectroscopy from 1510 to 2300 nm," *Optics Express* **21**, 6101–6108 (2013).
- [94] M. Muneeb, X. Chen, P. Verheyen, G. Lepage, S. Pathak, E. Ryckeboer, A. Malik, B. Kuyken, M. Nedeljkovic, J. Van Campenhout, G. Z. Mashanovich, and G. Roelkens, "Demonstration of Silicon-on-insulator mid-infrared spectrometers operating at $3.8 \mu\text{m}$," *Optics Express* **21**, 11659–11669 (2013).
- [95] N. Hattasan, B. Kuyken, F. Leo, E. M. P. Ryckeboer, D. Vermeulen, and G. Roelkens, "High-efficiency SOI fiber-to-chip grating couplers and low-loss waveguides for the short-wave infrared," *IEEE Photonics Technology Letters* **24**, 1536–1538 (2012).
- [96] I. H. Malitson, "Refraction and dispersion of synthetic sapphire," *Journal of the Optical Society of America* **52**, 1377–1379 (1962).
- [97] D. J. Albares and R. A. Soref, "Silicon-on-sapphire waveguides," in "Proceedings Volume 0704, Integrated Optical Circuit Engineering IV," (SPIE, 1987).
- [98] R. Shankar, I. Bulu, and M. Lončar, "Integrated high-quality factor silicon-on-sapphire ring resonators for the mid-infrared," *Applied Physics Letters* **102**, 051108 (2013).
- [99] A. Spott, Y. Liu, T. Baehr-Jones, R. Ilic, and M. Hochberg, "Silicon waveguides and ring resonators at $5.5 \mu\text{m}$," *Applied Physics Letters* **97**, 213501 (2010).

- [100] C. Y. Wong, Z. Cheng, X. Chen, K. Xu, C. K. Y. Fung, Y. M. Chen, and H. K. Tsang, "Characterization of mid-infrared silicon-on-sapphire microring resonators with thermal tuning," *IEEE Photonics Journal* **4**, 1095–1102 (2012).
- [101] S. Kalchmair, R. Shankar, S. Kita, C. Mittag, I. Bulu, and M. Lončar, "Cascaded four-wave mixing in silicon-on-sapphire microresonators at $\lambda=4.5\ \mu\text{m}$," in "CLEO: 2015, OSA Technical Digest (online)," (Optical Society of America, 2015), p. STu2I.3.
- [102] Y. Zou, H. Subbaraman, S. Chakravarty, X. Xu, A. Hosseini, W.-C. Lai, P. Wray, and R. T. Chen, "Grating-coupled silicon-on-sapphire integrated slot waveguides operating at mid-infrared wavelengths," *Optics Letters* **39**, 3070–3073 (2014).
- [103] Y. Yue, L. Zhang, H. Huang, R. G. Beausoleil, and A. E. Willner, "Silicon-on-nitride waveguide with ultralow dispersion over an octave-spanning mid-infrared wavelength range," *IEEE Photonics Journal* **4**, 126–132 (2012).
- [104] C. Lacava, S. Stankovic, A. Z. Khokhar, T. D. Bucio, F. Y. Gardes, G. T. Reed, D. J. Richardson, and P. Petropoulos, "Si-rich silicon nitride for nonlinear signal processing applications," *Scientific Reports* **7**, 22 (2017).
- [105] P. T. Lin, V. Singh, Y. Cai, L. C. Kimerling, and A. Agarwal, "Air-clad silicon pedestal structures for broadband mid-infrared microphotronics," *Optics Letters* **38**, 1031–1033 (2013).
- [106] J. Chiles and S. Fathpour, "Mid-infrared integrated waveguide modulators based on silicon-on-lithium-niobate photonics," *Optica* **1**, 350–355 (2014).
- [107] Y. Chen, H. Lin, J. Hu, and M. Li, "Heterogeneously integrated silicon photonics for the mid-infrared and spectroscopic sensing," *ACS Nano* **8**, 6955–6961 (2014).
- [108] J. Chiles and S. Fathpour, "Single-mode and single-polarization photonics with anchored-membrane waveguides," *Optics Express* **24**, 19337–19343 (2016).
- [109] K. Gallacher, R. Millar, U. Griškevičiūtė, L. Baldassarre, M. Sorel, M. Ortolani, and D. J. Paul, "Low loss Ge-on-Si waveguides operating in the 8–14 μm atmospheric transmission window," *Optics Express* **26**, 25667–25675 (2018).
- [110] M. Nedeljkovic, J. S. Penades, C. J. Mitchell, A. Z. Khokhar, S. Stankovic, T. D. Bucio, C. G. Littlejohns, F. Y. Gardes, and G. Z. Mashanovich, "Surface-grating-coupled low-loss Ge-on-Si rib waveguides and multimode interferometers," *IEEE Photonics Technology Letters* **27**, 1040–1043 (2015).
- [111] A. Malik, M. Muneeb, Y. Shimura, J. Van Campenhout, R. Loo, and G. Roelkens, "Germanium-on-silicon mid-infrared waveguides and Mach-Zehnder interferometers," in "2013 IEEE Photonics Conference," (IEEE, 2013).
- [112] Y.-C. Chang, V. Paeder, L. Hvozdar, J.-M. Hartmann, and H. P. Herzig, "Low-loss germanium strip waveguides on silicon for the mid-infrared," *Optics Letters* **37**, 2883–2885 (2012).
- [113] A. Malik, S. Dwivedi, L. Van Landschoot, M. Muneeb, Y. Shimura, G. Lepage, J. Van Campenhout, W. Vanherle, T. Van Opstal, R. Loo, and G. Roelkens, "Ge-on-Si and Ge-on-SOI thermo-optic phase shifters for the mid-infrared," *Optics Express* **22**, 28479–28488 (2014).
- [114] C. Grillet, P. Ma, B. Luther-Davies, D. Hudson, C. Monat, S. Madden, D. J. Moss, M. Brun, P. Labeye, S. Ortiz, and S. Nicoletti, "Low loss SiGe waveguides in the MID-IR," in "2013 Conference on Lasers & Electro-Optics Europe & International Quantum Electronics Conference CLEO EUROPE/IQEC," vol. 7112 (IEEE, 2013).
- [115] J. Favreau, C. Durantin, J.-M. Fédéli, S. Boutami, and G.-H. Duan, "Suspended mid-infrared fiber-to-chip grating couplers for SiGe waveguides," in "Optical Interconnects XVI," vol. 9753 (2016).



- [116] M. Brun, P. Labeye, G. Grand, J.-M. Hartmann, F. Boulila, M. Carras, and S. Nicoletti, "Low loss SiGe graded index waveguides for mid-IR applications," *Optics Express* **22**, 508–518 (2014).
- [117] P. Barritault, M. Brun, P. Labeye, J.-M. Hartmann, F. Boulila, M. Carras, and S. Nicoletti, "Design, fabrication and characterization of an AWG at 4.5 μm ," *Optics Express* **23**, 26168–26181 (2015).
- [118] L. Carletti, P. Ma, Y. Yu, B. Luther-Davies, D. Hudson, C. Monat, R. Orobtcouk, S. Madden, D. J. Moss, M. Brun, S. Ortiz, P. Labeye, S. Nicoletti, and C. Grillet, "Nonlinear optical response of low loss silicon germanium waveguides in the mid-infrared," *Optics Express* **23**, 8261–8271 (2015).
- [119] M. Sinobad, C. Monat, B. Luther-davies, P. Ma, S. Madden, D. J. Moss, A. Mitchell, D. Alioux, R. Orobtcouk, S. Boutami, J.-M. Hartmann, J.-M. Fedeli, and C. Grillet, "Mid-infrared octave spanning supercontinuum generation to 8.5 μm in silicon-germanium waveguides," *Optica* **5**, 360–366 (2018).
- [120] V. Vakarin, J. M. Ramírez, J. Frigerio, A. Ballabio, X. Le Roux, Q. Liu, D. Bouville, L. Vivien, G. Isella, and D. Marris-Morini, "Ultra-wideband Ge-rich silicon germanium integrated Mach-Zehnder interferometer for mid-infrared spectroscopy," *Optics Letters* **42**, 3482–3485 (2017).
- [121] J. M. Ramirez, Q. Liu, V. Vakarin, X. Le Roux, J. Frigerio, A. Ballabio, C. Alonso-Ramos, E. T. Simola, L. Vivien, G. Isella, and D. Marris-Morini, "Broadband integrated racetrack ring resonators for long-wave infrared photonics," *Optics Letters* **44**, 407–410 (2019).
- [122] V. Vakarin, W. N. Ye, J. M. Ramírez, Q. Liu, J. Frigerio, A. Ballabio, G. Isella, L. Vivien, C. Alonso-Ramos, P. Cheben, and D. Marris-Morini, "Ultra-wideband Ge-rich silicon germanium mid-infrared polarization rotator with mode hybridization flattening," *Optics Express* **27**, 9838–9847 (2019).
- [123] Q. Liu, J. M. Ramírez, V. Vakarin, D. Benedikovic, C. Alonso-Ramos, J. Frigerio, A. Ballabio, G. Isella, L. Vivien, and D. Marris-Morini, "7.5 μm wavelength fiber-chip grating couplers for Ge-rich SiGe photonics integrated circuits," in "Silicon Photonics: From Fundamental Research to Manufacturing," (SPIE, 2018).
- [124] W. Li, P. Anantha, S. Bao, K. H. Lee, X. Guo, T. Hu, L. Zhang, H. Wang, R. Soref, and C. S. Tan, "Germanium-on-silicon nitride waveguides for mid-infrared integrated photonics," *Applied Physics Letters* **109**, 241101 (2016).
- [125] J. Kang, X. Yu, M. Takenaka, and S. Takagi, "Impact of thermal annealing on Ge-on-Insulator substrate fabricated by wafer bonding," *Materials Science in Semiconductor Processing* **42**, 259–263 (2016).
- [126] J. Kang, M. Takenaka, and S. Takagi, "Novel Ge waveguide platform on Ge-on-insulator wafer for mid-infrared photonic integrated circuits," *Optics Express* **24**, 11855–11864 (2016).
- [127] J. Kang, S. Takagi, and M. Takenaka, "Design and characterization of Ge passive waveguide components on Ge-on-insulator wafer for mid-infrared photonics," *Japanese Journal of Applied Physics* **57**, 042202 (2018).
- [128] C. P. Ho, Z. Zhao, Q. Li, S. Takagi, and M. Takenaka, "Mid-infrared tunable Vernier filter on a germanium-on-insulator photonic platform," *Optics Letters* **44**, 2779–2782 (2019).
- [129] P. T. Lin, V. Singh, H.-Y. G. Lin, T. Tiwald, L. C. Kimerling, and A. M. Agarwal, "Low-stress silicon nitride platform for mid-infrared broadband and monolithically integrated microphotonics," *Advanced Optical Materials* **1**, 732–739 (2013).
- [130] P. Tai Lin, V. Singh, L. Kimerling, and A. Murthy Agarwal, "Planar silicon nitride mid-infrared devices," *Applied Physics Letters* **102**, 251121 (2013).

- [131] J. Cardenas, M. Yu, Y. Okawachi, C. B. Poitras, R. K. W. Lau, A. Dutt, A. L. Gaeta, and M. Lipson, "Optical nonlinearities in high-confinement silicon carbide waveguides," *Optics Letters* **40**, 4138–4141 (2015).
- [132] P. T. Lin, H. Jung, L. C. Kimerling, A. Agarwal, and H. X. Tang, "Low-loss aluminium nitride thin film for mid-infrared microphotronics," *Laser & Photonics Reviews* **8**, L23–L28 (2014).
- [133] B. Dong, X. Luo, S. Zhu, M. Li, D. Hasan, L. Zhang, S. J. Chua, J. Wei, Y. Chang, G.-Q. Lo, K. W. Ang, D.-L. Kwong, and C. Lee, "Aluminum nitride on insulator (AlNOI) platform for mid-infrared photonics," *Optics Letters* **44**, 73–76 (2019).
- [134] R. Grille, G. Martin, L. Labadie, B. Arezki, P. Kern, T. Lewi, A. Tsun, and A. Katzir, "Single mode mid-infrared silver halide asymmetric flat waveguide obtained from crystal extrusion," *Optics Express* **17**, 12516–12522 (2009).
- [135] T. Lewi and A. Katzir, "Silver halide single-mode strip waveguides for the mid-infrared," *Optics Letters* **37**, 2733–2735 (2012).
- [136] C. Vigreux-Bercovici, E. Bonhomme, A. Pradel, J.-E. Broquin, L. Labadie, and P. Kern, "Transmission measurement at $10.6 \mu\text{m}$ of $\text{Te}_2\text{As}_3\text{Se}_5$ rib waveguides on As_2S_3 substrate," *Applied Physics Letters* **90**, 011110 (2007).
- [137] H. Lin, L. Li, Y. Zou, S. Danto, J. D. Musgraves, K. Richardson, S. Kozacik, M. Murakowski, D. Prather, P. T. Lin, V. Singh, A. Agarwal, L. C. Kimerling, and J. Hu, "Demonstration of high-Q mid-infrared chalcogenide glass-on-silicon resonators," *Optics Letters* **38**, 1470–1472 (2013).
- [138] A. Gutierrez-Arroyo, E. Baudet, L. Bodiou, J. Lemaitre, I. Hardy, F. Fajjan, B. Bureau, V. Nazabal, and J. Charrier, "Optical characterization at $7.7 \mu\text{m}$ of an integrated platform based on chalcogenide waveguides for sensing applications in the mid-infrared," *Optics Express* **24**, 23109–23117 (2016).
- [139] V. Mittal, M. Nedeljkovic, D. J. Rowe, G. S. Murugan, and J. S. Wilkinson, "Chalcogenide glass waveguides with paper-based fluidics for mid-infrared absorption spectroscopy," *Optics Letters* **43**, 2913–2916 (2018).
- [140] X. Wang, J. Antoszewski, G. Putrino, W. Lei, L. Faraone, and B. Mizaikoff, "Mercury-cadmium-telluride waveguides – a novel strategy for on-chip mid-infrared sensors," *Analytical Chemistry* **85**, 10648–10652 (2013).
- [141] C. Xin, H. Wu, Y. Xie, S. Yu, N. Zhou, Z. Shi, X. Guo, and L. Tong, "CdTe microwires as mid-infrared optical waveguides," *Optics Express* **26**, 10944–10952 (2018).
- [142] M. Sieger, F. Balluff, X. Wang, S. S. Kim, L. Leidner, G. Gauglitz, and B. Mizaikoff, "On-chip integrated mid-infrared GaAs/AlGaAs Mach-Zehnder interferometer," *Analytical Chemistry* **85**, 3050–3052 (2013).
- [143] N.-L. Tran, M. Malerba, A. Talneau, G. Biasiol, O. Ouznali, A. Bousseksou, J.-M. Manceau, and R. Colombelli, "III-V on CaF_2 : a possible waveguiding platform for mid-IR photonic devices," *Optics Express* **27**, 1672–1682 (2019).
- [144] Z. Cheng, X. Chen, C. Y. Wong, K. Xu, C. K. Y. Fung, Y. M. Chen, and H. K. Tsang, "Focusing subwavelength grating coupler for mid-infrared suspended membrane waveguide," *Optics Letters* **37**, 1217–1219 (2012).
- [145] T.-H. Xiao, Z. Zhao, W. Zhou, C.-Y. Chang, S. Y. Set, M. Takenaka, H. K. Tsang, Z. Cheng, and K. Goda, "Mid-infrared high-Q germanium microring resonator," *Optics Letters* **43**, 2885–2888 (2018).

- [146] G. Z. Mashanovich, M. Nedeljkovic, J. Soler-Penades, Z. Qu, W. Cao, A. Osman, Y. Wu, C. J. Stirling, Y. Qi, Y. Cheng, L. Reid, C. G. Littlejohns, J. Kang, Z. Zhao, M. Takenaka, T. Li, Z. Zhou, F. Y. Gardes, D. J. Thomson, and G. T. Reed, "Group IV mid-infrared photonics [Invited]," *Optical Materials Express* **8**, 2276–2286 (2018).
- [147] J. Soler Penadés, A. Ortega-Moñux, M. Nedeljkovic, J. G. Wangüemert-Pérez, R. Halir, A. Z. Khokhar, C. Alonso-Ramos, Z. Qu, I. Molina-Fernández, P. Cheben, and G. Z. Mashanovich, "Suspended silicon mid-infrared waveguide devices with subwavelength grating metamaterial cladding," *Optics Express* **24**, 22908–22916 (2016).
- [148] J. Chiles, S. Khan, J. Ma, and S. Fathpour, "High-contrast, all-silicon waveguiding platform for ultra-broadband mid-infrared photonics," *Applied Physics Letters* **103**, 151106 (2013).
- [149] Y. Wei, G. Li, Y. Hao, Y. Li, J. Yang, M. Wang, and X. Jiang, "Long-wave infrared 1×2 MMI based on air-gap beneath silicon rib waveguides," *Optics Express* **19**, 15803–15809 (2011).
- [150] J. Soler Penadés, A. Khokhar, M. Nedeljkovic, and G. Mashanovich, "Low-loss mid-infrared SOI slot waveguides," *IEEE Photonics Technology Letters* **27**, 1197–1199 (2015).
- [151] F. Li, S. D. Jackson, C. Grillet, E. Magi, D. Hudson, S. J. Madden, Y. Moghe, C. O'Brien, A. Read, S. G. Duvall, P. Atanackovic, B. J. Eggleton, and D. J. Moss, "Low propagation loss silicon-on-sapphire waveguides for the mid-infrared," *Optics Express* **19**, 15212–15220 (2011).
- [152] L. Shen, N. Healy, C. J. Mitchell, J. S. Penades, M. Nedeljkovic, G. Z. Mashanovich, and A. C. Peacock, "Mid-infrared all-optical modulation in low-loss germanium-on-silicon waveguides," *Optics Letters* **40**, 268–271 (2015).
- [153] M. Nedeljkovic, J. S. Penades, V. Mittal, G. S. Murugan, A. Z. Khokhar, C. Littlejohns, L. G. Carpenter, C. B. E. Gawith, J. S. Wilkinson, and G. Z. Mashanovich, "Germanium-on-silicon waveguides operating at mid-infrared wavelengths up to $85 \mu\text{m}$," *Optics Express* **25**, 27431–27441 (2017).
- [154] U. Younis, S. K. Vanga, A. E.-J. Lim, P. G.-Q. Lo, A. A. Bettiol, and K.-W. Ang, "Germanium-on-SOI waveguides for mid-infrared wavelengths," *Optics Express* **24**, 11987–11993 (2016).
- [155] R. Halir, P. J. Bock, P. Cheben, A. Ortega-Moñux, C. Alonso-Ramos, J. H. Schmid, J. Lapointe, D.-X. Xu, J. G. Wangüemert-Pérez, Í. Molina-Fernández, and S. Janz, "Waveguide sub-wavelength structures: a review of principles and applications," *Laser & Photonics Reviews* **9**, 25–49 (2015).
- [156] P. Cheben, R. Halir, J. H. Schmid, H. A. Atwater, and D. R. Smith, "Subwavelength integrated photonics," *Nature* **560**, 565–572 (2018).
- [157] R. Halir, A. Ortega-Moñux, D. Benedikovic, G. Z. Mashanovich, J. G. Wangüemert-Pérez, J. H. Schmid, Í. Molina-Fernández, and P. Cheben, "Subwavelength-grating metamaterial structures for silicon photonic devices," *Proceedings of the IEEE* **106**, 2144–2157 (2018).
- [158] T. Visser, H. Blok, B. Demeulenaere, and D. Lenstra, "Confinement factors and gain in optical amplifiers," *IEEE Journal of Quantum Electronics* **33**, 1763–1766 (1997).
- [159] "Mode Solvers – Waveguide CAD Software – FIMMWAVE," <https://www.photond.com/products/fimmwave.htm>.
- [160] "FemSIM - Generalized Mode Solver - Finite Element Method," <https://www.synopsys.com/optical-solutions/rsoft/passive-device-femsim.html>.
- [161] S. M. Rytov, "Electromagnetic properties of a finely stratified medium," *Soviet Physics JETP* **2**, 466–475 (1956).

- [162] J. M. Luque-González, A. Herrero-Bermello, A. Ortega-Moñux, Í. Molina-Fernández, A. V. Velasco, P. Cheben, J. H. Schmid, S. Wang, and R. Halir, "Tilted subwavelength gratings: controlling anisotropy in metamaterial nanophotonic waveguides," *Optics Letters* **43**, 4691–4694 (2018).
- [163] "FDTD Simulation Software - FullWAVE - Finite Difference Time Domain — RSoft Products," <https://www.synopsys.com/optical-solutions/rsoft/passive-device-fullwave.html>.
- [164] J. Gonzalo Wangüemert-Pérez, P. Cheben, A. Ortega-Moñux, C. Alonso-Ramos, D. Pérez-Galacho, R. Halir, I. Molina-Fernández, D.-X. Xu, and J. H. Schmid, "Evanescent field waveguide sensing with subwavelength grating structures in silicon-on-insulator," *Optics Letters* **39**, 4442–4445 (2014).
- [165] V. A. Mandelshtam and H. S. Taylor, "Harmonic inversion of time signals and its applications," *The Journal of Chemical Physics* **107**, 6756–6769 (1997).
- [166] S. Otto, A. Rennings, K. Solbach, and C. Caloz, "Complex frequency versus complex propagation constant modeling and Q-balancing in periodic structures," in "2012 IEEE/MTT-S International Microwave Symposium Digest," (IEEE, 2012).
- [167] A. Taflove and S. C. Hagness, "Calculation of band structure," in "Computational Electrodynamics: The Finite-Difference Time-Domain Method," (Artech House, 2005), chap. Photonics, pp. 774–787, 3rd ed.
- [168] L. Zavargo-Peche, A. Ortega-Moñux, J. G. Wangüemert-Pérez, and Í. Molina-Fernández, "Fourier based combined techniques to design novel sub-wavelength optical integrated devices," *Progress In Electromagnetics Research* **123**, 447–465 (2012).
- [169] "Tanner L-Edit IC Layout — Mentor Graphics," <https://www.mentor.com/tanneredit/>.
- [170] Y. A. Vlasov and S. J. McNab, "Losses in single-mode silicon-on-insulator strip waveguides and bends," *Optics Express* **12**, 1622–1631 (2004).
- [171] J. Soler Penadés, "Group IV mid-infrared devices for sensing," Ph.D. thesis, University of Southampton (2017).
- [172] D. Marcuse, "Loss analysis of single-mode fiber splices," *The Bell System Technical Journal* **56**, 703–718 (1977).
- [173] L. Soldano and E. Pennings, "Optical multi-mode interference devices based on self-imaging: principles and applications," *Journal of Lightwave Technology* **13**, 615–627 (1995).
- [174] C.-L. Chen, *Foundations for Guided-Wave Optics* (John Wiley & Sons, Inc., 2006).
- [175] P. Cheben, J. H. Schmid, S. Wang, D.-X. Xu, M. Vachon, S. Janz, J. Lapointe, Y. Painchaud, and M.-J. Picard, "Broadband polarization independent nanophotonic coupler for silicon waveguides with ultra-high efficiency," *Optics Express* **23**, 22553–22563 (2015).
- [176] V. R. Almeida, R. R. Panepucci, and M. Lipson, "Nanotaper for compact mode conversion." *Optics Letters* **28**, 1302–1304 (2003).
- [177] A. Dewanjee, J. N. Caspers, J. S. Aitchison, and M. Mojahedi, "Demonstration of a compact bilayer inverse taper coupler for Si-photonics with enhanced polarization insensitivity," *Optics Express* **24**, 28194–28203 (2016).
- [178] M. Papes, P. Cheben, D. Benedikovic, J. H. Schmid, J. Pond, R. Halir, A. Ortega-Moñux, G. Wangüemert-Pérez, W. N. Ye, D.-X. Xu, S. Janz, M. Dado, and V. Vašinek, "Fiber-chip edge coupler with large mode size for silicon photonic wire waveguides," *Optics Express* **24**, 5026–5038 (2016).
- [179] T. Tamir and S. T. Peng, "Analysis and design of grating couplers," *Applied Physics* **14**, 235–254 (1977).



- [180] D. Taillaert, P. Bienstman, and R. Baets, "Compact efficient broadband grating coupler for silicon-on-insulator waveguides," *Optics Letters* **29**, 2749–2751 (2004).
- [181] P. K. Tien, R. Ulrich, and R. J. Martin, "Modes of propagating light waves in thin deposited semiconductor films," *Applied Physics Letters* **14**, 291–294 (1969).
- [182] R. Ulrich, "Theory of the prism–film coupler by plane-wave analysis," *Journal of the Optical Society of America* **60**, 1337–1350 (1970).
- [183] R. Ulrich, "Optimum excitation of optical surface waves," *Journal of the Optical Society of America* **61**, 1467–1477 (1971).
- [184] R. Ulrich and R. Torge, "Measurement of thin film parameters with a prism coupler," *Applied Optics* **12**, 2901–2908 (1973).
- [185] R. Halir, P. Cheben, S. Janz, D.-X. Xu, Í. Molina-Fernández, and J. G. Wangüemert-Pérez, "Waveguide grating coupler with subwavelength microstructures," *Optics Letters* **34**, 1408–1410 (2009).
- [186] A. Bozzola, L. Carroll, D. Gerace, I. Cristiani, and L. C. Andreani, "Optimising apodized grating couplers in a pure SOI platform to -0.5 dB coupling efficiency," *Optics Express* **23**, 16289–16304 (2015).
- [187] G. Floquet, "Sur les équations différentielles linéaires à coefficients périodiques," *Annales scientifiques de l'École normale supérieure* **12**, 47–88 (1883).
- [188] F. Bloch, "Über die Quantenmechanik der Elektronen in Kristallgittern," *Zeitschrift für Physik* **52**, 555–600 (1929).
- [189] C. Alonso-Ramos, X. Le Roux, J. Zhang, D. Benedikovic, V. Vakarin, E. Durán-Valdeiglesias, D. Oser, D. Pérez-Galacho, F. Mazeas, L. Labonté, S. Tanzilli, É. Cassan, D. Marris-Morini, P. Cheben, and L. Vivien, "Diffraction-less propagation beyond the sub-wavelength regime: a new type of nanophotonic waveguide," *Scientific Reports* **9**, 5347 (2019).
- [190] J. D. Joannopoulos, S. Johnson, J. N. Winn, and R. D. Meade, *Photonic Crystals: Molding the Flow of Light* (Princeton University Press, 2011).
- [191] C. Alonso-Ramos, A. Ortega-Moñux, I. Molina-Fernández, P. Cheben, L. Zavargo-Peche, and R. Halir, "Efficient fiber-to-chip grating coupler for micrometric SOI rib waveguides," *Optics Express* **18**, 15189–15200 (2010).
- [192] C. Alonso-Ramos, A. Ortega-Moñux, L. Zavargo-Peche, R. Halir, J. de Oliva-Rubio, I. Molina-Fernández, P. Cheben, D.-X. Xu, S. Janz, N. Kim, and B. Lamontagne, "Single-etch grating coupler for micrometric silicon rib waveguides," *Optics Letters* **36**, 2647–2649 (2011).
- [193] F. Van Laere, G. Roelkens, M. Ayre, J. Schrauwen, D. Taillaert, D. Van Thourhout, T. F. Krauss, and R. Baets, "Compact and highly efficient grating couplers between optical fiber and nanophotonic waveguides," *Journal of Lightwave Technology* **25**, 151–156 (2007).
- [194] D. Benedikovic, P. Cheben, J. H. Schmid, D.-X. Xu, B. Lamontagne, S. Wang, J. Lapointe, R. Halir, A. Ortega-Moñux, S. Janz, and M. Dado, "Subwavelength index engineered surface grating coupler with sub-decibel efficiency for 220-nm silicon-on-insulator waveguides," *Optics Express* **23**, 22628–22635 (2015).
- [195] D. Benedikovic, C. Alonso-Ramos, P. Cheben, J. H. Schmid, S. Wang, D.-X. Xu, J. Lapointe, S. Janz, R. Halir, A. Ortega-Moñux, J. G. Wangüemert-Pérez, I. Molina-Fernández, J.-M. Fédéli, L. Vivien, and M. Dado, "High-directionality fiber-chip grating coupler with interleaved trenches and subwavelength index-matching structure," *Optics Letters* **40**, 4190–4193 (2015).

- [196] T. Watanabe, M. Ayata, U. Koch, Y. Fedoryshyn, and J. Leuthold, "Perpendicular grating coupler based on a blazed antiback-reflection structure," *Journal of Lightwave Technology* **35**, 4663–4669 (2017).
- [197] D. Benedikovic, C. Alonso-Ramos, S. Guerber, X. Le Roux, P. Cheben, C. Dupré, B. Szlag, D. Fowler, É. Cassan, D. Marris-Morini, C. Baudot, F. Boeuf, and L. Vivien, "Sub-decibel silicon grating couplers based on L-shaped waveguides and engineered subwavelength metamaterials," *Optics Express* **27**, 26239–26250 (2019).
- [198] X. Chen and H. K. Tsang, "Polarization-independent grating couplers for silicon-on-insulator nanophotonic waveguides," *Optics Letters* **36**, 796–798 (2011).
- [199] L. Chrostowski and M. Hochberg, *Silicon Photonics Design: from Devices to Systems* (Cambridge University Press, 2015).
- [200] "Infrared Fiber Optics — IRFlex Corporation," <https://www.irflex.com/products/irf-series/>.
- [201] "SMF-28®," <https://www.corning.com/worldwide/en/products/communication-networks/products/fiber/smf-28-ultra.html>.
- [202] G. Roelkens, D. V. Thourhout, and R. Baets, "High efficiency grating coupler between silicon-on-insulator waveguides and perfectly vertical optical fibers," *Optics Letters* **32**, 1495–1497 (2007).
- [203] D. Benedikovic, C. Alonso-Ramos, D. Pérez-Galacho, S. Guerber, V. Vakarín, G. Marcaud, X. Le Roux, E. Cassan, D. Marris-Morini, P. Cheben, F. Boeuf, C. Baudot, and L. Vivien, "L-shaped fiber-chip grating couplers with high directionality and low reflectivity fabricated with deep-UV lithography," *Optics Letters* **42**, 3439–3442 (2017).
- [204] Y. Wang, W. Shi, X. Wang, Z. Lu, M. Caverley, R. Bojko, L. Chrostowski, and N. A. F. Jaeger, "Design of broadband subwavelength grating couplers with low back reflection," *Optics Letters* **40**, 4647–4650 (2015).
- [205] Y. Li, D. Vermeulen, Y. De Koninck, G. Yurtsever, G. Roelkens, and R. Baets, "Compact grating couplers on silicon-on-insulator with reduced backreflection," *Optics Letters* **37**, 4356–4358 (2012).
- [206] X. Chen, K. Xu, Z. Cheng, C. K. Y. Fung, and H. K. Tsang, "Wideband subwavelength gratings for coupling between silicon-on-insulator waveguides and optical fibers," *Optics Letters* **37**, 3483–3485 (2012).
- [207] C. R. Doerr, L. Chen, Y.-K. Chen, and L. L. Buhl, "Wide bandwidth silicon nitride grating coupler," *IEEE Photonics Technology Letters* **22**, 1461–1463 (2010).
- [208] Z. Xiao, T.-Y. Liow, J. Zhang, P. Shum, and F. Luan, "Bandwidth analysis of waveguide grating coupler," *Optics Express* **21**, 5688–5700 (2013).
- [209] M. Passoni, D. Gerace, L. Carroll, and L. C. Andreani, "Grating couplers in silicon-on-insulator: the role of photonic guided resonances on lineshape and bandwidth," *Applied Physics Letters* **110**, 041107 (2017).
- [210] "CorActive - Select Cutoff Singlemode Fibers," <http://coractive.com/products/mid-ir-fibers-lasers/select-cutoff-singlemode-fiber/index.html>.
- [211] "Thorlabs," https://www.thorlabs.com/newgrouppage9.cfm?objectgroup_id=7062.
- [212] F. Fesharaki, N. Hossain, S. Vigne, M. Chaker, and K. Wu, "Accurate theoretical and experimental characterization of optical grating coupler," *Optics Express* **24**, 21027–21037 (2016).

- [213] D. Taillaert, W. Bogaerts, P. Bienstman, T. Krauss, P. Van Daele, I. Moerman, S. Versteuyft, K. De Mesel, and R. Baets, "An out-of-plane grating coupler for efficient butt-coupling between compact planar waveguides and single-mode fibers," *IEEE Journal of Quantum Electronics* **38**, 949–955 (2002).
- [214] D. Taillaert, F. Van Laere, M. Ayre, W. Bogaerts, D. Van Thourhout, P. Bienstman, and R. Baets, "Grating couplers for coupling between optical fibers and nanophotonic waveguides," *Japanese Journal of Applied Physics* **45**, 6071–6077 (2006).
- [215] P. Cheben, S. Janz, D. X. Xu, B. Lamontagne, A. Delâge, and S. Tanev, "A broad-band waveguide grating coupler with a subwavelength grating mirror," *IEEE Photonics Technology Letters* **18**, 13–15 (2006).
- [216] Y. Chen, T. Domínguez Bucio, A. Z. Khokhar, M. Banakar, K. Grabska, F. Y. Gardes, R. Halir, Í. Molina-Fernández, P. Cheben, and J.-J. He, "Experimental demonstration of an apodized-imaging chip-fiber grating coupler for Si₃N₄ waveguides," *Optics Letters* **42**, 3566–3569 (2017).
- [217] X. Chen, D. J. Thomson, L. Crudginton, A. Z. Khokhar, and G. T. Reed, "Dual-etch apodised grating couplers for efficient fibre-chip coupling near 1310 nm wavelength," *Optics Express* **25**, 17864–17871 (2017).
- [218] K. Qin, D. Gao, C. Bao, Z. Zhao, X. Zhou, T. Lu, and L. Chen, "High efficiency and broadband two-dimensional blazed grating coupler with fully etched triangular holes," *Journal of Lightwave Technology* **30**, 2363–2366 (2012).
- [219] P. R. Cooper, "Refractive-index measurements of paraffin, a silicone elastomer, and an epoxy resin over the 500–1500-nm spectral range," *Applied Optics* **21**, 3413–3415 (1982).
- [220] J. E. Midwinter and F. Zernike, "Experimental studies of evanescent wave coupling into a thin-film waveguide," *Applied Physics Letters* **16**, 198–200 (1970).
- [221] J. D. Sarmiento-Merenguel, A. Ortega-Moñux, J.-M. Fédéli, J. G. Wangüemert-Pérez, C. Alonso-Ramos, E. Durán-Valdeiglesias, P. Cheben, Í. Molina-Fernández, and R. Halir, "Controlling leakage losses in subwavelength grating silicon metamaterial waveguides," *Optics Letters* **41**, 3443–3446 (2016).
- [222] "University of Waterloo," <https://uwaterloo.ca/institute-nanotechnology/facilities-equipment/quantum-nanofab-facility>.
- [223] "University of Washington," <https://ebeam.wnf.uw.edu/ebeamweb/>.
- [224] A. Ortega-Moñux, J. Čtyroký, P. Cheben, J. H. Schmid, S. Wang, Í. Molina-Fernández, and R. Halir, "Disorder effects in subwavelength grating metamaterial waveguides," *Optics Express* **25**, 12222–12236 (2017).